Studies on nano-inclusion assisted enhancement in thermal conductivity and photo-thermal conversion of organic phase change materials

By

Amit Kumar Mishra

Enrolment No: CHEM02201404005

Indira Gandhi Centre for Atomic Research, Kalpakkam,
Tamil Nadu, India 603 102

A Thesis submitted to the
Board of Studies in Chemical Sciences

In partial fulfillment of requirements
for the degree of

DOCTOR OF PHILOSOPHY

of

HOMI BHABHA NATIONAL INSTITUTE

August, 2019

Homi Bhabha National Institute

Recommendations of the Viva Voce Board

As members of the Viva Voce Board, we certify that we have read the dissertation prepared by **AMIT KUMAR MISHRA** entitled "**Studies on nano-inclusion assisted enhancement in thermal conductivity and photo-thermal conversion of organic phase change materials**" and recommend that it may be accepted as fulfilling the thesis requirement for the award of Degree of Doctor of Philosophy.

______________________________ **Date:**

Chairman-**Dr. D. Ponraju**

______________________________ **Date:**

Convener/Guide-**Dr. John Philip**

______________________________ **Date:**

Member 1-Examiner

______________________________ **Date:**

Member 2- **Dr. T. R. Ravindran**

______________________________ **Date:**

Member 3- **Dr. V. Jayaraman**

______________________________ **Date:**

Member 4- **Dr. S. Ningshen**

______________________________ **Date:**

Member 5- **Dr. B. B. Lahiri (Technology advisor)**

Final approval and acceptance of this thesis is contingent upon the candidate's submission of the final copies of the thesis to HBNI.

I hereby certify that I have read this thesis prepared under my direction and recommend that it may be accepted as fulfilling the thesis requirement.

Date: **Dr. John Philip**

Place: (Guide)

CERTIFICATE

I hereby certify that I have read this thesis prepared under my direction and recommend that it may be accepted as fulfilling the thesis requirement.

Date: **Dr. John Philip**

Place: (Guide)

STATEMENT BY AUTHOR

This dissertation has been submitted in partial fulfillment of the requirements for an advanced degree at Homi Bhabha National Institute (HBNI) and is deposited in the library to be made available to the borrowers under the rules of HBNI.

Brief quotations from this dissertation are allowable without special permission, provided that accurate acknowledgement of the source is made. Requests for permission for extended quotation from or reproduction of this manuscript in whole or in part may be granted by the Competent Authority of HBNI when in his or her judgment the proposed use of the material is in the interest of scholarship. In all other instances, however, permission must be obtained from the author.

(Amit Kumar Mishra)

DECLARATION

I, hereby declare that the investigation presented in this thesis has been carried out by me. The work is original and has not been submitted earlier, as a whole or in part, for a degree/diploma at this or any other Institution/University.

(Amit Kumar Mishra)

List of Publications arising from the thesis

Journals

1. "Thermal conductivity enhancement in organic phase change material (phenol-water system) upon addition of Al_2O_3, SiO_2 and TiO_2 nano-inclusions", **Amit Kumar Mishra,** B. B. Lahiri and John Philip, *J. Mol. Liq.*, **2018**, *269*, 47-63.

2. "Effect of surface functionalization and physical properties of nanoinclusions on thermal conductivity enhancement in hexadecane phase change material", **Amit Kumar Mishra,** B. B. Lahiri and John Philip, *ACS Omega* , **2018**, *3*, 9487-9504.

3. "Nano-inclusion aided thermal conductivity enhancement of palmitic acid/di-methyl formamide phase change material for latent heat thermal energy storage", **Amit Kumar Mishra,** B. B. Lahiri, Vijay Solomon and John Philip, *Thermochim. Acta,* **2019**, *678*, 178309.

4. "Superior thermal conductivity and photo-thermal conversion efficiency of carbon black loaded organic phase change material", **Amit Kumar Mishra,** B. B. Lahiri and John Philip, *J. Mol. Liq.,* **2019**, *285*, 640-657.

5. "Carbon black nano particle loaded lauric acid-based form-stable phase change material with enhanced thermal conductivity and photo-thermal conversion for thermal energy storage", **Amit Kumar Mishra,** B. B. Lahiri and John Philip, *Energy,* **2020**, *191*, 116572.

Conferences

1. **Amit Kumar Mishra,** B. B. Lahiri and John Philip, "*Thermal conductivity enhancement in organic phase change materials loaded with nano-inclusions*", National Symposium on Nano Science and Technology (NSNST), Centre for Nano Science and Engineering (CeNSE), IISC, Bangalore, India, July 2-4, **2017**, pp 12-13.

2. **Amit Kumar Mishra,** B. B. Lahiri and John Philip, "*Nano-inclusion assisted enhancement in thermal conductivity of phenol-water mixture for room temperature energy storage applications*", International Conference on Nanotechnology: Ideas, Innovation & Initiatives (ICN3I), IIT Roorkee, India, December 6-7, **2017**, p 289.

3. **Amit Kumar Mishra,** B. B. Lahiri and John Philip, *"Effect of silica nano-inclusion on thermal conductivity enhancement in organic phase change materials"*, International Seminar on Advanced Nanomaterials (ISAN), University of Madras, Chennai, India, February 27–28, 2018, pp 88.

4. **Amit Kumar Mishra,** B. B. Lahiri and John Philip," *Carbon black and nickel nano-inclusions assisted thermal conductivity enhancement of an organic phase change material for thermal energy storage*", 5th International Conference on Nanoscience and Nanotechnology (ICONN-2019), SRM Institute of Science and Technology, Chennai, India, January 28-30, 2019, CP746. (**Best Poster Presentation Award**)

5. **Amit Kumar Mishra,** B. B. Lahiri and John Philip, "*Multi-walled carbon nanotubes assisted thermal conductivity enhancement of lauric acid based phase change material for solar thermal energy storage applications*", International Conference on Advanced Materials (ICAM-2019), Nirmalagiri College, Kerala, India, June 12-14, 2019, p 60. (**Best Oral Presentation Award**)

6. **Amit Kumar Mishra,** B. B. Lahiri and John Philip, "*Enhanced Thermal Conductivity and Photo-Thermal Conversion in Carbon Black Nanopowder Loaded Organic Phase Change Material*", 6th International Conference on Thermophysical and Mechanical Properties of Advanced Materials (THERMAM-2019), Cesme, Izmir, Turkey**,** September 22-24, p 31.

Other Publications (not included in the thesis)

1. "Effects of polymeric additives on thermal and electrical conductivity of nanofluids", S. A. Angayarkanni, **Amit Kumar Mishra** and John Philip, *J. Nanofluids,* **2016**, 5, 661-668.

(**Amit Kumar Mishra**)

ACKNOWLEDGEMENTS

First and foremost, I express my deepest gratitude to my advisor, **Dr. John Philip**, for his guidance and insightful suggestions. I am grateful to him for motivating me to aim high and for being understanding and patient with me throughout my PhD tenure. I am extremely thankful to my technology advisor, **Dr. B. B. Lahiri** for his kind guidance, help and resourcefulness to pursue my research works throughout my PhD tenure.

I am thankful to my doctoral committee chairman, **Dr. D. Ponraju** and members, **Dr. T. R. Ravindran**, **Dr. V. Jayaraman** and **Dr. S. Ningshen** for their insightful comments and encouragement. I also thank my former doctoral committee members, particularly **Dr. M. P. Antony**, for valuable suggestions.

I thank **Dr. A. K. Bhaduri**, Director of IGCAR, and **Dr. G. Amarendra**, Director of Metallurgy and Materials Group, for giving me the opportunity to carry out my research works at Indira Gandhi Centre for Atomic Research (IGCAR). I express my gratitude to all the former directors for their support. I am also thankful to **Dean, HBNI, Chemical Sciences** for his kind help.

I thank all members of SMART section for their help and encouragement. I am particularly thankful to **Dr. S. A. Angayarkanni** and **Dr. A. W. Zaibudeen**, for training me in thermal conductivity measurements and for their valuable suggestions; **Mr. S. Kalyani** and **Mrs. C. Anushree,** for their help towards X-ray diffraction and differential scanning calorimetry measurements; **Mrs. Sangeetha Jayakumar** and **Dr. M. Vadivel,** for their help towards atomic force microscopy studies. I thank all the research scholars of SMART, **Mrs**. **Sithara Vinod**, **Mr. Surojit Ranoo**, **Mr. Dillip Kumar Mohapatra**, **Ms. Manali Nandy**, and **my batchmates** for all the fun and lively discussions throughout my PhD tenure.

Last, but not the least, I thank my parents, brothers and sister for everything they have done for me.

CONTENTS

Chapter 1

Introduction

Chapter 2
Experimental methods

Chapter 3
Effects of functionalization and physical properties of nano-inclusions on thermal conductivity enhancement of n-hexadecane based phase change materials

Chapter 4
Tuning of phase transition temperature of phenol and palmitic acid-based phase change materials and thermal conductivity enhancement upon loading with nano-inclusions

Chapter 5
Carbon black nano powder assisted enhancement in thermal conductivity and photo thermal conversion in paraffin wax and lauric acid-based phase change materials

Chapter 6
Development of binary form-stable PCM using palmitic acid and n-hexadecane

Chapter 7

Conclusions and recommendations for future work

SYNOPSIS

Research and development of green energy materials and associated technologies picked up momentum due to low carbon energy policies and rapid industrialization. Effective conversion, storage and management of renewable energy sources and energy harvesting are essential to close the gap between the supply and demand of energy and to curtail further environmental degradation. Thermal energy storage has been proposed for intermediate storage of solar energy, waste heat recovery from industrial processes and thermoregulation applications. Among different types of thermal energy storage schemes, latent heat thermal energy storage using phase change materials (PCM) has an ability to store excess energy at a constant or near constant temperature, corresponding to its phase transition temperature of the PCM and has a high storage density. For a typical temperature variation of 20 ^{0}C, approximately 3-4 times higher thermal energy storage per unit volume can be accomplished using a latent heat thermal energy storage system, as compared to a sensible heat storage system. Based on the chemical compositions, PCMs are categorized into inorganic and organic PCMs. The organic PCMs (like fatty acids, alcohols and long chain alkanes) have several advantages bovver their inorganic counterparts, which include high latent heat, lower vapour pressure during melting, self-nucleating ability, low degree of supercooling, thermal repeatability even after a large number of melting/freezing cycles, chemical stability and non-toxicity. In liquid-solid phase transition, thermal energy is stored and retrieved at near isothermal conditions during melting and solidification, respectively. Organic PCMs have found wide spread applications in cooling/heating of buildings, cooling of electronic devices and domestic/commercial refrigeration, solar water/air heater, solar receiver of direct steam generator of concentrated solar power plants, etc. In spite of immense industrial benefits of thermal energy storage using organic PCMs, the practical applicability of these materials is severely restricted due to their inherently low thermal conductivity. Hence, dispersing high thermal conductivity nano-inclusions within the continuous medium of PCM has been attempted to enhance thermal conductivity of the PCMs. However, the role of particle loading, surface functionalization, nature and physical properties of the nano-inclusions, the effects of size, shape and aspect ratio of these nano-inclusions are poorly understood. Also, the understanding of the exact mechanism of nano-inclusion assisted thermal conductivity enhancement in PCMs is unclear. Further, material losses, due to leakage, during solid-liquid phase transition warrants further studies on form-stable PCMs. These served as a motivation for undertaking the present problem. The major objectives of this thesis are (i) to probe the role of surface functionalization of nano-inclusions on long term thermal stability and thermal conductivity enhancement of PCMs loaded with nano-inclusions; (ii) to tune the phase transition temperature of composite PCMs by varying the constituent concentrations and thermal conductivity enhancements in these tuned PCMs by loading with various nano-inclusions; (iii) to probe the role of nano-inclusion concentration on thermal conductivity enhancement; (iv) to investigate micro-scale aggregation phenomena and formation of percolating network during solidification of the PCMs; (v) to study photo-thermal conversion of carbon black nano-inclusion loaded PCMs and the role of particle loading on conversion efficiency and (vi) to demonstrate a form-stable PCM with high latent heat storage capacity and phase transition temperature around 19 ^{0}C. The thesis consists of seven chapters and details of the chapters are summarized in the following sections. **Chapter 1** gives a brief introduction on various modes of thermal energy storage, classification of PCMs and some practical applications of latent heat thermal energy storage systems. The limitations of PCMs due to low thermal conductivity and material losses because of leakage during first order solid-liquid phase transitions and various strategies adopted to circumvent these limitations are also briefly discussed. **Chapter 2** describes the experimental methods for sample preparation, characterization of the nano-inclusions, PCMs, measurement of thermal conductivity and photo-thermal conversion efficiency. Various characterization tools, such as powder X-ray diffraction (XRD), small angle X-ray scattering (SAXS), dynamic light scattering (DLS), Fourier transform infrared spectroscopy (FTIR), scanning electron microscopy (SEM), atomic force microscopy (AFM), differential scanning calorimetry (DSC), infrared thermography (IRT), refractive index (RI) measurement and phase contrast optical microscopy are briefly discussed. This was followed by a detailed description of thermal conductivity measurement protocol employing the transient hot wire method. **Chapter 3** describes the role of surface functionalization and physical properties of nano-inclusions on thermal conductivity enhancement during liquid-solid phase transition of hexadecane based PCMs, upon loading with six different nano-inclusions, viz. carbon black nano powder (CBNP), nickel nanoparticles (NiNP), copper nanoparticles (CuNP), silver nanowires (AgNW), multi-walled carbon nanotubes (MWCNT) and graphene nanoplatelets (GNP). Experimental findings indicated that surface functionalization of the GNP nano-inclusions with oleic acid resulted better thermal stability of the nano-inclusion loaded PCMs, without significant reduction in thermal conductivity enhancement. **Chapter 4** presents the results of tuning phase transition temperature of composite PCMs, viz. phenol-water system and palmitic acid/di-methyl formamide (PA-DMF) mixtures. Experimental results indicated enhanced thermal conductivity during first order liquid-solid phase transition in the phenol-water system loaded with four different nano-inclusions. **Chapter 5** discusses CBNP assisted enhancement in thermal conductivity and photo-thermal conversion in paraffin wax (PW) and lauric acid (LA) based PCMs with varying loading concentrations. The superior volume filling capacity and fractal nature of CBNP aggregates enabled the formation of closely bound percolation network with reduced thermal barrier resistance that gave rise to significant thermal conductivity enhancements. Additionally, photo-thermal conversion of the CBNP loaded PCMs were enhanced by ~ 84 and 135 % for the PW and LA based PCMs loaded with 2.5 and 3.5 wt. % of CBNP nano-inclusions. This chapter also discusses the results of optical phase contrast video microscopy, where direct experimental evidence for microscale aggregation and cluster formation during solidification of the PCMs is observed. **Chapter 6** describes the formulation, thermophysical characterization and thermal conductivity enhancement of palmitic acid/hexadecane (PA-HD) based binary form stable PCM. For thermal cycling up to 40 ^{0}C, no leakage was observed and the binary PCM retained the shape and structural integrity, which are immensely beneficial for practical applications. The significant enhancement in thermal conductivity observed in the solid phase for the form-stable PCM loaded with CBNP nano-inclusions is attributed to the effective heat conduction through the quasi 2D- percolating networks. **Chapter 7** presents a summary of the results obtained, along with the conclusions drawn and recommendations for future work.

LIST OF FIGURES

LIST OF TABLES

LIST OF ABBREVIATIONS

2D	2 dimensional
AFM	Atomic force microscopy
AgNW	Silver nanowires
ASHRAE	American Society of Heating, Refrigerating and Air-conditioning Engineers
ATR	Attenuated total reflection
BTMS	Battery thermal management system
CA	Capric acid
CBNP	Carbon black nanopowder
CES	Chemical energy storage systems
CNF	Carbon nanofibers
CSP	Concentrated solar power plants
CTAB	Cetyl trimethyl ammonium bromide
CuNP	Copper nanoparticles
DFT	Density functional theory
DLS	Dynamic light scattering
DMF	Di-methyl formamide
DSC	Differential scanning calorimetry
EMT	Effective medium theory
FCC	Face centered cubic structure
FTIR	Fourier transform infrared
FWHM	Full width at half maxima
GNP	Graphene nanoplatelets
GNP-UC	Uncoated graphene nanoplatelets
HC	Hamilton-Crosser model
HD	n-hexadecane
HP	Hydrophobic
IR	Infrared
IRT	Infrared thermography
JCPDS	Joint Committee on Powder Diffraction Standard
LA	Lauric acid
LHTES	Latent heat thermal energy storage systems
MA	Myristic acid
MG	Maxwell-Garnett model
MWCNT	Multi-walled carbon nanotube
NETES	Nano-enhanced thermal energy storage
NiNP	Nickel nanoparticles
OA	Oleic acid
P	Phenol molecules
PA	Palmitic acid
PCMs	Phase change materials
PEO	Polyethylene oxide
PH	Phenol
PPO	Poly propylene oxide
PW	Paraffin wax
RI	Refractive index

ROI	Region of interest
SA	Stearic acid
SAXS	Small angle X-ray scattering
SDBS	Sodium dodecyl benzene sulphonate
SEM	Scanning electron microscopy
SHTES	Sensible heat thermal energy storage systems
TEM	Transmission electron microscope
TES	Thermal energy storage
TGA	Thermogravimetric analysis
W	Water molecules
XRD	Powder X-ray diffraction

LIST OF SYMBOLS

d_{hkl}	Spacing between crystallographic planes
θ	Bragg angle
n	Order of diffraction
λ_X	Wavelength of the incident X-ray
h, k & l	Miller indices of the crystallographic plane
d_{cryst}	Average crystallite size
β	full width at half maxima
$I(q)$	Scattering intensity
N	Number of objects
$F(q)$	Form factor
$S(q)$	Structure factor
q	Scattering wave vector
d_{np}	Diameter of nanoparticles
$\Delta\rho_e$	Electron density difference
V_p	Particle volume
$P(r)$	Distance distribution function
M'	Numerical damping factor
T^O	Onset temperature
T^P	Peak phase transformation temperature
T^E	Endset temperature
T_0	Initial temperature
Q_h	Heat flux per unit length
γ_a	Euler’s constant
r_a	Radial distance
α	Thermal diffusivity of the medium
ΔT_1	Temperature difference for time t_1
ΔT_2	Temperature difference for time t_2
$u(k)$	Standard measurement uncertainty in k
k_a/k_b	Thermal conductivity ratios
M_{cam}	Radiance received by the infrared detector
M_{obj}	Radiance emitted by the object under investigation
M_{env}	Radiance emitted by the surrounding
M_{atm}	Radiance emitted by the atmosphere
τ	Atmospheric transmittance
ε	Surface emissivity
k	Effective thermal conductivity of the nano-inclusion loaded PCM (entire system)
k_f	Thermal conductivity of the base fluid
k_{de}	Thermal conductivity of the cluster with dead ends alone
k_p	Total thermal conductivity of the cluster
k_c	Bulk thermal conductivity of the nano-inclusions
ϕ_{de}	Volume fraction of the nano-inclusions belonging to the dead-ends alone
ϕ_c	Volume fraction of the nano-inclusion within a cluster
ϕ_{bb}	Volume fraction of nano-inclusions belonging to the back-bone
d_f	Fractal dimension of the clusters

N_c	Number of nano-inclusions within a cluster
ϕ_p	Total volume fraction of nano-inclusions added to the PCM
ϕ_a	Volume fraction of cluster
d_1	Chemical dimension
k_c	Total thermal conductivity of the clusters
k_{nc}	Homogenized thermal conductivity
g	The aspect ratio of the cluster with respect to the nano-inclusions
R_g	Radius of gyration of the cluster
a	Size of the nano-inclusions
δ_R	Hypothetical Kaptiza radius
$S(r,t)$	Stress field at location r and time t
$E(t)$	Relaxation modulus function at time t
$e_0(\tau)$	Instantaneous mean strain at time $t = \tau$
$T(r,\tau)$	Temperature profile at a particular location (r) at instantaneous time τ
ν	Poisson’s ratio
α_l	Coefficient of thermal expansion
T_s	Solidification temperature
T_m	Melting temperature
k_f	Thermal conductivity of the base medium
V_s	Sedimentation velocity
M	Numerical constant (~ 4.6) for sedimentation velocity
V_0	Sedimentation velocity at infinite dilution
ϕ	Effective volume fraction of the nano-inclusions
R_K	Average interfacial thermal resistance (Kapitza resistaqnce)
k_g	Intrinsic thermal conductivity
k_x	Effective thermal conductivity along the in-plane
k_z	Effective thermal conductivity through thickness directions
L	Length
L_t	Thickness
k_m	Thermal conductivity of the composite matrix (without any nano-inclusions) in the solid state
H	Geometrical factor
k_{sp}	Thermal conductivity of the surface modified nanoparticles
k_s	Thermal conductivity of the surfactant (i.e. coating material)
k_p	Thermal conductivity of the uncoated nanoparticles
a_p	Radius of the nanoparticle
δ_s	Coating thickness
t_m	Maximum observation time
n_D	Refractive indices of the binary mixture
ϕ_1	Volume fractions of first component
ϕ_2	First component second component
ΔT_f	Freezing point depression
T_{fr}	Freezing point of the solvent and solution
K_f	Freezing point depression constant or cryoscopic constant
m_l	Molality
c_1	Van’t Hoff factor
$\Delta\rho$	Density difference
s	Synergistic effect

k_{CB}	Thermal conductivity of CBNP nano-inclusions
β_1& β_2	Empirical constants
ΔT_{max}	Maximum temperature rise
σ_{eff}	Total extinction coefficient
σ_{matrix}	Extinction coefficient of hot matrix (PCM)
σ_{CBNP}	Extinction coefficient of CBNP
λ	Incident wavelength
k_{matrix}	Complex component of the refractive index of the host matrix
Q_S	Scattering efficiency
Q_A	Absorption efficiency
D	Typical nano-inclusion dimension
Q_E	Total extinction efficiency
a_n & b_n	Mie scattering coefficients
ΔH_{PCM}	Latent heat of the nano-inclusion loaded PCMs
ΔH_{LA}	Experimentally determined latent heat for pristine LA
ε	Mass percentage of the host matrix in the nano-inclusion loaded PCMs
c_p	Specific heat capacity
T_i	Initial temperature
T_f	Final temperature
m	Mass
Q_{sen}	Energy storage in SHTES system
Q_{chem}	Energy storage in CES system
Δh	Heat of reaction
a_r	Extent of conversion
Q	Heat storage capacity of a LHTES
C_{ps}	Specific heat in the solid state
C_{pl}	Specific heat in the liquid state
a_m	Melting fraction
Δh_m	Specific enthalpy change
k_{eff}	Effective thermal conductivity
k_p	Thermal conductivity of the nanoparticles
Δ_{BM}	Volume fraction dependent Bruggeman constant
n_{HC}	Shape factor
ψ_s	Sphericity of the dispersed nanoparticles
β_m	Running variable used in Maxwell's effective medium theory
α_m	Running variable for Kapitza resistance in Maxwell's effective medium theory
k_{CB}	Thermal conductivity of CBNP
k_m	Thermal conductivity of n-hexadecane in the solid state without any nano-inclusions

Chapter 1

Introduction

Chapter 1 | Introduction

1.1 Introduction

Proper understanding and manipulation of thermal energy remains the cornerstone of technological progress of human race. Towards the middle of 19th century, path breaking scientific works of Joule and Clausius established the modern theory of heat and thermodynamics and conservation of heat energy was established as the principal scientific law governing heat flow. Later contributions of Boltzmann and others paved the way for kinetic theory of heat and established the concept of entropy as the driving force for heat transfer. Heat and thermodynamics revolutionized process industries, chemical and metallurgical plants, steam engines, combustion engines, steel and alloy making. Thermal energy remains the single most significant driving force towards industrial progress and technological marvels of mankind.

World-wide, fossil-fuel plants are the primary sources of energy and depletion of the fossil-fuel reserves and the ever-increasing gap between the demand and supply had resulted in dedicated scientific research on energy conservation, storage and management [1]. Further, stricter carbon-emission norms, environmental degradation and pollution control call for effective storage, conversion and optimal utilization of energy to close the energy-efficiency gap [2]. Due to the huge demand of thermal energy, improvement in thermal energy management will result in significant savings on energy economy [3]. Thermal energy storage has been proposed as the key element for efficient management and optimal usage of renewable energy and industrial waste heat [1, 3-5]. Thermal energy storage using sensible, latent and thermochemical modes have been successfully demonstrated [1, 6-22]. In the quest of optimizing energy storage, management and fabrication of thermal energy storage materials with higher energy storage density and desired thermo-physical properties, nanotechnology has been successfully adopted to prepare nano-enhanced thermal energy storage (NETES).

The word “nano” is derived from the Greek word ‘nanos’ meaning dwarf and nano scale indicate a length scale of 10^{-9} m (1 inch ~ 25, 400, 000 nm). Nanotechnology is largely defined as the science, engineering and technology at the nanoscale and is focussed on fundamental understanding and applications of such nano-objects in various branches of science, like physics, chemistry, biology, material science, energy and engineering [23]. Nanotechnology has found widespread application in various sustainable energy solutions [24], viz. photovoltaic technology [25, 26], hydrogen production [27, 28], hydrogen transport [29], fuel cells [30, 31], supercapacitors [32, 33], rechargeable batteries [34, 35], nanofluid coolants [36-51] and thermal energy storage [52-71].

1.2 Energy sources

The most widely used energy sources can be classified into two categories, viz. renewable and non-renewable sources. Solar-energy, geothermal, wind, wave and tide, biomass and hydroelectric energy sources are renewable sources [72]. On the other hand, fossil-fuel power plants (coal and natural gas based) and nuclear power plants are the major non-renewable energy sources. The following sections briefly discuss the most prominent energy sources.

a) Fossil-fuel power plants

Fossil fuel power plants are the most widely used energy sources in the world. Though, ~ 85 % of world’s energy demand is met with these kinds of power plants, fossil-fuel power plants also contribute to ~ 40 % of man-made CO_2 emissions, which is a global concern [3]. The fossil-fuel plants utilize, coal, natural gas and petroleum as primary fuels and plant thermodynamics is based on Rankine (steam as working fluid) or Brayton (air as working fluid) cycles with ~ 35 % efficiency. Though fossil-fuel power plants are the most popular source of energy, strict emission norms, depleting fuel levels and high parasitic losses have made alternative energy sources ecologically attractive. Further, research is also going on to improve the efficiency of fossil-fuel power plants.

b) Nuclear power plants

Nuclear power plants generate electricity from controlled nuclear fission of nuclear fuels (primarily uranium based). Though inherently safe, nuclear power plants are complex and requires highly trained man-power for operation. World-wide efforts are pursued to construct and operate more advanced nuclear powerplants with high efficiency and load cycling capabilities [3].

c) Geothermal energy sources

Due to planetary accretion and radioactive decay, huge amount of heat is stored in the layers below the earth's thin crust. Geo-thermal energy is renewable in the long term and geothermal power plants are mostly located near the earth's plate tectonics, where geo-thermal fluid is available at comparably lower depths with temperature ~ 180 ^{0}C, which is used for steam generation [73].

d) Biomass and other renewable power plants

Biomass power plants generate power from combustions of wood or municipal wastes, bio-gas and bio-fuels like ethanol. Though bio-mass plants emit CO_2, unlike fossil-fuel power plants, biomass plants are renewable [3]. Hydropower or tidal plants utilize the kinetic energy of water flow or tides. On the other hand, wind energy utilizes the kinetic energy of natural air flow.

e) Solar power plants

At present estimation, solar energy will be available for another 4 billion years and therefore it is one of the most reliable renewable sources of energy. Solar energy harvesting is under-utilized and world-wide active research is being pursued for optimizing the solar energy utilization. At the earth's surface, intensity of solar energy ~ 1000 W/m^2, which is sufficient for low energy applications [3]. For high energy applications, solar photo-voltaic plants (direct conversion of solar energy to electrical energy) or concentrated solar power plants (conversion of concentrated solar energy to thermal energy) are used [3, 74].

f) Industrial waste heat

Excess heat generated by various industrial processes, including fossil-fuel and nuclear power plants, are usually wasted, thereby adding more CO_2 emissions. In order to reduce greenhouse emissions, effective utilization of available energy resources and to optimize plant efficiency, industrial waste heat recovery is one of the most prudent approach [3]. Thermal energy storage using passive and active approaches are generally used for recovery and utilization of industrial waste heat in beverage, food, textile, paper, wood, chemical industries [75].

1.3 Thermal energy storage (TES) systems

In today's world, the main forms of energy consumption at the user-end are electrical, heat and mechanical work. Improvement in management of thermal energy is one of the most sagacious and prudent approach for energy economy and thermal energy storage (TES) systems positively impact energy security and green house emission. Different large-scale thermal energy storage systems have been coupled with renewable energy sources to improve the energy conversion efficiency and availability of power during off-peak hours. **Table 1.1** describes a few industrially commissioned large-scale operational thermal energy storage systems [17, 18, 76, 77]. Based on the type of heat energy involved, thermal energy storage systems are classified into three types of systems, viz. sensible heat thermal energy storage systems (SHTES), chemical energy storage systems (CES) and latent heat thermal energy storage systems (LHTES). **Fig. 1.1** shows the classification of thermal energy storage systems.

Table 1.1 Details of a few industrially commissioned large-scale thermal energy storage systems.

Location	Capacity (MWh)	Energy source	TES system	Applications	Reference
Nevada, USA	105	Solar	Solar salt	Electrical power generation	[18]
Themes, France	40	Solar	Hitect salt	Electrical power generation	[18]
Marstal, Denmark	19, 000	Solar + biomass	Water	District heating network	[76]
Friedrichshafen, Germany	4, 106	Solar + natural gass	Water	District heating network	[77]
Kungalv, Sweden	90, 000	Industrial waste heat	Water	District heating network	[76]
La Florida Badajoz, Spain	1, 010	Solar parabolic trough	Molten salt	Electrical power generation	[17]

1.3.1 Sensible heat thermal energy storage (SHTES) systems

Sensible heat thermal energy storage (SHTES) systems are the most commonly used thermal energy storage systems. Less technical complexity, low cost, mature technology and long lifetime are the major benefits of SHTES systems [5]. SHTES have been used for centuries, where the major drawback is the requirement of larger volume, as compared to other kinds of thermal energy storage systems [52]. In SHTES systems, the energy storage materials (solids, liquids or salts) absorb or release heat during the charging or discharging process without undergoing phase transformation.

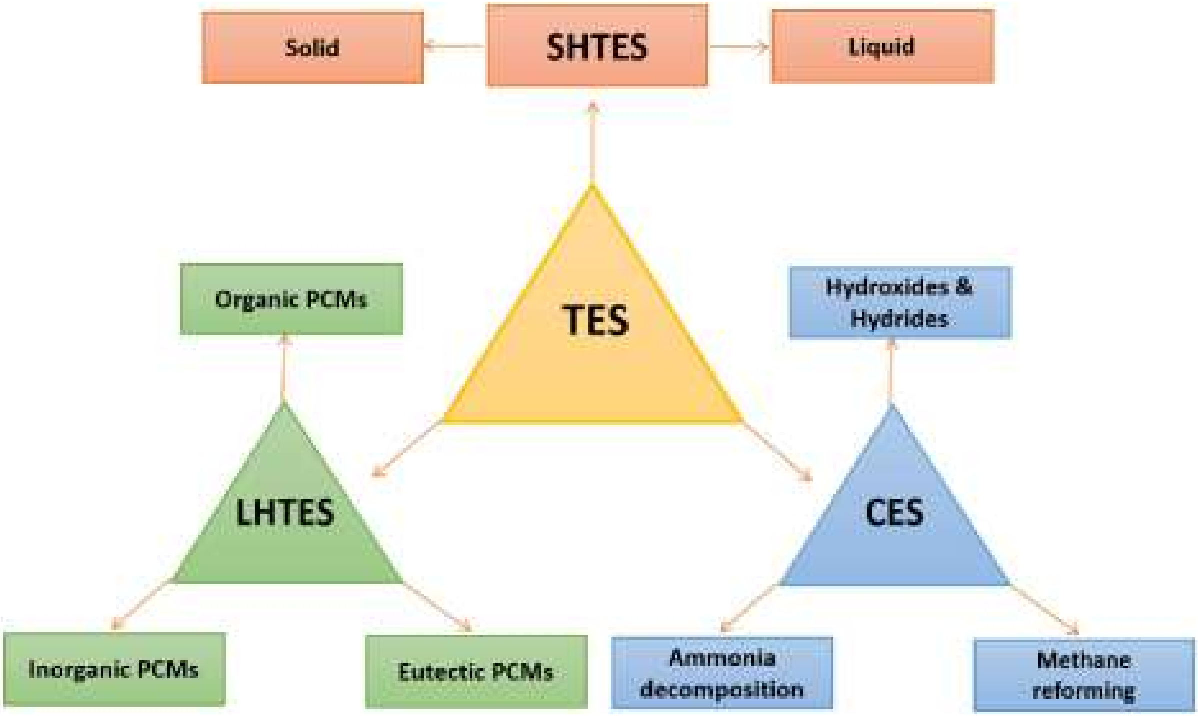

Figure 1.1 Classifications of thermal energy storage (TES). SHTES, CES and LHTES indicate sensible heat thermal energy storage, chemical energy storage and latent heat thermal energy storage systems, respectively.

During charging, temperature of the storage material increases due to heat transfer from the source to the material, which is subsequently extracted during the discharging process. The amount of energy storage depends on the specific heat capacity (c_p) and temperature change during the charging/discharging cycles. The energy storage in SHTES system (Q_{sen}) is expressed by the following equation [78, 79].

$$Q_{sen} = \int_{T_i}^{T_f} mc_p dT = mc_p(T_f - T_i) \tag{1.1}$$

Here, T_i and T_f indicate initial and final temperature and m is the mass of the SHTES system. Among various storage materials, water is the most beneficial one due to the highest specific heat capacity and low cost. However, several solids, liquids and salts have been used for sensible heat storage systems and Table 1.2 tabulates a few [5, 22]. The average density and thermal conductivity and heat capacity values are also indicated Table 1.2.

Table 1.2 Details of a few candidate materials for sensible heat thermal energy storage along with the operating temperature range, average density, thermal conductivity and specific heat capacity.

Type of media	Storage media	Temperature range (^{0}C)	Average density (kg/m^3)	Average thermal conductivity (W/mK)	Average specific heat capacity (kJ/kgK)
Liquid	Mineral oil	200-300	770	0.12	2.6
	Silicon oil	300-400	900	0.10	2.1
	Synthetic oil	250-350	900	0.11	2.3
	Liquid sodium	270-530	850	71.0	1.3
Solid	Cast iron	200-400	7200	37.0	0.56
	Cast steel	200-700	7800	40.0	0.60
	Sand-rock Mineral oil	200-300	1700	1.0	1.30
	Reinforced concrete	200-400	2200	1.5	0.85
	NaCl (solid)	200-500	2160	7.0	0.85
	Silica fire bricks	200-700	1820	1.5	1.0
	Magnesia fire bricks	200-1200	3000	5.0	1.15
Salts	Salt-ceramics $NaCO_3$-$BaCO_3$/MgO	500-850	2600	5.0	420
	Carbonate salts	450-850	2100	2.0	1.8
	Nitrite salts	250-450	1825	0.57	1.5
	Nitrate salts	265-565	1870	0.52	1.7

1.3.2 Chemical energy storage (CES) systems

During reversible chemical reactions, molecular bonds are broken and reformed in a reversible manner. During chemical reactions, there exist a difference between the enthalpy of the products and the reactants, which is called the heat of the reactions. Chemical reactions are classified as endothermic or exothermic depending on whether heat is absorbed or released during the reaction. In chemical energy storage (CES) systems, the thermal energy associated with a chemical reaction is stored. The amount of energy stored in a CES system (Q_{chem}) is expressed by the following equation [5].

$$Q_{chem} = m a_r \Delta h \tag{1.2}$$

Here, m, Δh and a_r indicate the mass of the storage material, heat of reaction and extent of conversion, respectively. The major TES systems include ammonia decomposition, methane reforming, metal hydride, redox and carbonate decomposition systems [5]. The major TES systems along with the relevant chemical equations and reaction temperatures are listed in **Table 1.3** [5, 7].

Table 1.3 Common chemical energy storage systems (CES) along with the chemical reactions and reaction temperatures.

CES system	Reaction equation	Reaction temperature (^{0}C)
Ammonia decomposition system	$NH_3 = \frac{1}{2}N_2 + \frac{3}{2}H_2$	400-700
Methane reforming system	$CH_4 + CO_2 = 2CO + 2H_2$ $CH_4 + H_2O = CO + 3H_2$	700-860 600-950
Metal hydride system	$MgH_2 = Mg + H_2$	250-500
The redox system	$2BaO_2 = 2BaO + O_2$ $2Co_3O_4 = 6CoO + O_2$	127-1027 700-850
Carbonate decomposition system	$CaCO_3 = CaO + O_2$	700-1000
Inorganic hydroxide system	$Ca(OH)_2 = CaO + H_2O$ $Mg(OH)_2 = MgO + H_2O$	350-900 100-167

Energy storage density of CES system is ~ 15 times that of SHTES systems and ~ 6 times of latent heat thermal energy storage systems [8]. Another major benefit of TES system is that theoretically, a closed system with reactants and products separated can store the energy indefinitely, which is essential for trans-regional transport of thermal energy [5]. The working principle and long-term energy storage of a typical CES system is schematically shown in **Fig. 1.2**. In the first step, the reactant C absorbs thermal energy, in a region where heat is in abundance, to form the products A and B during an endothermic charging process. The products A and B are separately encapsulated and transported to a region, where heat is not in abundance (cold environment). If the physical barrier between the products A and B is removed, then A and B chemically reacts together to form C and heat is extracted during the discharging process, which is exothermic in nature. The concept of CES systems is relatively new and the technology is immature. However, the high energy storage density and possibility of transregional transport have made CES one of the most promising thermal energy storage solution.

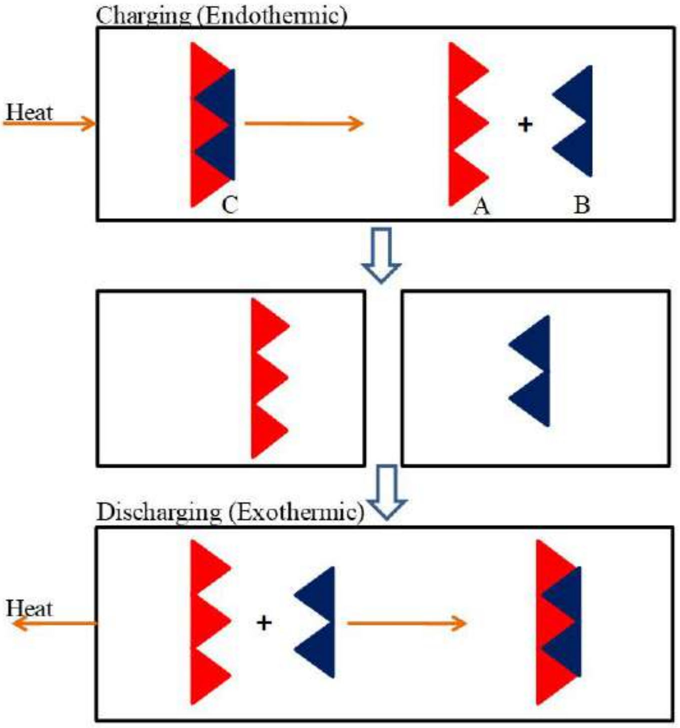

Figure 1.2 Schematic illustration of a chemical energy storage (CES) system.

1.3.3 Latent heat thermal energy storage (LHTES) systems

Latent heat thermal energy storage (LHTES) systems store thermal energy in the form of latent heat during phase transitions (like solid to liquid) of materials. Latent heat storage is one of the key areas of research in the last few decades due to its ability to store excess energy, that would otherwise be wasted, at a constant or near constant temperature corresponding to the phase transition temperature of the PCM and its high storage density [52, 80]. It has been reported that a typical latent heat storage system can store 3-4 times higher thermal energy per unit volume, as compared to a sensible heat storage system for a temperature increment of 20 ^{0}C [4]. **Fig. 1.3** schematically shows the sensible and latent heat thermal energy storage principles. The heat storage capacity of a LHTES can be expressed by the following equation [4].

$$Q = \int_{T_i}^{T_m} m C_{ps} dT + m a_m \Delta h_m + \int_{T_m}^{T_f} m C_{pl} dT \tag{1.3}$$

Here, Q, m, C_{ps}, C_{pl}, T_m, T_i, T_f, a_m and Δh_m indicate heat storage capacity, mass of the storage material, specific heat in the solid state, specific heat in the liquid state, melting point, initial temperature ($< T_m$), final temperature ($> T_m$), melting fraction and specific enthalpy change, respectively. The LHTES materials also absorb sensible heat before and after phase transitions. It is evident from Eq. 1.3 that the heat storage capacity of a LHTES is partly due to sensible heat and partly due to latent heat. It can be further seen from Eq. 1.3 that LHTES heat storage capacity primarily depends on the phase transition temperature and the associated enthalpy change.

The most widely used materials for LHTES are phase change materials (PCMs), which are discussed in the subsequent sections. **Table 1.4** compares the properties, advantages and drawbacks of three types of thermal energy storage systems, viz. sensible heat thermal energy storage, chemical energy storage and latent heat thermal energy storage systems [5].

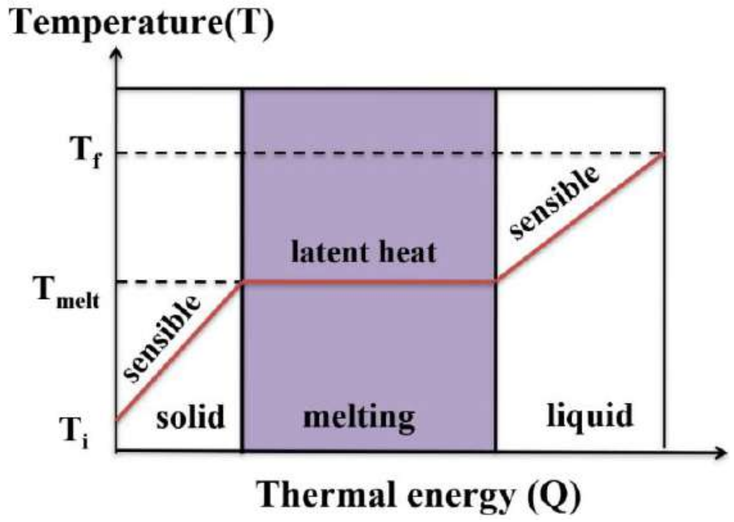

Figure 1.3 Schematic illustration of sensible and latent heat thermal energy storage principles.

Table 1.4 Properties, advantages and drawbacks of three types of thermal energy storage systems, viz. sensible heat thermal energy storage (SHTES), chemical energy storage (CES) and latent heat thermal energy storage (LHTES) systems.

Properties	SHTES	CES	LHTES
Heat loss	Significant heat loss over time	Small heat loss	Significant heat loss over time
Energy density	Low (0.2 GJ/m^3)	Very high (0.5-3 GJ/m^3)	High (0.3-0.5 GJ/m^3)
Temperature range	Charging step temperature	Ambient temperature	Charging step temperature
Transport	Small distance	Unlimited theoretically	Small distance
Lifetime	Long	Theoretically indefinite. Practically depends on reactant degradation and side reactions	Limited
Advantages	Low cost and mature technology	High storage density, long distance possibility, low heat losses	Small volume and moderately high energy storage density
Disadvantages	Significant heat loss over time, Large volume needed	Technologically complex, high costs	Low thermal conductivity, materials leakage during phase transition, significant heat losses
Technical complexity	Simple	Complex	Less complex

1.4 Phase change materials (PCMs)

Phase change materials (PCMs) are materials that absorb (during melting) and release (during solidification) relatively large amounts of latent heat during phase transition at a nearly constant temperature. The use of phase change material for latent heat thermal energy storage applications has attracted much attention in the recent years due to their self-nucleating properties, chemical stability, high heat of fusion, safe and non-reactive nature [81]. The temperature of PCMs increases during the heating process (charging) up to the phase transition temperature (melting point) and subsequently the stored energy is extracted during cooling (discharging process). **Fig. 1.4a** schematically shows the working principle of PCMs. During absorption of thermal energy, the vibrational energy of the molecules increases ultimately leading to breaking of bonds during the melting process. The latent heat of phase transition is associated with the energy required for overcoming the molecular interactions and breaking of bonds during the melting process [82]. During cooling solidification occurs and the energy gained is available for extraction. **Fig. 1.4b** schematically shows the flow of thermal energy during solidification and melting in a PCM.

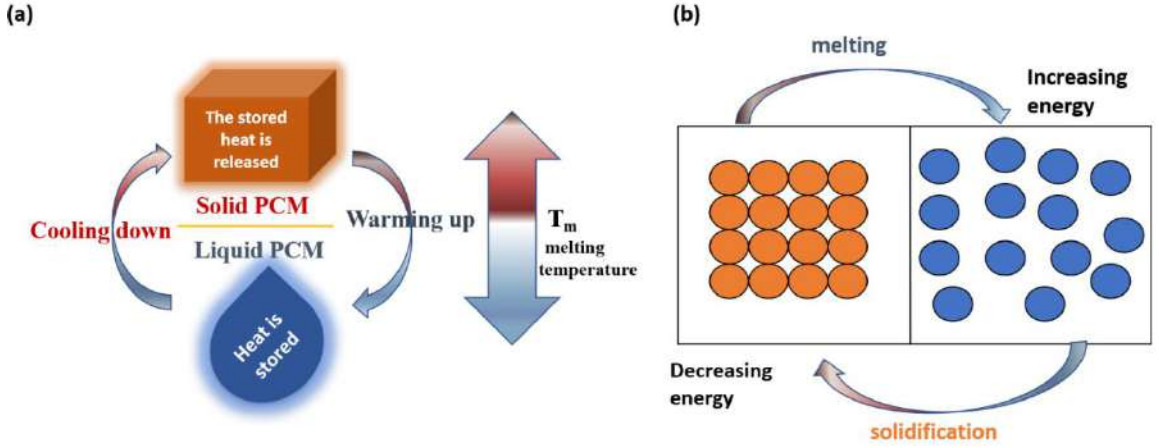

Figure 1.4 (a) Schematic illustration of the working principle of a typical PCM. (b) Schematic illustration of thermal energy flow during melting and solidification of a PCM.

1.4.1 Classifications of phase change materials

The PCMs are classified based on the range of phase transition temperature or types of phase transition and nature of PCMs (organic or inorganic) [1, 83]. PCMs which undergo phase transition below 15 ^{0}C are classified as low temperature PCMs. The low temperature PCMs are suitable for applications in food industry, air conditioning and low temperature solar-thermal applications [84]. PCMs with phase transition temperature in the range of 15-90 ^{0}C are classified as mid-temperature PCMs, which are found to be suitable for solar-thermal, bio-medical, textile, electronic and thermoregulation applications. On the other hand, high temperature PCMs (phase transition temperature beyond 90 ^{0}C) are useful for industrial and aerospace applications [80].

PCMs are also classified by the nature of phase transition, viz. solid-solid, solid-liquid or liquid-gas types PCMs. In solid-solid phase transitions, thermal energy is stored when material is transformed from one crystal structure to another. Generally, the latent heat values associated with solid-solid phase transitions are low, as compared to the solid-liquid or liquid-gas transitions. However, solid-solid transitions offer the advantages of less stringent container requirements and greater design flexibility [1]. **Table 1.5** shows a few solid-solid phase transformation type PCMs [1, 85-88]. In the cases of solid-liquid and liquid-gas types PCMs, the latent heat of phase transformation is higher. For liquid-gas types phase transformation, the change in volume is often huge, which restricts the applications of such liquid-gas PCMs for thermal energy storage due to pressure induced instability and complexity in fabrication. On the other hand, change in volume during phase transition is ~ 10% or less for liquid-solid phase transition types PCMs, which makes them ideal candidates for practical thermal energy storage applications [10, 78]. Based on chemical compositions, solid-liquid phase transition types PCMs can be further subdivided into three categories, viz. inorganic, organic and eutectic PCMs [19]. Inorganic PCMs can be further classified into three groups, viz. inorganic compounds, salt hydrates and metallics. On the other hand, organic PCMs can be paraffin based, fatty acid based and other types of organic compounds. Eutectic PCMs can be organic-organic or organic-inorganic type eutectics. **Fig. 1.5** shows the classifications of PCMs. The inorganic, organic and eutectic PCMs are briefly described in the subsequent sections. **Table 1.6** shows the advantages and disadvantages of inorganic, organic and eutectic PCMs [4, 10, 20, 78, 83, 89-94].

Table 1.5 Solid-solid phase transformation types PCMs.

Name	Phase transition temperature (^{0}C)	Latent heat (kJ/kg)	Reference
Pentaerythritol	~ 186	289-340	[1, 85-87]
Pentaglycerine	~ 82	~ 173	[1, 85, 88]
Neopentylglycol	~ 42-44	110-120	[1, 85, 86, 88]
Tris[hydroxymethyl]aminomethane	~ 132-135	~ 285-296	[1, 86, 87]

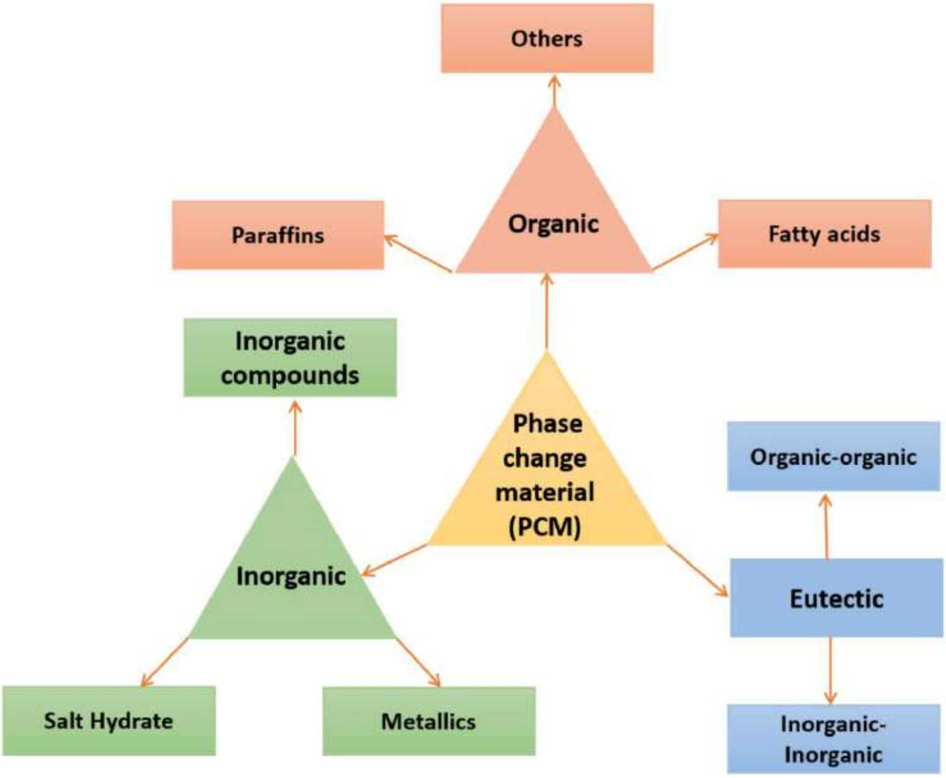

Figure 1.5 Classification of PCMs.

Table 1.6 Advantages and disadvantages of inorganic, organic and eutectic PCMs.

Type of PCMs	Advantages	Disadvantages
Inorganic	➢ High thermal conductivity. ➢ Sharp melting point. ➢ High latent heat. ➢ Low cost and wide availability. ➢ Low volume change during phase transition. ➢ High volumetric heat storage capacity. ➢ Compatible with plastic material. ➢ Non-flammable.	➢ Poor nucleating properties. ➢ Requires supercooling. ➢ Corrosive in nature. ➢ Decompose quickly. ➢ Not compatible with some construction materials. ➢ Phase segregation during transition. ➢ Thermal stability degrades with times.
Organic	➢ Large temperature range. ➢ High latent heat. ➢ Little or no supercooling requirements. ➢ High thermal & chemical stability. ➢ Congruent phase-change. ➢ Good compatibility with construction materials. ➢ Safe handling, non-reactive & recyclable.	➢ Inherent low thermal conductivity. ➢ Flammable. ➢ Comparatively large volume change. ➢ Not compatible with a few plastic materials. ➢ Lower volumetric latent heat storage capacity.
Eutectic	➢ Sharp melting temperature. ➢ Volumetric thermal storage density higher than organic PCMs. ➢ No phase segregation and congruent phase-change.	➢ Limited data on thermophysical properties. ➢ Preparation is more complex compared to inorganic or organic PCMs.

1.4.2 Inorganic PCMs

Inorganic PCMs can be classified into three subcategories, viz. metallic, inorganic substances and salt hydrates [1]. Metallic inorganic PCMs include low melting metals (caesium, gallium etc.), high melting metals (aluminum, magnesium, etc.) and their alloys. **Table 1.7** shows a few metallic PCMs along with the corresponding melting points and latent heat values [1, 95-97]. Metallic PCMs have large thermal conductivity, high thermal reliability and provide large volumetric storage capacity [98]. However, the use of such metallic PCMs are restricted due to the mechanical and structural problem associated with excess weight and comparatively lower latent heat values, especially for low melting metals and alloys.

Table 1.7 Description of a few metallic PCMs

Material	Melting point (^{0}C)	Latent heat (kJ/kg)	Reference
Caesium	~ 29	~ 16.5	[95]
Tin	~ 232	~ 60.5	[95]
Zinc	~ 419	~ 112	[96]
Magnesium	~ 648	~ 365	[96]
Aluminum	~ 661	~ 388	[96]
Bismuth-indium alloy	~ 72	~ 25	[97]
Gallium	~ 30	~ 80	[97]
Bismuth-cadmium-indium alloy	~ 61	~ 25	[97]

Several inorganic substances, like $NaNO_3$, KNO_3, $LiNO_3$, $MgCl_2$, KF, LiF etc. have been used as inorganic PCMs due to high latent heat per unit mass and lower cost [79]. Among various inorganic substances, LiH and $KClO_4$ exhibit high heat of fusion (~ 2678 and 1253 kJ/kg, respectively), which makes them attractive candidates for thermal energy storage applications [99]. **Table 1.8** shows a few inorganic substances used as inorganic PCMs for latent heat thermal energy storage applications [1, 99]. The melting temperature and heat of fusion are also indicated in **Table 1.8**. However, degradation in thermal stability over time and corrosiveness are the major drawbacks of such inorganic PCMs. Various salt hydrates have also been used as inorganic PCMs for thermal energy storage applications. In salt hydrates, water molecules are bound to the crystal matrix during solidifications and the general formula for such salt hydrates can be expressed as $AB.nH_2O$ [1]. Large latent heat and high thermal conductivity (~ double of that of organic PCMs) are the major benefits of such salt hydrates (like $CaCl_2.6H_2O$, $Na_2SO_4.10H_2O$, etc.) as PCMs [84]. **Table 1.9** shows a few salt hydrates used for latent heat thermal energy storage applications [1, 14, 100-105]. However, salt hydrates show instability due to separation of water molecules from the crystal matrix during consecutive thermal cycles, which results in a decrease of latent heat over a period of time [106]. Additionally, salt hydrates are also prone to supercooling requirements and are corrosive to metals [1, 106].

Table 1.8 A few inorganic substances suitable for latent heat thermal energy storage.

Material	Melting point (^{0}C)	Heat of fusion (kJ/kg)	Reference
NaF	~ 993	~ 750	[99]
MgF_2	~ 1271	~ 936	[99]
LiF	~ 868	~ 932	[99]
LiH	~ 699	~ 2678	[99]
$KClO_4$	~ 527	~ 1253	[99]
Na_2O_2	~ 360	~ 314	[99]
$LiNO_3$	~ 250	~ 370	[99]
$AlCl_3$	~ 192	~ 280	[99]
$NaNO_3$	~ 307	~ 172	[1]
KNO_3	~ 333	~ 266	[1]
$MgCl_2$	~ 714	~ 452	[1]
KF	~ 857	~ 452	[1]

Table 1.9 A few inorganic salt hydrates suitable for latent heat thermal energy storage.

Material	Melting point (^{0}C)	Heat of fusion (kJ/kg)	Reference
$Zn(NO_3)_2.6H_2O$	~ 36	~ 147	[1]
$CaCl_2.6H_2O$	28-30	190-200	[100, 101]
$Na_2SO_4.10H_2O$	~ 34	~ 256	[102]
$Mn(NO_3)_2.6H_2O$	~ 25	~ 126	[102]
$LiClO_3.3H_2O$	~ 8	~ 253	[103]
$Na_2CO_3.10H_2O$	~ 33	~ 247	[103]
$KF.4H_2O$	18-19	~ 231	[14]
$CaBr_2.6H_2O$	~ 34	~ 116	[104]
$Na_2HPO_4.12H_2O$	35-454	~ 280	[104]
$Na_2S_2O_3.5H_2O$	48-55	~ 201	[104]
$Na(CH_3COO).3H_2O$	~ 58	~ 226	[105]
$Ba(OH)_2.8H_2O$	~ 78	~ 266	[105]
$MgCl_2.6H_2O$	~ 117	~ 169	[105]

1.4.3 Organic PCMs

Compared to inorganic PCMs, organic PCMs have several advantages, viz. high latent heat, lower vapour pressure during melting, negligible requirement of supercooling, thermal stability even after a large number of melting/freezing cycles, chemical inertness and comparatively lower cost [80, 107]. Organic PCMs can be classified into three subgroups, viz. paraffin based, fatty acid based and other types of organic substances. Paraffins (C_nH_{2n+2}) consist of chains of saturated hydrocarbons (alkanes). The latent heat and melting point of paraffins are directly proportional to the chain length or molecular weight, and hence, phase transition temperature can be tuned by proper material selections. Paraffins are non-corrosive, non-toxic in nature and show good stability upon consecutive thermal cycles, without any significant supercooling requirements [108]. These advantages have made paraffin-based materials one of the most widely used organic PCMs. However, paraffins exhibit a few undesirable properties like inherently low thermal conductivity, comparatively higher volume change during phase transition, flammability and non-compatibility with plastic containers due to chemical similarity, resulting in the softening of containers [79, 109]. **Table 1.10** lists a few paraffin based materials used as organic PCMs for latent heat thermal energy storage applications, along with their physio-chemical properties [102, 104, 110-112]. Apart from paraffins, several fatty acids (general formula: CH_3 $(CH_2)_{2n}COOH$) have also been used as organic PCMs [113]. The superior thermophysical and kinetic properties during melting and solidifying cycles with negligible supercooling and repeatable thermal behaviour are the primary advantages of fatty acids based organic PCMs [106, 114]. **Table 1.11** shows the details of a few fatty acids used as organic PCMs, along with their physio-chemical properties [1, 111, 112, 115-124]. **Fig. 1.6** shows the number of articles published on organic PCMs during the years 1996-2014 [4]. It can be seen from **Fig. 1.6** that the research interest on organic PCMs steadily increased over the years resulting in a large increase in number of publications per year (total number of publications increased from 303, in 1996 to 2650, in 2014; an increase by ~ 775 % over a period of 18 years). It can also be seen from **Fig. 1.6** that the research interest on fatty acids increased at a much higher rate than paraffin, which might be due to the favourable thermo-physical properties of fatty acids and the possibility of preparing eutectic mixtures with sharp phase transition temperatures and improved latent heat values. Apart from paraffins and fatty acids, several other types of organic materials (like ketones, ethers, dienes, etc.) have also been used for latent heat thermal energy storage. **Table 1.12** shows a few other types of organic materials used as PCMs for LHTES [1, 14, 78, 102, 111, 112, 122, 125-129]. Among these other types of organic PCMs, sugars and oleochemical carbonates show very high latent heat values, which is beneficial for practical applications [127, 128]. In this work, unless otherwise mentioned, PCMs indicate organic phase change materials.

Table 1.10 A few paraffins used as organic PCMs for latent heat thermal energy storage along with their physio-chemical properties.

Paraffin	Number of carbon atoms in hydrocarbon chain	Melting temperature (^{0}C)	Latent heat (kJ/kg)	Reference
n-tetradecane	14	~ 6	227-229	[102, 110]
n-pentadecane	15	~ 10	~ 206	[102, 110]
n-hexadecane	16	18-20	216-236	[102, 104, 110-112]
n-heptadecane	17	22-23	164-214	[102, 104, 111, 112]
n-octadecane	18	28-29	200-244	[102, 104, 111, 112]
n-nonadecane	19	~ 32	~ 222	[1, 104]
n-eicosane	20	~ 37	~ 247	[1, 104]
n-heneicosane	21	~ 40	~ 213	[1, 104]
n-docosane	22	~ 44	~ 249	[1, 104]
n-tricosane	23	~ 47	~ 234	[1, 104]
n-tetracosane	24	~ 51	~ 255	[1, 104]
n-pentacosane	25	~ 53	~ 238	[1, 104]
n-hexacosane	26	~ 56	~ 256	[1, 104]
n-heptacosane	27	~ 59	~ 235	[1, 104]
n-octacosane	28	~ 61	~ 254	[1, 104]
n-nonacosane	29	~ 63	~ 239	[1, 104]
n-triacontane	30	~ 65	~ 252	[1, 104]

Table 1.11 A few fatty acids used as organic PCMs for latent heat thermal energy storage along with their physio-chemical properties.

Fatty acid	Number of carbon atoms in hydrocarbon chain	Melting temperature (^{0}C)	Latent heat (kJ/kg)	Reference
Caprylic acid	8	~ 16	~ 148	[1, 115]
Capric acid	10	31-32	~ 163	[115, 116]
Lauric acid	12	41-44	183-212	[117, 118]
Myristic acid	14	51-54	190-205	[115, 118-121]
Palmitic acid	16	61-63	203-212	[121-124]
Stearic acid	18	~ 70	~ 222	[116, 121, 123]
Arachidic acid	20	~ 74	~ 227	[1, 115]
Undecylenic acid	22	~ 25	~ 141	[111, 112]

Table 1.12 A few other types of organic PCMs suitable for latent heat thermal energy storage along with their physio-chemical properties.

Class of compound	Organic compound	Melting temperature (^{0}C)	Latent heat (kJ/kg)	Reference
Ketones	Phorone	~ 27	~ 124	[111]
Ethers	Diphenyl ether	~ 27	~ 97	[111]
Esters of fatty acids	Methyl palmitate Propyl palmitate Methyl stearate Butyl stearate Ethylene glycol distearate Vinyl stearate	~ 27 16-20 38-39 17-23 ~ 63 ~ 27	~ 163 186-190 ~ 161 140-200 ~ 216 ~ 122	[14, 122, 125, 126]
Sulphur compounds	Octadecyl 3-mercapto propionate Dilauryl thiopropionate	~ 21 ~ 39	~ 141 ~ 159	[122]
Amides	Acetamide	~ 82	~ 241	[78]
Dienes	Dicyclopentadiene	~ 29	~ 12	[102]
Sugars	Erythritol Sorbitol Mannitol Xylitol	~ 117 ~ 97 ~ 165 ~ 93	~ 344 ~ 110 ~ 341 ~ 280	[127]
Halogen derivative	1-Iodehexadecane 3-Iodoaniline	~ 22 ~ 23	~ 131 ~ 64	[111, 112]
Oleochemical carbonates	Dodecyl carbonate Tetradecyl carbonate Octadecyl carbonate	~ 19 ~ 34 ~ 52	~ 200 ~ 227 ~ 223	[128]
Monohydroxy alcohols	1-Tetradecanol 1-Dodecanol	~ 39 17-23	~ 221 184-189	[14, 125, 129]

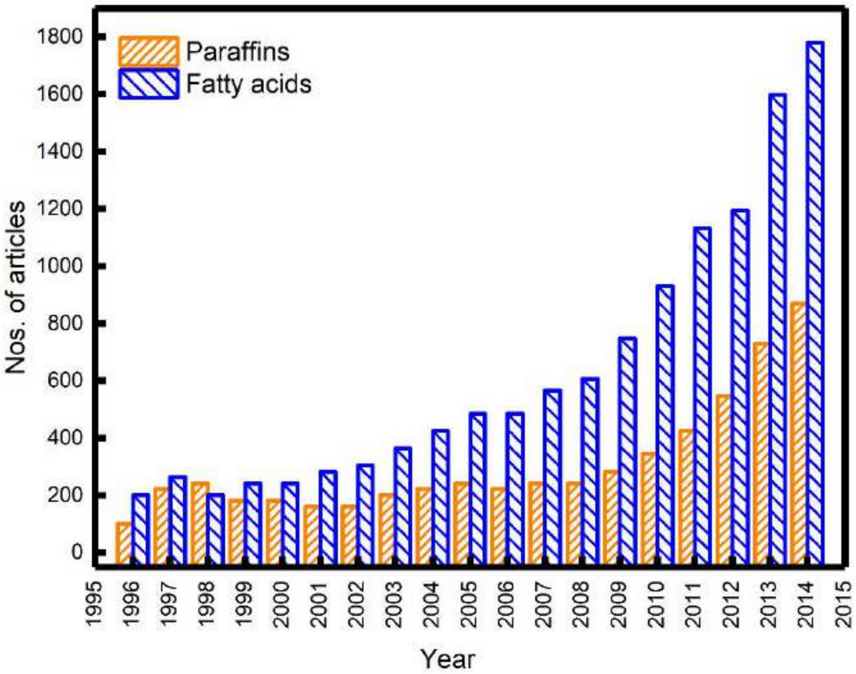

Figure 1.6 Number of scientific articles on paraffin based and fatty acid based organic phase change materials during the years 1996-2014 (source: Web of Science).

1.4.4 Eutectic PCMs

Eutectic PCMs are minimum-melting compositions consisting of two or more PCMs [78, 79]. Eutectic PCMs can be further classified as organic-organic and inorganic-inorganic eutectic PCMs [1]. The rationale behind preparation of eutectic PCMs is to achieve tunable melting temperature within the desired temperature range with improved thermal conductivity and latent heat and controlled flammability and supercooling [118]. However, preparation of such eutectic PCMs are time consuming and requires optimization of the system composition. On the positive side, such eutectic PCMs have relatively sharp phase transition temperature and phase segregation is unlikely due to simultaneous melting [79]. A few organic-organic and inorganic-inorganic eutectic PCMs used for thermal energy storage applications, along with their physio-chemical properties are listed in **Tables 1.13 and 1.14**, respectively [1, 14, 78, 105, 118, 120, 130-135].

Table 1.13 A few organic-organic eutectic PCMs suitable for latent heat thermal energy storage along with their physio-chemical properties (CA, LA, MA, PA and SA indicate capric acid, lauric acid, myristic acid, palmitic acid and stearic acid, respectively).

Components	Composition (wt. %)	Melting point (^{0}C)	Latent heat (kJ/kg)	Reference
CA-LA	45-55	17-21	~ 143	[14]
LA-MA	66-34	~ 34	~ 167	[118]
MA-PA	58-42	~ 43	~ 170	[120]
LA-PA	69-31	~ 35	~ 166	[130]
MA-SA	64-36	~ 44	~ 182	[130, 131]
PA-SA	64.2-35.8	~ 52	~ 182	[132]
LA-SA	75.5-24.5	~ 37	~ 183	[133]
CA-PA	76.5-23.5	~ 22	~ 171	[134]

Table 1.14 A few inorganic-inorganic eutectic PCMs suitable for latent heat thermal energy storage along with their physio-chemical properties.

Components & composition	Melting point (^{0}C)	Heat of fusion (kJ/kg)	Reference
45% $CaCl_2.6H_2O$ + 55% $CaBr_2.6H_2O$	~ 15	~ 140	[78]
40% $CH_3COONa.3H_2O$ + 60% NH_4NO_3	~ 30	~ 201	[78]
61.5% $Mg(NO_3)_2.6H_2O$ + 38.5 NH_4 NO_3	~ 52	~ 125	[78]
50% $CaCl_2$ + 50% $MgCl_2.6H_2O$	~ 25	~ 95	[78]
53% $Mg(NO_3)_2.6H_2O$+ 47% $Al(NO_3)_2.9H_2O$	~ 61	~ 148	[78]
47% Ca $(NO_3)_2.4H_2O$ + 53% Mg $(NO_3)_2.6H_2O$	~ 30	~ 136	[78]
59% $Mg(NO_3)_2.6H_2O$ + 41% $MgBr_2.6H_2O$	~ 66	~ 168	[78]
58.7% % $Mg(NO_3)_2.6H_2O$ + 41.3 $MgCl_2.6H_2O$	~ 59	~ 132	[78]
48% $CaCl_2$+4.3% NaCl + 0.4% KCl+47.3% H_2O	~ 27	~ 188	[105]
14% $LiNO_3$ + 86% $Mg(NO_3)_2.6H_2O$	~ 72	~ 180	[105]
66.6% $CaCl_2.6H_2O$ + 33.3% $MgCl_2.6H_2O$	~ 25	~ 127	[105]
66.3% urea + 33.6% NH_4Br	~ 76	~ 161	[135]

1.5 Desirable properties of an ideal phase change material

Though there exist a variety of phase change materials which are used for latent heat thermal energy storage applications, ideal PCMs shall exhibit a number of desirable physical, thermal, kinetic and chemical properties [1, 14, 20, 78-80, 91, 92, 136, 137]. **Table 1.15** tabulates the most desirable properties of an ideal PCM [1].

Table 1.15 Desirable properties of an ideal PCM.

Type	Desirable properties
Physical	➢ Lower vapour pressure during phase transition and at operating conditions.
	➢ Smaller volume change during phase transformation.
	➢ No material loss during phase transition.
	➢ Congruent melting.
	➢ Favourable and well understood phase equilibria.
Thermal	➢ High latent heat of phase transition.
	➢ Phase transition temperature at the desired operating range.
	➢ High thermal conductivity at solid and liquid phases.
	➢ High specific heat to provide additional sensible heat storage.
	➢ High charging/discharging rates.
	➢ Good thermal stability after several melting/freezing cycles.
Kinetic	➢ High nucleation rate
	➢ Negligible or no supercooling.
	➢ Absence of secondary phase transformation within the operating temperature range.
Chemical	➢ Long-term chemical stability.
	➢ Negligible or no corrosion.
	➢ Reversible melting/freezing cycles.
	➢ Compatibility with construction or container materials.
	➢ Non-toxic, non-flammable and non-explosive in nature.
Techno-commercial	➢ Low cost.
	➢ Wide availability.
	➢ Ease of preparation/fabrication.
	➢ Light weight.

1.5.1 Commercially available PCMs

It's unlikely that all the desirable properties are met by a single PCM and this primarily drives the scientific research for development and characterization of new phase change materials with improved properties [1]. Additionally, several studies are also being conducted to probe the carbon foot print, life-cycle cost and economic impacts of integrated or stand-alone thermal energy storage systems using PCMs [6, 138-148]. Recently, soft computing tools like artificial neural network [149] and fuzzy logic [150] has been utilized to optimize the performances of PCM based thermal energy storage systems. A few commercially available PCMs are listed in **Table 1.16** [151], where the exact material composition is not available in the public domain.

1.6 Various applications of phase change materials

Organic phase change materials (PCMs) are widely used for various latent heat thermal energy storage applications. **Fig. 1.7** shows the most important applications of organic PCMs. Buildings account for a substantial amount of global energy usage and applications of PCM for thermo-regulation and energy storage in buildings are essential for reducing energy consumption and distribution of energy between the peak and off-peak periods [93]. Organic PCMs have found wide spread applications in cooling/heating of buildings [11, 93], cooling of electronic devices and domestic/commercial refrigeration [152, 153], low temperature solar energy storage [78], solar water/air heater [154, 155], solar receiver of direct steam generator of concentrated solar power plants [146], automobile industry [156], food packaging and transportation [157, 158] and in bio-medical fields like vaccine boxes and thermotherapy based treatment of Buruli ulcer and arthritis [159, 160]. A few important applications of PCMs are discussed in the following sections.

Table 1.16 A few commercially available PCMs.

Commercial name	Melting temperature (^0C)	Latent heat (kJ/kg)	Type of PCM	Company
Micronal DS 5001	~ 26	~ 110	Paraffin based	M/s BASF, USA
RT 6	~ 8	~ 174	Paraffin based	M/s Rubitherm GmbH, Germany
SP 22 A4	~ 24	~ 165	Salt hydrate based	M/s Rubitherm GmbH, Germany
SN 33	~ -33	~ 218	Paraffin based	M/s Cristopia Energy Systems, France
IN 03	~ -3	~ 294	Paraffin based	M/s Cristopia Energy Systems, France
Latest 20T	19-21	~ 175	Salt hydrate based	M/s Teappcm, India
E-10	~ -10	~ 286	Unknown	M/s EPS Ltd., UK
A22	~ 22	~ 172	Unknown	M/s EPS Ltd., UK
ClimSel C 32	~ 32	~ 212	Salt hydrate based	M/s Climator Sweden AB, Sweden
ClimSel C 23	~ 23	~ 148	Salt hydrate based	M/s Climator Sweden AB, Sweden
STL-21	~ -21	~ 240	Salt solution based	M/s Mitsubishi Chemical Corporation, Japan
STL52	~ 52	~ 201	Salt hydrate based	M/s Mitsubishi Chemical Corporation, Japan
STL27	~ 27	~ 213	Salt hydrate based	M/s Mitsubishi Chemical Corporation, Japan
Mikra Thermic	~ 20	~ 140	Paraffin based	M/s Devan, Belgium

1.6.1 Temperature regulation of buildings using PCMs

For storage of solar thermal energy during day-time and prevention of overheating, encapsulated PCMs has been used in different parts of buildings like walls, floor and ceiling, which enhanced the thermal energy storage capacity [4]. The primary advantage of using PCMs incorporated in the building materials is that it provided higher energy storage density during melting (charging), thereby isothermally storing excess available energy in the day-time [82]. The stored energy was released by the PCM during solidification (discharging) at night, thereby providing thermal comfort to the inhabitants [13]. **Fig. 1.8** schematically shows the principle behind thermoregulation of building using PCM based thermal energy storage.

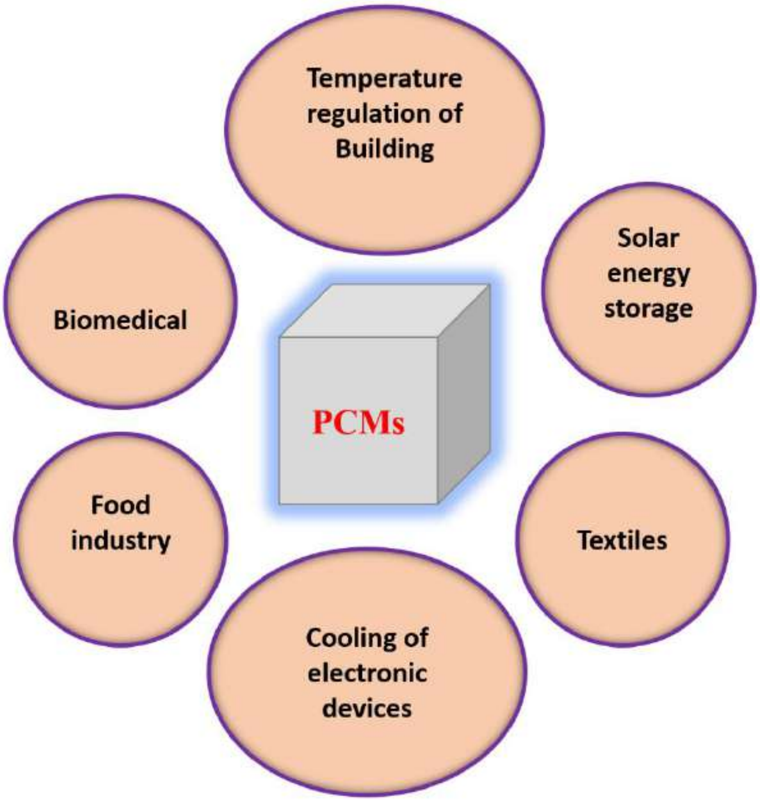

Figure 1.7 Various applications of phase change materials (PCMs).

PCM mediated storage of excess thermal energy during day-time significantly reduces the overall air-conditioning load and helps in maintaining the internal temperature of the building at comfort level for a longer time [4, 13]. Thermal energy storage using PCMs for building applications can be classified into two subclasses, viz. passive and active systems. For passive systems, the functions of heat collection, thermal energy storage and release of heat are achieved by the building structure itself, whereas for active systems, pumps or fans are required [161]. The capacity of solar thermal energy storage in PCM incorporated building materials is highly dependent on the latent heat of the PCM.

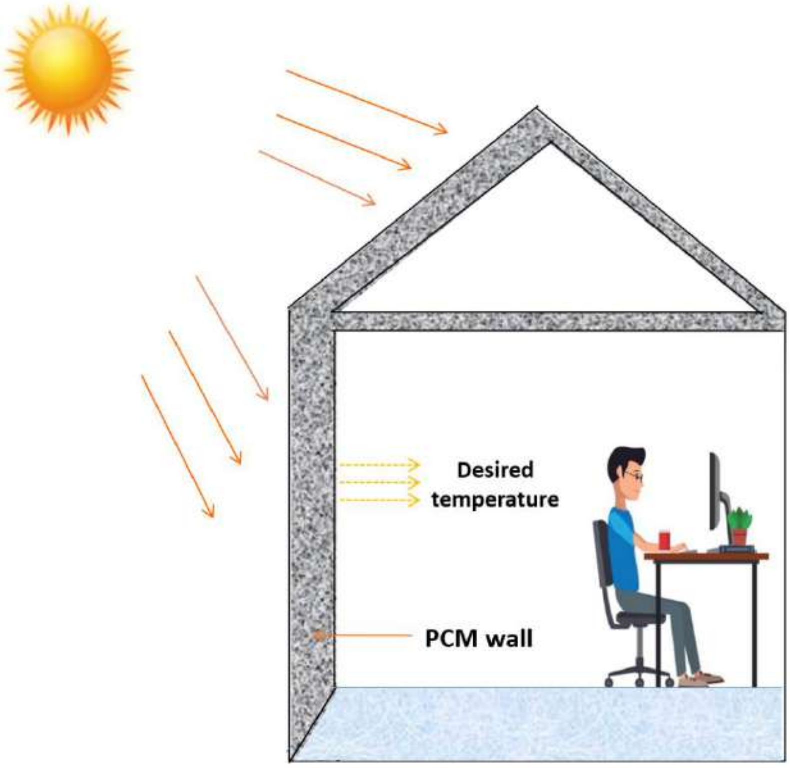

Figure 1.8 Schematic illustration of thermoregulation in a room with PCM integrated in walls.

Further as per the American Society of Heating, Refrigerating and Air-conditioning Engineers (ASHRAE) guidelines, phase transition temperature of a PCM selected for thermoregulation applications shall be within the temperature range of 20-30 ^{0}C [82]. Presently, PCM incorporated gypsum boards are being pursued for building thermoregulation. It has been reported that 1.5 cm thick PCM incorporated gypsum board stores ~ five times more thermal energy, as compared to laminated gypsum board and approximately same amount of energy as a ~ 12 cm thick brick wall within a comfortable temperature range of 20-30 ^{0}C [162].

1.6.2 Solar thermal energy storage using PCMs

Solar radiation is one of the most abundant form of renewable energy and PCM based storage of solar-thermal energy during day-time can pave the way for effective utilization of the stored energy during night-time [4, 163]. The solar-thermal applications of PCMs can be divided into two sub-classes, viz. low temperature solar-thermal applications (like solar water heater, solar air heater and solar dryer) and high temperature solar-thermal applications (like solar cooker and concentrated solar power plants) [4]. Low temperature solar-thermal applications require PCMs with phase transition temperature within 80 ^{0}C [4]. Solar water heaters are relatively simple, easy to fabricate and several experimental and theoretical studies have been conducted for PCM based solar water heaters [154, 164-166]. Solar water heater with various configurations like paraffin filled capsule [167], encapsulated PCMs [168], shell and tube geometry with solar collector [169], etc. have been reported in the literature. **Fig. 1.9** shows the schematic of a solar water heater system [169].

Solar air heater uses the stored solar-thermal energy to heat or condition the air for building. The use of PCM makes solar air heating system energy efficient, sustainable and economic [135]. Design and fabrication of thermally efficient solar air heaters have been studied numerically and experimentally [170-172]. Natural circulation solar air heater and solar air collectors have been studied by Enibe [173] and Alkilani et al [174]. Solar dryers are PCM incorporated devices that are used for drying or dehydrating various items, including agricultural products [175, 176]. Typical phase transition temperature of PCMs used for solar-thermal dryers are within the temperature range of 40-75 ^{0}C [4]. PCM incorporated solar-thermal dryers have been fabricated and demonstrated for various applications like peanut drying [4], drying of agricultural food products [177], dehydration of mushrooms [178], indirect solar drying [179], etc. High temperature solar thermal applications include solar cookers and concentrated solar power plants. PCM incorporated solar cookers store the excess solar-thermal energy during day-time and release the stored heat during night-time, thereby enhancing the efficacy of solar cookers. Solar cookers incorporating several types of PCMs have been fabricated and demonstrated [141, 180, 181]. On the other hand, concentrated solar power plants (CSP) use solar collector to increase the energy of working fluid beyond 100 ^{0}C, which is not possible using flat plate collectors [4]. CSP integrated with PCMs have shown significantly higher energy efficiency due to availability of stored thermal energy during nigh-time [5, 6, 18, 74, 140, 146, 182].

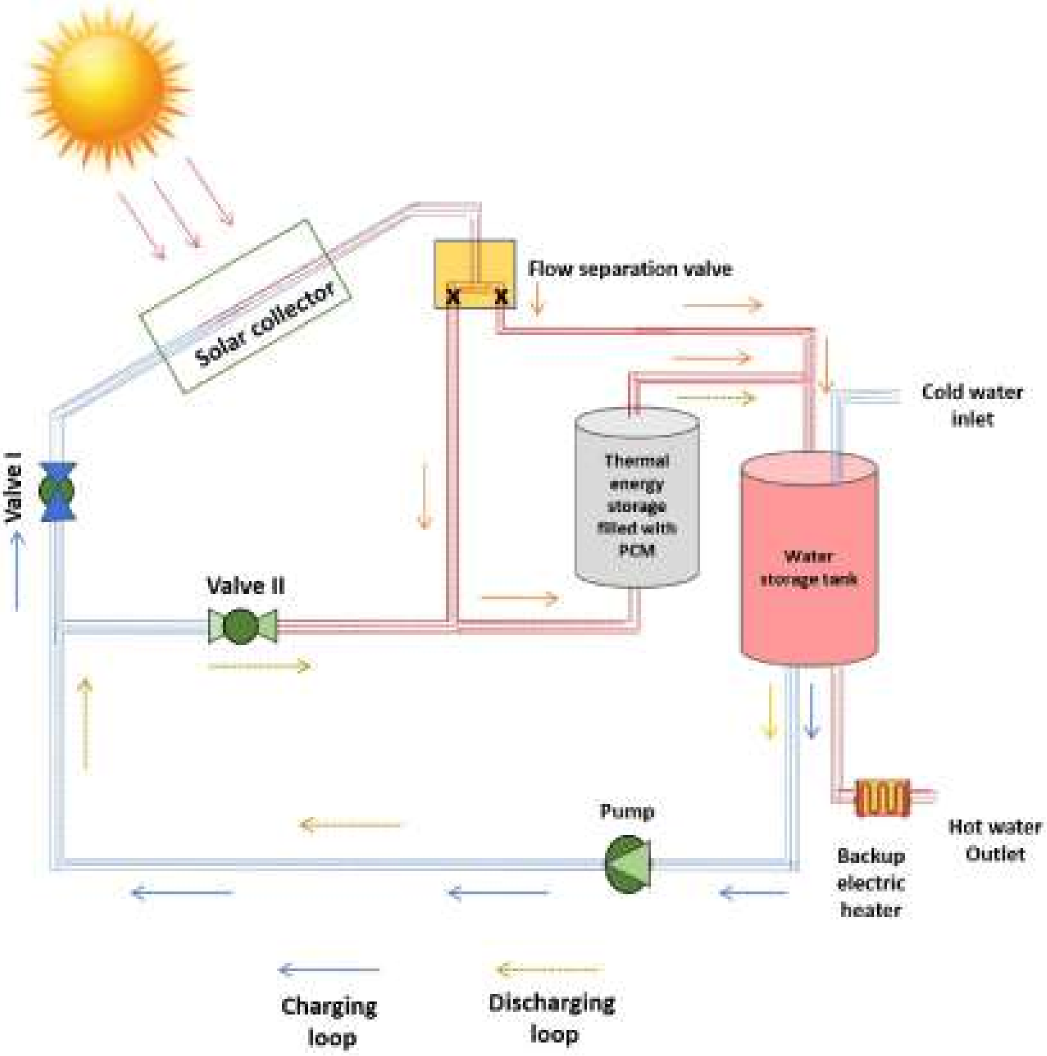

Figure 1.9 Schematic diagram of a solar water heating system incorporated with phase change material (PCM).

1.6.3 Other applications of PCMs

a) Applications of PCMs in textile industry

Textiles are primarily a single or multiple layer of fabrics, designed for human comfort. The thermo-regulatory effects of textiles can be enhanced by incorporating suitable phase change materials [183]. In textile industries, PCMs incorporated fabrics are predominantly used for blankets, sportswear, shoes, protective clothing and apparel [4, 21]. PCMs can be incorporated within the textile by coating or encapsulation techniques [4]. Several studies have reported the use of smart thermo-regulatory textiles with microencapsulated PCMs [21, 184, 185]. In textiles incorporated with microencapsulated PCMs, the PCM microbeads absorb heat during a rise in surrounding temperature and when ambient temperature decreases, the PCM microbeads release the stored thermal energy. This cyclic charging/discharging thermo-regulatory process keeps the body temperature within a comfortable range. **Fig. 1.10** schematically shows the microscopic structure of a textile matrix incorporated with microencapsulated PCM beads. The most widely used PCMs in smart textile includes various types of paraffins like hexadecane [186], heptadecane [187], eicosane [188], and octadecane [189], with phase transition temperature in the range of 18-36 ^{0}C [190]. On the other hand, PCMs can be directly incorporated into the fabrics by dispersion into the hollow fiber core, surface impregnation and polymer manipulation routes [4]. Polyethylene glycol has been found to be the most suitable PCM for direct incorporation in textiles [191, 192].

b) Applications of PCMs for cooling of electronic devices & domestic refrigeration

Overheating has been identified as one of the major reasons behind failure of electronic devices [193]. Hence, heat sinks, incorporated with thermal energy absorbing PCMs, have been utilized to enhance the thermal capacitance and cooling efficiency in electronic devices

[194]. Applications of PCMs for thermal management of electronic devices, li-ion batteries and photovoltaic modules have been extensively reviewed by Ling et al. [16].

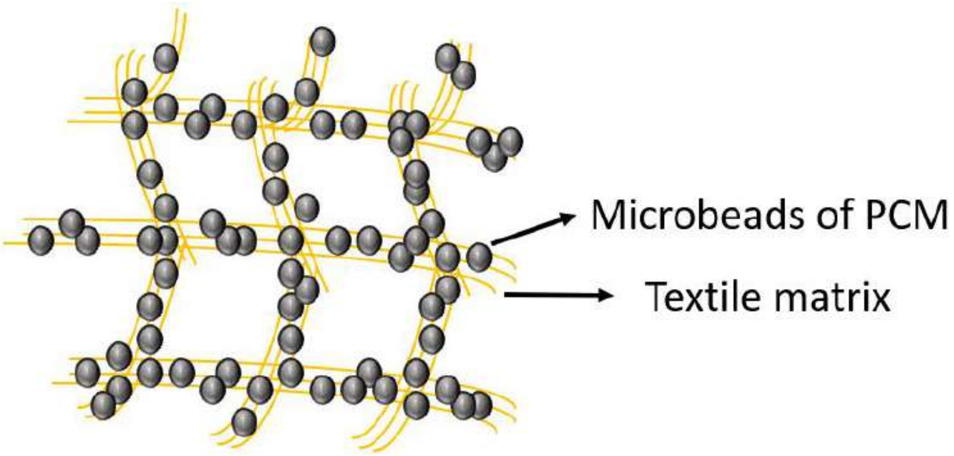

Figure 1.10 Schematic illustration of a textile matrix incorporated with microencapsulated PCM beads.

Paraffin and other hydrocarbon based PCMs have been widely used for cooling of mobile or hand-held electronic devices [4, 194-197]. Numerical models have also been developed to optimize the PCM assisted cooling efficiency of electronic gadgets [198, 199]. Domestic and commercial refrigeration are energy intensive processes and applications of PCM-based thermal energy storage systems had been explored to reduce energy consumption and wastage. Ahmed et al. [153] reported the use of refrigerated truck trailers, modified using a PCM for insulation in domestic refrigeration system. Gil et al. [200] reported the use of hydroquinone based PCM for solar cooling refrigeration.

c) Applications of PCMs in food, bio-medical and automobile industries

Applications of PCMs in food industry has been studied experimentally and numerically [157, 201]. The variation of temperature is detrimental towards the compositional stability and freshness of packaged food items and commercially available low-density packaging materials (likes polystyrene, polyethylene, etc.) are not suitable for thermal management. This makes latent heat thermal energy storage and management using organic PCMs an attractive choice for thermal protection of packaged food items [4]. In food industries, the most prominent applications of PCMs include food transportation [158, 202], food preservation [153, 203] and food packaging [157, 204].

Due to the large latent heat values and near isothermal phase transitions, PCMs have found applications in bio-medical industries. Non-electrical thermal management, ease of use, portability and reusability are the major advantages of PCM-based thermal management in bio-medical applications [160]. Mondieig et al. [205] fabricated and demonstrated a PCM-based double-walled packaging system for the transportation or storage of blood elements. Wang et al. [206] demonstrated a highly sensitive and selective bio-sensing application of thermal probes consisting of RNA aptamer-functionalized PCM for accurate detection of thrombin. PCMs have also found applications in fabrication of vaccine boxes and thermotherapy based treatment of Buruli ulcer and arthritis, respectively [159, 160].

PCMs has also found extensive applications in the automobile industry, especially for improving engine cooling [207, 208], thermal comfort of passengers [209], thermal management of power battery [210] and waste heat recovery [156, 211]. Recently, organic PCMs have been proposed for battery thermal management system (BTMS) of Li-ion batteries [212, 213] for electric hybrid vehicles, which are more energy efficient and poised to reduce global pollution levels by manifolds.

1.7 Improving thermal conductivity and form-stability of organic PCMs

In spite of the immense industrial benefits of PCM in thermal energy conservation and management, the practical applicability of organic PCM is severely limited due to its inherently low thermal conductivity [214]. For e.g., the values of thermal conductivity in liquid state are ~ 0.14, 0.17, 0.14, 0.15 and 0.16 W/mK for n-hexadecane, phenol, palmitic acid, paraffin wax and lauric acid, respectively [1, 215-218]. Such lower values of thermal conductivity decrease the charging and discharging rates, which is detrimental for industrial applications. As subsequently discussed various strategies have been used for enhancing the thermal conductivity of organic PCMs [52]. Material losses, due to leakage, during solid-liquid phase transition also makes conventional organic PCMs unsuitable for field deployment. Hence, to arrest such leakages, form-stable PCMs are being developed using various methods [219, 220].

1.7.1 Thermal conductivity enhancement of organic PCMs

The most commonly used techniques are encapsulation of the PCM using polymer or other inorganic material as shell and PCM as core [221, 222], impregnating porous materials [223-226], inserting a metal structure in the PCM [89, 213, 227] or metal pieces (like copper or stainless steel) [228], insertion of carbon fibres [229, 230] and dispersing high thermal conductivity particles [214, 231-233]. Performance enhancement in latent heat thermal energy storage systems was critically reviewed by Jegadheeswaran and Pohekar [12]. Among the above-mentioned techniques, micro or macro-encapsulation and nano-inclusion loading the most widely used techniques for thermal conductivity enhancement of organic PCMs. Nano-inclusion assisted thermal conductivity enhancement of organic PCMs is widely studied due to ease of sample preparation, cost effectiveness and physical similarity with thermal conductivity enhancement using colloidal dispersions of nanoparticles (nanofluids) [38, 217].

A large contrast in thermal conductivity (~ 250 % enhancement in the solid state) of n-octadecane, loaded with 0.25 wt. % of single-walled carbon nanotube, was reported by Harish et al. [234], which was attributed to the lower thermal barrier resistance in the solid state. Wu et al. [214] experimentally probed the effects of various carbon nano-fillers (nano-graphene with different layer numbers, multi-walled carbon nanotube and graphitized multi-walled carbon nanotubes) on thermal properties of paraffin and reported 52.4 % enhancement in thermal conductivity for the PCM loaded with 3 wt. % of nano-graphene. Recent studies indicate significant enhancement in thermal conductivity of n-hexadecane using inverse miceller templating and various other nano-inclusions like copper nano-wire, multi-walled carbon nanotubes and graphene nanoplatelets [231, 232]. Superior thermal properties have been reported for PCM consisting of n-octadecane/stearic acid loaded with hexagonal boron nitride [235]. Reversible thermal switching across solid liquid phase transition near room temperature has been demonstrated for carbon black/octadecane (phase transition temperature ~ 28-29 ^{0}C) [236], carbon nanotube/hexadecane (phase transition temperature ~ 18 ^{0}C) [237] and graphite/hexadecane (phase transition temperature ~ 18 ^{0}C) PCMs [238]. Wang et al. [58] reported ~ 15 % enhancement in thermal conductivity of paraffin wax based PCM upon addition of 7 wt. % of TiO_2 nano-inclusions. On the other hand, Lin et al. [239] reported a comparatively higher (~ 46.3 %) enhancement in thermal conductivity of paraffin wax based PCM loaded with 2 wt. % copper nanoparticles, which was attributed to the higher bulk thermal conductivity of copper. Studies show improved thermal conductivity of paraffin wax, loaded with various other metallic nano-inclusions, viz., carbon-coated aluminum, CuO and SiO_2 nanoparticles [212, 240, 241]. Apart from metallic nano-inclusions, thermal conductivity enhancement has been experimentally reported for paraffin wax-PCMs, loaded with various carbon based nano-inclusions, like expanded natural graphite [242], carbon nanofibers [243], graphene nanoplatelets [244], multiwalled carbon nanotubes (pristine or functionalized) [214, 245, 246]. Sharma et al. [54] and Ezhumalai et al. [247] reported enhanced thermal conductivity of palmitic acid based PCMs upon loading with metallic additives (TiO_2 and CuO, respectively). Enhanced thermal conductivity of lauric acid based

PCMs had been reported for various types of nano-inclusion loading, viz. activated carbon [248], SiO_2 [249], carbon nanotubes [68, 250] and graphene nanoplatelets [65]. Thermal conductivity enhancement had also been achieved in stearic acid based PCMs loaded with TiO_2 [49, 251], graphene oxide [252], graphene nanoplatelets [66], carbon fibres [253] and hexagonal boron nitride [235] nano-inclusions.

1.7.2 Improving form-stability of organic PCMs

To arrest material leakage during phase transition of organic PCMs, form-stability is primarily achieved by two techniques, viz, micro-encapsulation and shape-stable PCM fabrication [1]. Microencapsulated PCMs are fabricated due to three major advantages, viz. avoiding direct contact between the PCM and the environment, arresting leakage of the PCM in liquid state and increasing heat transfer area [1, 4]. Microencapsulation can be achieved by various chemical methods, viz. coacervation (involving more than one colloids) based microencapsulation for paraffin @ gelatine and acacia [254], paraffin wax @ gelatine and acacia [255] and coco fatty acid @ melamine-formaldehyde [256]; suspension polymerization based microencapsulation for non-polar PCMs @ polystyrene [257]; emulsion polymerization based microencapsulation for n-octacosane @ poly(methyl methacrylate) [258] and docosane @ poly(methyl methacrylate) [259]; polycondensation based microencapsulation for hexadecane @ melamine-formaldehyde resin [260], octadecane @ melamine-formaldehyde resin [260], n-tetradecane @ urea-formaldehyde resin [261] and n-octadecane @ polyurea [262] and polyaddition based microencapsulation for paraffin @ epoxy resin [263]. The above-mentioned chemical strategies are adopted for preparation of microencapsulated PCMs with the desired size distribution, shell thickness and morphology. However, the micro-encapsulated techniques are comparably complex and time consuming [1]. Macroencapsulation (size > 1 mm) technique had also been proposed to restrict material leakages during phase transition of PCMs. In macroencapsulation technique, PCMs are contained within larger structures like tubes, spheres or panels with cylindrical, spherical or square geometries [4].

To save cost and time, shape-stabilized PCMs had been prepared using alternate methods, which are less complex. These techniques primarily include shape-stabilization with a polymer or graphite matrices [1]. Due to its chemical affinity towards paraffins, polyethylene has been widely used as a supporting material for preparing shape-stabilized paraffin-based PCMs [264-266]. Acrylic polymers, like poly (methyl methacrylate) and its various blends had also been used for preparation of shape-stable PCMs [267, 268]. Poly (vinyl chloride)-palmitic acid based shape-stable PCM was reported by Sari et al. [269]. Composite PCMs with poly (vinyl chloride)/fatty acid ratio up to 50: 50 (by wt. %) was found to be shape-stable even after repeated melting/freezing cycles [270]. Polyurethane foams modified with n-hexadecane and n-octadecane or impregnated with polyethylene glycol also exhibited excellent shape-stability with high latent heat values [271, 272]. Shape-stable PCMs consisting of mixtures of poly (vinyl alcohol) and various fatty acids (like lauric acid, stearic acid and palmitic acid) had also been reported by Sari and Kaygusuz [273]. Expandable graphite matrix supported n-docosane based shape-stable PCMs were prepared by absorbing liquid PCM within the matrix of expandable graphite [274]. Various fatty acid based shape-stable PCMs have been prepared by vacuum impregnation of expandable graphite matrices, where the maximum fatty acid concentration was found to be ~ 80 wt. % [275, 276]. However, the latent heat of such shape stable PCMs were slightly lower than the latent heat values of pristine fatty acids [1]. In general, it is observed that latent heat proportionally decreases with increasing concentration of the supporting material [1, 4]. In such shape-stable PCMs, the capillary and surface tension forces arrest leakage of molten PCMs, thereby retaining the structural integrity during phase transition [274, 277, 278]. Paraffin/silica gel and lauric acid/mesocellular foam silica based shape-stable PCMs had been reported by Xing et al. [279] and Mitran et al. [280], respectively. Novel shape-stable PCMs based on lauric acid/diatomite composites [281], lauric acid/expanded perlite [282], lauric acid/modified sepiolite [283], lauric acid/expanded vermiculite [284], paraffin/expanded vermiculite [277], capric-myristic acid/vermiculite [223], stearic acid/expanded vermiculite [285], paraffin/expanded perlite [286], capric-myristic acid/expanded perlite [233], stearic acid/expanded graphite [253], palmitic acid/expanded graphite [276], n-octadecane/expanded graphite [287] and paraffin/expanded graphite [241, 274, 278] had been reported.

1.8 Heat transfer properties of nanofluids

Nano-inclusion loaded PCMs have shown superior thermal conductivity enhancement and significant increase in charging/discharging rates, which makes them important candidates from practical applications as well as model physical systems for probing the role of nano-inclusion loading and clustering on effective thermo-physical properties. Such nano-inclusion loaded PCMs are physically similar to colloidal dispersions of nanoparticles (nanofluids) and thermal properties of nanofluids are essential for understanding the underlying physical phenomena of thermal conductivity enhancement in nano-inclusion loaded PCMs.

Nanofluids are stable colloidal dispersions of nanoparticles in a continuous media [51, 288]. Very often, to ensure long-term colloidal stability, nanoparticle surfaces are functionalized, to attain steric, electro-steric or electrostatic stability [37, 289, 290]. Nanofluids are prepared through various methods, viz. direct evaporation technique [291, 292], chemical reduction [293, 294], laser ablation [295, 296], polyol process [297, 298], phase-transfer process [299, 300], microwave irradiation [301, 302], etc. Nanoparticles tend to aggregate in the dispersion medium due to van der Waal's attraction, resulting in sedimentation or phase separation. Colloidal stability of nanofluids can be improved by decreasing the size of the nanoparticles, increasing the viscosity of the base fluid or reducing the density difference between the nanoparticle and the base fluid [38]. As per Derjaguin, Landau, Verwey and Overbeek (DLVO) theory, the stability of the nanofluids are in general governed by the sum of the van der Waal's forces and electrostatic double layer repulsive forces between the nanoparticles [303-305]. The stability of nanofluids can be probed using various experimental techniques [306], viz. light scattering [307], sedimentation and centrifugation method [308, 309], zeta potential measurement [295], spectral analysis [310], etc.

Nanofluids have shown higher thermal conductivity with respect to the conventional cooling liquids (like water, ethylene glycol, kerosene, etc.) and nanofluid based cooling had been reported for solar devices [311, 312], domestic refrigeration [313], automobile coolant [36, 314-316], engine coolant [317], heat-exchanger systems [318], electronic cooling [39, 40, 319], CPU coolant [320], brake fluid [321] and convective heat transfer applications [322, 323]. Nanofluids have also shown to increase critical heat flux, which made them a potential candidates as coolants in nuclear power plants [46, 324-326].

1.8.1 Factors influencing thermal conductivity of nanofluids

The thermal conductivity of nanofluids are influenced by several factors, viz. size, shape, concentration of the nanoparticles, density, viscosity and temperature of the base fluids, presence of surfactants, etc. [38, 51].

a) Effect of nanoparticle size

Size of the dispersed nanoparticle plays a major role on the stability and thermal conductivity of nanofluids [327]. Majority of the studies reported an increase in thermal conductivity with decreasing size [328-331]. On the other hand, a few studies reported a decrease in effective thermal conductivity with increasing nanoparticle size [332, 333].

b) Effect of nanoparticle aspect ratio

Various experimental and numerical studies show an increase in thermal conductivity of nanofluids with increasing aspect ratio of nanoparticles [334-337]. Nanoparticles with large aspect ratio leads to higher effective thermal conductivity of nanoparticles due to enhanced heat transfer along the length of the rod shaped particles [38]. By varying external magnetic field, the aspect ratio of dispersed magnetic particles have been varied to achieve tunable thermal properties of magnetic nanofluids [288, 337].

c) Effect of nanoparticle concentration & aggregation

Experimental results indicate an increase in nanofluid thermal conductivity with increasing concentration of nanoparticles, much beyond the theoretical expectations of effective medium theory [338-340]. However, very high loading concentration resulted in a decrease in nanofluid thermal conductivity, due to increased interparticle interactions and aggregations, and studies reported the existence of an optimal concentration for the highest thermal conductivity enhancement of nanofluids [341, 342]. Experimental studies reported that nanoparticle agglomeration can lead to an enhancement in effective thermal conductivity [338, 343]. However, sedimentation of nanoparticles results in a decrease of effective thermal conductivity [344, 345]. Karthikeyan et al. studied time dependent thermal conductivity of aqueous nanofluids containing CuO nanoparticles and it was reported that thermal conductivity decreased with elapsed time, which was attributed to clustering and confirmed using optical microscopy [346].

d) Effect of nanoparticle thermal conductivity, other additives & temperature

In general, effective thermal conductivity of nanofluids increased with bulk thermal conductivity of the dispersed nanoparticles [347-350]. On the other hand, few other studies reported that, under dilute limit, the bulk thermal conductivity of the dispersed nanoparticles did not influence or was not the primary influencing factor for the effective thermal conductivity of the nanofluids [51, 351, 352].

Most of the experimental studies indicate an increase in effective nanofluid thermal conductivity upon addition of suitable concentration of additives [38, 44, 353, 354]. Thioglycolic acid [44], polyisobutene succinimide [336] and sodium dodecyl benzene sulphonate (SDBS) [354] additives resulted in improved thermal conductivity of nanofluids, whereas, addition of cetyl trimethyl ammonium bromide (CTAB) did not cause any appreciable changes in effective thermal conductivity of nanofluids [355].

Water and ethylene glycol based Al_2O_3 nanofluids showed an increase in effective thermal conductivity with increasing temperature in the range of 21-50 & 10-60 ^{0}C [338, 356]. On the other hand, lowering of effective thermal conductivity had been reported for water based TiO_2 nanofluid [357] and hexane based nanofluid containing Bi_2Te_3 nanorods [358]. A few studies indicated temperature independent effective thermal conductivity of nanofluids [359-361].

1.8.2 Models for heat transfer in nanofluids

Thermal conductivity enhancement in nanofluids, in general, has been a topic of intense scientific scrutiny and various theoretical models has been proposed to explain the experimental data sets, by considering clustering, micro-convection and Brownian motion, ballistic heat transfer and interfacial layer [38, 50, 346, 362, 363]. Various theoretical models had been proposed for explaining the thermal conductivity enhancement in nanofluids by Maxwell [364], Bruggeman [365], Hamilton and Crosser [366], Hashin and Shtrikman [367], Yu and Choi [368], Avsec and Oblak [369], Xuan and Li [370], Pak and Cho [371], Kumar et al. [372], Prasher et al. [342, 373], Leong et al. [374], Yamada and Ota [375], Gupte et al.

[376], Hasselman and Johnson [377], Xie et al. [378], Jang and Choi [379], Wang et al. [380], Corcione [381], Kihm et al. [382], Evans et al. [45, 341], Braginsky and Shklover [383], Vajjha and Das [330], and Ho et al [384]. Among these theories, however, nanoparticle clustering and associated percolative heat transfer is the most widely accepted theory that shows significant agreement with most of the experimental data sets [341, 342, 346, 362, 385, 386]. Similarly, clustering of nano-inclusions has been found to be one of the primary factors towards thermal conductivity enhancement in nano-inclusion loaded PCMs, especially in the vicinity of the phase transition regions [217, 218, 237, 387]. The essential features of Maxwell's effective medium theory (EMT) [364], modification of EMT by Bruggeman [365] and Hamilton-Crosser [366] model are briefly described below.

By considering spatially homogeneous electromagnetic response, Maxwell explained the effective thermal conductivity of a two-phase system on the basis of effective medium theory (EMT) [364, 388]. The basic assumptions of EMT are that the particles are embedded within a continuous matrix at low concentration and under static condition [38]. According to Maxwell's EMT, the effective thermal conductivity (k_{eff}) can be expressed by the following equation [364].

$$k_{eff} = \frac{k}{k_f} = \frac{1 + 2\beta_M \phi}{1 - \beta_M \phi} \tag{1.4}$$

Here, k_f is the thermal conductivity of the base fluid, ϕ is the volume fraction of the nanoparticles and $\beta_M = \frac{k_p - k_f}{k_p + 2k_f}$, where k_p is the thermal conductivity of the nanoparticles.

EMT model does not consider the effects of interparticle interactions and interfacial thermal resistance. To account for the interfacial thermal resistance (or Kapitza resistance, R_K), k_f in Eq. 1.4 is modified by $k_f + \alpha_M k_p$, where $\alpha_M = \frac{2R_K k_f}{d_{np}}$ and d_{np} is the diameter of the nanoparticles [38]. However, for practical applications of such models, the value of Kapitza resistance needs to be precisely evaluated, which is not straight forward [389]. At higher loading concentrations, the interparticle distance between the dispersed nanoparticles decreases leading to an enhancement in interparticle interaction, where EMT is not valid. Bruggeman modified the EMT to incorporate the effects of interparticle interactions and according to this model the effective thermal conductivity is expressed by the following equation [365].

$$k_{eff} = \frac{k}{k_f} = k_f \frac{(3\phi - 1)\frac{k_p}{k_f} + (2 - 3\phi) + \sqrt{\Delta_{BM}}}{4} \tag{1.5}$$

Here, Δ_{BM} is the volume fraction dependent Bruggeman constant and is expressed by the following equation [365].

$$\Delta_{BM} = (3\phi - 1)^2 (\frac{k_p}{k_f})^2 + (2 - 3\phi)^2 + 2(2 + 9\phi - 9\phi^2)(\frac{k_p}{k_f}) \tag{1.6}$$

Hamilton-Crosser further modified the Maxwell's EMT to incorporate the effects particle shape and according to this model, the effective thermal conductivity is expressed by the following equation [366].

$$k_{eff} = \frac{k}{k_f} = k_f [\frac{k_p + (n_{HC} - 1)k_f - (n_{HC} - 1)(k_f - k_p)\phi}{k_p + (n_{HC} - 1)k_f + (k_f - k_p)\phi}] \tag{1.7}$$

Here, n_{HC} is the shape factor, which is defined as $n_{HC} = 3/\psi_s$, where ψ_s is the sphericity of the dispersed nanoparticles. The values of ψ_s are 1 and 0.5 for perfectly spherical and prolate ellipsoid shaped nanoparticles, respectively [366]. Yu and Choi [368], further modified the Hamilton-Crosser model to incorporate the effects of interfacial layers. Considering parallel and series modes of heat transfer Agari and Uno [390] had proposed a logarithmic heat transfer model for nanocomposite matrices loaded with various types of nanofillers. Hashin and Shtrikman upper and lower bounds on thermal conductivity enhancements also considers series and parallel modes of heat transfer in nanofluids [367]. It must be noted in this regard that under the auspices of mean field models, parallel mode of heat transfer allows for the highest thermal conductivity enhancement in nanofluids [391].

Various forms and modifications of these primary models had been utilized to explain the role of nano-inclusion loading on thermal conductivity enhancements in various types of PCMs, viz. lauric acid loaded with graphene nanoplatelets [65], PCMs loaded with single walled carbon nanotubes [234], PCM/expanded graphite composites [392], PCMs used in concentrated solar power plants [393], molten salts PCMs [394],

1.9 Motivation

Research and development of green energy materials and associated technologies picked up momentum due to low carbon energy policies and rapid industrialization. Effective conversion, storage and management of renewable energy sources and energy harvesting are essential to close the gap between the supply and demand of energy and to curtail further environmental degradation [144]. In this context, intermediate storage of solar energy, waste heat recovery from industrial processes and thermoregulation applications in buildings by latent heat thermal energy storage using organic PCMs is one of the most prudent approach towards energy security [78].

In spite of immense industrial benefits of thermal energy storage using organic PCMs, the practical applicability of these materials is severely restricted due to their inherently low thermal conductivity [214]. Hence, dispersing high thermal conductivity nano-inclusions within the continuous medium of PCM has been attempted to enhance thermal conductivity of the PCMs [237, 238, 387, 395]. However, the role of particle loading, the effect of surface functionalization, nature and physical properties of the nano-inclusions, the effects of size, shape and aspect ratio of these nano-inclusions are poorly understood. Moreover, the understanding of the exact mechanism of nano-inclusion assisted thermal conductivity enhancement in PCMs is unclear [65, 234, 341, 342]. Further, material losses, due to leakage, during solid-liquid phase transition calls for further studies on form-stable PCMs [241, 268, 283, 396]. The above-mentioned aspects serve as motivation for undertaking the present study. This thesis attempts to obtain new insight into nano-inclusion aided thermal conductivity enhancement of organic phase change materials and photo-thermal conversion in organic phase change materials. Besides an attempt is made to prepare shape-stable organic phase change materials to arrest material leakage during phase transition.

1.10 Objectives

The main goals of the thesis are to probe the role of surface functionalization of nano-inclusions, particle loading, cluster formation and nature of nano-inclusions on thermal conductivity enhancement of organic phase change materials (PCMs) and demonstrate photo-thermal conversion in shape-stable PCMs. The major objectives of this thesis are mentioned below.

i) To probe the role of surface functionalization of nano-inclusions on long term thermal stability and thermal conductivity enhancement of PCMs loaded with nano-inclusions.

ii) To tune the phase transition temperature of composite PCMs by varying the constituent concentrations and probe thermal conductivity enhancements in these tuned PCMs, upon loading with various nano-inclusions.

iii) To probe the role of nano-inclusion concentration on thermal conductivity enhancement.

iv) To investigate micro-scale aggregation phenomena and formation of percolating network during solidification of the PCMs.

v) To study photo-thermal conversion of carbon black nano-inclusion loaded PCMs and the role of particle concentration on conversion efficiency.

vi) To demonstrate a form-stable PCM with high latent heat storage capacity and phase transition temperature around ~ 19 ^{0}C.

1.11 Overview of the thesis

This thesis consists of 7 chapters and details of the chapters are summarized below. **Chapter 1** gives a brief introduction on various modes of thermal energy storage, classification of PCMs and some practical applications of latent heat thermal energy storage systems. The limitations of PCMs due to low thermal conductivity and material losses because of leakage during first order solid-liquid phase transitions and various strategies adopted to circumvent these limitations are also briefly discussed. Thermal properties of nanofluids and factors influencing thermal conductivity of nanofluids are also briefly discussed in this chapter. **Chapter 2** describes the experimental methods for sample preparation, characterization of the nano-inclusions, PCMs, measurement of thermal conductivity and photo-thermal conversion efficiency. **Chapter 3** describes the role of surface functionalization and physical properties of nano-inclusions on thermal conductivity enhancement during liquid-solid phase transition of hexadecane based PCMs, upon loading with various nano-inclusions. Experimental findings indicated that surface functionalization of the nano-inclusions resulted in better thermal stability of the nano-inclusion loaded PCMs, without significant reduction in thermal conductivity enhancement. **Chapter 4** presents the results of tuning phase transition temperature of composite PCMs, viz. phenol-water system and palmitic acid/di-methyl formamide (PA-DMF) mixtures. Experimental results indicated enhanced thermal conductivity of the tuned PCMs, loaded with various nano-inclusions. **Chapter 5** discusses carbon black nanopowder assisted enhancement in thermal conductivity and photo-thermal conversion in paraffin wax (PW) and lauric acid (LA) based PCMs with varying loading concentrations. The superior volume filling capacity and fractal nature of CBNP aggregates resulted in higher thermal conductivity enhancement. **Chapter 6** describes the formulation, thermophysical characterization and thermal conductivity enhancement of palmitic acid/hexadecane (PA-HD) based binary form stable PCM with a phase transition temperature ~ 19 ^{0}C. For thermal cycling up to 40 ^{0}C, no leakage was observed and the binary PCM retained the shape and structural integrity. **Chapter 7** summarizes the results along with conclusions drawn and recommendation for future work.

Chapter 2

Experimental methods

Chapter 2 Experimental methods

2.1 Materials

The organic phase change materials (PCMs) n-hexadecane (HD), phenol (PH), palmitic acid (PA), paraffin wax (PW) and lauric acid (LA) were used without any further purifications. The PCMs were selected for a wide range of phase transition temperature region suitable for thermal energy storage applications. **Table 2.1** shows the source, purity, density, typical phase transition temperature and bulk thermal conductivity in liquid state for the various PCMs. For tuning the phase transition temperature of phenol and palmitic acid based PCMs, Milli-Q water and di-methyl formamide (DMF: C_3H_7NO) were used. DMF was obtained from M/s Loba Chemie Pvt. Ltd., India. For enhancing thermal conductivity of the PCMs, various nano-inclusions were used, viz. carbon black nanopowder (CBNP), multi-walled carbon nanotube (MWCNT), graphene nanoplatelets (GNP), nickel nanoparticles (NiNP), copper nanoparticles (CuNP), silver nanowires (AgNW), alumina (α-Al_2O_3), silica (SiO_2) and titania (TiO_2). **Table 2.2** shows the source, purity, bulk density, typical dimensions and bulk thermal conductivity of the various nano-inclusions.

2.2 Tuning of phase transition temperature of PCMs

For applications near ambient temperature, e.g. maintaining constant building temperature, cooling of electronic devices, thermal management of batteries and low energy solar thermal apparatus, development of PCMs with phase transition temperatures around room temperature is desired [4]. However, solid-liquid phase transition temperature of pure phenol and palmitic acid is ~ 40 and ~ 60-63 ^{0}C, respectively [276, 397], which limits their applications in room temperature thermal energy storage. The phase transition temperature of phenol and palmitic acid based PCMs were tuned by adding required amount of water and DMF, respectively.

Table 2.1 Physical and chemical properties of organic phase change materials (PCMs).

PCMs	Abbreviation used	Source	Purity (in %)	Density (g/cm^3)	Phase transition temperature (^{0}C)	Thermal conductivity in liquid state (W/mK)
n-Hexadecane	HD	M/s Sigma Aldrich	~ 99	~ 0.77	~ 18	~ 0.141
Phenol	Ph	M/s Merck	~ 99	~ 1.07	~ 40	~ 0.170
Palmitic acid	PA	M/s Central Drug House Pvt. Ltd.	~ 99	~ 0.85	~ 60-63	~ 0.140
Paraffin wax	PW	M/s Thermo Fisher Scientific India Pvt. Ltd.	Sulphated ash content ~0.05	~ 0.90	~ 58-60	~ 0.150
Lauric acid	LA	M/s SD Fine Chem Limited	~ 99	~ 0.88	~ 45	~ 0.155

Freezing point of the phenol-water system was tuned by adjusting the phenol-water ratio. Four different concentrations of phenol-water system were prepared by mixing 0.74, 1.56, 2.55 and 3.25 wt. % of water (neglecting the impurity water content). Phenol is hygroscopic in nature and the purity of the phenol, used in the present study, was 99.5 % with a water content < 0.5 %. However, moisture ingress in phenol based PCM is expected. The melting point of pure phenol (99.5 %) was estimated from differential scanning calorimetry studies.

The freezing points of the phenol-water systems with varied water concentrations were also estimated from the temperature dependent refractive index measurements [215].

Table 2.2 Properties of various nano-inclusions.

Nano-inclusions	Abbreviation used	Source	Purity (in %)	Dimensions	Bulk density (g/cm^3)	Bulk thermal conductivity (W/mK)
Carbon black nano powder	CBNP	M/s Reinste	> 99 (ash content < 0.02)	~ 29 ± 1 nm	~ 0.1	~ 0.250
Multi-walled carbon nanotube	MWCNT	M/s Nano-Amor	> 99	Length: 5-15 μm Outer diameter: 10-20 nm	~ 0.07	~ 6600
Graphene nanoplatelets	GNP	M/s Reinste	~ 91 atom %	Thickness: 6-10 nm	~ 2.26	~ 3000
Nickel nanoparticles	NiNP	M/s Nano-Amor	~ 99.9	~ 29 ± 3 nm	~ 8.91	~ 91
Copper nanoparticles	CuNP	M/s Nano-Amor	~ 99.8	~ 13 ± 2 nm	~ 8.94	~ 385
Silver nanowires	AgNW	M/s Reinste	~ 99.5	Length: < 50 μm Outer diameter: ~ 100 nm	~ 10.5	~ 427
Alumina	α-Al_2O_3	M/s Nano-Amor	~ 99.5	~ 43 ± 3 nm	~ 4.1	~ 35
Silica	SiO_2	M/s Sigma Aldrich	~ 99.5	~ 26 ± 3 nm	~ 2.2-2.6	~ 1.4
Titania	TiO_2	M/s Chempure Private Limited	~ 99.5	~ 28 ± 2 nm	~ 4.23	~ 15

For the palmitic acid based PCMs, PA-DMF weight ratio was varied to tune the phase transition temperature. Four different PA-DMF composite PCMs were prepared by adding 16.6, 27.4, 50.5 and 59.4 wt. % of DMF in PA. DMF (liquid at room temperature) was added in the required proportion to the pristine PA in the liquid state at 65 ± 1 ^{0}C. Thereafter, the mixtures were subjected to magnetic stirring for 1200 s at 62 ± 1 ^{0}C, followed by water bath sonication for 600 s at T = 60 ± 1, 50 ± 1, 40 ± 1 and 35 ± 1 ^{0}C for the composite PCMs with 16.6, 27.4, 50.5 and 59.4 wt. % of DMF, respectively. The water bath temperature was kept constant at ~ 5 ^{0}C higher than the corresponding melting points of the composite PCMs for proper mixing [218]. Phase transition temperatures of pure PA and PA-DMF composite PCMs were accurately estimated from differential scanning calorimetry and temperature dependent refractive index measurements.

2.3 Preparation of nano-inclusion loaded PCMs

Nano-inclusions of various concentrations were dispersed in the continuous phase of the PCMs, in the liquid state, i.e. at temperature higher than the corresponding melting points. To ensure uniform dispersion of the nano-inclusions within the PCM host matrix, water bath or horn sonication (using Sonic Vibra-cell) were done. The sonication time was optimized to ensure homogenous distribution of the nano-inclusions. For the n-hexadecane based PCMs, the CBNP, NiNP, AgNW and GNP nano-inclusions were surface functionalized with oleic acid, before adding to the PCM host matrix [216]. Detailed description of same preparation are provided in the subsequent chapters. **Fig. 2.1** schematically shows the steps followed for preparation of the nano-inclusion loaded PCMs.

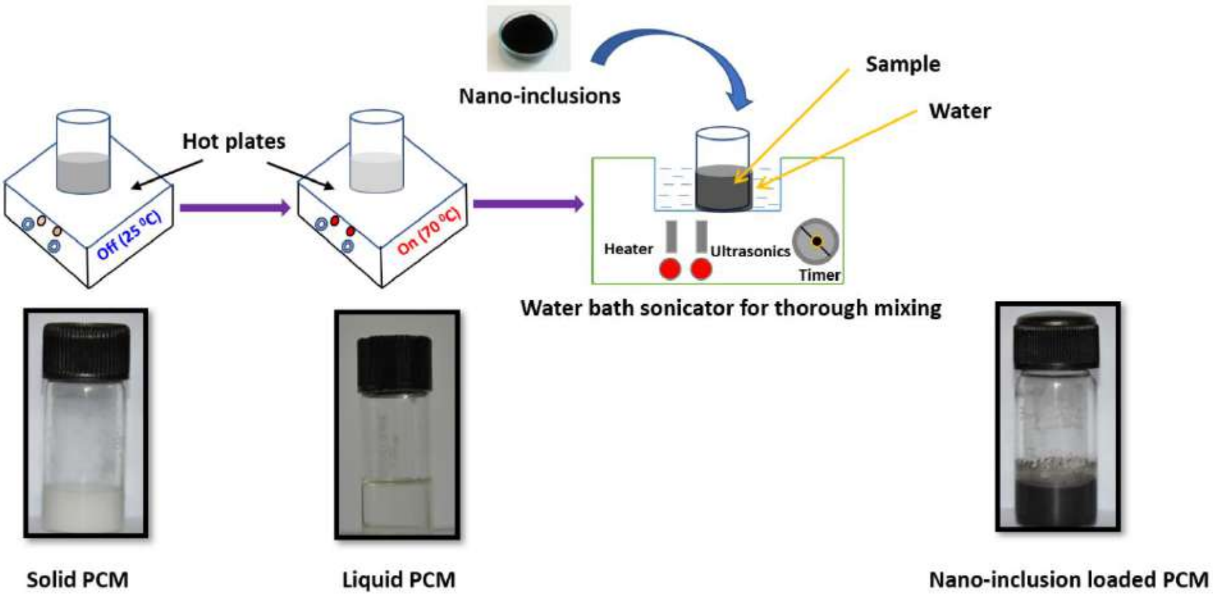

Figure 2.1 Schematic illustration of the experimental steps followed for preparation of phase change materials loaded with various types of nano-inclusions.

2.4 Thermo-physical characterization of the nano-inclusions & PCMs

The various nano-inclusions and PCMs were characterized using different techniques, such as powder X-ray diffraction (XRD), small angle X-ray scattering (SAXS), scanning and transmission electron microscopy (SEM & TEM), atomic force microscopy (AFM), phase contrast optical microscopy, Fourier transform infrared spectroscopy (FTIR), dynamic light scattering (DLS), differential scanning calorimetry (DSC) and refractive index measurement. Thermal conductivity and photo-thermal conversion efficiency of the PCMs, with or without nano-inclusion loading, were measured using a transient hot-wire method and infrared thermography (IRT), respectively. **Fig. 2.2** schematically categorize the various thermo-physical characterization techniques, used in the present study. The basic working principles of the characterization techniques are briefly discussed in the following sections.

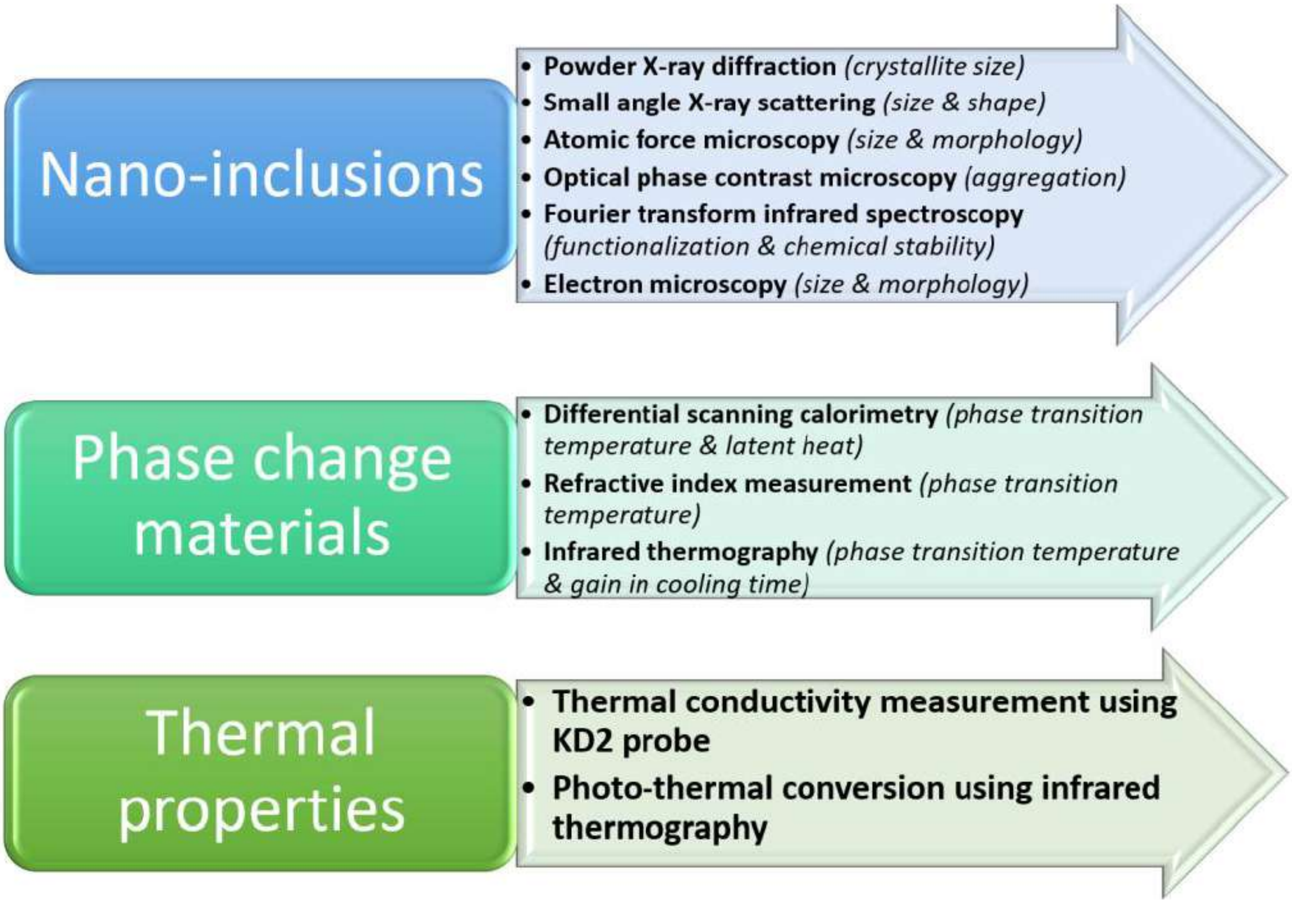

Figure 2.2 Characterization techniques used in the present study to probe the thermo-physical properties of the nano-inclusions and PCMs.

2.4.1 Powder X-ray diffraction

Powder X-ray diffraction (XRD) is one of the most common techniques used to determine crystal structure and crystallite size of nanoparticles. In XRD, the wavelength of hard X-ray is close to size of atoms (in angstrom). In Powder X-ray diffraction the received diffracted pattern is from powder of the materials and hence, present information from all possible crystallographic planes. The fundamental principal of X-ray diffraction is based on Bragg's law of diffraction [398], which is schematically shown in **Fig. 2.3a**.

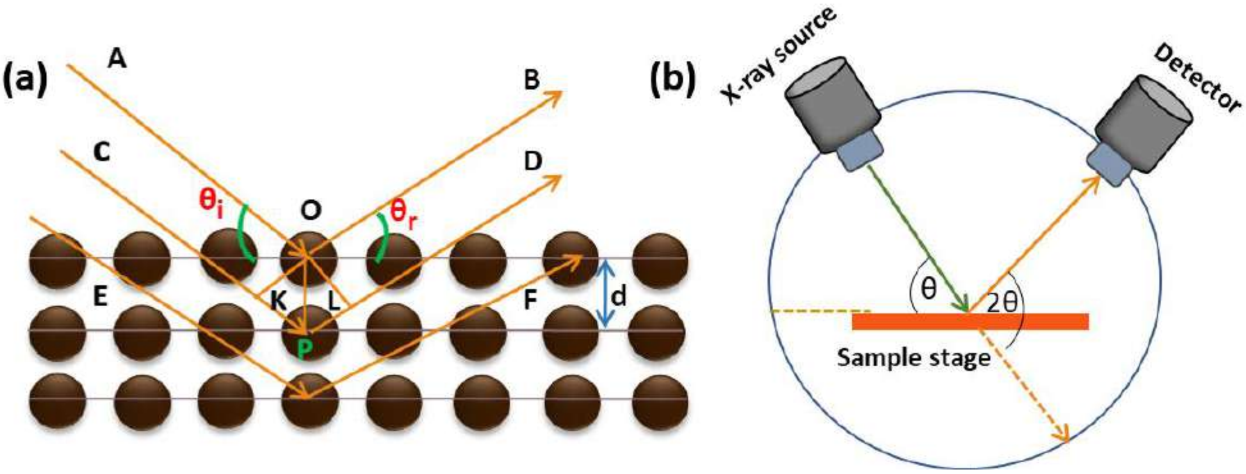

Figure 2.3 (a) Schematic showing Bragg's diffraction. (b) Schematic showing the θ-2θ geometry of a typical powder X-ray diffractometer showing the positions of the X-ray source, detector and sample.

As shown in **Fig. 2.3a** AO & CP are the two incident X-rays on two consecutive crystal planes, whereas, OB & PD are the corresponding diffracted rays, respectively. OK & OL are two perpendicular lines drawn from point O to the lines CP and PD, respectively. The path difference between the two rays can be by expression KP+PL= $2d_{hkl}\sin\theta$. For constructive interference, the Bragg's law satisfies $2d_{hkl}\sin\theta = n\lambda_X$, were d_{hkl} is the spacing between two consecutive planes, θ is the Bragg angle, n is the order of diffraction, λ_X is the wave length of the incident X-ray and h, k & l are the miller indices of the crystallographic plane. **Fig. 2.3.b** shows the schematic of the θ-2θ geometry of a powder X-ray diffractometer and during measurements, the X-ray source and the detector lie on the circumference of a focussing circle and depending on the phase of the diffracted X-rays, constructive interference occurs at specific directions. Apart from crystal structure, powder XRD is also useful for determining the phase and crystallite sizes. For spherical particles of average crystallite size (d_{cryst}), Scherrer's equation indicate that $d_{cryst} = 0.89\lambda_X / \beta\cos\theta$, where 0.89 is a proportionality constant for spherical particles, β represented full width at half maxima (FWHM) of the diffraction peaks and θ is the half of the diffraction angle [399]. In the present study, room temperature powder XRD measurements were carried out in the 2θ range of 20-80^0, using a Rigaku X-ray diffractometer, which employs CuK$_\alpha$ radiation (wavelength = 1.5416 Å) in the Bragg-Brentano geometry. The scan rate and step size were fixed at 2^0 per minute and 0.02^0, respectively.

Figure 2.4a shows the powder XRD pattern of α-Al_2O_3 at room temperature, where the Bragg's reflection peaks corresponding to (012), (104), (110), (113), (024), (116), (018), (214), (300) and (119) planes of the rhombohedral crystal structure (JCPDS 46-1212) [400] were seen. The XRD pattern indicated the highly crystalline structure of α-Al_2O_3. The average crystallite size determined from the strongest reflection peak of (113) plane, using Scherrer's equation was found to be ~ 43 (± 3) nm. **Fig. 2.4b** shows the powder XRD pattern of TiO_2, at room temperature, where Bragg's reflection peaks corresponding to (110), (101), (200), (111), (211), (220) and (301) planes of the tetragonal crystal structure of rutile TiO_2 (JCPDS 88-1175) were discernible. The strong diffraction peaks at ~ 27^0, 36^0 and 55^0 confirmed the presence of TiO_2 in the rutile phase [401]. The average crystallite size determined from the strongest reflection peak of (110) plane was found to be ~ 28 (± 2) nm. **Fig. 2.4c** shows the powder XRD pattern of NiNP at room temperature, where clear Bragg reflection peaks corresponding to (111), (200) and (220) planes of FCC nickel were observed for 2θ values of 44.5, 51.8 and 76.4 ^{0}, respectively (JCPDS 04-0850) [402]. The average crystallite size, determined from the strongest reflection peak of (111) plane using Scherrer's equation, was found to be ~ 29 (±3) nm. **Fig. 2.4d** shows the powder XRD pattern of CuNP at room temperature, where the Bragg reflection peaks indicated the presence of elemental Cu and monovalent and divalent oxides of Cu (Cu_2O and CuO). The Bragg reflection peaks corresponding to (111), (200) and (220) planes of FCC Cu were observed at 2θ values of 43.4, 50.5 and 74.1 ^{0}, respectively (JCPDS 71-4610) [403]. The average crystallite size obtained from the strongest reflection peak of (111) plane, using Scherrer's equation, was found to be ~ 13 (± 2) nm. **Table 2.3** summarizes the crystal structure and average crystallite sizes of the various nano-inclusions obtained from powder X-ray diffraction studies.

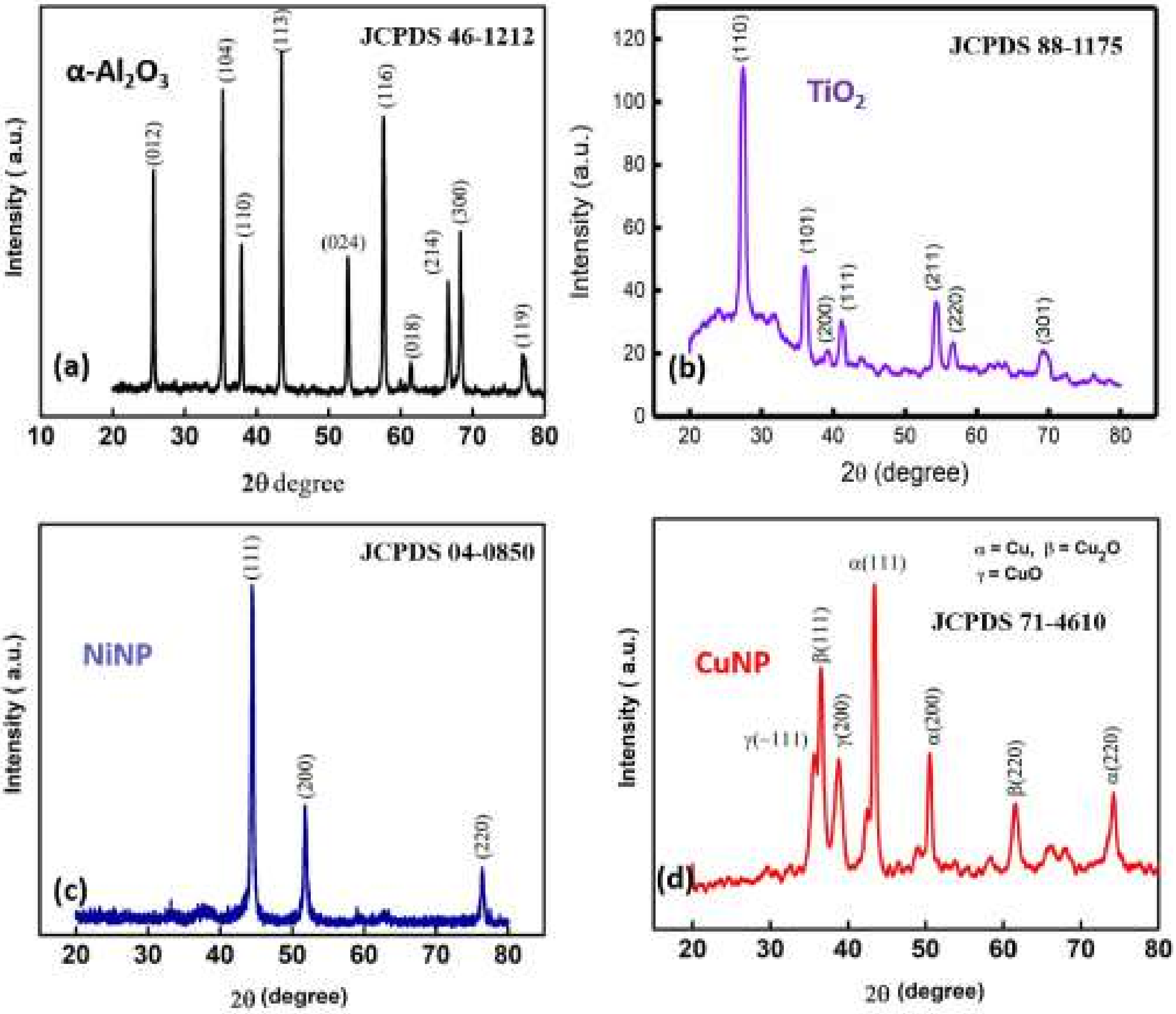

Figure 2.4 Room temperature powder XRD patterns of (a) α-Al_2O_3, (b) TiO_2, (c) NiNP and (d) CuNP nanoinclusions. All the major Bragg diffraction peaks are indexed.

Table 2.3 Summary of powder X-ray diffraction studies of various nano-inclusions. Crystal structure, JCPDS matched data, strongest peak and average crystallite sizes are tabulated.

Nano-inclusions	JCPDS	Crystal Structure	Strongest peak	Average crystallite size (nm)
α-Al_2O_3	JCPDS 46-1212	rhombohedral	(113)	~ 43 ± 3
TiO_2	JCPDS 88-1175	tetragonal	(110)	~ 28 ± 2
NiNP	JCPDS 04-0850	face-centered cubic	(111)	~ 29 ± 3
CuNP	JCPDS 71-4610	face-centered cubic	(111)	~ 13 ± 2

2.4.2 Small angle X-ray scattering

Small angle X-ray scattering (SAXS) is a well-established characterization technique for obtaining information about the size, shape and periodicity of structures ranging from ten to thousands of angstroms. A well-collimated X-ray beam with a small cross-section and extended sample-detector distance to reduce background are the primary requirement for SAXS studies. In SAXS, I(q) represent the scattering intensity from a collection of objects and is expressed as I(q) = N.F(q).S(q),where N is the number of objects, F(q) is the form factor and S(q) is the structure factor and q is the scattering wave vector , which is expressed as $q = 4\pi \sin\theta / \lambda_X$ [404]. The scattering intensity from a spherical particle of diameter d_{np} is expressed by the following equation [404, 405].

$$I(q) = (\Delta\rho_e)^2 V_p^{\,2} [3 \frac{\sin({}^{qd_{np}}/_2) - ({}^{qd_{np}}/_2)\cos({}^{qd_{np}}/_2)}{({}^{qd_{np}}/_2)^3}]^2 \tag{2.1}$$

Here $\Delta\rho_e$ and V_p indicate electron density difference between the particle and surrounding medium and particle volume, respectively. By using Fourier transform of the intensity profile, the distance distribution function [P(r)] is calculated using the following equation [406].

$$P(r) = \frac{2}{\pi}\int_0^\infty I(q)qr\sin(qr)\exp(-M^{/}q^2)dq \tag{2.2}$$

Here, M′ is a numerical damping factor related to the termination effects of the Fourier transform. To obtain information on the shapes and sizes of α-Al_2O_3, SiO_2, TiO_2 and carbon black Nanopowder (CBNP) SAXS experiments were carried out using Rigaku Ultima IV instrument in the transmission geometry (2θ range = 0-2.2^0 in steps of 0.01^0). The scattering intensity, I(q) was measured as a function of q and parasitic scattering from air and sample cell was removed before data analysis using NANO-solver software. The variation of P(r) as a function of diameter is shown in **Fig. 2.5** for α-Al_2O_3, TiO_2, SiO_2 and CBNP nano-inclusions. The average sizes were found to be ~ 50 (± 2), 28 (± 2), 26 (± 2) and 21 (± 2) nm for α-Al_2O_3, TiO_2, SiO_2 and CBNP, respectively.

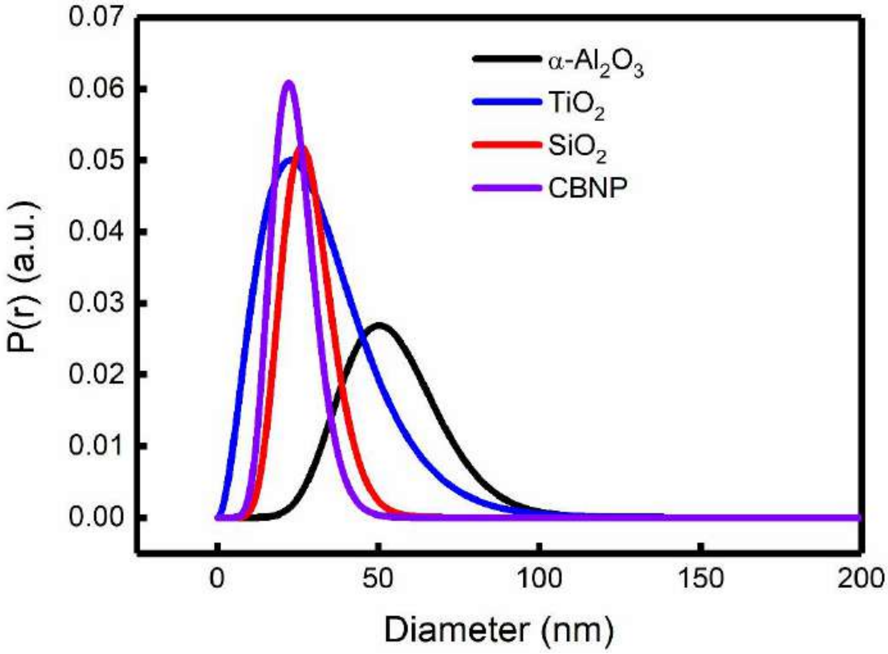

Figure 2.5 Variation of P(r) as a function of diameter for α-Al_2O_3, TiO_2, SiO_2 and CBNP nano-inclusions.

2.4.3 Scanning and transmission electron microscopy

Electron microscopy is a technique for obtaining high resolution images of the object under investigation using electron as a source of illuminating radiation. The higher resolution of electron microscopy is due to the use of electrons, which are of shorter wavelength. However, special techniques are required for sample preparation for electron microscopy. Electron microscopy can be broadly classified into two methods, viz. scanning electron microscopy (SEM) and transmission electron microscopy (TEM). In conventional SEM, image is formed by scanning a focussed beam of electrons over the sample surface in a raster mode. The secondary electrons emitted from the surface is detected by a suitable detector for image constitution. On the other hand, in TEM, electron beam passes through the sample, thereby generating a projection image (bright field) or a diffracted image (dark field). Typical resolutions of standard modern SEM and TEMs are ~ 1 nm and sub-nm, respectively. TEM images of the nano-inclusions (provided by the suppliers) are shown in **Figs. 2.6a-e** for CBNP, NiNP, CuNP, AgNW and MWCNT nano-inclusions, respectively. The scale bars are also shown along with the corresponding images.

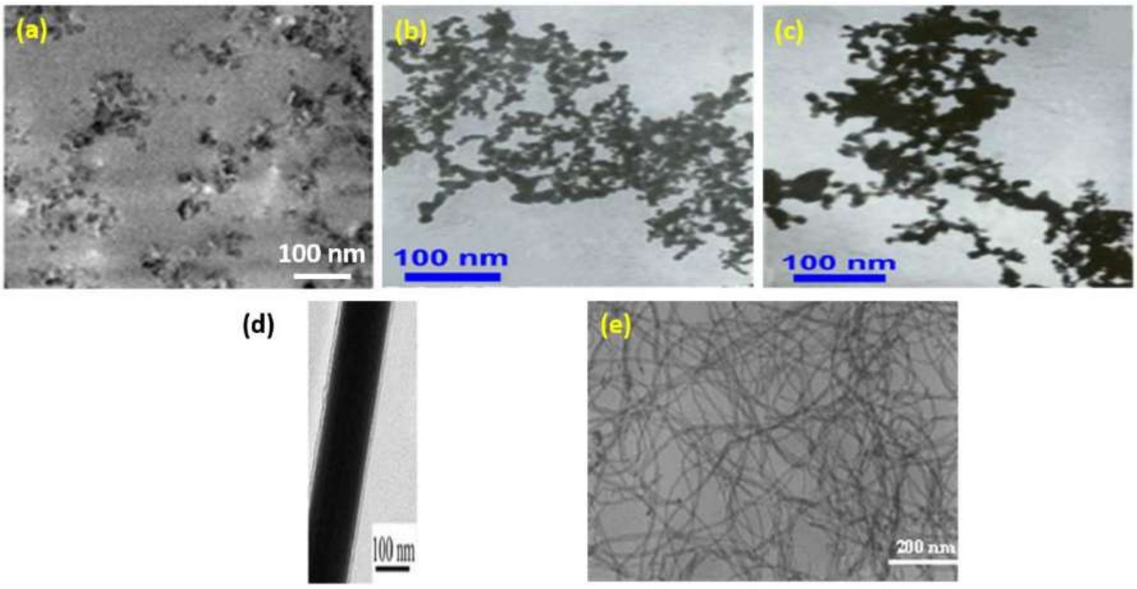

Figure 2.6 Typical TEM images of (a) CBNP, (b) NiNP, (c) CuNP, (d) AgNW and (e) MWCNT nano-inclusions. The TEM images were provided by the suppliers.

Figures 2.7a-b show the size distributions for the NiNP and CuNP samples obtained from TEM image analyses along with the corresponding log-normal fits. The most probable sizes were obtained as 23.4 ± 2.3 and 12.8 ± 2.8 nm for NiNP and CuNP, respectively, which were found to be in good agreement with the average crystallite sizes, obtained from the room temperature powder XRD patterns.

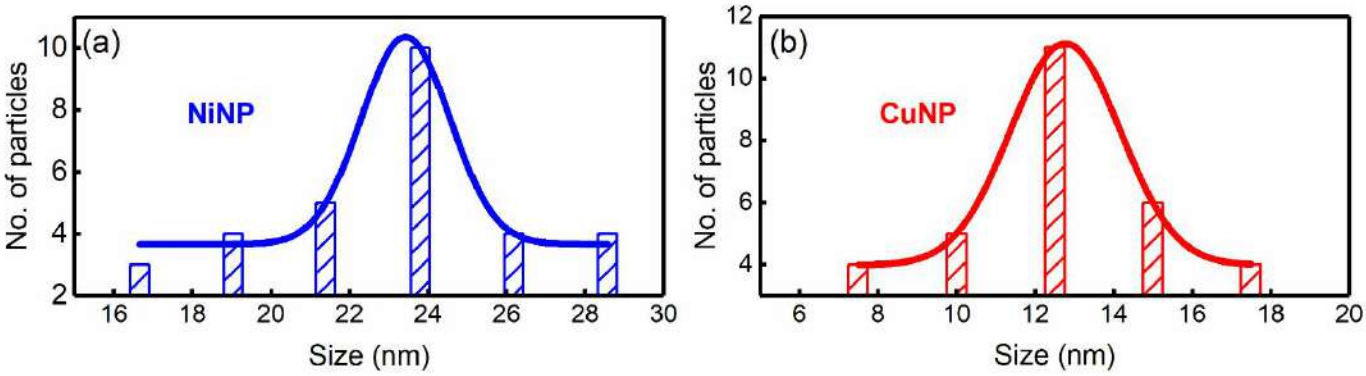

Figure 2.7 Size distribution obtained from TEM image analyses for (a) NiNP and (b) CuNP nano-inclusions. The log-normal fits are also shown in the figures.

Figures 2.8a shows a typical scanning electron microscopy (SEM) image of the α-Al_2O_3 nanoparticles (obtained from the supplier), where the spherical shape of the nanoparticles was clearly discernible. The SEM imaging was carried out at 50000X magnification and working distance of 6.5 mm under an accelerating voltage of 15.0 kV. The size distribution, obtained from SEM image analysis, is shown in the **inset of Fig. 2.8a** and the average particle size was obtained as ~ 50 (± 4) nm which was in good agreement with the sizes obtained from SAXS (~ 50 ± 2 nm) and XRD (~ 43 ± 3 nm). **Fig. 2.8b** shows the SEM image of the CBNP nano-inclusions, where the spherical morphology of the CBNP nodules was clearly discernible. It has been reported that CBNP nano-inclusions form aciniform aggregates [407] and a few such aciniform structures were clearly seen from the SEM image. The **inset of Fig. 2.8b**

shows the size distributions of the CBNP nano-inclusions, obtained from SEM image analysis, along with the log-normal fits for statistical analyses. The most probable size of the CBNP nano-inclusions was found to be ~ 31 ± 1 nm. **Fig. 2.8c** show the SEM images of the MWCNT nano-inclusions. From SEM image, the average length of MWCNT nano-inclusions was found to be ~ 1-3 µm. For CBNP nano-inclusions, SEM imaging was performed using a Carl Zeiss Sigma HV instrument, under vacuum environment. The working distance, accelerating voltage and magnification were kept constant at 3.9 mm, 10 kV and 100030X, respectively. For MWCNT nano-inclusions, SEM imaging was carried out using a Phenom-Pro desktop instrument, under standard vacuum conditions. The accelerating voltage and magnification were kept constant at 10 kV and 18000X, respectively.

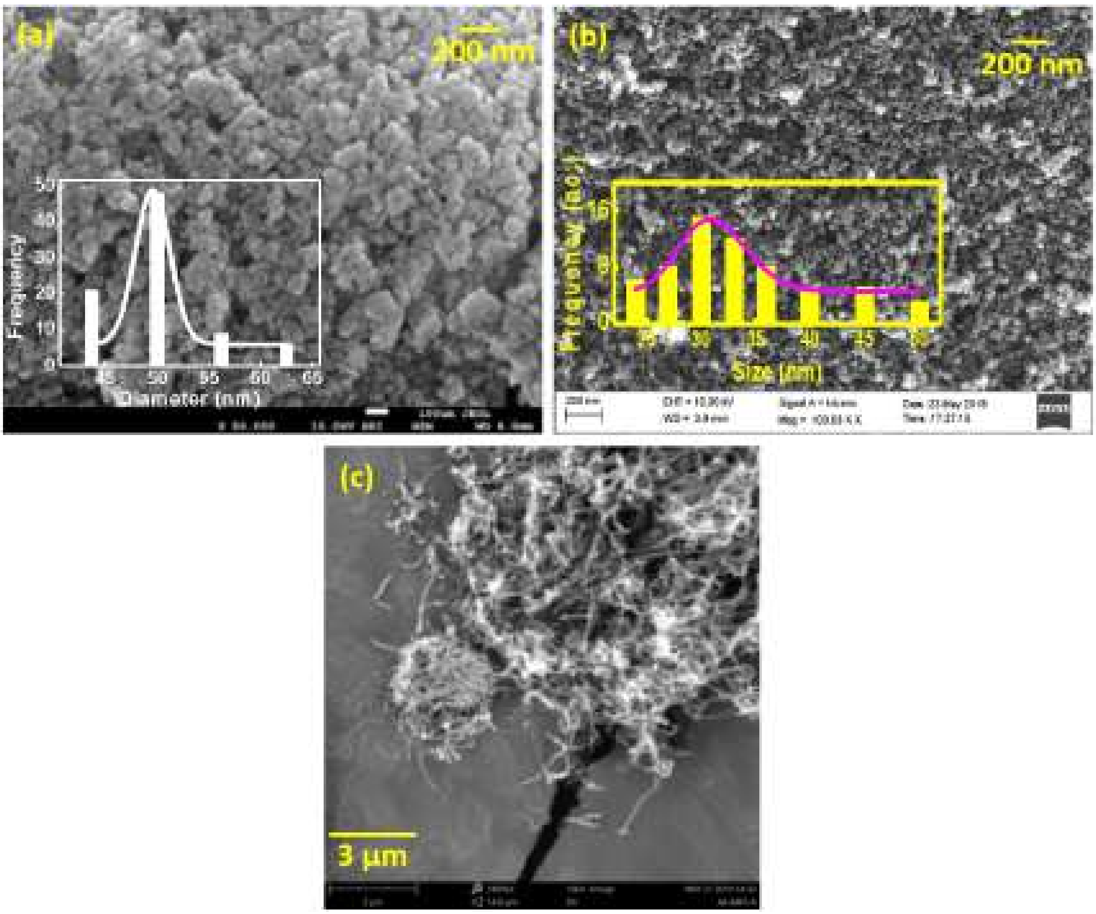

Figure 2.8 Typical SEM images of (a) α-Al_2O_3, (b) CBNP and (c)MWCNT nano-inclusions. The number distributions obtained from SEM image analyses are shown in the insets of (a) & (b).

2.4.4 Atomic force microscopy

Atomic force microscopy (AFM) is one of the most widely used scanning probe microscope, invented by Binning, Quate and Gerber in 1986 [408]. AFM is one of the most important tools for imaging nanoparticles and their morphologies. In AFM, a cantilever, with a sharp tip attached to its end, is used for scanning the sample surface. During scanning, the interaction force between the sample surface and the tip is indirectly measured. When the tip travels near the sample surface, the tip experiences the interaction forces, due to which the cantilever bend, thereby deflecting the reflected laser light that is measured using a position sensitive photo diode. From cantilever deflection measurements, the tip-surface force is assessed, through which the surface morphology is mapped in real space. **Fig. 2.9a** shows a schematic diagram of a typical AFM, where all the essential parts are indicated.

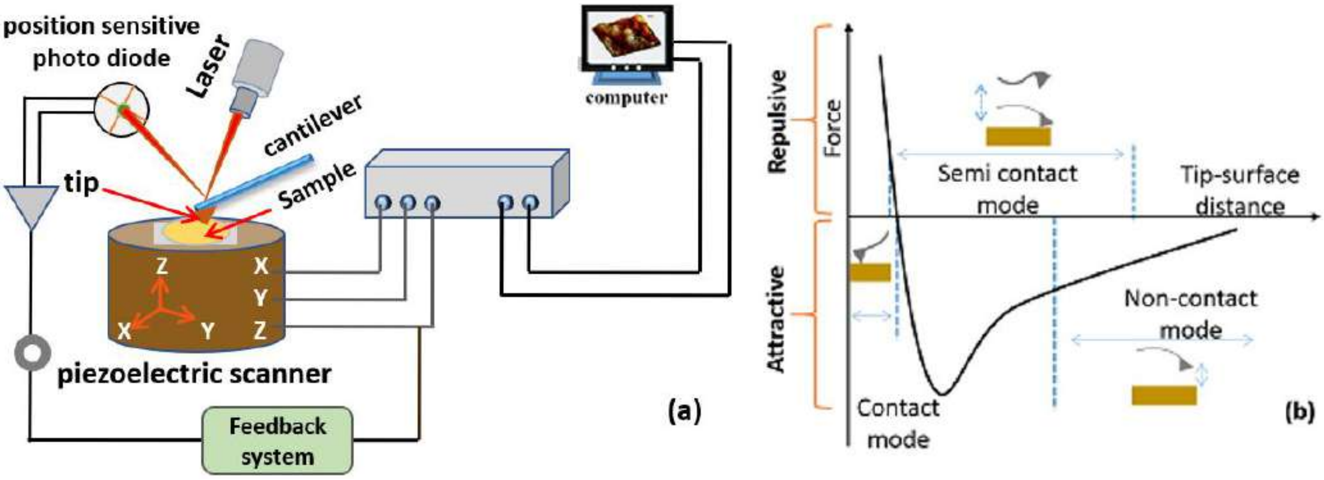

Figure 2.9 (a) Schematic of a typical atomic force microscope, where all the essential parts are indicated. (b) Schematic illustration of the different modes of operation in an atomic force microscope.

During measurement, the sample is placed on a piezoelectric sensor with independent X, Y and Z motion controller which are in-turn controlled by a robust feedback system that is driven by the output of the position-sensitive photo-diode indicating the deflection of the cantilever in real time. The set-point, amplitude and gain of the phase-lock loop are optimized for each sample. **Fig. 2.9b** schematically illustrates a typical force-distance curve and the different operating regions of AFM, viz., contact mode in repulsive regime, non-contact mode in attractive regime (large tip-surface separation) and tapping or semi-contact mode in the intermediate regime.

In the present study, atomic force microscopy was carried out, using a Ntegra Prima microscope (M/s NT-MDT, Russia) to obtain information on the shape and size of the various nano-inclusions. The aqueous dispersions of the nano-inclusions (concentration~ 0.1 wt. %) were sonicated for 30 minutes and drop-casted on freshly cleaved mica substrates, which were then allowed to dry *in-situ* at ~ 22 ± 1 ^{0}C. AFM studies were performed in the semi-contact mode using commercially available silicon tip (~ 10 nm bending radius and ~ 198 kHz resonant frequency). Before quantitative analysis, tip-shape de-convolution was performed using the NOVA-Px software.

Figure 2.10a shows the topographic image (5μm × 5 μm) of MWCNT drop casted on a mica substrate, where the tube-like structure is clearly observed. Sectional analysis was performed to quantify the topographic heights and **Fig. 2.10b** shows the variation in topographic height along three horizontal sections (indicated in **Fig. 2.10a**). The topographic height was found to vary between ~ 10-20 nm, against the specified outer diameter values of ~ 8-20 nm. Average length of the MWCNT were ~ 5-15 μm. **Fig. 2.10c** shows the topographic image (10 μm × 10 μm) of CBNP dispersion, where the spherical shape of the individual CBNP nodules were seen. Horizontal line scans were performed to analyze the topographic heights of several individual nodules and **Fig. 2.10d** shows the size distribution along with the log-normal fitting, where the most probable size was ~ 32 ± 2 nm. **Fig. 2.10e** shows the topographic image (10 μm × 10 μm) of GNP, where the planar structures of GNP are clearly discernible. Horizontal line scans were performed to probe the thickness of the individual GNP flakes and

Fig. 2.10f shows the variation in topographic height for two cases. The average values of thickness and planar dimensions were found to be ~ 6.5-9 nm and ~ 1.5-2.0 µm, respectively. The topographic image (50 µm × 50 µm) α-Al_2O_3 nanoparticles, drop-casted on a mica substrate, is shown in **Fig. 2.10g**, where the spherical morphology is clearly seen. **Fig. 2.10h** shows the topographic height distribution, along with the log-normal fitting, where the most probable size was ~ 48 ±1 nm.

2.4.5 Phase contrast optical microscopy

Phase contrast microscopy is an illumination technique in which small phase shifts in the light passing through a transparent specimen is converted into amplitude or contrast changes in the image. The basic governing principle of phase contrast microscopy is that small phase shifts in light rays induced by different thickness and refractive index of different parts of an object under investigation can be transformed into differences in brightness or light intensity. **Fig. 2.11** schematically shows the working principle of a phase contrast microscope. The illuminating light (yellow) passes through the condenser annulus and is focused on the specimen, where some part of the incident light is scattered (blue) and the remaining part is unaffected thereby forming the background light (orange). The scattered light is weak and typically phase shifted by -90°, relative to the background light, resulting in a low image contrast as the foreground and the background have nearly same intensity. In negative phase contrast microscopy, the background light is phase shifted -90° by passing it through a phase shift ring, which nullifies the phase difference between the background and the scattered light resulting in an increased intensity difference between foreground and background. Further, the background light is also diminished using a gray filter, thereby enhancing the phase contrast effect. In the present study, optical phase contrast microscopy was carried out at 10X magnification using an inverted phase contrast microscope (Carl Zeiss) in the liquid and solid states of the PCM with or without nano-inclusion loading.

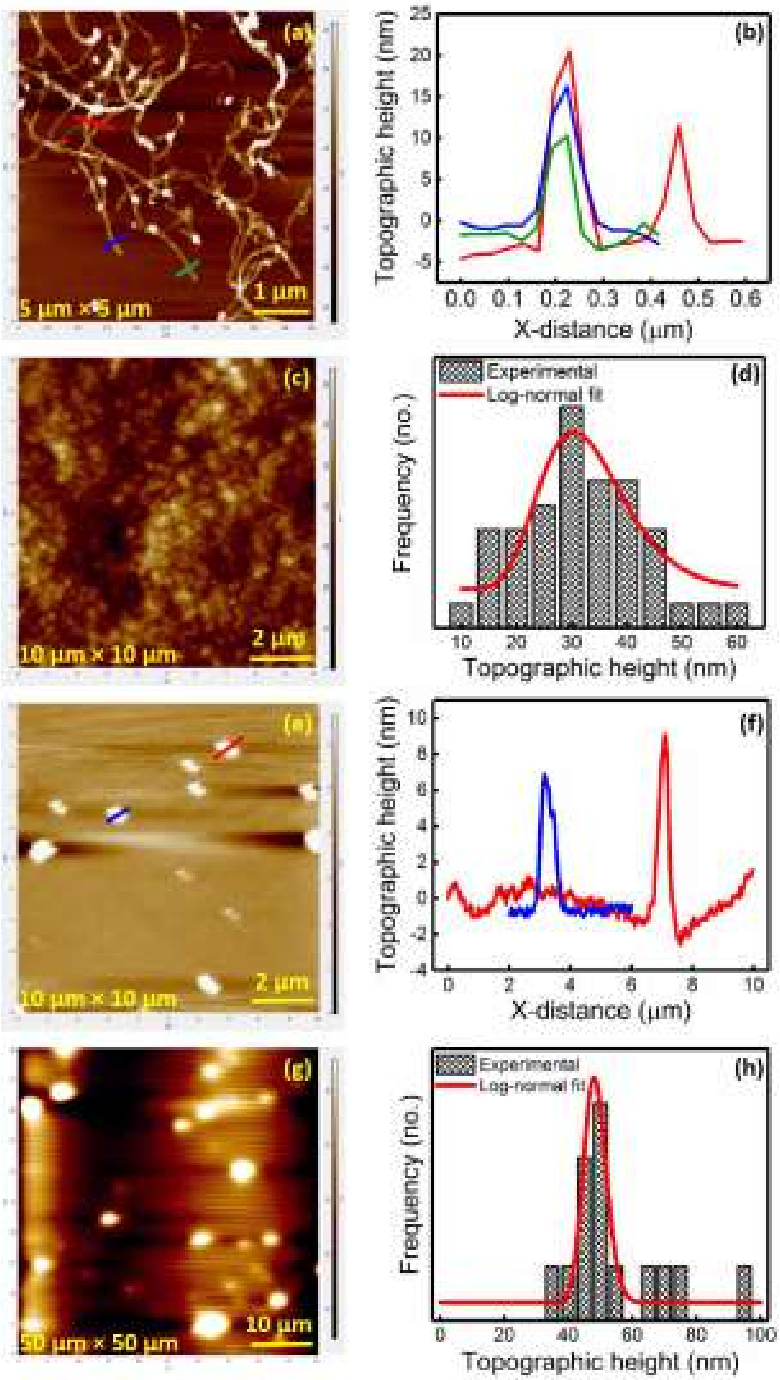

Figure 2.10 (a) Topographic image of MWCNT. (b) The variation in topographic height for MWCNT, along three horizontal sections, as indicated in (a). (c) Topographic image of CBNP dispersion. (d) Size distribution of CBNP along with the log-normal fitting. (e) Topographic image of GNP. (f) Variation in topographic height for GNP nano-inclusions. (g) Topographic image α-Al_2O_3 nanoparticles. (h) Topographic height distribution, along with the log-normal fitting for α-Al_2O_3.

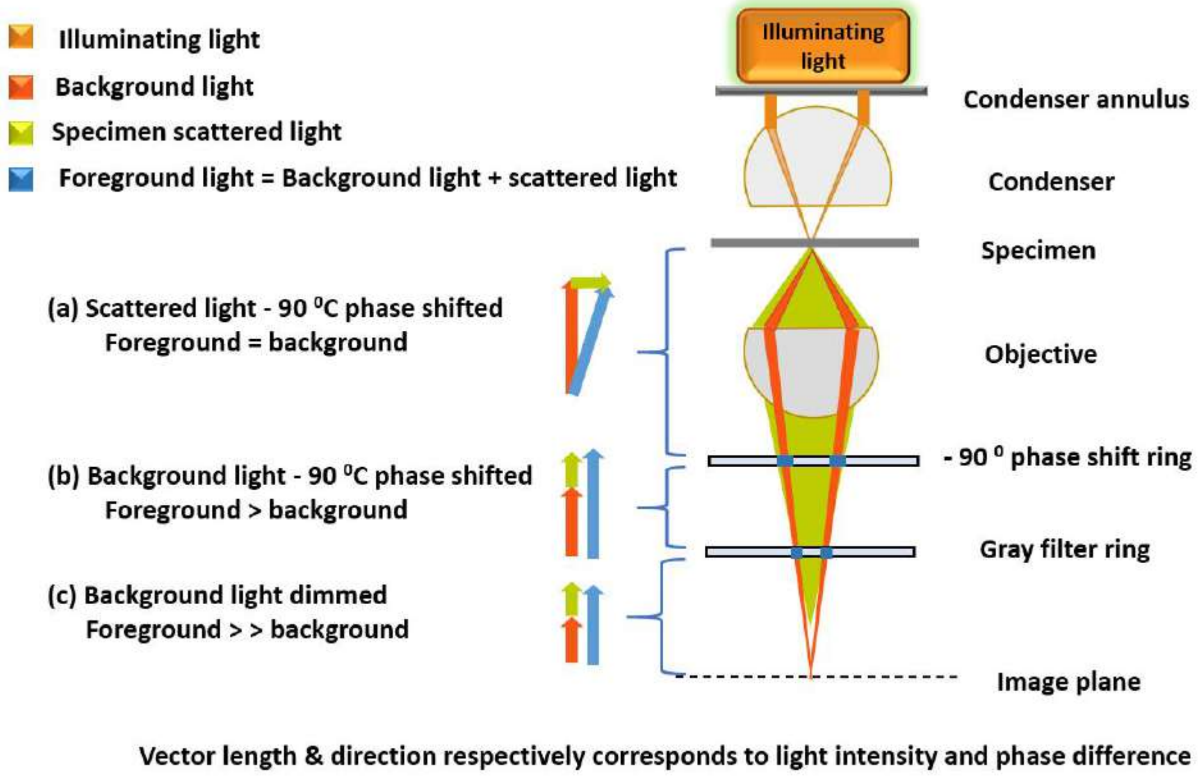

Figure 2.11 Schematic illustration of the working principle of an optical phase contrast microscope.

Additionally, real-time video was acquired for the PCM loaded with various nano-inclusions during freezing. Initially, the nano-inclusion loaded PCMs were kept in liquid state and drop casted on a transparent cover glass slip, which was allowed to be in thermal equilibrium with a microscope compatible peltier stage (Linkam PE 120XY). The solidification process was observed under the phase contrast optical microscope in real time and a time stamped video file was recorded. The sample temperature was kept slightly below the peak melting temperature of the PCMs to facilitate faster freezing.

2.4.6 Fourier transform infrared spectroscopy

Fourier Transform Infrared (FTIR) spectroscopy is used to the record the infrared (IR) spectra of the samples. In transmission mode, as infrared radiation is passed through the sample, some parts of the incident infrared radiation is absorbed by the sample and the remaining part is transmitted. For absorption of IR radiation by the molecule, there must be a net change of induced dipole moment by vibration modes within the molecule [409]. The resulting spectrum represents a molecular fingerprint of the sample. FTIR spectroscopy has several advantages as compare to conventional IR spectroscopy, such as multiplexing, high signal-to-noise ratio, wavenumber precision and fast scanning. The working principle of a FTIR spectroscope is based on the Michelson's interferometry technique and **Fig. 2.12** shows a schematic illustration of a typical FTIR spectrometer. The laser (coherent light source) is passed through a beam splitter, which allows 50 % of the incident light to transmit and hit the moving mirror. The other 50 % of the light is reflected and allowed to fall on the fixed mirror. When the reflected light waves are combined, interference patterns occur which passes through sample. The infrared light emanating from the sample is detected by a suitable infrared detector. In the present study, ABB Bomem MB 3000 FTIR spectrometer is used in the wavenumber range of 400-4000 cm^{-1}. The spectral resolution of the spectrometer is ~ 4 cm^{-1}. For solid powders, the samples were embedded in KBr pellets, after thorough mixing. For liquid samples, FTIR spectroscopy was carried out in the attenuated total reflection (ATR) mode using a ZnSe crystal in the wavenumber range of 500-3600 cm^{-1}. The ATR mode works on the principle of total internal reflection, where, infrared waves are allowed to pass through the ATR crystal in such a way that at least one reflection off the internal surface occurs, resulting in evanescent wave, which propagates into the sample (typical penetration depth is ~ 0.5-2 μm) [409]. The number of reflections and depth of penetration depend on several parameters, viz., the angle of incidence, wavelength, refractive indices of the crystal and medium, actual design and geometry of the crystal, etc. In the present study, single bounce ZnSe crystals were used. **Figs. 2.13a-b** show the schematic illustration of the transmission and ATR modes, respectively.

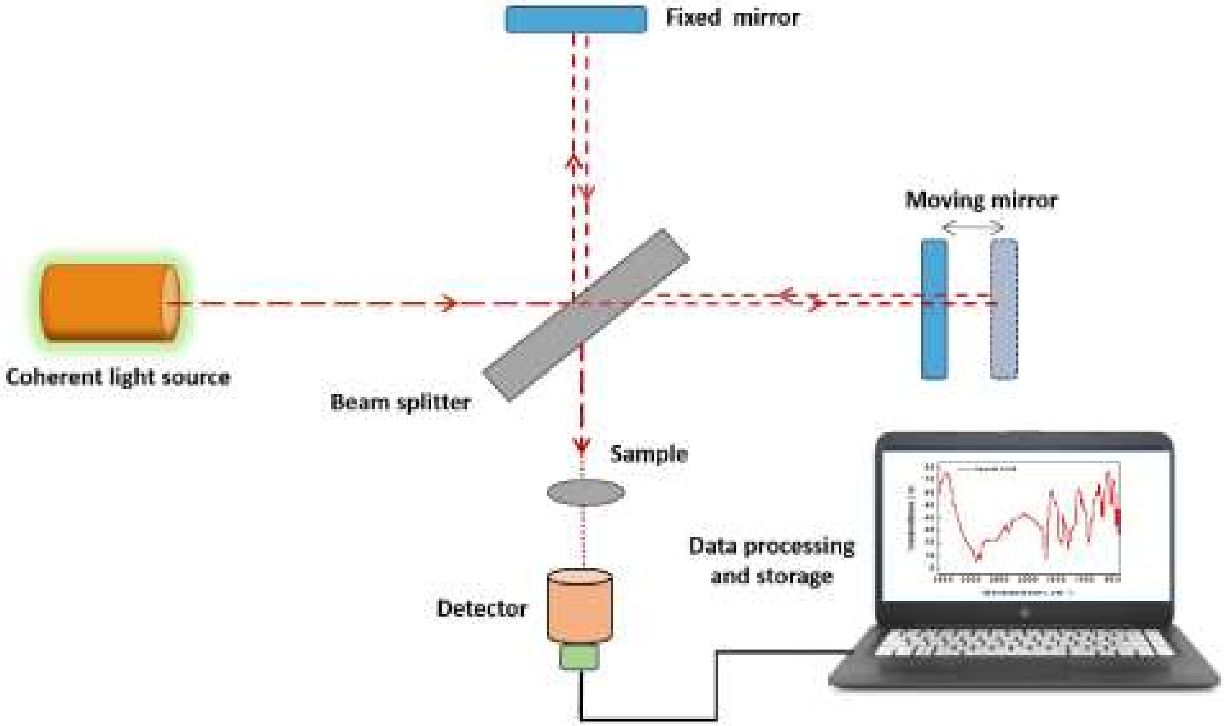

Figure 2.12 Schematic illustration of a typical FTIR spectrometer. All the essential components are indicated.

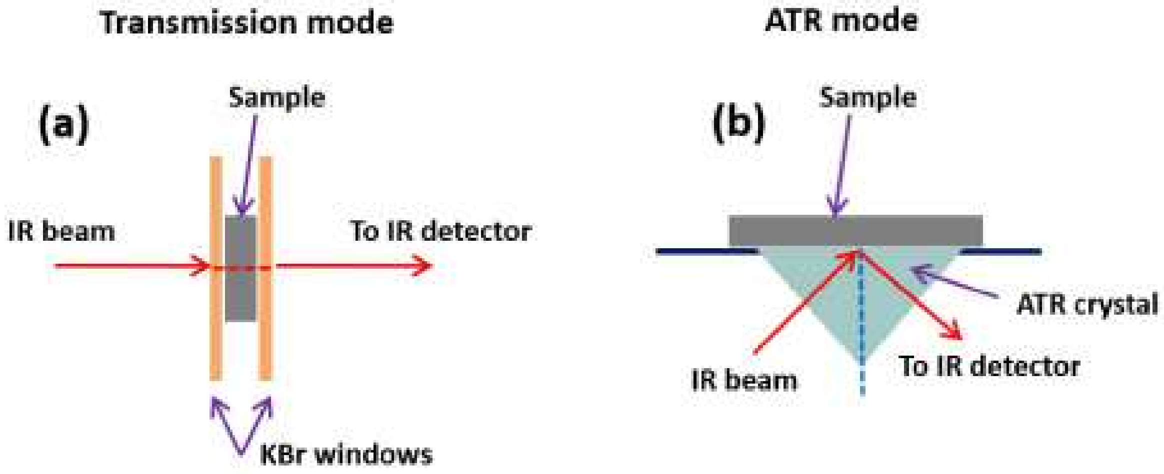

Figure 2.13 Schematic illustration of (a) Transmission and (b) ATR modes of working in a FTIR spectrometer.

2.4.7 Differential scanning calorimetry

Differential scanning calorimetry (DSC) is widely used to examine the material properties such as glass transition temperature, melting, crystallization, latent heat, specific heat capacity, cure process, purity, oxidation behaviour and thermal stability, under a controlled inert atmosphere (like argon or nitrogen) with controlled flow rates [410]. In the present study, DSC was extensively used to determine the phase transition temperature and latent heat values of the PCMs [411]. **Fig. 2.14** shows the schematic of a typical DSC. In DSC, the difference between the heat flow required to increase the temperature of a material (placed in a sample pan) and a reference pan is measured as a function of temperature. The applied heat from the heater goes though the electrical constantan disk toward the reference and sample pan. Temperature measurements are performed using precision thermocouples. A positive output of electrical potential of the thermocouples is shown when the sample temperature is higher than the reference temperature. On the other hand, the output is negative for higher reference temperature. To maintain a constant temperature for the sample and the reference pans, a differential voltage is supplied to the heaters. Typical DSC experiments indicate heat flow as a function of temperature (thermogram), from which the onset temperature (T^O), peak phase transformation temperature (T^P), endset temperature (T^E) and latent heat values are determined [412]. In the present study, DSC experiments were performed using a Mettler Toledo TGA-DSC-1, 1100 LF (Switzerland) combined TGA-DSC equipment, under an inert atmosphere of argon, in the temperature range of 25-80 ^{0}C at a heating rate of 3 ^{0}C per minute.

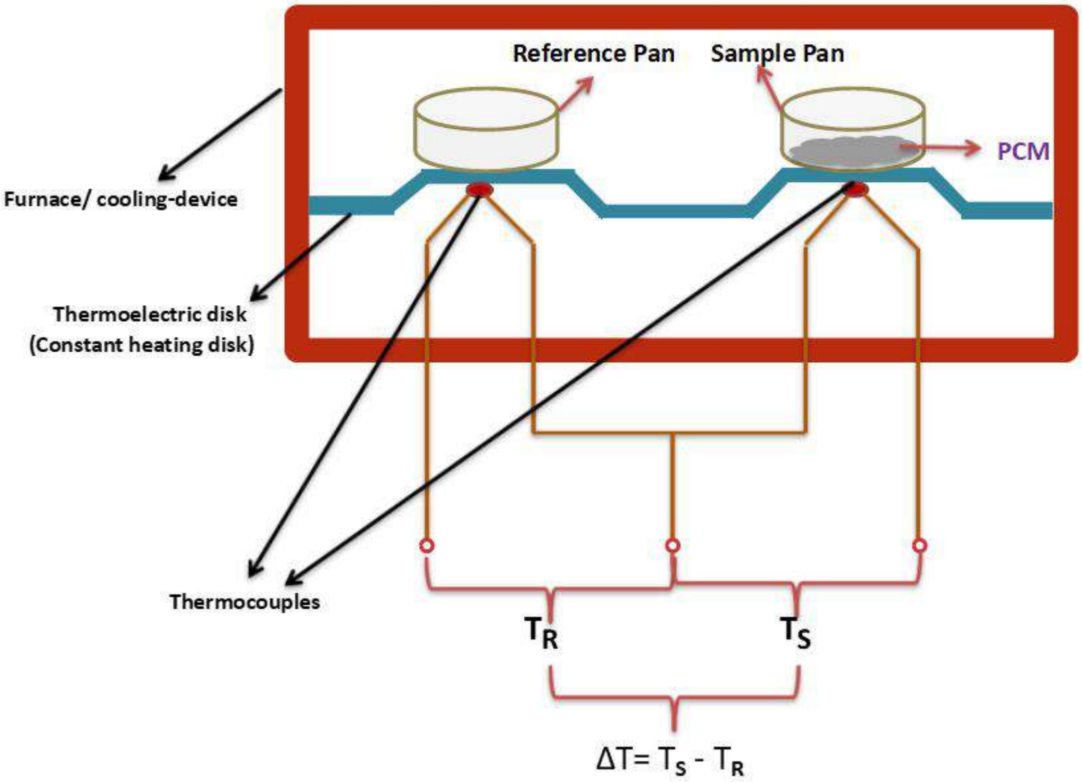

Figure 2.14 Schematic illustration of a differential scanning calorimeter

2.4.8 Refractive index measurements

An automatic refractometer (J357 series, Rudolph Research Analytical, USA) is used to measure the phase transition (freezing and melting point) of PCMs from the temperature dependent variations of refractive index. The sample temperature is precisely controlled using a Peltier heating/cooling stage within ± 0.05 ^{0}C. The automatic refractometer consists of a point LED light source (wavelength = 589.3 nm), sapphire prism of refractive index 1.75 and a diode detector array. It operates on the principle of critical angle measurement and is capable of measuring refractive index from 1.26 to 1.70, as a function of temperature in the range of 15 –100 °C. The measurement accuracy for refractive index is ~ 0.00004.

Refractive index is defined as the ratio of velocity of light in vacuum to the velocity of light in the medium. During liquid-solid phase transition, density of the PCM changed discontinuously, giving rise to a change in refractive index. The phase transition temperature estimated from refractive index measurements were found to be in good agreement with the DSC data.

2.4.9 Measurement of thermal conductivity using a transient hot wire probe

The thermal conductivity of the PCMs (with or without nan-inclusions) was measured using a transient hot wire probe (KD2 Pro, M/s Decagon, USA). Here, the thermal conductivity is quantified by monitoring the heat dissipation from a long linear heat source and the temperature rise is expressed by the following equation [38].

$$T - T_0 \cong \frac{Q_h}{4\pi k}[\ln(t) - \gamma_a - \ln(\frac{r_a^2}{4\alpha t})] \tag{2.3}$$

Here, T, T_0, Q_h, k, t, γ_a, r_a and α indicate temperature, initial temperature, heat flux per unit length, thermal conductivity of the medium, Euler's constant (= 0.5772…), radial distance and thermal diffusivity of the medium, respectively. For small values of the radial distance, thermal conductivity is quantified from the slope of variation of ΔT (=$T - T_0$) as a function of ln(t) and the following expression is obtained for thermal conductivity [38].

$$k = \frac{Q_h}{4\pi(\Delta T_2 - \Delta T_1)}\ln(\frac{t_2}{t_1}) \tag{2.4}$$

Here, ΔT_1 and ΔT_2 indicate the temperature difference for time t_1 and t_2, respectively. Thermal conductivity measurements at different temperatures were carried out by immersing the sample holder along with the transient hotwire probe in a re-circulating water bath with precise temperature control (within ± 0.1 °C). To establish thermal equilibrium, the sample assembly was insulated using a custom-made non-conducting fixture and thermal conductivity measurements were carried out after a time delay of 600 s to ensure temperature homogeneity in the samples. Additionally, the sample assembly was also isolated from mechanical vibrations to ensure proper contact between the probe and the sample. Before proceeding with quantitative measurements, the transient hot wire probe was calibrated for three standard liquids, viz. water, kerosene and ethylene glycol. To ascertain the temporal and thermal stability of the nano-inclusions loaded PCM, thermal cycling was performed by repeated freezing and melting, for at least four cycles. All thermal conductivity measurements were repeated three times and the values were expressed as mean ± standard deviation. It must be noted in this regard, that the repeatability and stability of the measured thermal conductivity values were found to be lower in the phase transition regions, as compared to the liquid and solid states. The standard deviation values were considered as the standard measurement uncertainties, i.e. u(k). On the other hand, standard uncertainties for thermal conductivity ratios (k_a/k_b) were obtained from law of error propagation, i.e. $u(k_a/k_b) = (k_a/k_b) \times [(u(k_a)/k_a)^2 + (u(k_b)/k_b)^2]^{0.5}$ [217]. **Fig. 2.15a** shows the schematic illustration of the basic working principle of KD2 probe, where all the essential parts are indicated. KD2 probe works on the principle of Wheatstone bridge principle. **Fig. 2.15b** shows the typical photograph of the experimental set-up for thermal conductivity measurement.

2.4.10 Phase transition temperature and photo-thermal conversion efficiency measurement using infrared thermography (IRT)

Infrared thermography (IRT) is a non-contact temperature measurement methodology, where the infrared rays emitted from the surface of the object under investigation is detected using a suitable infrared detector and the object temperature is measured from the intensity of the infrared radiation using the following radiometric equation [413].

$$M_{cam} = \tau\varepsilon M_{obj} + \tau(1-\varepsilon)M_{env} + (1-\tau)M_{atm} \tag{2.5}$$

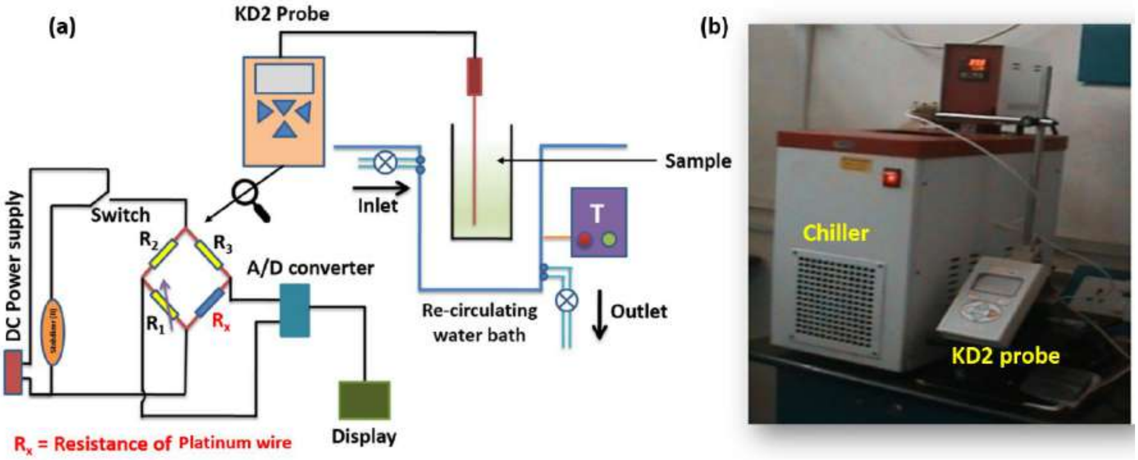

Figure 2.15 (a) Schematic illustration of the working principle of a transient hot wire probe (KD2 Pro, M/s Decagon, USA). (b) Typical photograph of the thermal conductivity measurement set-up.

Here, M_{cam} is the radiance received by the infrared detector, which is housed inside a suitable infrared camera along with the appropriate electronics, optics and cooling mechanisms. M_{obj}, M_{env} and M_{atm} are the radiance emitted by the object under investigation, surrounding environment and atmosphere, respectively. τ and ε indicate atmospheric transmittance and surface emissivity, respectively. For laboratory experiments, $\tau \sim 1$ and for real objects, $\varepsilon<1$ (for a hypothetical perfect blackbody, $\varepsilon=1$). Under these assumptions, Eq. 2.5 can be simplified as $M_{cam} = \varepsilon M_{obj} + (1-\varepsilon) M_{env}$. The radiance received by the infrared detector is converted into an electrical signal and object temperature is obtained from suitable calibration curves. Detailed description and numerous applications of various IRT based experimental techniques can be found elsewhere [413-416]. In the present study, FLIR SC5000 infrared camera was used for non-contact temperature measurement, which is equipped with a 27 mm germanium made infrared transparent lens with field of view of $20^0 \times 16^0$ and indium antimonide (InSb) based (spectral range = 2.0-5.1 μm) focal plane array detector with 320 × 256 elements (Stirling cycle cooled).

For determination of phase transition temperature and gain in cooling time using IRT, the liquid PCMs (initial temperature higher is than the phase transition temperature) were placed in recirculating water bath, whose temperature was kept constant at 8.0 (± 0.1) ^{0}C and the decay in sample temperature was monitored using the infrared camera, which was placed vertically above the sample surface to minimize the viewing angle errors. The camera to sample distance was maintained at 0.35 m. At a distance of 0.35 m, the horizontal and vertical spatial resolution were found to be ~ 0.4 mm/pixel. In the present study, for recording infrared images, reflected background temperature and atmospheric transmittance were considered as 28.45 ^{0}C and 1, respectively. The acquired infrared images were emissivity corrected to represent correct temperature of the PCMs. The acquired infrared images were later analyzed using Altair software.

IRT based experiments were carried out to study the photo-thermal conversion efficiency of the PCMs loaded with various concentrations of CBNP nano-inclusions, where the samples were exposed to an artificial solar spectrum using two 1 kW halogen lamps, working at 50 % efficiency. The halogen lamps were placed at 45 ^{0} from the hypothetical straight line passing through the centre of the sample holder on either side. The sample-to-lamp distance was fixed at ~ 0.15 m throughout the experiments. The rise in sample temperature was remotely monitored using an infrared camera, placed vertically above the sample at a distance of ~ 0.35 m. For comparison, experiments were also performed on the PCMs without any nano-inclusion loading. All experiments were repeated thrice and the average values of temperature rise were considered for further data analysis. **Fig. 2.16a** shows the schematic of the experimental set-up, where all the essential parts are indicated. **Fig. 2.16b** shows a typical photograph of the experimental set-up.

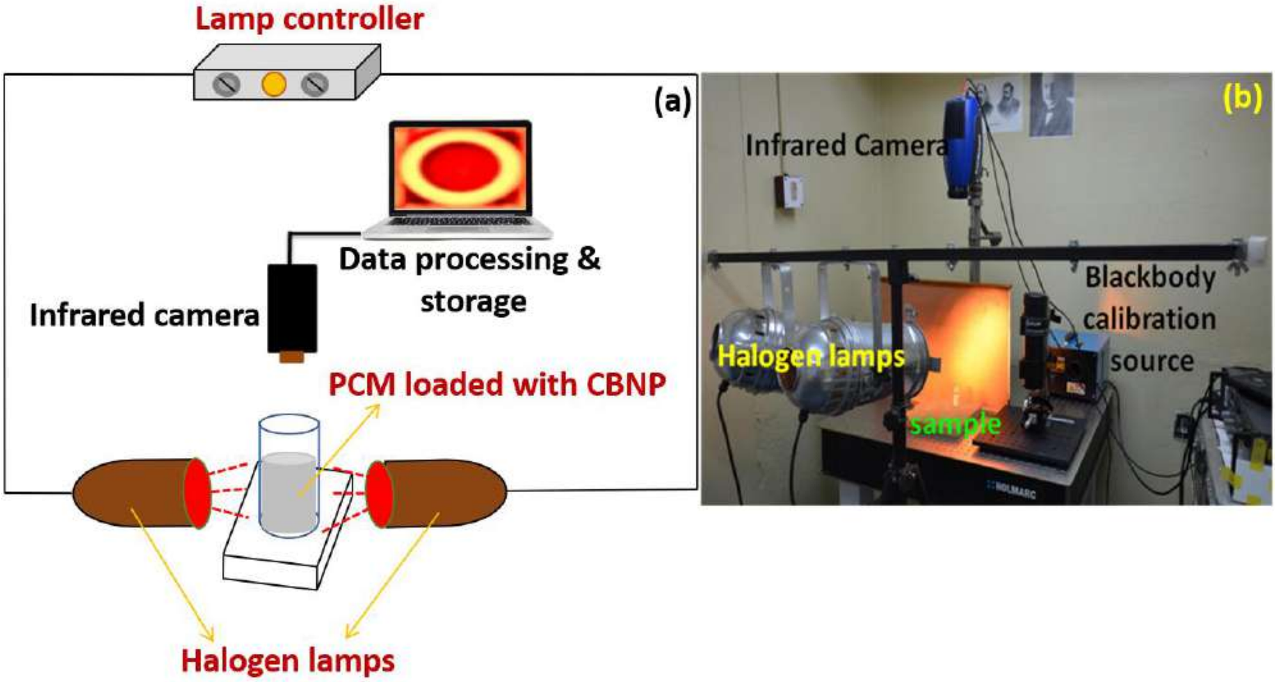

Figure 2.16 (a) Schematic illustration of the IRT-based experimental set-up for measurement of photo-thermal conversion efficiency. (b) Typical photograph of the experimental set-up.

Chapter 3

Effect of functionalization and physical properties of nano-inclusions on thermal conductivity enhancement of n-hexadecane based phase change materials

Chapter 3

Effects of functionalization and physical properties of nano-inclusions on thermal conductivity enhancement of n-hexadecane based phase change materials

3.1 Introduction

Hexadecane based PCMs are technologically important candidates for room temperature (phase transition temperature near 18 ^{0}C) thermal energy storage. Zheng et al. [387] reported reversible thermal switching across the liquid-solid phase transition of graphite/hexadecane PCM at T = 18 ^{0}C and observed ~ 3.2 times enhancement in thermal conductivity of the PCM, loaded with 0.8 vol. % of graphite nano-inclusions, in the solid state. Sun et al. [237] reported ~ 3 times enhancement in thermal conductivity of functionalized multi-walled carbon nano tube loaded hexadecane, in the solid state, for 0.4 vol. % loading. Schiffres et al. [395] reported 2.3-3 times enhancement in thermal conductivity of multilayer graphene/hexadecane PCM, in the solid state, for a loading of 1 vol. % of graphene. Such large thermal conductivity enhancements for nano-inclusion loaded hexadecane, in the solid state, was attributed to the formation of needle like microstructure during solidification and aggregation of the nano-inclusions along the grain boundaries forming a percolating network with higher thermal transport efficiency [237, 387, 395]. Recently, significant enhancement in thermal conductivity of n-hexadecane was achieved by inverse miceller templating and loading with various nano-inclusions like graphene nanoplatelets, multi walled carbon nano tube and copper nano-wires [231, 232].

Though nano-inclusion assisted thermal conductivity enhancement of hexadecane is well studied, the effect of aggregation and cluster formation is not fully understood [50, 342]. Earlier studies on hexadecane based nano-inclusions were primarily focussed on carbon-based nano-inclusions and reports on the effects of metallic nano-inclusions (apart from copper nano-wire [231]) on thermal conductivity enhancement during liquid-solid phase transition are scarce. Further, the effect of surface functionalization of the nano-inclusions on thermal conductivity enhancement and long-term stability in hexadecane based PCM is not known. Xia et al. [417] reported that surface functionalization can result in superior stability but adversely affects the thermal conductivity enhancement. Hermida-Merino et al. [418] also reported that surface functionalization decisively influences the transport properties.

Here, the effects of various types of nano-inclusions on the thermal conductivity enhancement and the effects of surface functionalization and aggregation on thermal conductivity and thermal stability of such PCM are probed in detail. The enhancement in thermal conductivity of hexadecane based PCM loaded with three different carbon-based nano-inclusions, viz. carbon black nano powder, multi-walled carbon nano tube, graphene nanoplatelets and three metallic nano-inclusions, viz. silver nano wire, nickel nanoparticles and copper nanoparticles are systematically studied. In addition, the effect of surfactant capping on thermal conductivity enhancement and thermal stability is also probed.

3.2 Preparation of nano-inclusion loaded PCMs

Before adding to the PCM (hexadecane), CBNP, NiNP, AgNW and GNP were surface functionalized with oleic acid. Appropriate quantity of CBNP, NiNP, AgNW and GNP were added in 2 mL of oleic acid and the samples were sonicated for 20 minutes, followed by magnetic stirring for 40 minutes at a temperature of ~ 70 ^{0}C for completion of the coating process. Thereafter, the samples were washed multiple times with acetone and centrifuged at 4000 rpm to remove the excess oleic acid. The surface functionalized nano-inclusions were dispersed in the PCM using a horn sonicator (Sonic Vibra-Cell), operating at 30 % power for 5 minutes.

3.3 Experimental methods

The nano-inclusions were characterized using powder X-ray diffraction, small angle X-ray scattering and dynamic light scattering techniques, as described in chapter 2. Fourier transform infrared (FTIR) spectroscopy was carried out to ascertain possible interactions between the PCM and nano-inclusions. The solidification and melting temperatures and latent heat of fusion of the PCM were determined from differential scanning calorimetry (DSC) studies using Q200 (TA Instruments) in the temperature range of 0.1-80 ^{0}C with heating and cooling rates of 3 ^{0}C/minute under nitrogen atmosphere. Infrared thermography and refractive index measurements were also carried out to probe the phase transition temperature of the PCM. Thermal conductivity measurements were carried out using a KD2 probe (detailed description in chapter 2).

3.4 Mechanism of thermal conductivity enhancement

Thermal conductivity enhancement of nano-inclusion loaded organic phase change materials is primarily governed by the aggregation phenomena [341, 386]. The nano-inclusions, when dispersed within a matrix of PCM, form clusters, which act as efficient percolating structures for heat transfer [342]. Moreover, during solidification, the clusters are squeezed towards the grain boundary, forming a network of percolating structures which results in large enhancement of thermal conductivity in the solid state [237, 387].

3.4.1 Effect of cluster formation

The aggregation dynamics and the effects of cluster formation on thermal conductivity enhancement in nano-inclusion loaded PCM is explained on the basis of three level homogenization model of Prasher & Evans [341]. The nano-inclusions form aggregates due to Van der Waal's interaction and these aggregates grow in size with increasing concentration of the nano-inclusions, resulting in an enhancement of thermal conductivity, as the nano-inclusions, of higher thermal conductivity as compared to the PCM, are in physical contact with each other within the aggregates with a radius of gyration several times larger than the individual nano-inclusions [342]. Formation of larger aggregates (but within the limit of well dispersed aggregates) is beneficial for thermal conductivity enhancement of the nano-inclusion loaded PCM primarily due to three reasons, viz. phonon mediated efficient heat conduction through a larger network of percolating structure, reduced interfacial thermal resistance due to improved contact between the nano-inclusions within an aggregate and increased near field radiative heat transfer between the closely packed nano-inclusions with inter particle separation lower than the typical dimensions of the individual nano-inclusions [342, 419, 420].

The aggregates or clusters have fractal morphologies consisting of a backbone and dead-ends [342]. The backbone is a quasi-continuous network of percolating nano-inclusions, spanning the entire aggregate volume with characteristic length scale equal to the radius of gyration of the aggregate. On the other hand, the randomly placed nano-inclusions form the dead-ends within the aggregates [342]. Under such a scenario, the effective thermal conductivity of a cluster is attributed to two different sources, viz. thermal conductivity of the homogenized medium with dead ends alone (first level homogenization) and superimposition of the backbone over this homogenized medium (second level homogenization) [341]. Finally, the effective thermal conductivity of the entire system is obtained from homogenization of the clusters with the medium (third level of homogenization) [341].

Let k, k_f, k_{de}, k_p and k_c indicate the effective thermal conductivity of the nano-inclusion loaded PCM (entire system), thermal conductivity of the PCM in liquid state, thermal conductivity of the cluster with dead ends alone, total thermal conductivity of the cluster and bulk thermal conductivity of the nano-inclusions, respectively. Then according to Bruggeman model, the thermal conductivity of the cluster with dead ends alone can be expressed by the following equation [341, 342].

$$k_{de} = k_f + \phi_{de}(k_p - k_f) \tag{3.1}$$

Here, ϕ_{de} indicate the volume fraction of the nano-inclusions belonging to the dead-ends alone and $\phi_{de} = \phi_c - \phi_{bb}$, where ϕ_c and ϕ_{bb} indicate volume fraction of the nano-inclusion within a cluster and volume fraction of nano-inclusions belonging to the back-bone, respectively [341]. ϕ_{bb}, ϕ_{de} and ϕ_c were calculated in terms of the fractal dimension of the clusters (d_f). The number of nano-inclusions within a cluster is expressed as $N_c = (R_g / a)^{d_f}$. Let ϕ_p be the total volume fraction of nano-inclusions added to the PCM. Then $\phi_p = \phi_c \times \phi_a$, where ϕ_c and ϕ_a indicate the volume fraction of nano-inclusion within a cluster and volume fraction of cluster, respectively. From fractal analyses, it can be shown that $\phi_c = (R_g / a)^{d_f - 3}$ and volume fraction of nano-inclusions within a cluster that belong to the back bone (ϕ_{bb}) is given by $\phi_{bb} = (R_g / a)^{d_l - 3}$, where d_l is the chemical dimension (ranging from 1 to d_f) [341]. Then the volume faction of nano-inclusion, within a cluster, belonging to dead-ends (ϕ_{de}) is given by $\phi_{de} = \phi_c - \phi_{bb}$ [341].

The total thermal conductivity of the clusters (k_c) is estimated with an assumption that the backbone is superimposed on a medium with homogenized thermal conductivity of k_{nc} [341]. The total thermal conductivity of the cluster is obtained from the following equation originally proposed by Nan et al. [421].

$$k_c = k_{de} \frac{3 + \phi_{bb}[2\beta_{11}(1 - L_{11}) + \beta_{33}(1 - L_{33})]}{3 - \phi_{bb}[2\beta_{11}L_{11} + \beta_{33}L_{33}]} \tag{3.2}$$

Here, $L_{33} = 1\text{-}2L_{11}$, where $L_{11} = 0.5g^2/(g^2-1) - 0.5g \times \cosh^{-1}[g(g^2-1)^{-1.5}]$ and g is the aspect ratio of the cluster with respect to the nano-inclusions, defined as $g = R_g/a$, where R_g and a indicate the radius of gyration of the cluster and size of the nano-inclusions, respectively [421]. The term β_{ii} (i = 1 and 3) is expressed by the following equations [421].

$$\beta_{ii} = \frac{k_{ii}^{/} - k_{de}}{[k_{de} + L_{ii}(k_{ii}^{/} - k_{de})]}, i = 1, 3 \tag{3.3}$$

$$k_{ii}^{/} = \frac{k_p}{(1 + \omega L_{ii} k_p / k_f)} \tag{3.4}$$

Here, $\omega = (2+1/g) \times (\delta_R/a)$, where δ_R indicates the hypothetical Kaptiza radius, which signify the lengths scale in the host matrix over which temperature drop is comparable to the temperature drop at the nano-inclusion/host interface [341, 421]. Finally, the effective thermal conductivity of the entire sample (nano-inclusion loaded PCM) is obtained from the Maxwell-Garnet model using the following equation [341].

$$\frac{k}{k_f} = \frac{(k_c + 2k_f) + 2\phi_a(k_c - k_f)}{(k_c + 2k_f) - \phi_a(k_c - k_f)} \tag{3.5}$$

Nano-inclusion aided enhancement in thermal conductivity of the PCM is calculated from Eq. 3.5 in the liquid state. However, thermal conductivity enhancement drastically increases in the solid state and during liquid solid phase transition, which is attributed to the squeezing of nano-inclusions towards the grain boundaries, as explained in the following section.

3.4.2 Network of clusters in solid state

When crystal forming liquids are loaded with nano-inclusions, the nano-inclusions are driven towards the inter-crystal regions or grain boundaries during freezing [387, 395]. Internal stress fields are generated within the PCM (considering linear viscoelastic properties) during freezing, which is expressed by the following relation [422].

$$S(r,t) = \frac{1}{1-\nu}\int_0^t E(t-\tau)\frac{\partial[e_0(\tau) - \alpha_l T(r,\tau)]}{\partial\tau}d\tau \tag{3.6}$$

Here, S(r,t), E(t), $e_0(\tau)$, T(r,τ), ν and α_l indicate stress field at location r and time t, relaxation modulus function at time t, instantaneous mean strain at time t = τ, temperature profile at a particular location (r) at instantaneous time t = τ, Poisson's ratio and coefficient of thermal expansion, respectively [422].

The solidification induced internal stress squeezes the nano-inclusions towards the grain boundaries and increases the contact area between the nano-inclusions, thereby reducing the thermal contact resistance (Kapitza resistance), which results in an enhancement in thermal conductivity of the nano-inclusion loaded PCM due to the formation of a quasi-2D network of percolation pathways with high heat transfer efficiency [234, 237, 238, 342, 387]. **Fig. 3.1** schematically shows the solidification induced formation of 2D network of percolating structures with enhanced heat transfer properties.

Domingues et al. [419] proposed that stress induced squeezing of the nano-inclusions also leads to a substantially lower inter particle separation distances, as compared to the typical dimensions of the nano-inclusions, which results in an enhancement of near field radiative heat transfer.

3.5 Experimental results

From transmission electron microscopy (TEM) image analyses the average sizes of NiNP and CuNP were obtained as ~ 23.4 ± 2.3 and 12.8 ± 2.8 nm, respectively. Using room temperature powder XRD, the average crystallite sizes were found to be ~ 29 ± 3 and 13 ± 2 nm for NiNP and CuNP, respectively, which were in good agreement from the sizes obtained from TEM. Small angle X-ray scattering (SAXS) studies [423] indicated the most probable sizes of CBNP and GNP as ~ 21 ± 2 and ~ 12 ± 2 nm, respectively. Analyses of the scattering intensity at high q (wave vector) region, i.e. Porod's region [423] indicated the fractal dimension of GNP, which was in agreement with the earlier reported results [418, 424]. The average hydrodynamic sizes were 295 ± 59, 296 ± 82 and 615 ± 141 nm for NiNP, CuNP and CBNP, respectively, which were significantly higher than the sizes obtained from XRD, TEM and SAXS. This indicated significant aggregation of the nano-inclusions on dispersion in hexadecane. The larger hydrodynamic size of CBNP nano-inclusions was attributed to the formation of aciniform aggregates of the primary particles (nodules) [407].

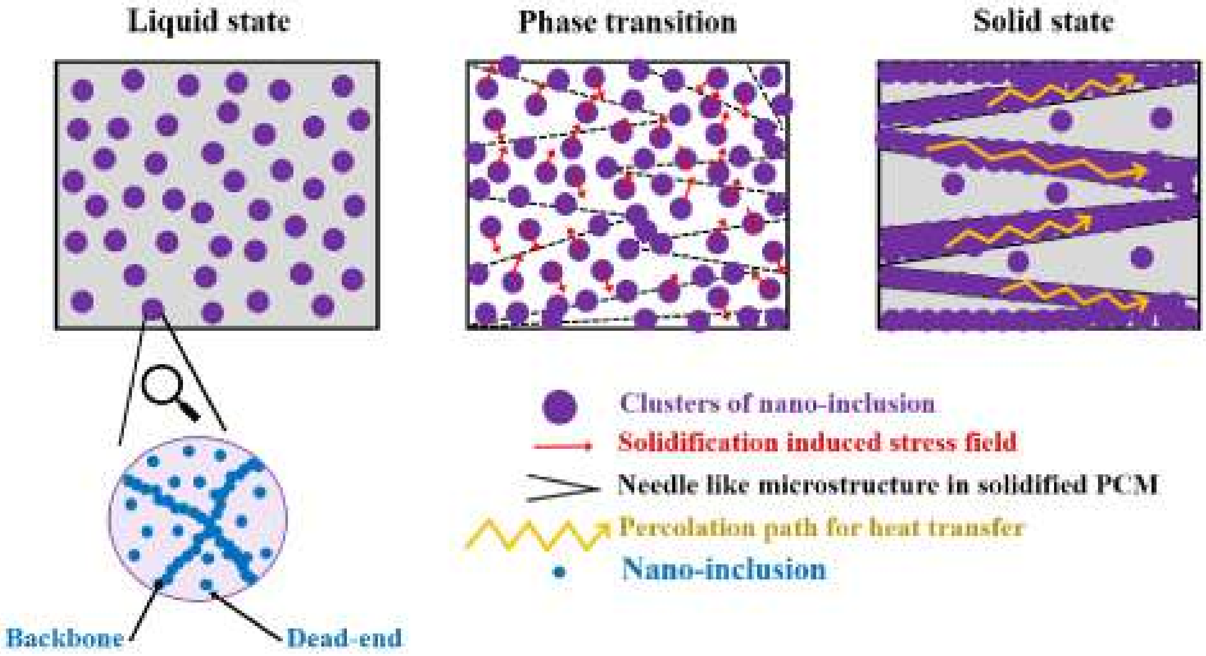

Figure 3.1 Schematic representation of the solidification induced formation of 2D network of percolating structures with enhanced heat transfer properties. In the liquid state (left figure), the clusters are randomly dispersed. During phase transition (middle figure), needle like structures develop and the clusters experience a stress field, which drives them towards the grain boundaries. The formation of quasi 2-D percolating network is complete in the solid state (right figure), which causes a large enhancement in thermal conductivity. The inset shows the expanded view of a cluster, where the back-bones and dead-ends, consisting of individual nano-inclusions are seen. Thermal conductivity enhancement within a cluster is primarily through phonon mediated heat transfer via the interconnected back-bones, which span the entire length of a cluster.

In the Fourier transform infrared (FTIR) spectra, the strong absorption band, at1716 cm^{-1}, for the pure oleic acid, corresponding to the stretching of carbonyl group [425], was missing for the oleic acid capped nano-inclusions, where two new absorption bands appeared at 1667 and 1598 cm^{-1}, which corresponded to the asymmetric and symmetric stretching of –COO^{-}, respectively [426]. The difference between the symmetric and asymmetric bands was found to be ~ 69 cm^{-1}, indicating the formation of chelating bidentate on the surface of the nano-inclusions, upon coating with oleic acid due to strong electronic interaction of the polar carboxylic head group of oleic acid with the nano-inclusions [426]. **Fig. 3.2** shows the FTIR spectra, where major absorption bands are indexed. **Table 3.1** describes the absorption bands in detail. FTIR spectra confirmed that the major absorption bands were not shifted for the PCM loaded with various nano-inclusions[425-427], which clearly indicated the absence of any chemical reaction between the PCM and the nano-inclusions.

3.5.1 Characterization of the PCM

Figure 3.3a shows the heat flow curves, during solidification and melting of the PCM (hexadecane), obtained from differential scanning calorimetry studies. The solidification (T_s) and melting (T_m) temperatures were found to be 14.5 and 19.3 ^{0}C, respectively. These values are in good agreement with the phase transition temperature of ~ 17-18 ^{0}C reported by Velez et al. [428], Sun et al. [237], Zheng et al [387] and Su et al. [19]. The latent heat values were found to be ~ 238.6 and 241.4 kJ/kg during solidification and melting, respectively, which were also in agreement with the values reported elsewhere (~ 236 kJ/kg by Velez et al. [428], ~ 238 kJ/kg by Su et al. [19], etc.). The degree of supercooling (difference between T_s and T_m) was found to be ~ 4.8 ^{0}C, which was higher than the value of ~ 1 ^{0}C reported by Velez et al. [428].

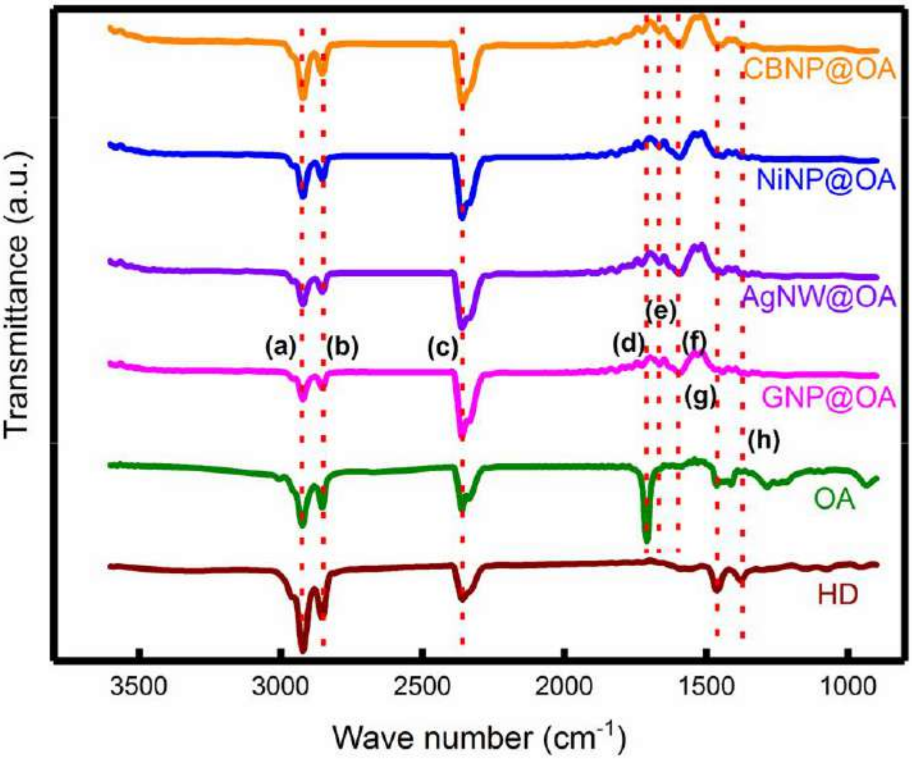

Figure 3.2 FTIR spectra of the oleic acid capped CBNP, NiNP, AgNW, and GNP nano-inclusions, dispersed in hexadecane. For comparison, the FTIR spectra of pure oleic acid (OA) and hexadecane (HD) are also shown in the figure. The major absorption bands are indexed.

Table 3.1 Absorption bands indicated in the FTIR spectra.

Legend	Wave number (cm^{-1})	Description	Reference
(a)	2923	Asymmetric stretching of $–CH_2$ group	[425]
(b)	2855	Symmetric stretching of $–CH_2$ group	[425]
(c)	2362	Stretching vibration of C=O bond from atmospheric CO_2	[425]
(d)	1716	Stretching of carbonyl group of free oleic acid	[425]
(e)	1667	Asymmetric stretching of $–COO^-$ group	[426]
(f)	1598	Symmetric stretching of $–COO^-$ group	[426]
(g)	1471	Asymmetric $–CH_3$ bend	[427]
(h)	1378	Symmetric $–CH_3$ bend	[427]

Figure 3.3b shows the variation of refractive index of the PCM as a function of temperature during solidification and melting. It can be seen from **Fig. 3.3b** that refractive index increased with decreasing temperature up to the phase transition temperature of the PCM and beyond that refractive index decreased. Due to absorption and re-emission of light along the travelling path, speed of light in a medium is lower than that in the vacuum. With decreasing temperature, the density of the PCM increases leading to a decreased speed of light in the medium, resulting in an increase in refractive index. The phase transition temperature of the PCM was found to be ~ 17 ^{0}C, which was in agreement with the results obtained from differential scanning calorimetry studies. It can be further seen from **Fig. 3.3b** that the refractive index decreased sharply below the phase transition temperature, which was attributed to the cracking of the solidified pellets, which allowed the light to pass through. Extensive cracking of the solidified pellets was observed due to the formation of needle like microstructure after freezing [237, 387]. The **insets of Fig. 3.3b** show the photograph of the PCM in the liquid and solid states and the presence of needle like microstructure and cracks in the solidified pellet are clearly discernible from the photographs. **Fig. 3.3c** shows the variation of k/k_f as a function of temperature for the PCM. Here, k and k_f indicate the temperature dependent thermal conductivity of the PCM and thermal conductivity of the PCM at T = 25 ^{0}C (= 0.140 ± 0.002 $Wm^{-1}K^{-1}$), respectively. The percentage enhancement in thermal conductivity [$100 \times (k-k_f)/k_f$] is also shown in **Fig. 3.3c**. The thermal conductivity enhancement was insignificant in the liquid state, whereas significant enhancement in thermal conductivity was observed in the phase transition region and solid state. In the solid state, thermal conductivity decreased slightly with decreasing temperature but remained constant below 10 ^{0}C. Thermal conductivity of the PCM in the solid state, at T = 10 ^{0}C was found to 0.249 (± 0.003) $Wm^{-1}K^{-1}$ which was slightly higher than the earlier reported value of 0.21 $Wm^{-1}K^{-1}$ [19]. The increase in thermal conductivity in the solid state was attributed to the formation of closely packed nano-crystalline structure. Similar enhancement in thermal conductivity in the solid state has been experimentally reported by Sun et al. [237] and Zheng et al. [387] for n-hexadecane. Using molecular dynamics simulation, Babaei et al. [429] confirmed the formation of nanocrystalline phase during solidification of PCM, which caused an enhancement in thermal conductivity due the phonon mediated heat transfer. It has been reported that hexadecane crystals exhibit strong anisotropic growth kinetics resulting in formation of needle like microstructure and ice-templating [237, 387, 395]. The **inset of Fig. 3.3c** shows a phase contrast optical micrograph of hexadecane in the solid state, where the presence of needle like microstructures is clearly discernible (indicated by the arrows). For establishing repeatability and thermal stability of the PCM, thermal cycling was carried out and five thermal conductivity measurements were performed at regular time intervals in the solid (at T = 10 ^{0}C) and liquid (at T = 25 ^{0}C) states. **Fig. 3.3d** shows the variation of k/k_f during thermal cycling of the PCM, where it can be seen that freezing and melting cycles were reversible, even after four cycles. The k/k_f in the solid state (at T = 10 ^{0}C) was ~ 1.779, indicating a thermal conductivity enhancement of 77.9 % for the PCM, which was significantly higher than the earlier reported values of ~ 28 % by Sun et al. [237] and ~ 50 % by Su et al. [19]. The observed reversible thermal cycles indicated the superior thermal stability and efficacy of hexadecane based PCM for thermal energy storage applications.

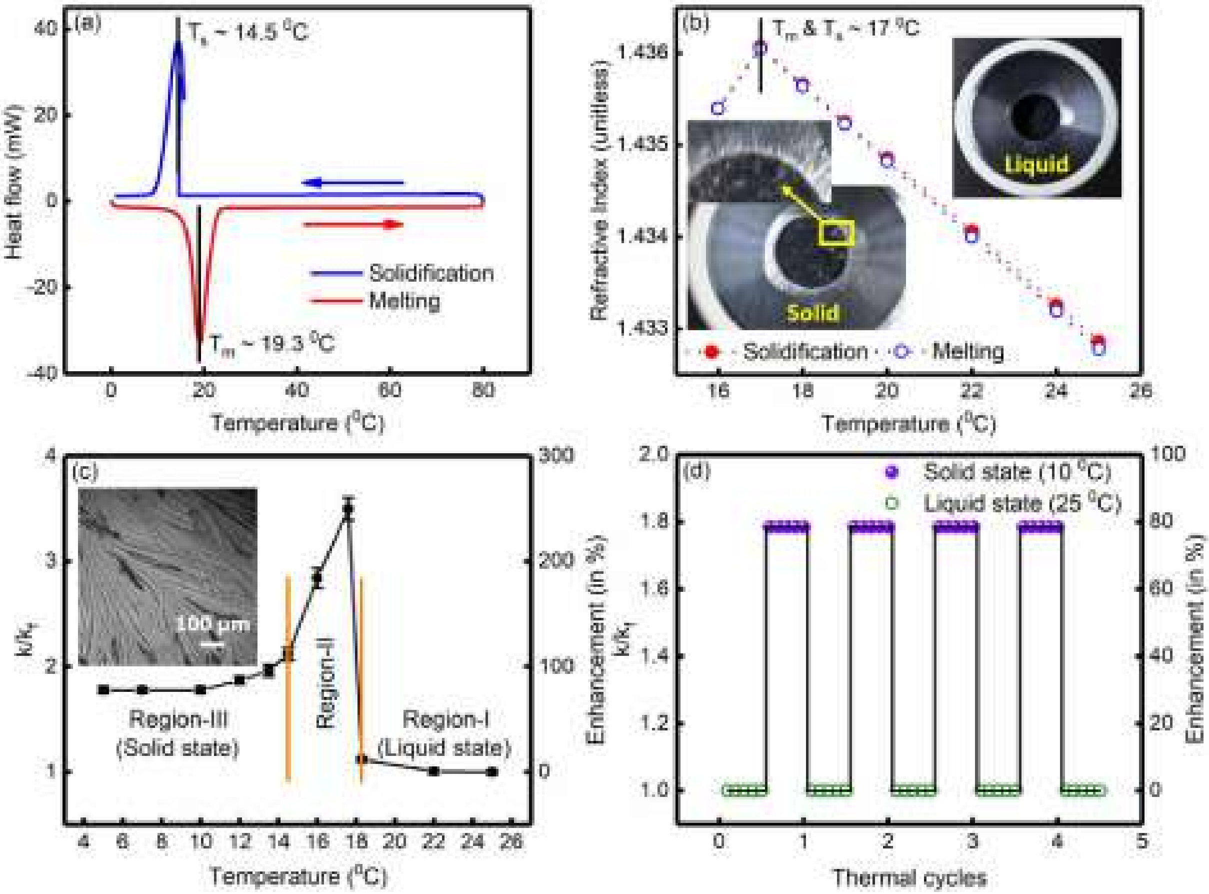

Figure 3.3 (a) Heat flow curves, during solidification and melting of hexadecane, obtained from differential scanning calorimetry studies. The solidification (T_s) and melting (T_m) temperatures were ~ 14.5 and 19.3 ^{0}C, respectively, as indicated in the figure. (b) The variation of refractive index of hexadecane as a function of temperature during solidification and melting. The phase transition temperature was ~ 17 ^{0}C. (Inset) Typical photographs of hexadecane in the liquid and solid states. The presence of needle like microstructure and cracks in the solidified pellet of the PCM are clearly discernible. (c) Variation of k/k_f and percentage enhancement in thermal conductivity, as a function of temperature, for the PCM, without any nano-inclusions. The variation of k/k_f can be divided into three regions, viz. region-I (liquid state), region-II (phase transition) and region-III (solid state). (Inset) Optical phase contrast microscopy image of the PCM in solid state, where the needle like microstructure is clearly discernible. (d) Variation of k/k_f and percentage enhancement in thermal conductivity during thermal cycling of the PCM, without any nano-inclusions.

3.5.2 Nano-inclusion assisted thermal conductivity enhancement of the PCM

Figures 3.4a-f show the variation of k/k_f and percentage (%) enhancement in thermal conductivity as a function of temperature for the PCM loaded with various concentrations of CBNP, NiNP, CuNP, AgNW, MWCNT and GNP nano-inclusions, respectively. For comparison, the variation of k/k_f in the case of PCM, without any nano-inclusions, is also shown in the figures. It can be clearly seen from **Figs. 3.4a-f** that the variation of k/k_f as a function of temperature can be divided into three distinct regions, which were indicated as regions I, II and III, respectively. For, T> 18.3 ^{0}C, the PCM, with or without nano-inclusions, was found to be in the liquid state and this region was categorized as region-I. Region-II indicated the phase transition region for 14.5 ^{0}C<T<18.3 ^{0}C, and region-III, corresponded to the temperature range well below the freezing point, where the PCM, with or without nano-inclusions, was in the solid state.

Figure 3.4a shows that the thermal conductivity enhancements in the liquid state (at T = 25 ^{0}C) were ~ 1.4, 5.0, 5.5, 5.5 and 6.4 % for 0.001, 0.0025, 0.005, 0.0075 and 0.01 wt. % of CBNP loading, respectively. In the phase transition region (region -II), maximum enhancements of thermal conductivity were ~ 260, 267, 339, 293 and 300 % for the PCM loaded with 0.001, 0.0025, 0.005, 0.0075 and 0.01 wt. % of CBNP, respectively. **Fig. 3.4a** further shows that the thermal conductivity enhancement decreased with temperature in the solid state (region-III) and attained a steady value below 10 ^{0}C. In the solid state, thermal conductivity enhancements were ~ 87.9, 105.0, 117.4, 115.5 and 121.4 % for the PCM loaded with 0.001, 0.0025, 0.005, 0.0075 and 0.01 wt. % of CBNP, respectively.

The higher thermal conductivity in the solid state (region-III), as compared to the liquid state (region-I) was due to the formation of crystalline structure of the PCM after freezing and phonon assisted efficient heat transfer in the solid state [237, 387]. The maximum enhancement in thermal conductivity was observed in the phase transition region, which was attributed to the strong anisotropic growth kinetics induced formation of continuous networking structure, during liquid-solid phase transition in hexadecane [231, 237, 387]. Formation of such needle like microstructure, during liquid-solid phase transition has been reported experimentally [231, 237, 387, 395]. Schiffres et al. [395] reported that slower cooling rate results in formation of microstructure with thicker and longer needles leading to a comparatively larger thermal conductivity enhancement due to anisotropic templating. Zheng et al. [387] mapped the internal stress distribution in frozen hexadecane and reported an uneven stress distribution with an average pressure of ~ 160 p.s.i., which was attributed to the anisotropic growth kinetics and formation of needle like microstructure in frozen hexadecane. Formation of needle like microstructure during liquid-solid phase transition of hexadecane is also confirmed in the present study from optical phase contrast microscopy images (**inset of Fig. 3.3c**). During freezing, due to internal stress fields, the nano-inclusions are driven towards the intercrystal regions or grain boundaries [387, 395, 422]. This results in an enhancement in thermal conductivity of the nano-inclusion loaded PCM due to the formation of a quasi-2D network of percolation pathways with high heat transfer efficiency [234, 237, 238, 342, 387]. Increased near field radiative heat transfer, due to low inter-particle separation distance (spatially localized near the grain boundaries) also leads to an enhancement of thermal conductivity [419]. On the other hand, the lowering of thermal conductivity enhancements in the region-III, well below the freezing point, was attributed to the microstructural changes, where longer needles were broken down to shorter needles, probably due to the solidification induced residual stress fields [387, 422].

It can be seen from **Fig. 3.4b** that, in region-I, the thermal conductivity enhancements were ~ 2.1, 4.3, 5.7, 5.0 and 2.1 % for the PCM loaded with 0.001, 0.0025, 0.005, 0.0075 and 0.01 wt. % of NiNP, respectively. In the phase transition region, the maximum enhancement in thermal conductivity were ~ 248, 273, 313, 316 and 310 % for the PCM loaded with 0.001, 0.0025, 0.005, 0.0075 and 0.01 wt. % of NiNP, respectively. In the region-III, the enhancements in thermal conductivity were ~ 85.7, 102.1, 112.9, 101.4 and 102.9 % for the PCM loaded with 0.001, 0.0025, 0.005, 0.0075 and 0.01 wt. % of NiNP, respectively. **Fig. 3.4c** shows the variation of k/k_f and percentage enhancement in thermal conductivity, as a function of temperature for the PCM loaded with CuNP, where it can be seen that the enhancements in thermal conductivity in the liquid state were ~ 2.9, 5.7, 9.3, 10.0 and 11.4 % for the PCM loaded with 0.001, 0.0025, 0.005, 0.0075 and 0.01 wt. % of CuNP, respectively. Thermal conductivity enhancements in the phase transition region were ~ 301, 231, 221, 283 and 348 % for the PCM loaded with 0.001, 0.0025, 0.005, 0.0075 and 0.01 wt. % of CuNP, respectively. On the other hand, in region-III, thermal conductivity enhancements (at T = 10 ^{0}C) were ~ 85.5, 87.9, 100.7, 102.9 and 117.1 % for the PCM loaded with 0.001, 0.0025, 0.005, 0.0075 and 0.01 wt. % of CuNP, respectively. Thermal conductivity enhancements for CuNP loaded PCM were found to be higher than the earlier reported values of ~ 3 and 182 % enhancement in the liquid and phase transition regions, respectively, for hexadecane loaded with 0.01 wt. % copper nanowires (outer diameter and length ~ 50 nm and 1-50 μm, respectively) [231]. On the other hand, in the solid state, thermal conductivity enhancement was higher (~ 130 %) in the case of PCM loaded with 0.01 wt. % of copper nanowires [231], as compared to the CuNP nano-inclusions, used in the present study (maximum enhancement ~ 117.1 %). This was probably due to the higher aspect ratio of the copper nanowires that formed efficient percolating trajectories along the grain boundaries during freezing.

Figure 3.4d shows that the thermal conductivity enhancements, in the liquid state, were ~ 2.9, 7.1, 2.9, 8.6 and 9.3 % for the PCM loaded with 0.001, 0.0025, 0.005, 0.0075 and 0.01 wt. % of AgNW, respectively. In the region-II, thermal conductivity enhancements were ~ 382, 337, 326, 287 and 348 % for the PCM loaded with 0.001, 0.0025, 0.005, 0.0075 and 0.01 wt. % of AgNW, respectively. On the other hand, 87.9, 117.1, 129.3, 102.1 and 117.9 %

enhancements in thermal conductivity were observed in the solid state (at T = 10 ^{0}C) for AgNW loading of 0.001, 0.0025, 0.005, 0.0075 and 0.01 wt. %, respectively. **Fig. 3.4e** shows the variation of thermal conductivity enhancement for the PCM loaded with MWCNT, where it can be seen that the thermal conductivity enhancements in the liquid state, were ~ 1.4, 2.9, 4.3, 5.0 and 5.7 % for the PCM loaded with 0.001, 0.0025, 0.005, 0.0075 and 0.01 wt. % of MWCNT. The thermal conductivity enhancements in the phase transition region were ~ 238, 264, 273, 274 and 209 % for the PCM loaded with 0.001, 0.0025, 0.005, 0.0075 and 0.01 wt. % of MWCNT, respectively. In the solid state, thermal conductivity enhancements were ~ 80.0, 85.0, 87.9, 105.0 and 87.9 % for the PCM loaded with 0.001, 0.0025, 0.005, 0.0075 and 0.01 wt. % of MWCNT. In the present study, the maximum thermal conductivity enhancement, in the solid state (at T = 10 ^{0}C), was ~ 105 %, for the PCM loaded with 0.0075 wt. % of MWCNT, which was lower than the ~ 200 % enhancement in thermal conductivity reported by Sun et al. [237], for hexadecane loaded with carboxylic acid functionalized MWCNT (loading = 0.4 % volume fraction). On the other hand, experimental results indicated a maximum enhancement in thermal conductivity of ~ 274 % for the PCM loaded with 0.0075 wt. % of MWCNT, in the phase transition region, which was substantially higher than the values reported by Sun et al. [237]. It can be seen from **Fig. 3.4f** that the thermal conductivity enhancements in the liquid state were ~ 1.4, 2.9, 4.3, 5.7 and 7.1 % for the PCM loaded with 0.001, 0.0025, 0.005, 0.0075 and 0.01 wt. % of GNP, respectively. Thermal conductivity enhancements in the phase transition region were ~ 257, 263, 271, 278 and 282 % for the PCM loaded with 0.001, 0.0025, 0.005, 0.0075 and 0.01 wt. % of GNP, respectively. Thermal conductivity enhancements of ~ 84.3, 91.4, 100.0, 107.1 and 111.4 % were observed for the PCM loaded with 0.001, 0.0025, 0.005, 0.0075 and 0.01 wt. % of GNP, respectively, in the solid state. The maximum enhancement in thermal conductivity in the phase transition region was found to be ~ 282 % for the PCM loaded with 0.01 wt. % of

GNP, which was higher than the enhancement values of ~ 220 % and 110-160 % reported by Zheng et al. [387] and Schiffres et al. [395], respectively.

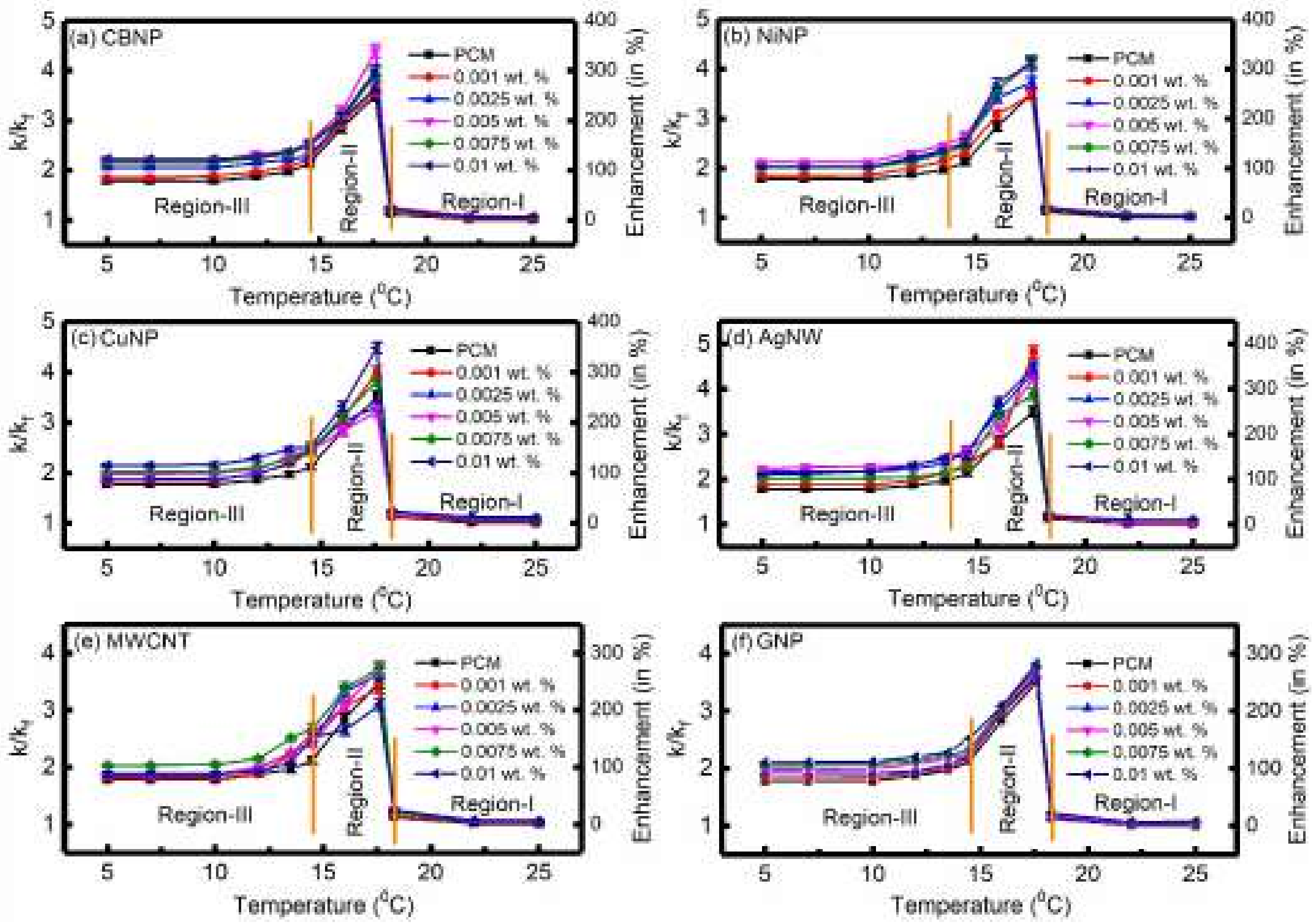

Figure 3.4 Variation of k/k_f and percentage enhancement in thermal conductivity, as a function of temperature, for the PCM loaded with various concentrations of (a) CBNP, (b) NiNP, (c) CuNP, (d) AgNW, (e) MWCNT and (f) GNP nano-inclusions. For comparison, the variation of k/k_f in the case of PCM, without any nano-inclusions, is also shown in the figures. The variation of k/k_f can be divided into three regions, viz. region-I (liquid state), region-II (phase transition) and region-III (solid state).

Figures 3.5a-f show the variation of k/k_f and percentage enhancement in thermal conductivity, as a function of sample concentration, in the solid (T = 10 ^{0}C) and liquid (T = 25 ^{0}C) states for the PCM loaded with six different nano-inclusions, viz. CBNP, NiNP, CuNP, AgNW, MWCNT and GNP, respectively. In the liquid state, maximum enhancements in thermal conductivity were ~ 6.4, 5.7, 11.4, 9.3, 5.7 and 7.1 % for the PCM loaded with 0.01 wt. % of CBNP, 0.005 wt. % of NiNP, 0.01 wt. % of CuNP, 0.01 wt. % of AgNW, 0.01 wt. % of MWCNT and 0.01 wt. % of GNP, respectively. It can be clearly seen from **Figs. 3.5a-f** that for the PCM loaded with CBNP, CuNP, MWCNT and GNP, thermal conductivity increased with the concentration of the nano-inclusions in the liquid state. On the other hand, for the PCM loaded with NiNP and AgNW, thermal conductivity decreased at higher concentrations of the nano-inclusions, which was due to the sedimentation of the larger aggregates at higher concentrations of the nano-inclusions. The sedimentation velocity (V_s) of a concentrated solution is expressed as $V_s = \frac{V_0(1-\phi)}{1+M\phi(1-\phi)^{-3}}$ [50]. Here, M and ϕ indicate a numerical constant (M ~ 4.6) and effective volume fraction of the solute, respectively. V_0 indicates the sedimentation velocity at infinite dilution, which is linearly proportional to the density difference of the solute and the solvent [50]. Due to higher density of AgNW and NiNP (density ~ 10.5 and 8.9 g/cc, respectively), these nano-inclusions were prone to form unstable aggregates at higher concentrations, which resulted in the decrease of thermal conductivity enhancements at higher concentrations, as can be seen from **Figs. 3.5b & d**.

It can be further seen from **Figs 3.5a-f** that the thermal conductivity enhancement was substantially higher for the nano-inclusion loaded PCM in the solid state, which was attributed to the formation of the crystalline structure of the PCM, on freezing, and phonon mediated efficient heat transfer through the quasi-2D network of percolating structures [231, 237, 387]. In the present study, the maximum thermal conductivity enhancements, in the solid state, were ~ 121.4, 112.9, 117.1, 129.3, 105.0 and 111.4 % for the PCM loaded with 0.01 wt. % of CBNP, 0.005 wt. % NiNP, 0.01 wt. % of CuNP, 0.005 wt. % of AgNW, 0.0075 wt. % of MWCNT and 0.01 wt. % of GNP, respectively. The aggregates grow in size with increasing concentration of the nano-inclusions due to Van der Waal's interaction, resulting in an enhancement of thermal conductivity. As discussed earlier in section 3.3, formation of such larger aggregates is beneficial for thermal conductivity enhancement due to phonon mediated efficient heat conduction through a larger network of percolating structure with reduced interfacial thermal resistance and increased near field radiative heat transfer [342, 419, 420]. Initial increase in thermal conductivity enhancement of nano-inclusion loaded PCM with increasing loading fraction has also been reported earlier for hexadecane based PCM [231, 237, 387].

It has been reported that thermal conductivity of nanofluids initially increases with aggregate size and attains an optimal value for the well dispersed aggregates due to the formation of high efficiency percolation network and beyond that, thermal conductivity decreases for larger aggregates [342]. Formation of such large aggregates cause a saturation or a slight decrease in thermal conductivity enhancements at higher concentrations of the nano-inclusions, as can be seen from **Figs 3.5a-f**. This was attributed to the fractal morphologies of the aggregates consisting of a backbone and dead-ends as discussed earlier in the theoretical section and schematically shown in **Fig. 3.1** [341]. Thermal conductivity enhancement occurs via phonon mediated effective heat transport through the backbone and the dead-ends are, in general, insignificant towards enhancement of thermal transport [342]. This is also evident from Eq. 3.1 (after first order homogenization involving dead-ends only), where considering the highest volume fraction as 7.33×10^{-6} for 0.01 wt. % loading of AgNW and thermal conductivities of Ag and PCM (in solid state) as 427 $Wm^{-1}K^{-1}$ [38] and 0.249 $Wm^{-1}K^{-1}$, respectively, the effective thermal conductivity of AgNW loaded PCM was found to be ~ 0.252 $Wm^{-1}K^{-1}$. This shows that if the contributions from dead-ends are only considered, the maximum thermal conductivity enhancement is ~ 1.2 %, which was approximately two orders of magnitude lower than the experimentally measured value of ~ 120 %. In larger aggregates the number of dead-ends increases, which does not contribute towards thermal conductivity enhancement and moreover, such larger aggregates are not well dispersed and prone to sedimentation causing a saturation or decrease in thermal conductivity of the nano-inclusion loaded PCM at higher loading fractions. Decrease in thermal conductivity for higher concentrations of MWCNT loading in hexadecane based PCM were experimentally reported by Angayarkanni and Philip [231] and Sun et al. [237], which are in good agreement with the findings of the present study.

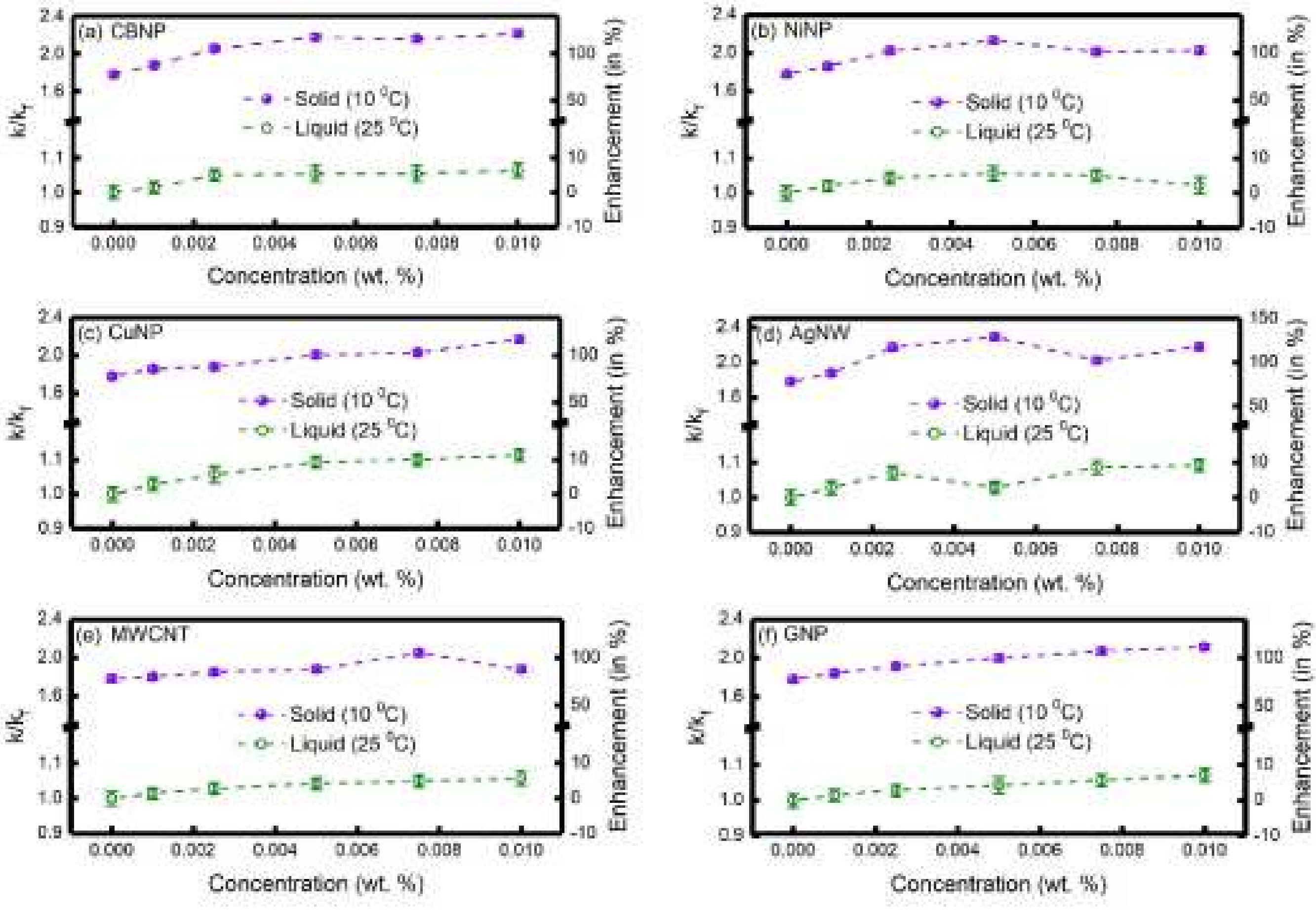

Figure 3.5 Variation of k/k_f and percentage enhancement in thermal conductivity, as a function of sample concentration, in the solid (T = 10 ^{0}C) and liquid (T = 25 ^{0}C) states for the PCM loaded with (a) CBNP, (b) NiNP, (c) CuNP, (d) AgNW, (e) MWCNT and (f) GNP nano-inclusions.

Figures 3.6a-f show the variation of k/k_f, in the liquid state, as a function of concentration (in volume fraction), for the PCM loaded with CBNP, NiNP, CuNP, AgNW, MWCNT and GNP nano-inclusions, respectively. The theoretical plots, for the effective medium theory ($k/k_f = 1+3\phi$, ϕ being the effective volume fraction of the nano-inclusions, which is considered as the theoretical upper limit of Eq. 3.5 after three level homogenization following Prasher & Evans model [341]) are also shown in the figures. It can be clearly seen from **Figs. 3.6a-f** that the experimentally measured k/k_f values were higher than the theoretically predicted values, which indicated the presence of agglomeration in these systems [38, 231].

The six different nano-inclusions, used in the present study, were classified into two groups, viz., carbon-based nano-inclusions (CBNP, GNP and MWCNT) and metallic nano-inclusions (AgNW, CuNP and NiNP). **Figs 3.7a-b** show the bar charts comparing the k/k_f and percentage enhancement in thermal conductivity in the solid state, at loading concentration of 0.01 wt. % for the carbon-based and metallic nano-inclusions, respectively. For comparison, the thermal conductivity enhancement of the PCM (without any nano-inclusions) is also shown in **Figs. 3.7a-b**. Among the three carbon-based nano-inclusions, bulk thermal conductivity is the highest for MWCNT (~ 6600 $Wm^{-1}K^{-1}$), followed by GNP (~ 3000 $Wm^{-1}K^{-1}$) and CBNP (~ 0.25-0.4 $Wm^{-1}K^{-1}$) [38]. Nevertheless, it can be clearly seen from **Fig. 3.7a** that the highest enhancement in thermal conductivity was for the PCM loaded with CBNP, followed by GNP and MWCNT, in the decreasing order. This was attributed to the variations in morphology and Kapitza resistance of the nano-inclusions. For the nano-inclusion loaded PCM in the solid state, the enhancement in thermal conductivity is due to the formation of percolation trajectories along the inter-crystallite regions and GNP, being two-dimensional, forms better percolation pathways with comparatively larger networking structures [65].

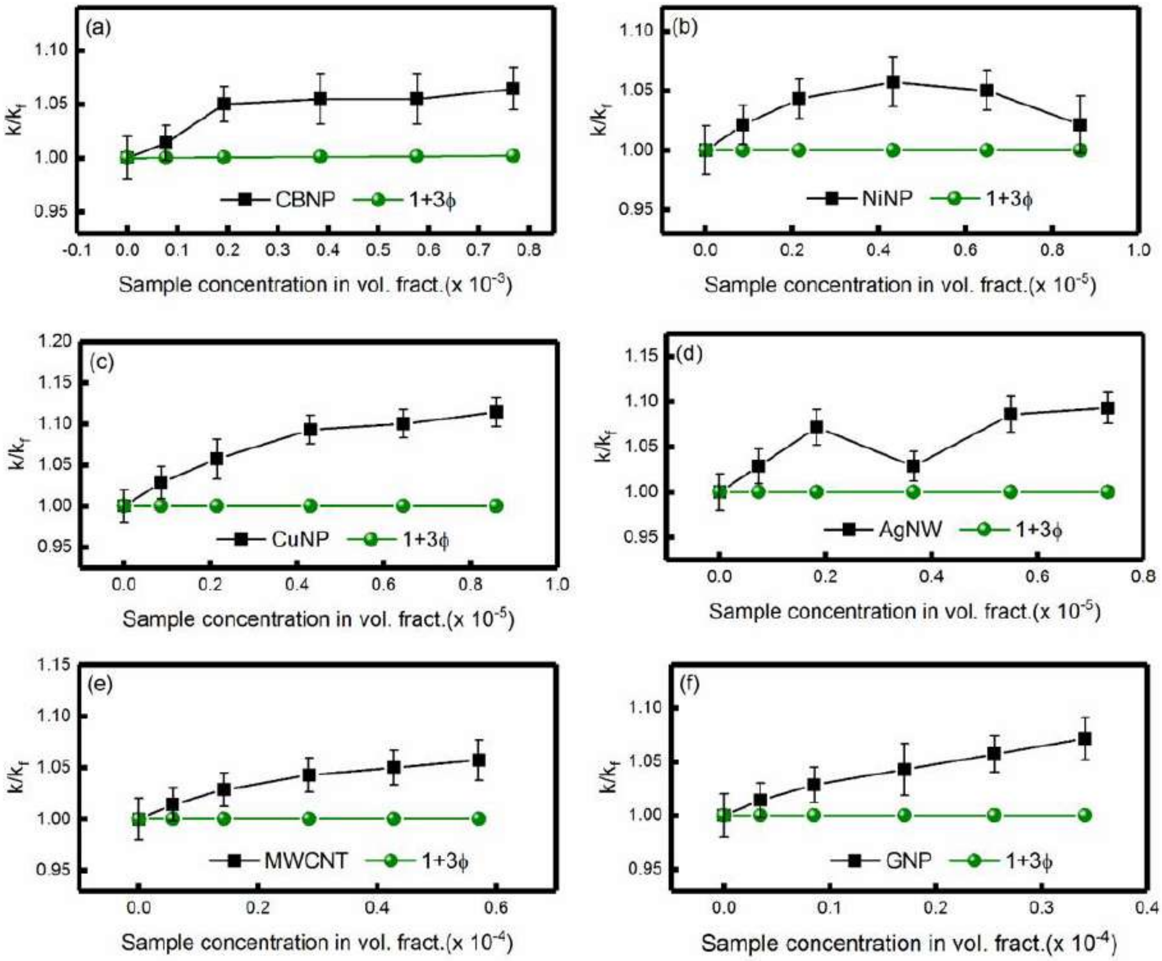

Figure 3.6 Variation of k/k_f, in the liquid state, as a function of concentration (in volume fraction), for the PCM loaded with (a) CBNP, (b) NiNP, (c) CuNP, (d) AgNW, (e) MWCNT and (f) GNP nano-inclusions. The theoretical plots, for the effective medium theory are also shown.

Using molecular dynamics simulations, Yang et al. [430] showed that carbon nanotubes and graphene nanoplatelets act as nucleation sites during freezing, which leads to orientational ordering near the PCM/nano-inclusions interface resulting in an enhanced phonon coupling [65]. It was further shown by Yang et al. [430] that the nucleation rate is lower for the PCM loaded with GNP. In the case of hexadecane based PCM, a lower freezing rate leads to the formation of a longer and thicker needle like microstructure with improved heat transfer efficiency [395].

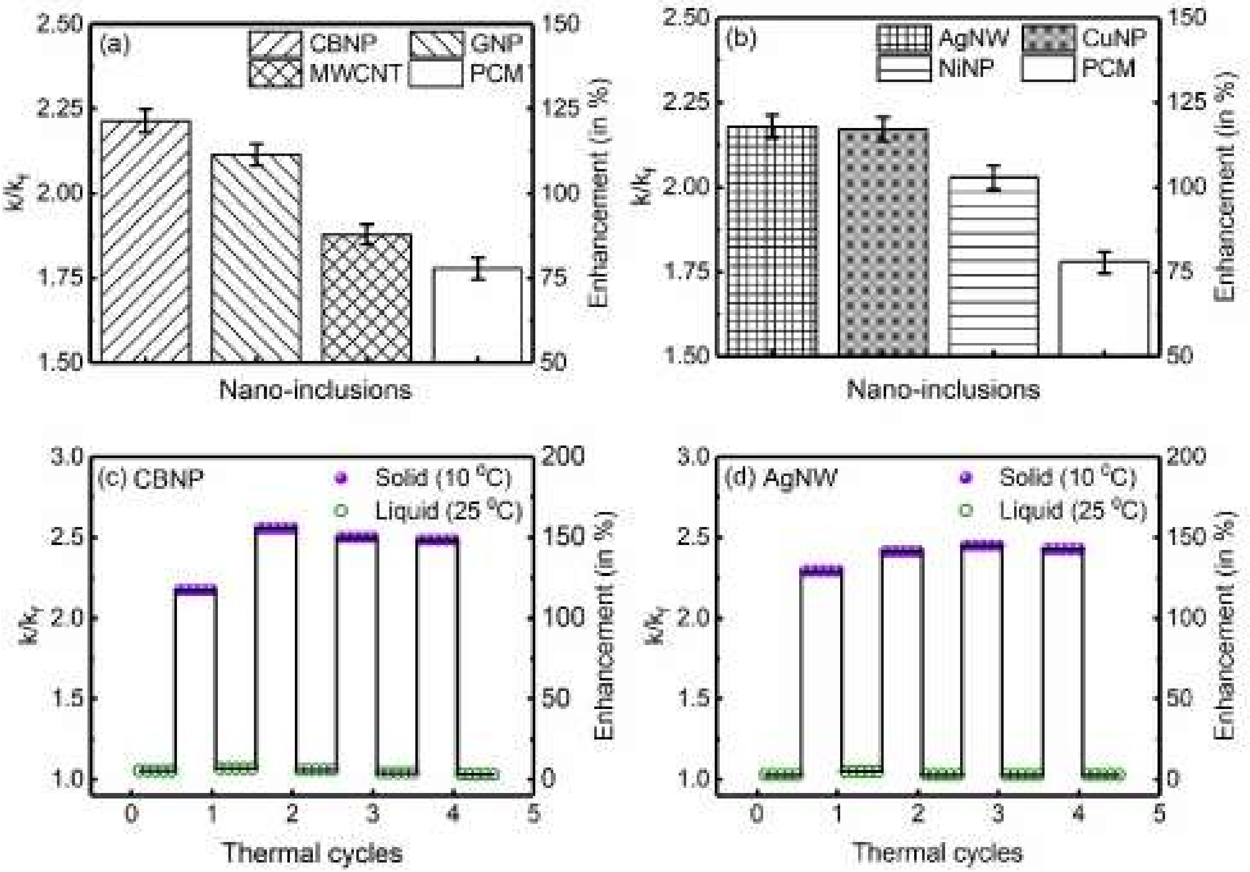

Figure 3.7 Bar charts comparing the k/k_f and percentage enhancement in thermal conductivity in the solid state, at loading concentration of 0.01 wt. % for the (a) carbon-based and (b) metallic nano-inclusions. For comparison, the thermal conductivity enhancement of the PCM, without any nano-inclusions, is also shown in the figures. Variation of k/k_f and percentage enhancement in thermal conductivity during thermal cycling for the PCM loaded with 0.005 wt. % of (c) CBNP and (d) AgNW.

The higher thermal conductivity enhancement in the case of PCM loaded with GNP was also attributed to the lower Kapitza resistance of GNP, as compared to MWCNT [65]. On the other hand, the PCM loaded with CBNP nano-inclusions showed the highest thermal conductivity enhancement, which was attributed to the fractal nature of the aggregates of CBNP, consisting of nodules of primary particles. An earlier study showed that CBNP loading in PCM leads to the formation of high thermal conductivity percolation trajectories with reduced inter-aggregate gaps [431]. Higher thermal conductivity for CBNP loaded octadecane based PCM was reported by Wu et al. [236], which was attributed to the low fractal dimensions and volume filling capability of the CBNP aggregates. Thermal conductivity enhancement through the percolating network of the nano-inclusions, loaded within a PCM, is limited due to the interfacial thermal resistance of the aggregate/aggregate and aggregate/PCM interfaces and phonon mismatch due to the random curvatures of the aggregate/aggregate interfaces [432, 433]. CBNP, due to its aciniform structure and low fractal dimension, forms tightly packed aggregates with improved aggregate/aggregate interactions leading to higher thermal conductivity trajectories, which explains the highest thermal conductivity enhancement for the PCM loaded with CBNP, as shown in **Fig. 3.7a**. On the other hand, it is evident from **Fig. 3.7b**, that in the cases of metallic nano-inclusions, the highest thermal conductivity enhancement was obtained for the PCM loaded with AgNW, followed by CuNP and NiNP, in the decreasing order. Among the three metallic nano-inclusions, bulk thermal conductivity is the highest for AgNW (~ 427 $Wm^{-1}K^{-1}$) followed by CuNP (~ 385 $Wm^{-1}K^{-1}$) and NiNP (~ 91 $Wm^{-1}K^{-1}$) [38]. Though the thermal conductivity enhancements for the PCM loaded with metallic nano-inclusions showed a similar trend, other physical factors, viz., larger aspect ratio of AgNW and larger size of NiNP (average crystallite sizes of NiNP and CuNP were ~ 29 ± 3 and 13 ± 2 nm, respectively) also played a significant role according to earlier studies [434], which showed a higher thermal conductivity enhancement for lower particle size and larger aspect ratios of the dispersed phase. On the other hand, an increase in the effective thermal conductivity of the PCM loaded with metallic nano-inclusions as a function of the bulk thermal conductivity of the nano-inclusions suggested a series or parallel ordering, under aggregation in these systems [435]. **Figures 3.7c-d** show the results of thermal cycling for the PCM loaded with 0.005 wt. % of CBNP and AgNW, respectively. During thermal cycling, several thermal conductivity measurements were performed in the liquid state (at T = 25 ^{0}C, well above the freezing point) and then the samples were frozen well below the phase transition temperature and several thermal conductivity measurements were performed in the solid state (at T = 10 ^{0}C). In the case of pure PCM (without any nano-inclusions), the melting and freezing cycles were perfectly reversible (as can be seen from **Fig. 3.3d**), whereas some deviations were observed for the PCM loaded with 0.005 wt. % of CBNP and AgNW. In the case of PCM loaded with CBNP, thermal conductivity enhancements in the liquid state were ~ 7.0, 6.0, 4.0 and 3.0 % after 1st, 2nd, 3rd and 4th cycles, respectively. On the other hand, thermal conductivity enhancements in the solid state were ~ 117.4, 155.7, 150.0 and 148.6 % after 1st, 2nd, 3rd and 4th cycles, respectively. In the case of the PCM loaded with AgNW, thermal conductivity enhancements in the liquid state were ~ 5.0, 2.9, 2.9 and 2.9 % after 1st, 2nd, 3rd and 4th cycles, respectively. In the solid state, for the PCM loaded with AgNW, thermal conductivity enhancements were ~ 129.3, 141.4, 145.0 and 142.9 % after 1st, 2nd, 3rd and 4th cycles, respectively. It can be seen from **Figs. 3.7c-d** that the variations in thermal conductivity enhancements, during thermal cycling, were negligible in the liquid state, but significant in the solid state. This was attributed to the difference in aggregate sizes and aggregates numbers after subsequent melting/freezing cycles. The individual nano-inclusions form aggregates due to Van der Waal's interaction and after subsequent thermal cycles, the aggregates do not re-disperse reversibly [237]. Phase contrast optical microscopy studies were carried out to ascertain the microstructural evolution after subsequent thermal cycles and **Figures 3.8a-d** show the optical phase contrast microscopy images for the PCM loaded with 0.005 wt. % of CBNP after 1st, 2nd, 3rd and 4th cycles, respectively, in the liquid sate. The formation of micron sized aggregates of CBNP (encircled in the figure for better visualization), after 2nd freezing cycle is clearly discernible from **Fig 3.8b**, which resulted in a larger thermal conductivity enhancement in the 2nd cycle (as can be seen from **Fig. 3.7c**). On the other hand, **Fig. 3.8c** clearly shows that after 3rd thermal cycle, larger aggregates were formed with lower number density, which caused a slight decrease in thermal conductivity enhancement in the 3rd thermal cycle (thermal conductivity enhancement ~ 150.0 % at 3rd cycle, against ~ 155.7 % after 2nd cycle). **Fig. 3.8d** shows the phase contrast microscopy image after 4th cycle, where lower number of aggregates were visible, as larger aggregates were prone to sedimentation, causing a further decrease in thermal conductivity enhancement in the 4th cycle, as can be seen from **Fig. 3.7c**.

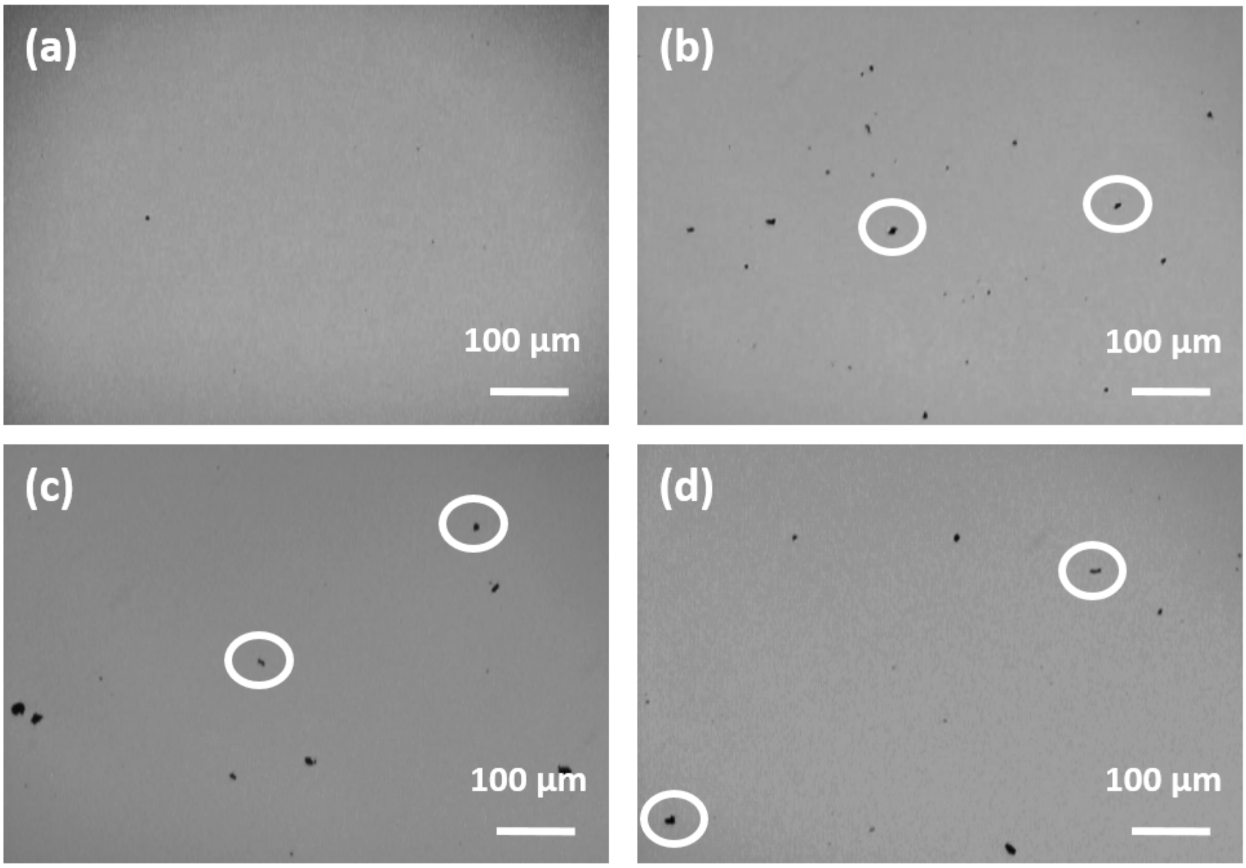

Figure 3.8 Optical phase contrast microscopy images for the PCM loaded with 0.005 wt. % of CBNP after (a) 1st, (b) 2nd, (c) 3rd and (d) 4th cycles, in the liquid sate. The formation of micron-sized aggregates of CBNP are clearly discernible from the images. A few aggregates are encircled in the figures for easy identification.

Figures 3.9a-c show the results of thermal cycling for the PCM loaded with 0.005 wt. % of MWCNT, NiNP and CuNP, respectively. In the case of the PCM loaded with MWCNT, thermal conductivity enhancements in the liquid state were ~ 2.1, 2.9, 1.4 and 0.0 % after 1st, 2nd, 3rd and 4th cycles, respectively. On the other hand, thermal conductivity enhancements in the solid state were ~ 87.9, 112.1, 96.4, 89.3 % after 1st, 2nd, 3rd and 4th cycles, respectively. For the PCM loaded with NiNP nano-inclusions, thermal conductivity enhancements were ~ 4.3, 8.6, 5.7 and 5.5 % after 1st, 2nd, 3rd and 4th cycles, respectively, in the liquid state and 112.9, 117.1, 124.3, 125.2 % after 1st, 2nd, 3rd and 4th cycles, respectively, in the solid state. For CuNP nano-inclusion loaded PCM, thermal conductivity enhancements in the liquid state were ~ 3.6, 2.1, 2.9 and 2.1 % after 1st, 2nd, 3rd and 4th cycles, respectively. Thermal conductivity enhancements in the solid state were ~ 100.7, 121.4, 134.3 and 132.1 % after 1st, 2nd, 3rd and 4th cycles, respectively. The variations in the thermal conductivity enhancements in the solid state, during thermal cycling, were attributed to the irreversible aggregation dynamics after subsequent melting/freezing cycles. Similar variation in thermal conductivity enhancements were reported for hexadecane based PCM loaded with MWCNT and graphite suspensions by Sun et al. [237], Zheng et al. [387] and Angayarkanni and Philip [231], where the variations were attributed to irreversible aggregation dynamics and weak solid-fluid interaction induced negative thermal conductivity enhancement for positive Kapitza lengths.

3.5.3 Effect of surface functionalization on thermal conductivity enhancement

To study the effect of surface functionalization on thermal conductivity enhancement, experiments were performed using uncoated graphene nanoplatelets (GNP-UC) loaded PCM. **Fig. 3.10a** shows the variation of k/k_f and percentage enhancement in thermal conductivity, as a function of temperature for the PCM loaded with five different concentrations (viz., 0.001, 0.0025, 0.005, 0.0075 and 0.01 wt. %) of GNP-UC. For comparison, thermal conductivity variation of the PCM (without any nano-inclusion) is also shown in **Fig. 3.10a**. It can be clearly seen from **Fig. 3.10a** that the variation of k/k_f, as a function of temperature, can be divided into three regions, viz. region-I (liquid state, for T> 18.3 ^{0}C), region-II (phase transition region, 14.5 ^{0}C<T<18.3 ^{0}C) and region-III (solid state, for T < 14.5 ^{0}C), which is in agreement with the earlier observations.

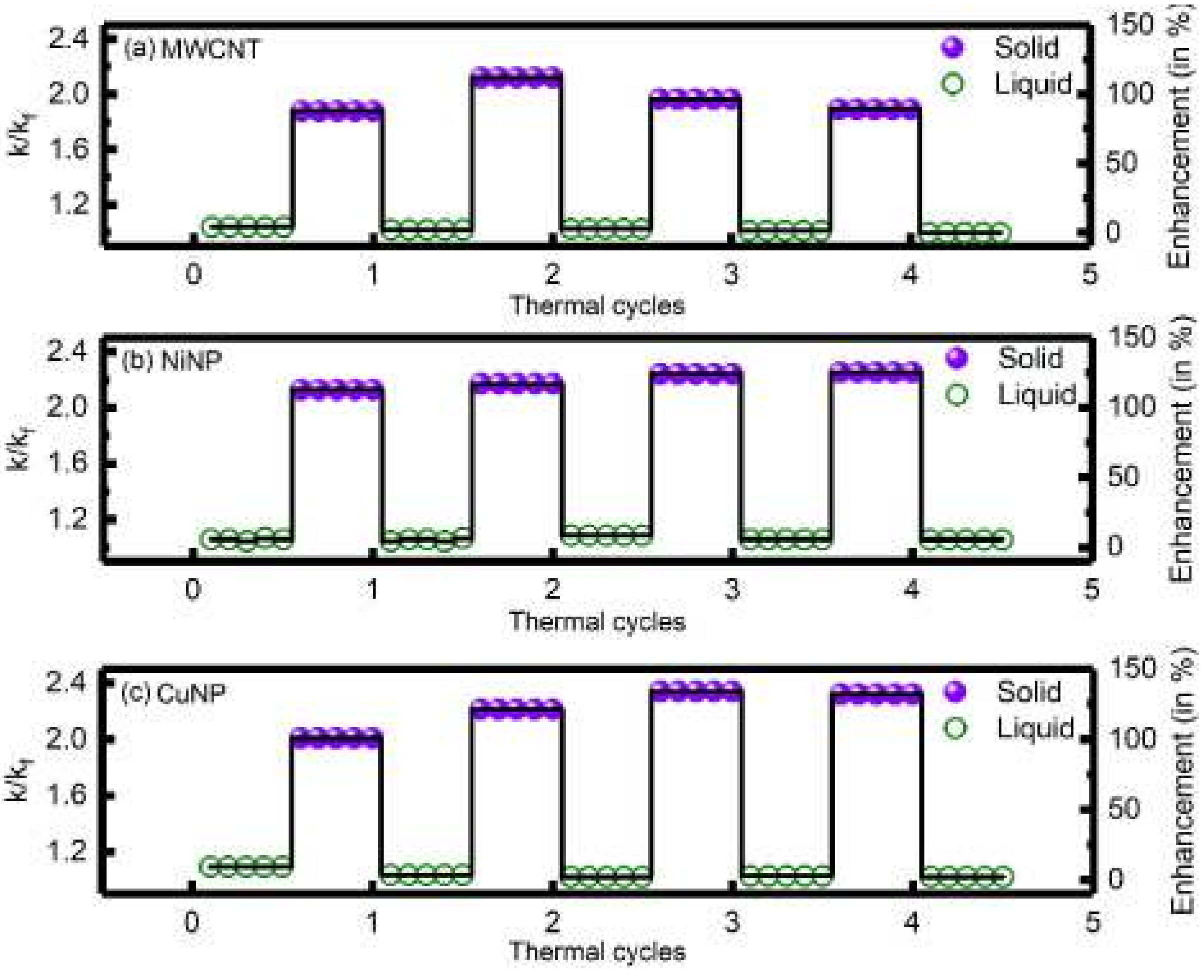

Figure 3.9 Variation of k/k_f and percentage enhancement in thermal conductivity during thermal cycling of the PCM loaded with 0.005 wt. % of (a) MWCNT, (b) NiNP and (c) CuNP nano-inclusions.

Thermal conductivity enhancements in the liquid state (at T = 25 ^{0}C) were ~ 0.0, 2.9, 4.3, 7.9 and 5.7 % for the PCM loaded with 0.001, 0.0025, 0.005, 0.0075 and 0.01 wt. % of GNP-UC. In the phase transition region, thermal conductivity enhancements were ~ 300, 283, 279, 280 and 299 % for loading concentrations of 0.001, 0.0025, 0.005, 0.0075 and 0.01 wt. %. On the other hand, thermal conductivity enhancements decreased in the solid state and became constant below 10 ^{0}C. Thermal conductivity enhancements in the solid state (at T = 10 ^{0}C) were ~ 82.9, 105.7, 105.7, 121.4 and 89.3 % for the PCM loaded with 0.001, 0.0025, 0.005, 0.0075 and 0.01 wt. % of GNP-UC. **Table 3.2** shows the comparison of the k/k_f values, as a function of loading concentration for the PCM loaded with GNP and GNP-UC in the liquid and solid states, where it can be seen that the variation of k/k_f in the liquid state is insignificant, whereas, in the solid state, k/k_f was slightly higher for the PCM loaded with GNP-UC. Nevertheless, at the highest concentration of 0.01 wt. %, k/k_f, in the case of GNP-UC, was substantially lower, which was attributed to the intense agglomeration for the uncoated nano-inclusions.

The presence of an organic coating on the surface of the GNP increases the interfacial thermal resistance (Kapitza resistance) of the nano-inclusions leading to a lower effective thermal transport efficiency due to phonon scattering at the nano-inclusion/coating/PCM interfaces, which is partially specular and partially diffusive depending on the local curvature and roughness of the interface [436]. This is more evident in the solid state, where the thermal transport is primarily though the percolating network of the aggregates, which resulted in a comparatively lower thermal conductivity enhancements for the PCM loaded with oleic acid functionalized graphene nanoplatelets (GNP). Vales-Pinzon et al. [437] also reported an effective decrease in thermal conductivity of ethylene glycol based nanofluid containing iron nanoparticles after surface capping with carbon. On the other hand, Li et al. [438] reported an increase in thermal conductivity of water-based SiO_2-coated-graphene nanofluid, which was attributed to the increased hydrophilic interaction of silica coated graphene resulting in lower interfacial thermal resistance and larger stability in the aqueous medium. The significant influence of surface functionalization and the role of adsorbing moieties on thermal conductivity enhancement is studied in details [37, 439].

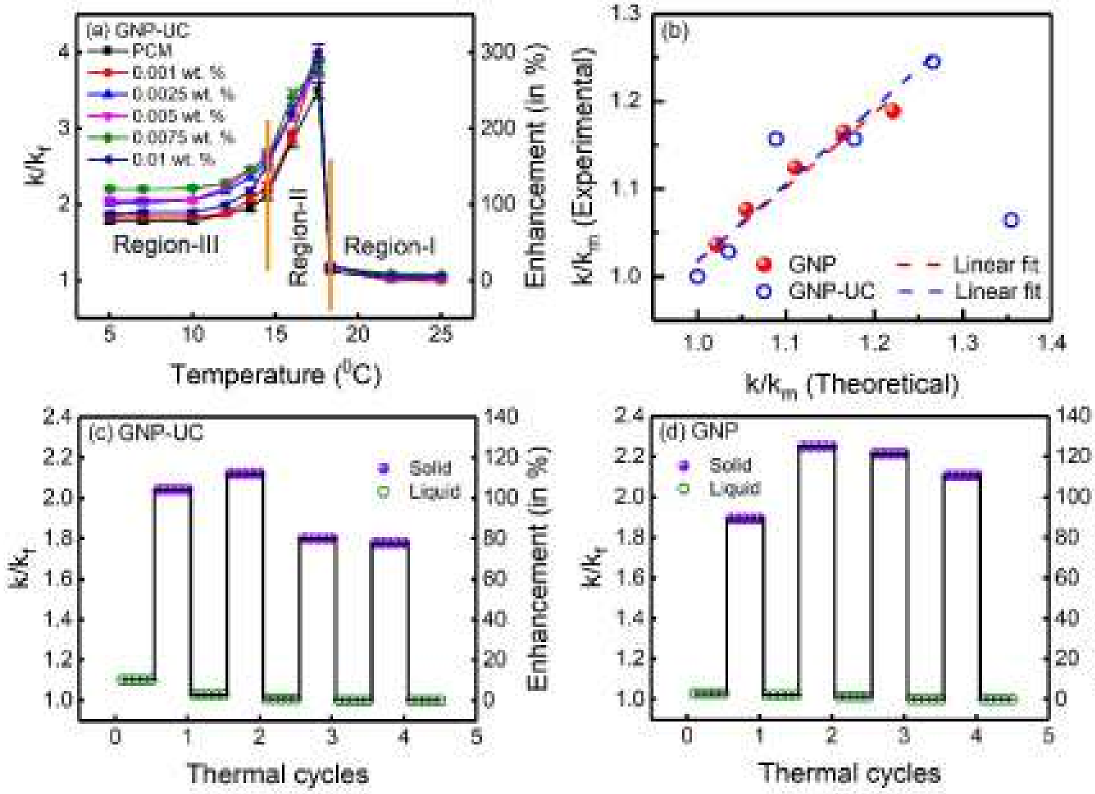

Figure 3.10 (a) Variation of k/k_f and percentage enhancement in thermal conductivity, as a function of temperature for the PCM loaded with five different concentrations of uncoated GNP (GNP-UC). For comparison, thermal conductivity variation of the PCM, without any nano-inclusion, is also shown in the figure. (b) Variation of experimentally measured k/k_m as a function of theoretically calculated k/k_m values for the PCM loaded with various concentrations of oleic acid functionalized GNP and uncoated GNP (GNP-UC). Here, k_m indicates the thermal conductivity of the PCM, without any inclusions, in the solid state. The experimental and theoretical data were found to be linearly correlated and the linear regression analyses are also shown in the figure. The errors associated with the theoretical values were less than ± 5%. Variation of k/k_f and percentage enhancement in thermal conductivity during thermal cycling of the PCM loaded with 0.005 wt. % of (c) uncoated GNP (GNP-UC) and (d) oleic acid functionalized GNP.

Table 3.2 Comparison of k/k_f as a function of loading concentration for the PCM loaded with GNP and GNP-UC.

Loading (wt. %)	GNP				GNP-UC			
	Liquid state (T = 25 ^{0}C)		Solid state (T = 10 ^{0}C)		Liquid state (T = 25 ^{0}C)		Solid state (T = 10 ^{0}C)	
	k/k_f	error	k/k_f	error	k/k_f	error	k/k_f	error
0.001	1.01	0.02	1.84	0.03	1.00	0.02	1.83	0.03
0.0025	1.03	0.02	1.91	0.03	1.03	0.02	2.06	0.03
0.005	1.04	0.02	2.00	0.03	1.04	0.02	2.06	0.03
0.0075	1.06	0.02	2.07	0.03	1.08	0.02	2.21	0.04
0.01	1.07	0.02	2.11	0.03	1.06	0.02	1.89	0.04

Effective thermal conductivity enhancements in the PCM loaded with GNP and GNP-UC were analyzed using the model proposed by Chu et al. [440]. This model considers an isotropic composite structure with GNP inclusions distributed randomly and the interfacial thermal losses are represented by an average interfacial thermal resistance (R_K) between the GNP and the composite. Hence, the GNP is assumed as a two-dimensional plate of intrinsic thermal conductivity (k_g), surrounded by a hypothetical layer of material with thermal resistance of R_K. Hence, the effective thermal conductivity of GNP can be expressed by the following equations [440].

$$k_x = \frac{k_g}{(2R_K k_g)/L + 1} \tag{3.7}$$

$$k_z = \frac{k_g}{(2R_K k_g)/L_t + 1} \tag{3.8}$$

Here, k_x and k_z indicate effective thermal conductivity along the in-plane and through thickness directions, respectively. L and L_t indicate length and thickness of the GNP, respectively. For $k_x >> k_z$, using micromechanics theory, it can be shown that the effective thermal conductivity (k) of a composite loaded with randomly distributed GNP inclusions can be obtained from the following equation [440].

$$\frac{k}{k_m} = \frac{\phi}{3}\left[\frac{2}{H + \frac{1}{(k_x/k_m)-1}} + \frac{1}{\frac{1-H}{2} + \frac{1}{(k_z/k_m)-1}}\right] + 1 \tag{3.9}$$

Here, k_m is the thermal conductivity of the composite matrix (without any nano-inclusions) in the solid state, ϕ is the effective volume fraction of the nano-inclusions (after cluster homogenization) and H is a geometrical factor that depends on the aspect ratio ($p = L/L_t$) and can be expressed by the following equation [440].

$$H = \frac{\ln(p + \sqrt{p^2-1})p}{\sqrt{(p^2-1)^3}} - \frac{1}{p^2-1} \tag{3.10}$$

For large values of thermal anisotropy and aspect ratio, Eq. 3.10 can be reduced to a simplified form, which is expressed by the following expression [440].

$$\frac{k}{k_m} = \frac{2\phi/3}{H + \frac{1}{(k_x/k_m)-1}} + 1 \tag{3.11}$$

Theoretical values of k/k_m, in the case of PCM loaded with GNP and GNP-UC, were computed using Eq. 3.11, where the value of R_K was considered as 5×10^{-8} m^2KW^{-1} for GNP-UC [441]. Here, k_m indicates the thermal conductivity of the PCM, without any inclusions, in the solid state. **Fig. 3.10b** shows the variation of experimentally measured k/k_m as a function of theoretically calculated k/k_m values. It can be seen that the experimentally measured values were linearly correlated with the theoretical values and the data was fitted with linear regression analysis. The slope and adjusted R^2 for the linear regression analyses were ~ 0.9 ± 0.2 and 0.85, respectively, indicating quantitative agreement between the experimental and theoretical values. It can be further seen from **Fig. 3.10b** that the experimentally measured k/k_m for the highest loading concentration of 0.01 wt. % was significantly lower than the theoretically calculated value, which was attributed to the sedimentation of the large unstable aggregates of GNP-UC, which was also confirmed from the optical phase contrast microscopy images, as subsequently discussed.

Due to the presence of oleic acid capping on the surface, the Kapitza resistance of the surface functionalized GNP nano-inclusions were expected to be higher and the value was approximated based on the following equation for thermal conductivity of coated nano-spheres [437].

$$\frac{k_{sp}}{k_s} = 1 + \frac{3\phi_s(k_p - k_s)}{3k_s + (1-\phi_s)(k_p - k_m)} \tag{3.12}$$

Here, k_{sp}, k_p and k_s indicate thermal conductivity of the surface modified nanoparticles, uncoated nanoparticles and that of surfactant (i.e. coating material), respectively. ϕ_s is expressed as $\phi_s = [a_p/(a_p+\delta_s)]^3$, where a_p and δ_s indicate radius of the nanoparticle and coating thickness, respectively [437]. The typical thickness of oleic acid coating was considered as 2 nm [232]. The values of k_{sp}/k_s and k_p/k_s were obtained as 51.46 and 62.29, respectively, which clearly showed that the effective thermal conductivity of the coated nanoparticles was lower, as compared to the uncoated nanoparticles. Moreover, for the above calculations, a spherical morphology of the nano-inclusions was assumed, whereas, GNP agglomerates are fractal in nature with larger surface to volume ratio [418, 424]. The enhancement in surface area to volume ratio from a sphere to a cube is ~ 1.24 (surface area to volume ratios of a sphere and cube are ~ 4.836 and 6, respectively). Hence, the Kaptiza resistance for the oleic acid functionalized GNP was approximated as $5 \times 10^{-8} \times 1.21$ (effect of surface functionalization with spherical morphology approximation) $\times$ 1.24 (correction factor for non-spherical morphology) ~ 8×10^{-8} m^2KW^{-1}. This value was then plugged in Eq. 3.11 to obtain the theoretical values of k/k_m. **Fig. 3.10b** shows the variation of the experimentally measured k/k_m values as a function of theoretically calculated k/k_m values for the PCM loaded with oleic acid functionalized GNP, where it can be seen that the experimental and theoretical values were linearly correlated. The slope and adjusted R^2 of the linear regression analysis were ~ 0.8 ± 0.1 and 0.96, respectively, which indicated quantitative agreement between the calculated and experimental values. It can be further seen from **Fig. 3.10b** that the agreement between the experimental and theoretical values were superior in the case of the PCM loaded with oleic acid functionalized GNP, as compared to the PCM containing uncoated nano-inclusions, which was attributed to the lower aggregation probability of the former.

Figures 3.10c-d show the results of the thermal cycling for the PCMs loaded with 0.005 wt. % of GNP-UC and surface functionalized GNP, respectively. In the case of PCM loaded with GNP-UC, thermal conductivity enhancements in the liquid state were ~ 2.9, 0.7, 0 and 0 % after 1st, 2nd, 3rd and 4th cycles, respectively. In the solid state thermal conductivity enhancements were 104.3, 112.1, 80 and 77.9 % after 1st, 2nd, 3rd and 4th cycles, respectively. On the other hand, in the case of the PCM loaded with oleic acid functionalized GNP, thermal conductivity enhancements in the liquid state were ~ 2.1, 1.4, 0 and 0 % after 1st, 2nd, 3rd and 4th cycles, whereas, in the solid state thermal conductivity enhancements were ~ 89.3, 125.0, 121.4 and 110.7 % after 1st, 2nd, 3rd and 4th cycles, respectively. It can be seen from **Figs. 3.10c-d**, that the thermal conductivity enhancements decreased after repeated thermal cycling, which was attributed to the irreversible aggregation dynamics during subsequent melting and freezing cycles [237]. For the PCM loaded with uncoated GNP (GNP-UC), due to intense aggregation, during 3rd and 4th thermal cycles, a significant decrease in thermal conductivity enhancement was seen. For increasing domain size in the case of larger aggregates, acoustic mismatch model for long wavelength phonon predicts a lowering of interfacial heat flux leading to a reduced effective thermal conductivity [442]. Moreover, surface roughness increases with aggregate size, which leads to enhancement in interfacial scattering of high frequency phonons (diffuse mismatch model) leading to an effective lowering of thermal conductivity for very large aggregates [443].

Optical phase contrast microscopy was carried out on the PCMs loaded with GNP and GNP-UC to probe the microstructural evolution during thermal cycling. **Figs. 3.11a-d** and **Figs. 3.11e-h** show the phase contrast microscopy images for the PCMs loaded with GNP and GNP-UC, respectively, in the liquid state, after 1st, 2nd, 3rd and 4th thermal cycles. For the PCM loaded with GNP, it can be clearly seen from **Figs. 3.11a-d** that the size and number density of the aggregates increased during 2nd thermal cycle and in the case of 3rd and 4th cycles, aggregates numbers were nearly constant. Nevertheless, number density was the highest during 2nd cycles and decreased during subsequent cycling due to slight agglomeration. This resulted in a small decrease in the thermal conductivity enhancement in the solid state for the PCM loaded with GNP during 3rd and 4th cycles, as shown in **Fig. 3.10d**. On the other hand, it can be seen from **Figs. 3.11e-h** that for the PCM loaded with GNP-UC, intense agglomeration occurred during 3rd and 4th thermal cycles resulting in sedimentation of the larger aggregates, which were not visible in **Fig. 3.11h**. This caused a large decrease in thermal conductivity for the PCM loaded with GNP-UC during 3rd and 4th thermal cycles, as can be seen from **Fig. 3.10c**.

These studies clearly show that the presence of a surfactant (oleic acid) capping on the surface of the GNP increased the stability of the nano-inclusions resulting in good thermal stability under cycling, without significant reduction in thermal conductivity, which is beneficial for practical applications. The carboxylic acid group of oleic acid is bound to the surface of the nano-inclusions, whereas the aliphatic chain is extended into the non-polar matrix of hexadecane (PCM), which reduced the aggregation probability of the coated nano-inclusions by providing additional steric stabilization [444]. Similarly, Zeng et al. [445] reported a superior stability of stearic acid capped MoS_2 in cyclohexane, which was attributed to the extension of the long aliphatic chains of stearic acid in the organic medium.

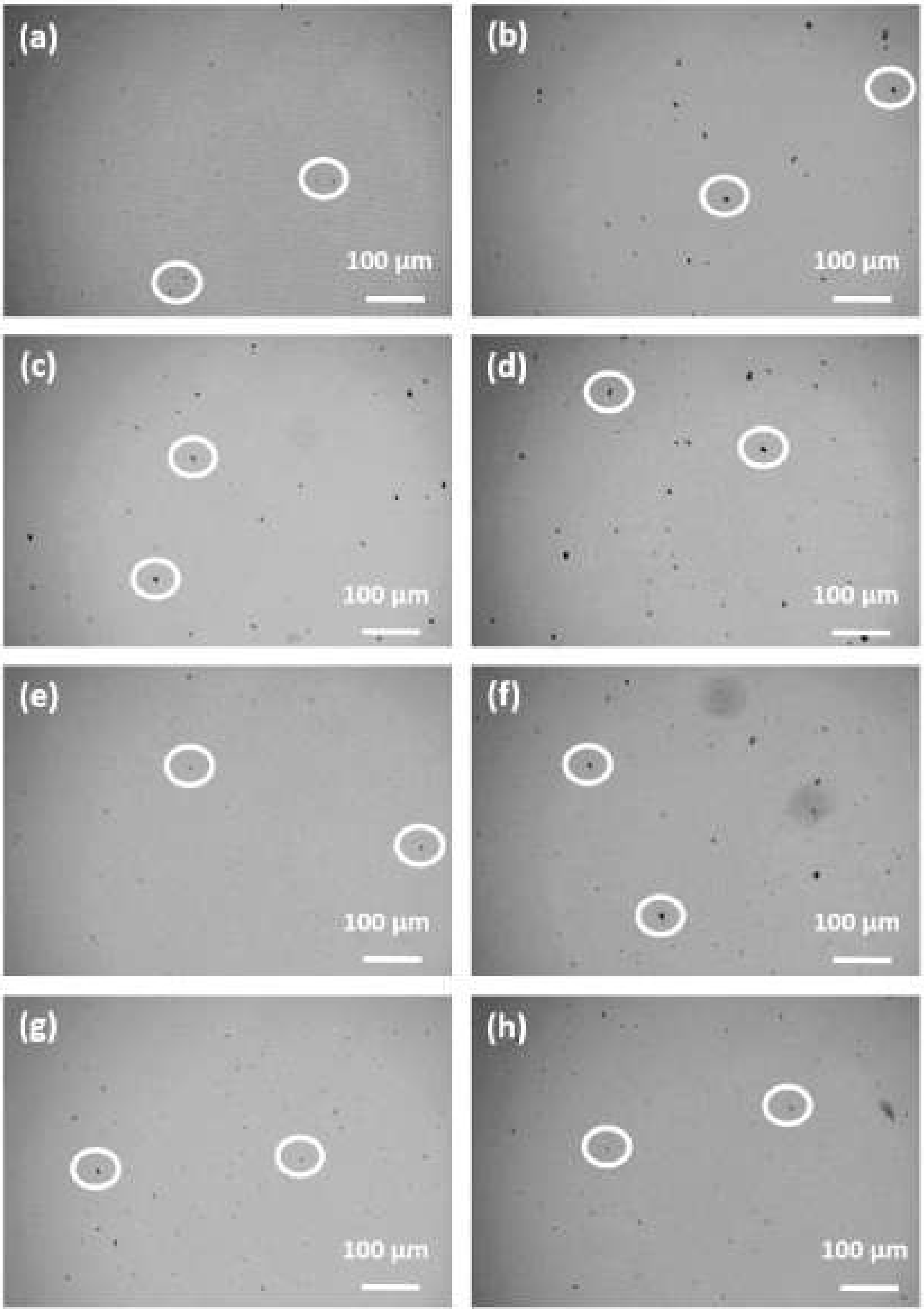

Figure 3.11 (a-d) Optical phase contrast microscopy images of the PCM loaded with 0.005 wt. % of oleic acid functionalized GNP, in the liquid state after 1st, 2nd, 3rd and 4th thermal cycles, respectively. (e-h) Optical phase contrast microscopy images of the PCM loaded with 0.005 wt. % of uncoated GNP (GNP-UC), in the liquid state after 1st, 2nd, 3rd and 4th thermal cycles, respectively. A few aggregates are encircled in the figures for easy identification.

Moreover, it has been reported that, for surfactant capped nano-inclusions, the thickness of the solvation monolayer is larger (determined by the chain length of the surfactant as compared to a few atomic distances in the case of uncoated nano-inclusions), which enhances the coupling of the nano-inclusions with the host matrix [446]. Xia et al. [417] also reported that surfactant capping increased the stability of the nano-inclusions. They also reported a slight reduction in thermal conductivity for surface capped nano-inclusions, especially for surfactants with longer chain lengths, which was attributed to the increase in Kapitza resistance upon surface functionalization. These observations are in good agreement with the experimental findings obtained from the present study.

3.5.4 Infrared thermography-based studies on the n-hexadecane based PCM

Infrared thermography (IRT)-based studies were carried out to map the surface temperature distribution of the PCM (with or without nano-inclusions) during freezing and the results were compared with the cooling curve of deionized water. For IRT-based studies, the samples (initial temperature ~ 29 ^{0}C, i.e. well above the phase transition temperature) were placed in a recirculating water bath maintained at T = 8 (±0.1) ^{0}C and the sample temperature was monitored as a function of time. **Figs. 3.12a-d** show the typical infrared images during cooling of water at t = 0, 500, 1000 and 1500 s, respectively. The pseudo colour coded temperature scale is also shown along with the images. **Figs. 3.12e-h** show the typical infrared images during the freezing of the PCM (without any nano-inclusions) at t = 0, 500, 1000 and 1500 s, respectively. The infrared images were emissivity corrected to reflect the correct temperature of the sample. **Fig. 3.12** shows that the sample temperature decreased with time, but the rate of temperature fall was lower in the case of PCM (**Figs. 3.12b & f**). For quantitative analyses, a region of interest (ROI) was selected and the average temperature, as a function of time, was determined by spatial averaging over several pixel locations within the ROI. Caution was exercised to avoid the edge pixels within the ROI to minimize temperature fluctuations.

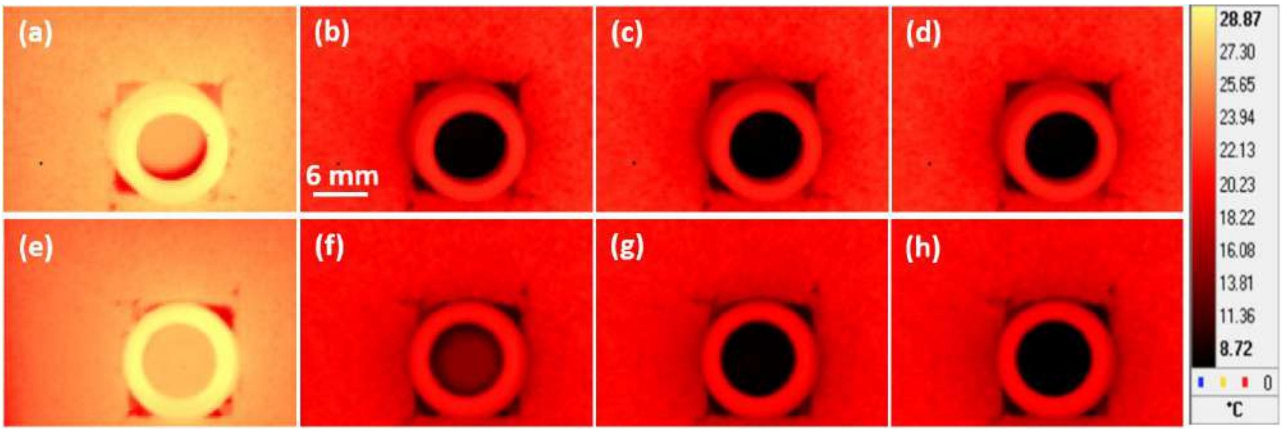

Figure 3.12 (a-d) Typical infrared images during cooling of water at t = 0, 500, 1000 and 1500 s, respectively. (e-h) Typical infrared images during the freezing of the PCM, without any nano-inclusions, at t = 0, 500, 1000 and 1500 s, respectively. The pseudo colour-coded temperature scale is also shown along with the images.

Figure 3.13 shows the variation of normalized temperature difference [$(T-T_0)/T_0$, where T_0 is the initial temperature] as a function of normalized time (t/t_m, where t_m is the maximum observation time = 2000 s) for water, PCM without any nano-inclusions and PCM loaded with 0.0025 and 0.0075 wt. % of GNP. **Fig. 3.13** shows that water temperature decreased exponentially with time and attained the surrounding temperature very rapidly, whereas the PCM (with and without nano-inclusions) underwent phase transition near the freezing point and hence, surrounding temperature was attained at a much longer time, as compared to water, which is beneficial for practical applications in thermal energy storage and management. The presence of the humps (the regions of the temperature-time curves with negligible slope) in the normalized temperature decay curves indicated the phase transition regions for the PCM (with or without nano-inclusions). The slight variations in the freezing temperatures of the PCM, with or without nano-inclusions, were attributed to the convection losses from the top surface, which was kept exposed to the surrounding to ensure obstructed field of view for thermal mapping.

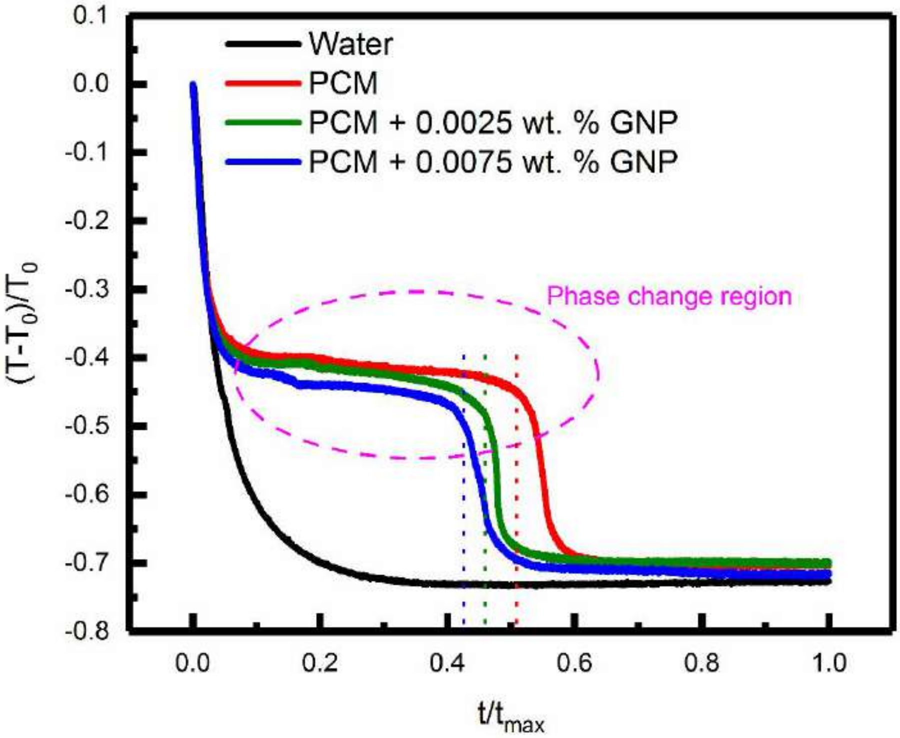

Figure 3.13 Variation of the normalized temperature difference [$(T-T_0)/T_0$, where T_0 is the initial temperature] as a function of normalized time (t/t_m, where t_m is the maximum observation time = 2000 s) for water, PCM without any nano-inclusions and PCM loaded with 0.0025 and 0.0075 wt. % of GNP nano-inclusions. The presence of the phase transition regions for the PCM (with or without nano-inclusions) is also indicated in the figure.

It can be further seen from **Fig. 3.13** that the freezing process was the fastest for the PCM loaded with 0.0075 wt. % of GNP, followed by the PCM loaded with 0.0025 wt. % of GNP and the PCM without any nano-inclusions, in the decreasing order. This was attributed to the higher thermal conductivity of the PCM loaded with GNP. The freezing time was estimated as ~ 1014 (± 1), 921 (± 1) and 846 (± 1) s for the PCM without any nano-inclusions, PCM loaded with 0.0025 and 0.0075 wt. % of GNP, respectively. For the PCM loaded with 0.0075 wt. % of GNP, the gain in freezing time was ~ 16.5 %, that indicated a proportionate increase in charging/discharging rate, which is immensely beneficial for practical applications of the nano-inclusions loaded PCM for thermal energy storage [38]. Faster freezing time was also reported by Harikrishnan et al. [49] for stearic acid-TiO_2 based PCM, where the gain in freezing time was ~ 7.03 % for 0.05 wt. % of TiO_2 loading. Sari and Karaipekli [276] reported ~ 21.4 % gain in freezing time for palmitic acid/expanded graphite based PCM with loading concentration of 20 wt. %. On the other hand, in the present study, a moderately high gain (~ 16.5 %) in freezing time was achieved for extremely low concentration of nano-inclusion loading (0.0075 wt. %), which is beneficial from cost factor point of view for practical applications.

Experimental results clearly show the efficacy of IRT-based studies to remotely map the surface temperature distribution of PCM during liquid-solid phase transition, where freezing time can be obtained in a non-contact way. Additional advantages of IRT-based temperature measurements include simultaneous measurement over a wide area, non-contact and non-invasive temperature mapping, real-time temperature acquisition and pseudo-colour coded images for easy representation and data analyses.

3.6 Summary and conclusions

Thermal conductivity enhancements across the liquid-solid phase transition of hexadecane-based PCM, incorporated with six different nano-inclusions, viz. CBNP, NiNP, CuNP, AgNW, MWCNT and GNP were systematically probed. The phase transition temperature was determined from differential scanning calorimetry studies and the refractive index of the PCM, in the liquid state, was found to increase with decreasing sample temperature due an increase in density. After liquid-solid phase transition, refractive index was found to decrease due to solidification induced cracking of the pellets. Incorporation of nano-inclusions caused an enhancement in thermal conductivity of the PCM, which was more prominent in the solid state. The higher thermal conductivity in the solid state was attributed to the formation of nano-crystalline phase on solidification, consisting of needle like microstructure, which was confirmed from optical phase contrast microscopy. In the solid state, the nano-inclusions were squeezed towards the inter-crystallite grain boundaries, forming a quasi 2D network of percolating structures with high thermal transport efficiency due to the enhancement of phonon mediated heat transfer and near-field radiative heat transfer along the thermal trajectories. For the PCM loaded with CBNP, CuNP, MWCNT and GNP nano-inclusions, thermal conductivity enhancements increased with concentration of the nano-inclusions due to the formation of larger-sized aggregates with improved conduction path. On the other hand, for the PCM loaded with NiNP and AgNW, thermal conductivity decreased at higher concentrations of the nano-inclusions, due to the formation of larger aggregates, which were prone to sedimentation. Among the carbon-based nano-inclusions, the highest enhancement in thermal conductivity was obtained for the PCM loaded with CBNP nano-inclusions, which was attributed to the low fractal dimensions and volume filling capacity of CBNP aggregates with efficient phonon coupling. In the case of metallic nano-inclusions, the highest thermal conductivity enhancement was obtained for the PCM loaded with AgNW nano-inclusions, which was attributed to the large aspect ratio of AgNW. Experimental findings indicated that surface functionalization of the GNP nano-inclusions with oleic acid resulted in better thermal stability of the nano-inclusion loaded PCM, without significant reduction in thermal conductivity, which is beneficial for practical applications. The carboxylic group of oleic acid was bound to the nano-inclusions, whereas, the long aliphatic chain was extended into the non-polar matrix of hexadecane (PCM), thereby providing additional steric stability, that prevented formation of large and unstable aggregates, at higher loading concentration or after repeated thermal cycling, which was also confirmed from optical phase contrast microscopy images. Increased interfacial thermal resistance, for the surface functionalized nano-inclusions, was also studied theoretically and the theoretical and experimental results were found to be in good agreement. Infrared thermography-based experiments were carried out to monitor the sample temperature during phase transition, in a non-contact way and freezing time gain for the nano-inclusion loaded PCM was quantified remotely using infrared thermography. This study clearly shows the significant role of aggregation and volume filling networks on thermal conductivity enhancement and thermal stability of nano-inclusion loaded hexadecane. The findings from the present study will be beneficial for tailoring the properties of nano-inclusion loaded hexadecane-based PCM for thermal energy storage and reversible thermal switching applications at room temperature.

Chapter 4

Tuning of phase transition temperature of phenol and palmitic acid-based phase change materials and thermal conductivity enhancement upon loading with nano-inclusions

Chapter 4

Tuning of phase transition temperature of phenol and palmitic acid-based phase change materials and thermal conductivity enhancement upon loading with nano-inclusions

4.1 Introduction

Thermoregulation of buildings, thermal management of batteries, low temperature solar-thermal applications require phase change materials with phase transition temperatures near ambient temperatures [80]. Solid-liquid phase transition temperatures of phenol and palmitic acids are ~ 40 and 60-63 ^{0}C [215, 217], respectively, which limits their usage in domestic applications. Hence, the phase transition temperature of phenol and palmitic acid based PCMs were varied by adding required amount of water and di-methyl formamide, respectively. Thermo-physical characterization was carried out on the composite PCMs with tunable phase transition temperatures and thermal conductivity enhancements, upon loading with varied concentrations of different types of nano-inclusions, were systematically probed.

4.2 Tuning phase transition temperature of phenol based PCMs and nano-inclusion assisted thermal conductivity enhancement

Phenolic resin/poly-ethylene oxide (PEO)-poly propylene oxide (PPO) block copolymer based solid-solid phase transition type PCM has been studied earlier. However, no other previous studies existed on PCM (solid-liquid phase transition type) consisting of phenol-water system. Though slightly toxic and corrosive, phenol-water system is one of the most widely studied classical two-phase system with in-depth knowledge on various physical properties, viz., solidification temperature, vapour pressure, latent heat, refractive index, density and solubility [447, 448]. Moreover, other factors like long term stability, lack of chemical reactions between the component, thermal repeatability and possibility of easy scaling of phase transition temperature by varying the phenol to water ratio were also considered for selecting the phenol-water system as PCM in the present study. Though nano-inclusion assisted thermal conductivity enhancement of phase change materials is well studied, the effects of agglomeration kinetics and interfacial layer formation on thermal conductivity enhancement are not well understood [50, 231, 342, 449], which also serves as objectives of the present work.

4.2.1 Tuning of phase transition temperature of the PCM

Under ideal solution theory, Raoult’s law indicates that the vapour pressure of a solvent is reduced by the presence of a solute and is proportional to the mole fraction [450]. Hence, freezing point of the phenol-water system was tuned by adjusting the phenol-water ratio. Four different concentrations of phenol-water system were prepared by mixing 0.74, 1.56, 2.55 and 3.25 wt. % of water (neglecting the impurity water content). Phenol is hygroscopic in nature and the purity of the phenol, used in the present study, was 99.5 % with water content < 0.5%, as indicated by the supplier. However, moisture ingress in phenol based PCM is expected during practical applications and hence, was neglected in the present study. The melting point of pure phenol (99.5 % purity) was estimated from differential scanning calorimetry studies under argon atmosphere with a heating rate of 5 ^{0}C/minute. The freezing points of the phenol-water systems with varied water concentrations were also approximately estimated using an automatic refractometer.

4.2.2 Preparation of nano-inclusion loaded PCM

Metal oxide nanoparticles of various concentrations were dispersed in the phenol-water system with 1.56 wt. % of water concentration (PCM) using a horn sonicator (Sonic Vibra-cell) operating at 30% power for approximately 1800 s. Four different concentrations of α-Al_2O_3 and TiO_2 were used, viz., 1, 2, 3 and 4 wt. %, whereas, in the case of hydrophilic SiO_2, three different concentrations were used, viz., 1, 2 and 3 wt. %. Additionally, CBNP was added (at concentrations of 0.02 and 0.04 wt. %) to the PCM loaded with 4 wt. % of Al_2O_3 and 3 wt. % of TiO_2 and SiO_2, respectively. For comparing the effect of hydrophobic interactions, PCM loaded with 1 and 3 wt. % of HP-SiO_2 were also prepared using the horn sonication technique. To study the effect of concentration of nano-inclusions on agglomeration and subsequent percolation pathways of heat transfer, atomic force microscopy (AFM, Ntegra Prima, NT-MDT, Russia) studies were carried out on phenol samples loaded with 1 and 4 wt. % α-Al_2O_3 nanoparticles. Thermal conductivity measurements were carried out using the KD2 probe, as discussed in the 2nd chapter.

4.2.3 FTIR analysis of phenol-water system

Phenol molecules (P) can form hydrogen bonded clusters, similar to water molecules (W), leading to the formation of complex P_iW_j (i >1) clusters. Ebata et al. [451] reported possible geometries for P_2, P_3 and PW_n (n = 1-5) clusters, using vibrational spectroscopy of phenol and phenol-water mixtures. Using ab-initio and density functional theory based calculations, Parthasarathi et al. [452] evaluated the stabilization energies of the P_iW_j clusters and it was reported that P_3W clusters were the most stable, with cluster stabilization energy of 23.6 kcal/mol (calculated using Hartee-Fock method and corrected for basis set superposition error). Moreover, P_3W clusters were found to have 4 numbers of primary hydrogen bonds (OH…O), with typical bond lengths of 2.8-2.9 Å and 2 numbers of comparatively weaker secondary hydrogen bonds (CH…O), with typical bond lengths of 3.6-4.2 Å [452]. Hence, P_3W type clusters (**Fig. 4.1a** shows a typical schematic) were assumed to exist in the phenol-water mixture, used in the present study. **Fig. 4.1b** shows the FTIR spectra of the phenol-water mixture (water concentration = 1.56 wt. %) loaded with α-Al_2O_3, TiO_2 and SiO_2 nano-inclusions, where the major absorption bands are indexed. For comparison, the FTIR spectra of the phenol-water mixture is also shown in **Fig. 4.1b**. The strong absorption band, observed at 2358 cm^{-1}, was attributed to the stretching vibrations of C=O from atmospheric CO_2 [444]. The multiple bands between 1470-1595 cm^{-1} were due to the aromatic C=C bending and the two relatively feeble absorption bands, at 3037 and 3068 cm^{-1}, were attributed to the aromatic C-H stretching [453]. The sharp absorption band, observed at 1218 cm^{-1}, corresponded to the C-O stretching of phenol [453]. Additionally, an absorption band at 1360 cm^{-1} was observed due to the in-plane O-H bending [453]. The broad peak at 3330 cm^{-1} was attributed to the hydrogen bonded O-H stretching vibrations of phenol [453, 454]. Intermolecular hydrogen bonding leads to the weakening of the O-H bond resulting in lower energy and a free O-H absorption band is, in general, observed at higher energy (left of the hydrogen bonded O-H band) for dilute solutions. Nevertheless, the free O-H absorption band was not observed in the present study, as the FTIR spectrum was recorded within 3500-900 cm^{-1}. The O-H scissor mode absorption band (around ~ 1630 cm^{-1} [453]) of water was not observed in the present study, possibly due to lower concentration of water (1.56 wt. %) and overlapping with the aromatic C=C absorption bands. It can be seen from **Fig. 4.1b** that the major absorption bands were not shifted for phenol-water mixture loaded with various nano-inclusions, which clearly shows the lack of chemical reactions between the functional groups of phenol and the nano-inclusions. FTIR spectroscopy based similar analyses were also used by several other groups to confirm the absence of chemical reactions between the host matrices and nano-inclusions [214, 235, 455].

4.2.4 Phenol-water based PCMs with tunable phase transition temperature

The intersection of the vapour pressure curves of a solution and the pure solvent is the freezing point of the solution at a fixed concentration. Addition of solute changes the vapour pressure of the solution leading to a depression of the freezing point. In the present study, freezing point of phenol-water system was tuned by adding required amount of water in phenol. **Fig. 4.2a** shows the heat flow curve, obtained from DSC, for the pure phenol (99.5 % purity), used in the present study.

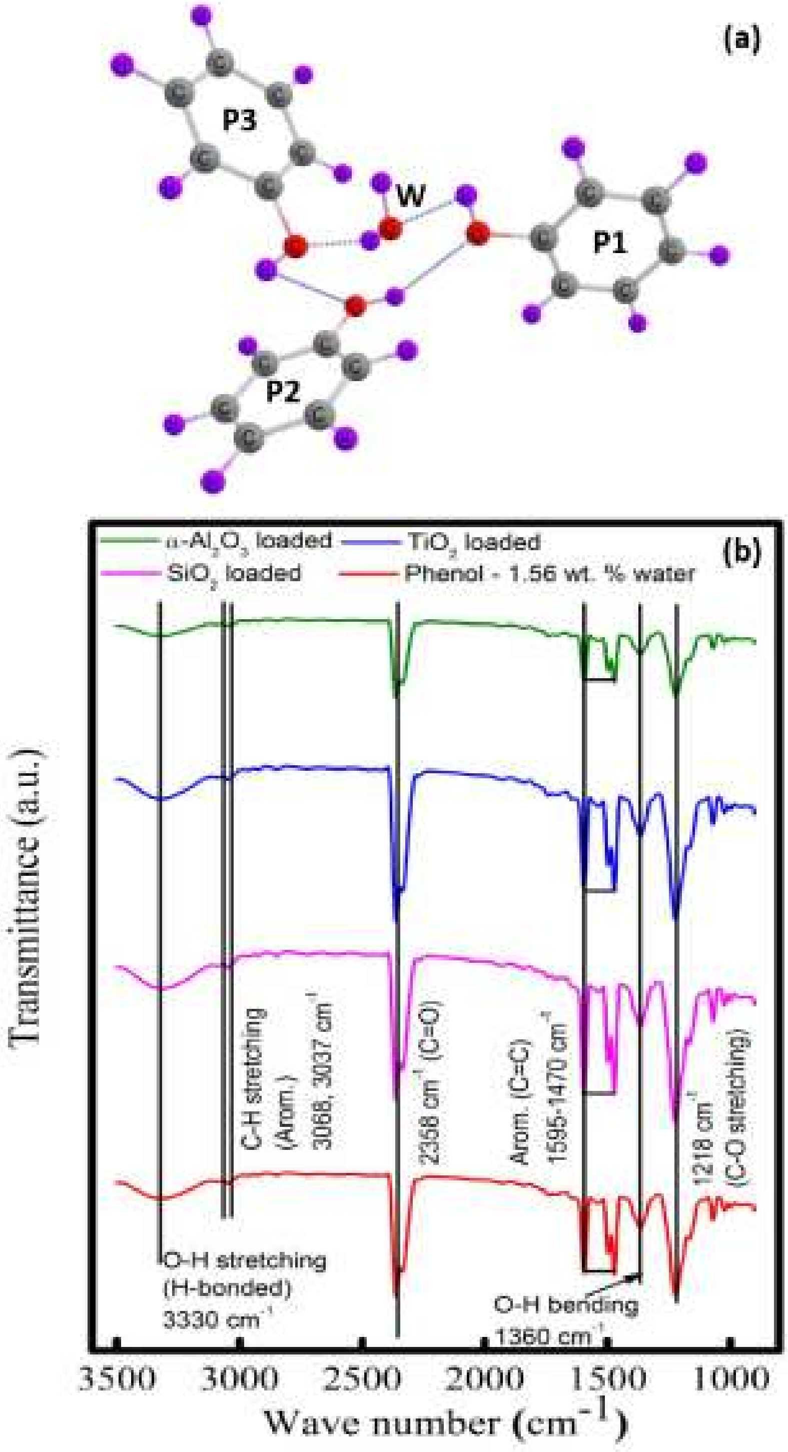

Figure 4.1 (a) Schematic structure of phenol-water system consisting of 3 phenol (P1, P2 and P3) and one water (W) molecules. (b) FTIR spectra of the phenol-water mixture (water concentration = 1.56 wt. %) loaded with α-Al_2O_3, TiO_2 and SiO_2 nanoparticles, where the major absorption bands are indexed. For comparison, the FTIR spectra of the phenol-water mixture is also shown in the figure.

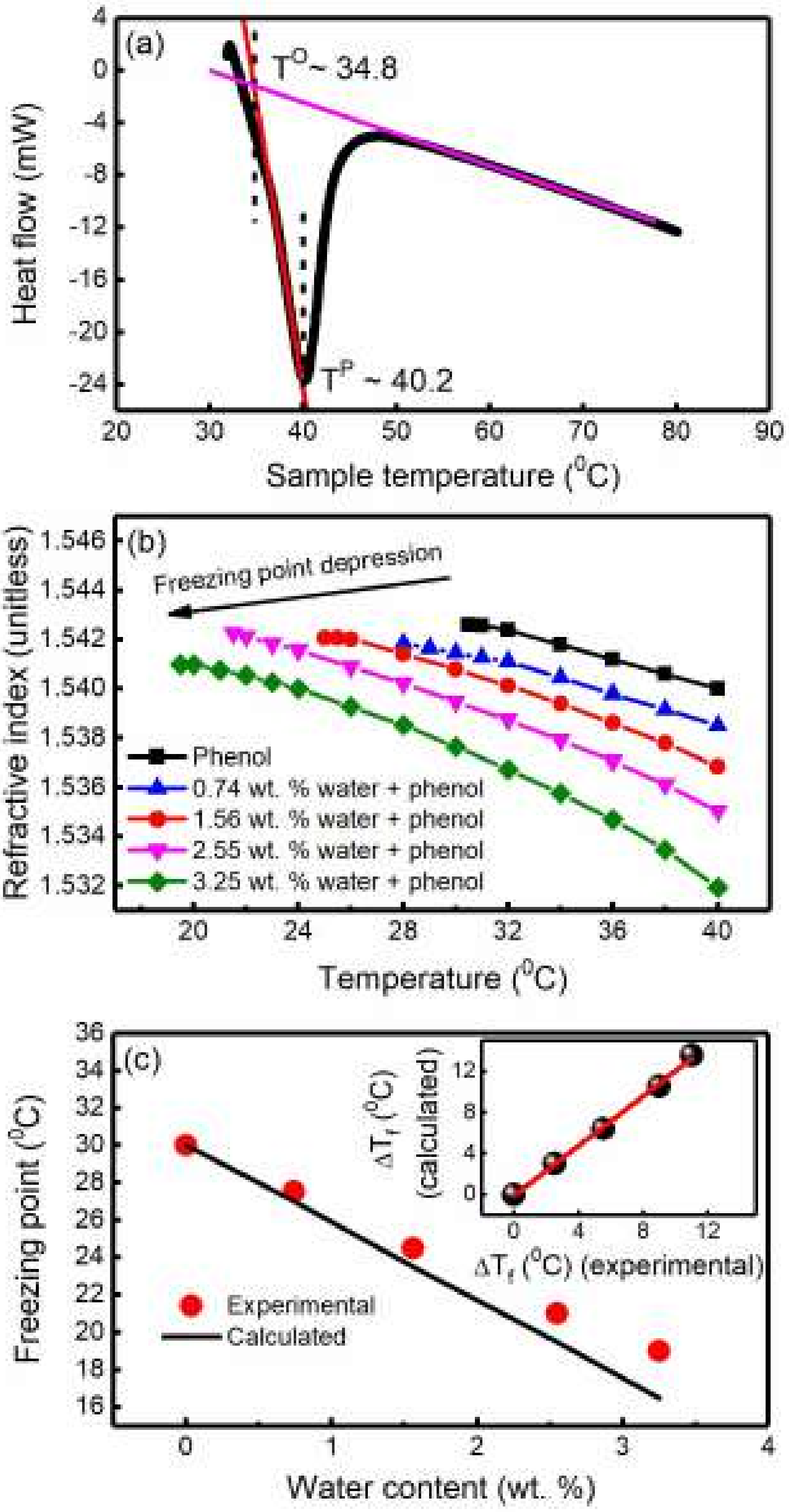

Figure 4.2 (a) Heat flow curve for pure phenol (99.5 % purity), obtained from DSC studies. (b) Variation of refractive index as a function of temperature for phenol and four different phenol-water mixtures with 0.74, 1.56, 2.55 and 3.25 wt. % water. The depression in freezing point is shown by the arrow. (c) Experimentally measured and theoretically calculated values of the freezing point of phenol and phenol-water mixture containing 0.74, 1.56, 2.55 and 3.25 wt. % of water. (Inset) Variation of theoretically calculated values of freezing point depression (ΔT_f) as a function of experimentally measured ΔT_f.

It can be clearly seen from **Fig. 4.2a** that the peak phase transition temperature (T^P) was ~ 40.2 ± 0.5 ^{0}C (313.4 ± 0.5 K), which was found to be in good agreement with the values reported in the literature, viz. ~ 40.9 ^{0}C by Cheng [456] and You et al. [457], ~ 40 ^{0}C by Klauck et al. [397], 40.7 ^{0}C by Jones [458], etc. On the other hand, the melting process started earlier and the melting point was estimated as ~ 34.8 ± 0.5 ^{0}C from the extrapolated onset temperature (T^O), which was found to be lower than the values reported in literature and was attributed to the presence of water as impurity (< 0.5 wt. %).

Figure 4.2b shows the variation of refractive index as a function of temperature for phenol and four different phenol-water mixtures with 0.74, 1.56, 2.55 and 3.25 wt. % of water. It can be seen from **Fig. 4.2b** that refractive indices increased monotonically with decreasing temperature up to the freezing point for all the cases and beyond that refractive indices sharply decreased due to the cracking of the solidified pellets, as subsequently discussed. As light is being absorbed and re-emitted in a medium, the speed of light in a medium is lower than that in the vacuum. With decreasing temperature, density of the liquid increases leading to a lowering of the speed of light, which resulted in an increased refractive index of the liquids with decreasing temperature as shown in **Fig. 4.2b**. In the present study, the effect of density on variation of refractive indices with temperature was only considered and the effect of variation of effective polarizability with temperature of the liquids was neglected [459]. The effective refractive index of a binary liquid mixture can be expressed by the Eykman's model which is expressed by the following equation [460, 461].

$$\frac{n_D^2 - 1}{n_D + 0.4} = \left(\frac{n_{D1}^2 - 1}{n_{D1} + 0.4}\right)\phi_1 + \left(\frac{n_{D2}^2 - 1}{n_{D2} + 0.4}\right)\phi_2 \qquad (4.1)$$

Here, n_D, n_{D1}, n_{D2}, ϕ_1 and ϕ_2 indicate refractive indices of the binary mixture, first component, second component and volume fractions of first and second components, respectively. **Table 4.1** shows the experimental as well as theoretically calculated values of the refractive index of the phenol-water system as a function of water concentration at 40 ^{0}C. It can be seen from

Table 4.1 that the experimentally obtained values were in good agreement with the calculated values. The measured refractive index of phenol at 40 ^{0}C (1.54001 ± 0.00004) was in agreement with the refractive index values of 1.5408 reported by Klauck et al. [397].

Table 4.1 Experimental and theoretical refractive indices of phenol and phenol-water systems measured at a fixed wavelength and temperature of 589.3 nm and 40 ^{0}C, respectively.

Water concentration (wt. %)	Refractive index (experimental) (± 0.00004)	Refractive index (theoretical)
0	1.54001	1.540
0.74	1.53850	1.538
1.56	1.53684	1.537
2.55	1.53504	1.535
3.25	1.53193	1.533

It can be seen from **Fig. 4.2b** that the freezing point decreased with increasing water concentration and the freezing point for pure phenol (99.5 % purity) was estimated as ~ 30 ^{0}C from refractive index measurement which was ~ 16% lower than the value estimated from DSC (~ 34.8 ± 0.5 ^{0}C). The discrepancy of ~ 4.8 ^{0}C was attributed to the refractive index-based measurement procedure. The estimation of freezing point from refractive index-based measurement relies on the fact, that the pellet shaped sample cracks (as subsequently shown in **Fig. 4.3c**) due to solidification induced stress, leading to the opening up of free trajectories for light propagation, resulting in a lowering of the refractive index in the solid state. It must be noted in this regard, that appearance of such cracks occurs after complete or partial crystallization (as solidification induced stress is essential for formation and propagation of such cracks) and not exactly at the phase transition temperature. Hence, it is expected that the melting points determined from refractive index measurements will be lower, as compared to the data obtained from calorimetry studies. Such discrepancies are further enhanced for liquids with strong anisotropic growth kinetics leading to the formation of needle like microstructure during freezing (like phenol and hexadecane [237, 387]). Existence of such needle like microstructure in phenol is subsequently shown in **Fig. 4.4d**. A similar discrepancy of ~ 7 ^{0}C in the melting point of nitro-phenol was reported by Frediani [462], using refractive index-based and standard calorimetry techniques. From refractive index measurements the freezing points of phenol-water mixture with water concentration of 0.74, 1.56, 2.55 and 3.25 wt. % were found to be 27.5, 24.5, 21.0 and 19.0 ^{0}C, respectively. Nevertheless, apart from a negative offset of ~ 16 %, the freezing points measured from refractive index-based technique were found to be consistent and hence, were used for further studies.

As the change in vapour pressure of the solution is linearly proportional to the mole fraction of the solute, freezing point depression increased with increasing water concentration which can be expressed by the following equation [463].

$$\Delta T_f = T_{fr}(solvent) - T_{fr}(solution) = -K_f \times m_l \times c_1 \tag{4.2}$$

Here, ΔT_f, T_{fr}, K_f, m_l and c_1 indicate freezing point depression, freezing point of the solvent and solution, freezing point depression constant or cryoscopic constant, molality and Van't Hoff factor, respectively. In the present study, considering the value of the cryoscopic constant for phenol as 7.27 [464] and Van't Hoff factor for water as 1, the freezing point depression for different phenol-water mixture was theoretically calculated and **Fig. 4.2c** shows the experimental and theoretically calculated values of the freezing point of phenol and phenol-water mixture containing 0.74, 1.56, 2.55 and 3.25 wt. % of water. For this study, the impurity water content was neglected and the freezing points obtained from refractive index measurements were used. The **inset of Fig. 4.2c** shows the variation of theoretically calculated ΔT_f as a function of experimentally measured ΔT_f, where it can be seen that the theoretically calculated values were in good agreement with the experimental values and the data was fitted with a linear regression analysis. The adjusted R^2 of the linear regression was found to be ~ 0.99 indicating good accuracy of the theoretical calculations. From refractive index measurements, the phase transition temperature of phenol-water mixture with 1.56 wt. % of water was found to be ~ 24.5 ^{0}C and considering a negative offset of ~ 16 %, the true phase transition region was expected to be within ~ 20.6-24.5 ^{0}C, which is ideal for practical applications towards room temperature thermal energy storage and thermal switching and hence, this composition was chosen as PCM in the present study.

Figure 4.3a shows the variation of refractive indices as a function of temperature, for pure phenol (99.5 % purity) and phenol-water mixture with 1.56 wt. % of water in the liquid and solid states, during backward (liquid to solid by decreasing the sample temperature) and forward (solid to liquid by increasing the sample temperature) thermal cycles. It can be seen that the freezing and melting points were ~ 30 and 32 ^{0}C; 24.5 and 30 ^{0}C for phenol and phenol-water mixture during backward and forward thermal cycles, respectively. The shift in freezing point during consecutive thermal cycles is common for such systems and various other groups have reported such thermal hysteresis for different PCMs, using differential scanning calorimetry measurements [214, 233] and molecular dynamics simulations [429]. The difference between the freezing and melting point (i.e. the supercooling degree) was found to be ~ 2 and 5.5 ^{0}C for phenol and phenol-water system with 1.56 wt. % of water, respectively, which were significantly lower than the values obtained for paraffin wax loaded with various carbon nano-fillers (~ 8.5-7.3 ^{0}C) [214]. A reduced supercooling degree is beneficial for improving the thermal performance of the PCM during practical applications [465]. It can be further seen from **Fig. 4.3a** that the refractive indices decreased sharply after solidification, which was attributed to the cracking of the solidified pellets. **Figs. 4.3b & c** show the typical photographs of the liquid and solid phenol samples, used for refractive index measurements and the presence of cracks were clearly discernible in the solidified pellet (**Fig.**

4.3c). The cracking of the solidified pellets was attributed to the development of needle like microstructure, during freezing, leading to the formation of solidification induced stress field within the sample. **Figs. 4.3d & e** show the typical photographs of the liquid and solidified phenol samples. Typical photographs of the liquid and solidified phenol-water system with 1.56 wt. % of water are shown in **Figs. 4.3f & g**.

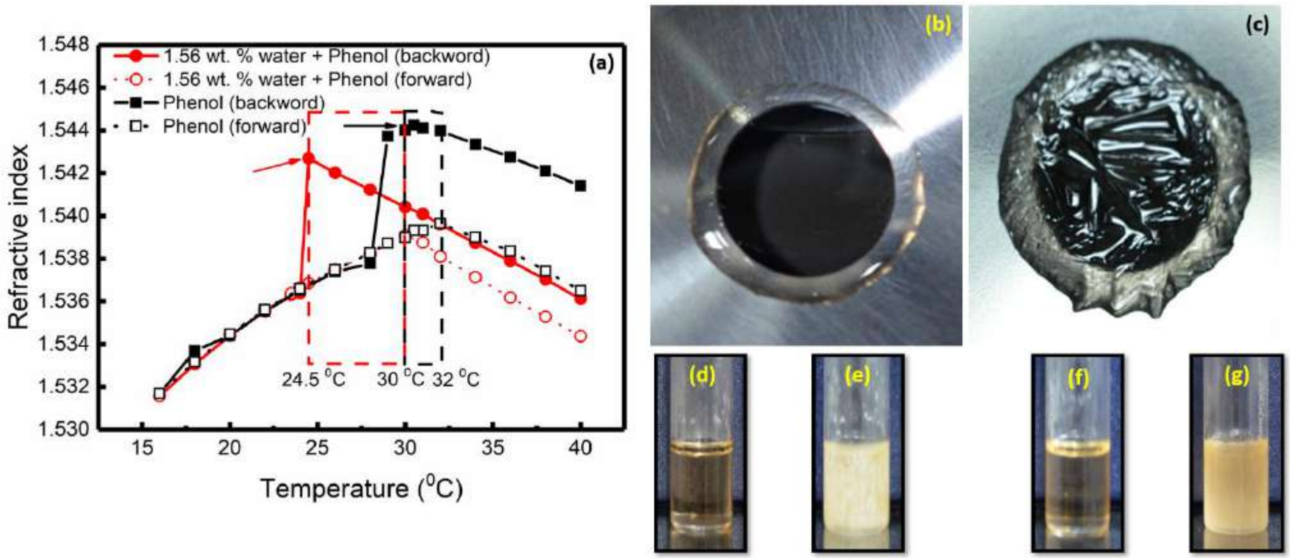

Figure 4.3 (a) Variation of refractive indices as a function of temperature for phenol and phenol-water mixture with 1.56 wt. % water concentration in the liquid and solid states, during backward (liquid to solid: decrease in sample temperature) and forward (solid to liquid: increase in sample temperature) thermal cycles. The melting and freezing points during forward and backward cycles are indicated in the figure. Typical photographs of the phenol samples used for refractive index measurement in the (b) liquid and (c) solid state. Typical photographs of the (d) liquid and (e) solid phenol samples, used for thermal conductivity measurements. Typical photographs of the (f) liquid and (g) solid phenol-water (1.56 wt. %) samples, used for thermal conductivity measurements.

4.2.5 Nano-inclusion assisted enhancement in thermal conductivity

Figure 4.4a shows the variation of k/k_f, as a function of water concentration, in the solid state for the phenol-water system. Here, k and k_f indicate the thermal conductivity of the phenol-water system and that of phenol (0.195 W/mK) in the solid state (i.e. well below the corresponding freezing point), respectively. At T = 15 ^{0}C, the phenol-water mixture appeared solid, macroscopically, and hence, for T< 15 ^{0}C, the system was assumed to be in solid state for all practical purposes, without considering the existence of biphasic mixture of liquid water entrapped in crystalline phenol. It can be seen from **Fig. 4.4a** that k/k_f increased with water concentration, which was attributed to the higher thermal conductivity of water. The value of k/k_f, for phenol-water system with 1.56 wt. % of water, was found to be ~ 1.03 (± 0.05), which indicated ~ 3 % enhancement in thermal conductivity compared to phenol. **Fig. 4.4b** shows the variation of k/k_f during repeatability test (i.e. consecutive thermal cycling) of the phenol-water system with 1.56 wt. % of water. Here, k_f indicate the thermal conductivity of the phenol-water system in the liquid state (= 0.170 W/mK). For establishing repeatability, several measurements of thermal conductivity were performed at a regular time interval in the liquid state (i.e. well above the freezing point) and thereafter, the sample was allowed to freeze below its freezing point and thermal conductivity measurements were then repeated in the solid state (T = 15 ^{0}C). It can be clearly seen from **Fig. 4.4b** that the freezing and melting cycles were perfectly reversible for the phenol-water system, even after four melting/freezing cycles. This indicated the good thermal stability of the phenol-water system, which is beneficial for practical applications. The k/k_f value was ~ 1 in the liquid state and increased up to ~ 1.18 (± 0.06) in the solid state, indicating ~ 18 % enhancement in the thermal conductivity of the phenol-water system in the solid state. This value is slightly higher than the reported value of 15 % enhancement across liquid-solid transition of phenol [466], which was attributed to the presence of water with higher thermal conductivity (~ 0.6 W/mK at 30 ^{0}C). The increase in thermal conductivity in the solid state was due to the formation of closely packed nanocrystalline structure, during freezing, with regular molecular arrangement. Similar increase in thermal conductivity across liquid-solid phase transition has been reported by Sutherland et al. [467] and Powell et al. [468] for n-octadecane. Using molecular dynamics based simulation studies, Babei et al. [429] confirmed the formation of a nanocrystalline structure, during solidification of PCM, that caused an enhancement in thermal conductivity in the solid state, as compared to the liquid state, which was attributed to the lack of polarized thermal waves (phonons) in the liquid state. Crystallization and formation of needle like microstructure in solidified phenol has been confirmed in the present study using optical phase contrast microscopy. **Figs. 4.4c & d** show the phase contrast optical microscopy images for phenol in the liquid and solid states, respectively. The anisotropic growth and formation of needle like microstructure in the solid state were clearly discernible from **Fig. 4.4d**. Anisotropic effects in phenol, just before solidification, has been earlier reported by Venart and Prasad [466] using thermal conductivity measurements. Strong anisotropic growth kinetics and formation of needle like microstructure has also been reported for hexadecane [387].

Figure 4.5 shows the variation of k/k_f and the percentage (%) enhancement in thermal conductivity as a function of temperature for different concentration of α-Al_2O_3 loading in phenol-water system (PCM) with 1.56 wt. % of water. The effect of CBNP addition (0.02 and 0.04 wt. %) on k/k_f is also shown in **Fig. 4.5**. It can be clearly seen from **Fig. 4.5** that the variation of k/k_f with temperature can be divided into three distinct regions. For $T > 25\ ^0C$, the PCM was in the liquid state and this region was categorized as region-I. The region-II corresponded to the phase transition region, starting from 24. 5 ^0C to temperature just below the freezing point. Region-III, on the other hand, signified temperature below the freezing point ($T < 15\ ^0C$) where the PCM was macroscopically in the solid state. In the liquid state, the thermal conductivity enhancements were ~ 2.9, 5, 5.8 and 7.0 % for 1, 2, 3 and 4 wt. % of α-Al_2O_3 loading.

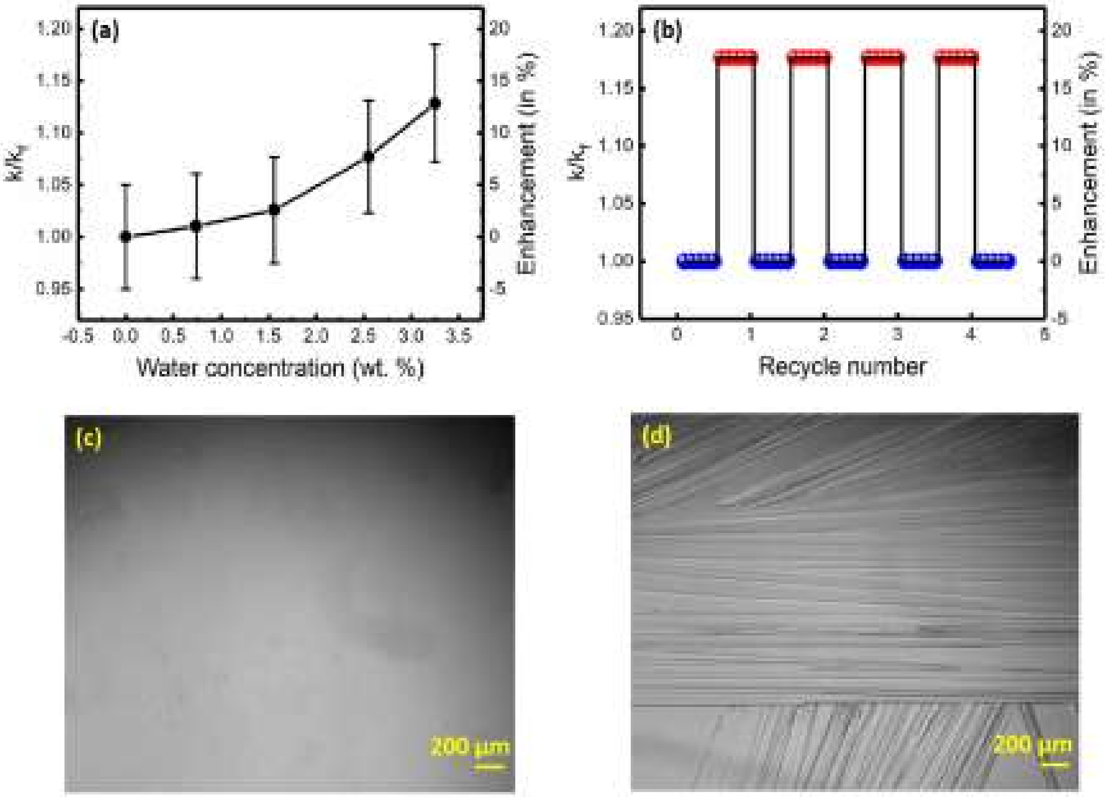

Figure 4.4 (a) Variation of k/k$_f$ as a function of water concentration in the solid state for the phenol-water system. Here, k and k$_f$ indicate the thermal conductivity of the phenol-water system and that of phenol in the solid state, respectively. (b) Variation of k/k$_f$ during consecutive thermal cycling of the phenol-water system with 1.56 wt. % water concentration. Here, k$_f$ indicate the thermal conductivity of the phenol-water system in the liquid state. Optical phase contrast microscopy images for phenol in the (c) liquid and (d) solid states. The presence of needle like microstructure in the solid state can be clearly seen from (d).

Addition of CBNP caused a slight increase (~ 7.6 %) in the thermal conductivity enhancement in the liquid state. The **inset of Fig. 4.5** shows the enlarged view of the variation of k/k$_f$ as a function of temperature in the liquid state. In the phase transition region (region-II) the thermal conductivity enhancements were ~ 68.8, 75.3, 82.3 and 93.5 % for 1, 2, 3 and 4 wt. % of α-Al_2O_3 loading. With further decrease of temperature well below the freezing point (region-III), the thermal conductivity values were found to decrease and attained a constant value below T = 15 ^{0}C for all concentration of α-Al_2O_3. The enhancement in thermal conductivity were ~ 25.3, 31.2, 34.1 and 41.2 % for 1, 2, 3 and 4 wt. % of α-Al_2O_3

loading in the solid state. Addition of 0.02 and 0.04 wt. % of CBNP to the PCM loaded with 4 wt. % of α-Al_2O_3 resulted in further enhancement of thermal conductivity, viz. 44.7 and 45.9 %, respectively, in the solid state. The thermal conductivity enhancement values, obtained in the present study were substantially higher than the earlier reported value of ~ 31 % enhancement (in solid state) for nano-Al_2O_3 (10 wt. %) loaded paraffin [469].

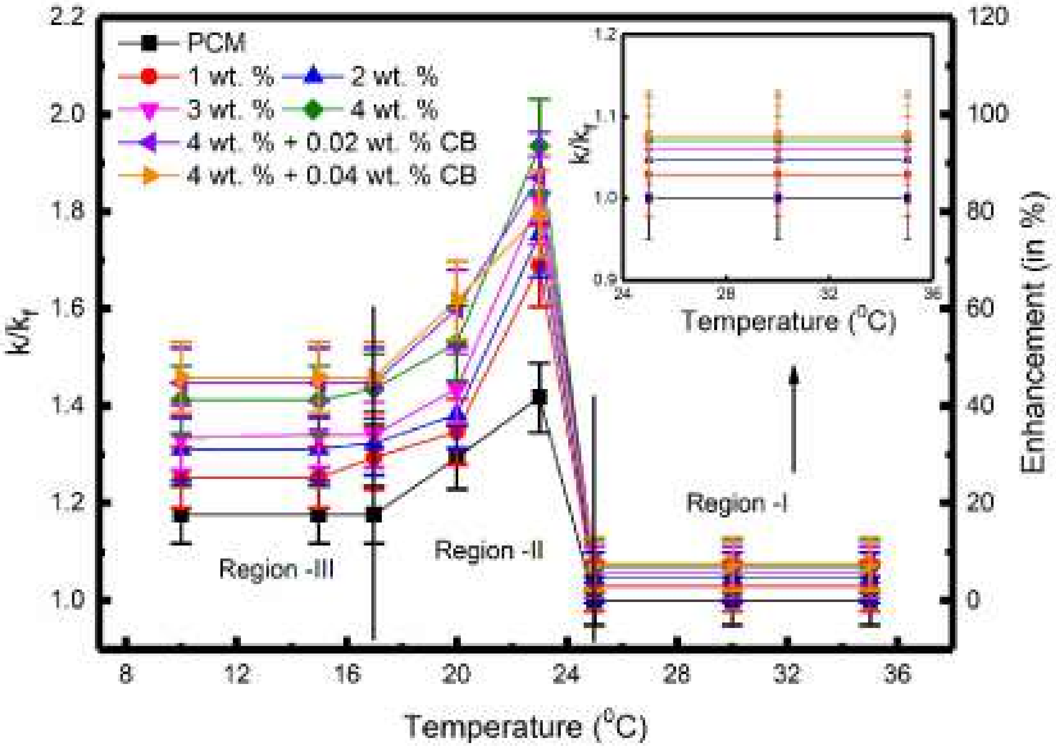

Figure 4.5 Variation of k/k_f and percentage (%) enhancement in thermal conductivity as a function of temperature for different concentrations of α-Al_2O_3 loading in phenol-water system with 1.56 wt. % water concentration (PCM). Here k_f indicates the thermal conductivity (= 0.170 W/mK) of the PCM in liquid state. The effect of CBNP addition (0.02 and 0.04 wt. %) on k/k_f is also shown. (Inset) Enlarged view of the variation of k/k_f as a function of temperature in the liquid state.

The increase in thermal conductivity in the solid state was due to the formation of crystalline structure of the PCM after freezing [231, 387, 468]. The observed higher thermal conductivity in the phase transition region was attributed to the effective heat transfer through the continuous networking structures formed during phase transition due to strong anisotropic growth kinetics of phenol-water system [231, 466]. Formation of needle like microstructure during freezing (as confirmed from phase contrast optical microscopy images in **Fig. 4.4d**) resulted in an improved contact between the dispersed nano-inclusions [387]. It has been reported that, in crystal forming liquids loaded with nano-inclusions, the nanoparticles are squeezed towards the grain boundaries during freezing [387, 470, 471]. The internal stress generated during freezing increased the contact area between the nano-inclusions, thereby reducing the thermal barrier resistance leading to an enhancement in thermal conductivity through a quasi-2D network of percolating structures [234, 237, 387]. Studies show that slower cooling rate leads to the formation of longer and thicker needle like microstructure with larger enhancement in thermal conductivity [395]. The scenario is schematically shown in **Fig. 4.6**, where the presence of percolating structures (i.e. aggregates of nano-inclusions) is shown along the grain boundaries. It is hypothesized that in the solid state (region-III), well below the freezing point, thermal conductivity enhancement was lower, as compared to the phase transition region (region-II) due to changes in the microstructure, where longer needles were broken down to shorter needles, probably due to solidification induced stress [387].

Figure 4.7 shows the variation of k/k_f and the percentage (%) enhancement in thermal conductivity as a function of temperature for the PCM loaded with different concentration of SiO_2. Here the concentration of SiO_2 was limited to 3 wt. % to avoid gel formation. The effect of CBNP addition (0.02 and 0.04 wt. %) on k/k_f and % enhancement in thermal conductivity is also shown in **Fig. 4.7.** For comparison, thermal conductivity variation of the PCM (without any nano-inclusions) is also shown in **Fig. 4.7**. It can be clearly seen from **Fig. 4.7** that the general trend of k/k_f as a function of temperature remained similar to that obtained for the PCM loaded with various concentrations of α-Al_2O_3. The **inset of Fig. 4.7** shows the enlarged view of the variation of k/k_f in the liquid state.

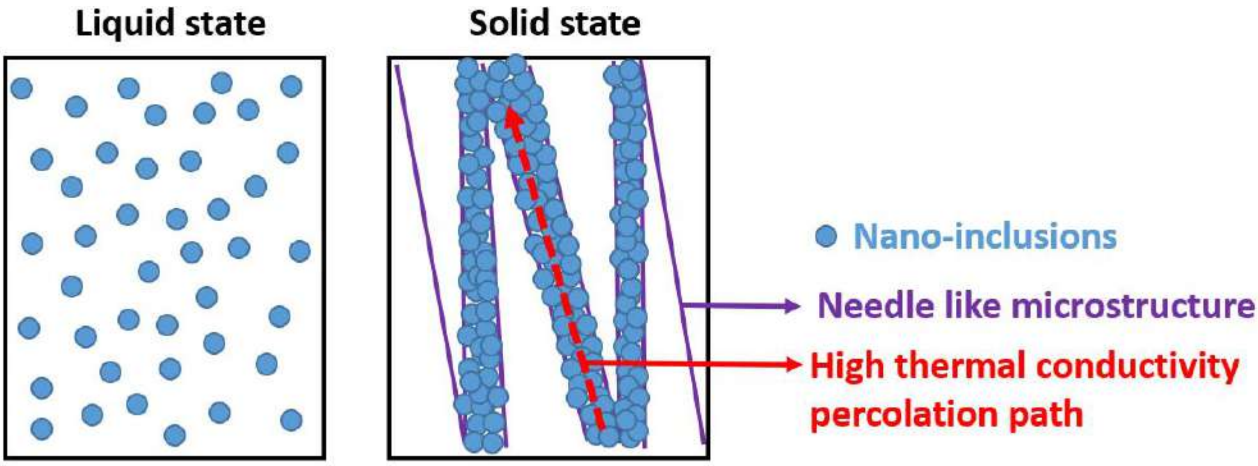

Figure 4.6 Schematic diagram showing the aggregation induced thermal conductivity enhancement of nano-inclusion loaded PCM. During liquid-solid phase transitions, the nano-inclusions are squeezed towards the grain boundary forming a network of percolating structures which enhances the thermal conductivity. The percolation path and needle like microstructures are indicated suitably in the figure.

In region-I, the enhancement in thermal conductivity were ~ 1.8, 4.1 and 2.9 % for 1, 2 and 3 wt. % of SiO_2 loading, respectively. Addition of 0.02 and 0.04 wt. % of CBNP, in the liquid state, caused a slight increase in thermal conductivity resulting in an enhancement of ~ 3.5 and 4.1 %, respectively. It must be noted in this regard that for SiO_2 nano-inclusions, increase in concentration did not cause a monotonic rise in thermal conductivity in the liquid state, which was in contrast to the observations made for α-Al_2O_3 (**Fig. 4.5**). In the phase transition region (region-II), the thermal conductivity enhancements were ~ 50.5, 58.8 and 68.2 % for 1, 2 and 3 wt. % of SiO_2 loading. In region-III, well below the freezing point, the thermal conductivity values were found to decrease and attained a constant value below T = 15 ^{0}C for all concentration of SiO_2. In this region, the enhancement in thermal conductivity were ~ 25.2, 30.0 and 38.2 % for 1, 2 and 3 wt. % of SiO_2 loading. In the solid state, enhancement in thermal conductivity increased with increasing concentration of the nano-inclusions which was found to be in agreement with the earlier observations made for PCM loaded with different concentrations of α-Al_2O_3. Addition of 0.02 and 0.04 wt. % of CBNP to the PCM loaded with 3 wt. % of SiO_2 caused the thermal conductivity to increase further resulting in ~ 41.7 and 45.3 % enhancement in thermal conductivity, respectively, in the solid state.

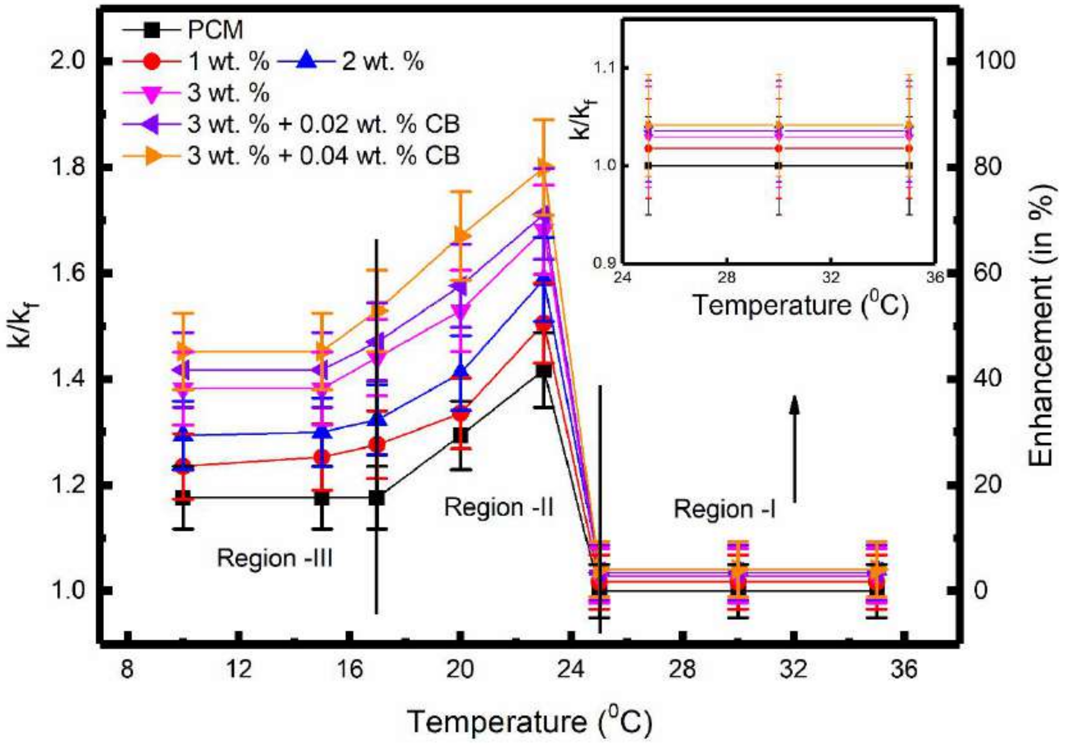

Figure 4.7 Variation of k/k_f and percentage (%) enhancement in thermal conductivity as a function of temperature for different concentrations of SiO_2 loading in phenol-water system with 1.56 wt. % water concentration (PCM). The effect of CBNP addition (0.02 and 0.04 wt. %) on k/k_f is also shown. (Inset) Enlarged view of the variation of k/k_f as a function of temperature in the liquid state.

Due to the presence of silanol (Si-OH) groups on its surface, fumed SiO_2 is generally hydrophilic. Hydrophobic silica (HP-SiO_2), on the other hand, has polydimethylsiloxane group (hydrophobic) chemically bonded to its surface. To study the effects of hydrophobic interactions on thermal conductivity enhancement, further experiments were performed on PCM loaded with 1 and 3 wt. % of HP-SiO_2 and the results were compared with those obtained from PCM loaded with hydrophilic silica (SiO_2). **Fig. 4.8** shows the variation of k/k_f

and percentage (%) enhancement in thermal conductivity as a function of temperature for the PCM loaded with 1 and 3 wt. % of HP-SiO_2. For comparison, thermal conductivity variation of the PCM (without any nano-inclusions) is also shown in **Fig. 4.8**. The **inset of Fig. 4.8** shows the enlarged view of the variation of k/k_f in the liquid state.

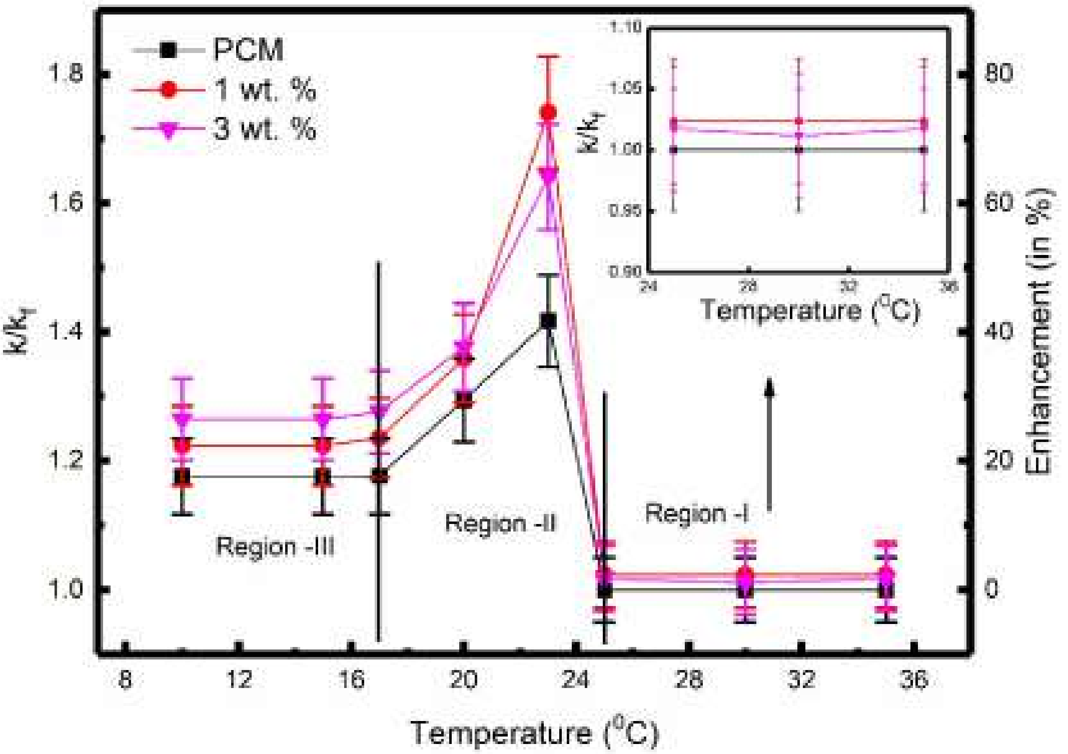

Figure 4.8 Variation of k/k_f and percentage (%) enhancement in thermal conductivity as a function of temperature for two different concentrations (1 and 3 wt. %) of hydrophobic SiO_2 (HP-SiO_2) loading in phenol-water system with 1.56 wt. % water concentration (PCM). (Inset) Enlarged view of the variation of k/k_f as a function of temperature in the liquid state.

In the liquid state, thermal conductivity enhancements were ~ 2.4 and 1.7 % for the PCM loaded with 1 and 3 wt. % of HP-SiO_2, respectively. In the phase transition region (region-II), the thermal conductivity enhancements were ~ 75.6 and 64.7 % for 1 and 3 wt. % of HP-SiO_2 loading, respectively. On the other hand, for temperature well below the freezing point (in region-III), 22.3 and 26.5 % enhancement in thermal conductivity were observed for PCM loaded with 1 and 3 wt. % of HP-SiO_2, respectively. **Table 4.2** shows the comparison of % enhancement in thermal conductivity of the PCM loaded with 1 and 3 wt. % of SiO_2 and HP-SiO_2.

Table 4.2 Comparison between the % enhancements in thermal conductivity for PCM loaded with 1 and 3 wt. % of SiO_2 and HP-SiO_2.

Region	SiO_2		HP-SiO_2	
	Concentration	% enhancement in thermal conductivity	Concentration	% enhancement in thermal conductivity
Liquid (region-I) (T = 35 ^{0}C)	1 wt. %	1.8 ± 0.1	1 wt. %	2.4 ± 0.1
	3 wt. %	2.9 ± 0.1	3 wt. %	1.7± 0.1
Solid (region-III) (T = 15 ^{0}C)	1 wt. %	25.2 ± 1.2	1 wt. %	22.3 ± 1.1
	3 wt. %	38.2 ± 1.9	3 wt. %	26.5 ± 1.3

It can be clearly seen from **Table 4.2** that thermal conductivity enhancement was lower for the PCM loaded with HP-SiO_2 and this was attributed to the higher thermal barrier resistance or Kaptiza resistance (resistance to heat flow across an interface) for hydrophobic interaction [391]. Theoretical studies indicate that thermal barrier resistance is significantly higher for negligible or limited wettability (i.e. hydrophobic interfaces) [472, 473]. Shenogina et al. [474] reported that the Kapitza conductance is linearly proportional to the work of adhesion and hence, thermal barrier resistance was higher for hydrophobic interactions. Ge et al. [475] reported the typical values of thermal barrier resistance for hydrophilic and hydrophobic interfaces as 0.67×10^{-8} and 2.0×10^{-8} Km^2W^{-1}, respectively, where the higher (~ 3 times) thermal barrier resistance for the hydrophobic interfaces was attributed to the critical role of the hydration layer across the solid-liquid interface with different surface properties. Hence, the lower enhancement in thermal conductivity of the PCM loaded with HP-SiO_2, as compared to the PCM loaded with SiO_2 was attributed the hydrophobicity of the PCM/HP-SiO_2 interfaces which resulted in a higher Kapitza resistance, thereby reducing the effective heat transfer through the percolating structures. It can be further observed from **Table 4.2** that the detrimental effect of hydrophobic interaction on thermal conductivity was more evident at higher concentration of the nano-inclusions, where the effective heat transfer is primarily through the percolating structures [342] and hence, thermal barrier resistance played a more prominent role on the efficiency of heat transfer. This clearly shows that the surface properties of the nano-inclusions also plays an important role in the Kapitza resistance and in the effective thermal transport [439].

Figure 4.9 shows the variation of k/k_f and the percentage (%) enhancement in thermal conductivity as a function of temperature for the PCM loaded with 1, 2, 3 and 4 wt. % of TiO_2. The effect of CBNP addition (0.02 and 0.04 wt. %) on k/k_f and % enhancement in thermal conductivity is also shown in **Fig. 4.9**. The **inset of Fig. 4.9** shows the enlarged view of the variation of k/k_f with temperature in the liquid state. In the liquid state, thermal conductivity enhancements were ~ 2.4, 7.1, 8.2 and 9.4 % for 1, 2, 3 and 4 wt. % of TiO_2 loading, respectively. Addition of 0.02 and 0.04 wt. % of CBNP to the PCM loaded with 3 wt. % of TiO_2 resulted in thermal conductivity enhancements of ~ 8.8 and 5.9 %, respectively in the liquid state. In the phase transition region, thermal conductivity enhancements were ~ 55.9, 64.7, 76.5 and 70.6 % for 1, 2, 3 and 4 wt. % of TiO_2 loading, respectively. On the other hand, in the solid state, well below the freezing point, thermal conductivity values were constant below 15 ^{0}C and the thermal conductivity enhancements were ~ 26.5, 32.3, 38.2 and 33.5 % for the PCM loaded with 1, 2, 3 and 4 wt. % of TiO_2, respectively. It was observed from **Fig. 4.9**, that the thermal conductivity increased with concentration of TiO_2 in the liquid state, whereas in the solid state, for TiO_2 concentration beyond 3 wt. %, thermal conductivity decreased. Addition of 0.02 and 0.04 wt. % of CBNP to the PCM loaded with 3 wt. % of

TiO_2 resulted in ~ 41.2 and 39.4 % enhancement in thermal conductivity, respectively, in the solid state.

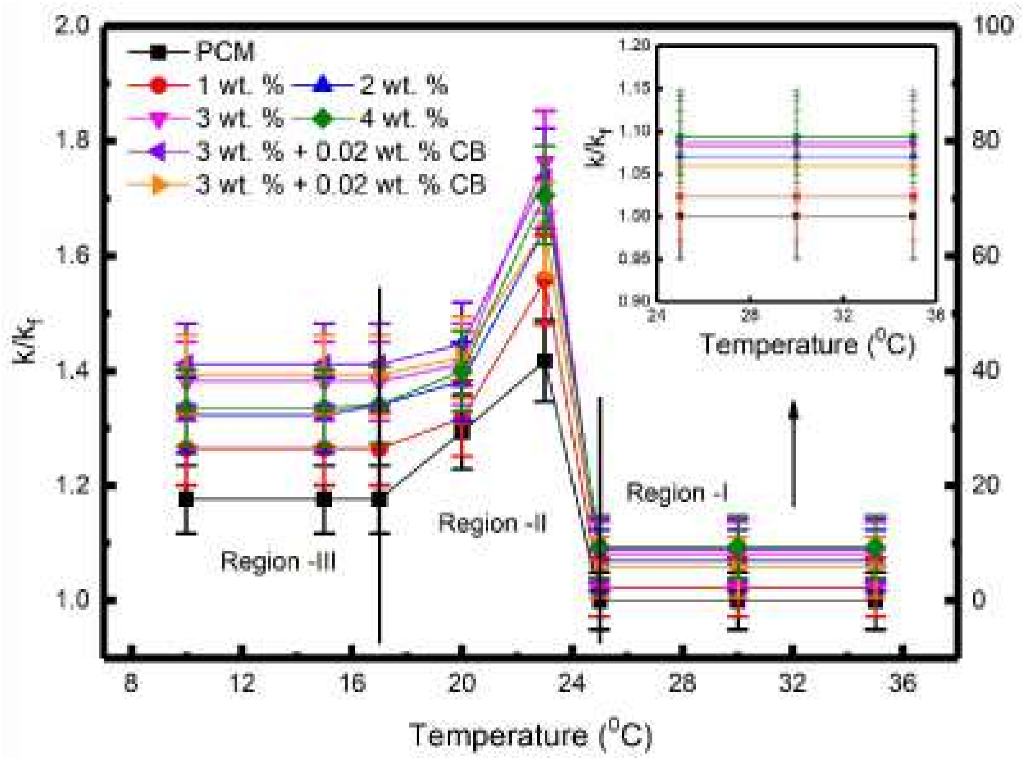

Figure 4.9 Variation of k/k_f and percentage (%) enhancement in thermal conductivity as a function of temperature for different concentrations of TiO_2 loading in phenol-water system with 1.56 wt. % water concentration (PCM). The effect of CBNP addition (0.02 and 0.04 wt. %) on k/k_f is also shown. (Inset) Enlarged view of the variation of k/k_f as a function of temperature in the liquid state.

Figures 4.10a-c show the variation of k/k_f and % enhancement in thermal conductivity in the solid (T = 15 ^{0}C) and liquid (T = 35 ^{0}C) states for the PCM loaded with different concentrations of α-Al_2O_3, SiO_2 and TiO_2, respectively. For all three nano-inclusions, thermal conductivity increased with concentration in the liquid state. In the liquid state, the maximum enhancements in thermal conductivity were ~ 7, 2.9 and 9.4 % for 4, 3 and 4 wt. % of α-Al_2O_3, SiO_2 and TiO_2, respectively. On the other hand, the thermal conductivity enhancements were substantially higher in the solid state, which was attributed to the formation of needle like microstructure of the PCM during freezing that squeezed the nano-inclusions towards the grain boundaries, thereby, forming a network of percolating structures for efficient heat transfer [231, 237, 387]. It can be further seen from **Figs. 4.10a-c** that the thermal conductivity of the nano-inclusion loaded PCM in the solid state increased with concentration of the nano-inclusions. In the present study, the maximum enhancements in thermal conductivity were ~ 41.2 and 38.2 % for PCM loaded with 4 and 3 wt. % of α-Al_2O_3 and SiO_2, respectively. The nano-inclusions tend to form aggregates due to weak van der Waal's interaction and such aggregation leads to an increase in thermal conductivity due to the percolation effects, as nanoparticles of higher thermal conductivity (as compared to the PCM) are in physical contact with each other within an aggregate characterized by their radius of gyration (R_g), which is several times larger than the size of the individual nano-inclusions [342]. With increasing concentration of the nano-inclusions, the aggregates grow in size (but within the limit of well dispersed aggregates), thereby, enhancing the thermal conductivity of the PCM loaded with nano-inclusions primarily due to two reasons, viz. effective heat conduction through a larger network of percolating structure and reduced thermal barrier resistance due to the improved contact between the nano-inclusions. Higher enhancement in thermal conductivity for larger concentration of nano-inclusions have been reported for various other types of organic phase change materials due to the formation of percolating structures [214, 231, 237, 387].

On the other hand, in the case of PCM loaded with TiO_2 nanoparticles, initially thermal conductivity increased with concentration of the nano-inclusion and attained a maximum value of ~ 38.2 % at 3 wt. % and beyond that decreased to ~ 33.5 % at 4 wt. % concentration of TiO_2. The sedimentation velocity (V_s) of a concentrated sample is expressed as $V_s = V_0[(1-\phi)/1+M\phi/(1-\phi)^3]$ [341], where M is a numerical constant (~ 4.6), ϕ is the effective volume fraction of the solute and V_0 is the sedimentation velocity at infinite dilution, which is linearly proportional to the density difference ($\Delta\rho$) of the nano-inclusion and the PCM, i.e. $V_0 \sim \Delta\rho$ [50]. As the density of TiO_2 is the highest among the three nano-inclusions, used in the present study (typical values for density of TiO_2, α-Al_2O_3 and SiO_2 are ~ 4.23, 4.1 and 0.16 g/cc, respectively [38]), it is prone to agglomeration at higher concentration, which seems to have caused the decrease in the thermal conductivity for the PCM loaded with 4 wt. % of TiO_2. Initially thermal conductivity increases with aggregate size and the enhancement in thermal conductivity is optimal for well-dispersed aggregates (due to formation of high thermal conductivity percolation network) and beyond that, thermal conductivity decreases for larger aggregates [342].

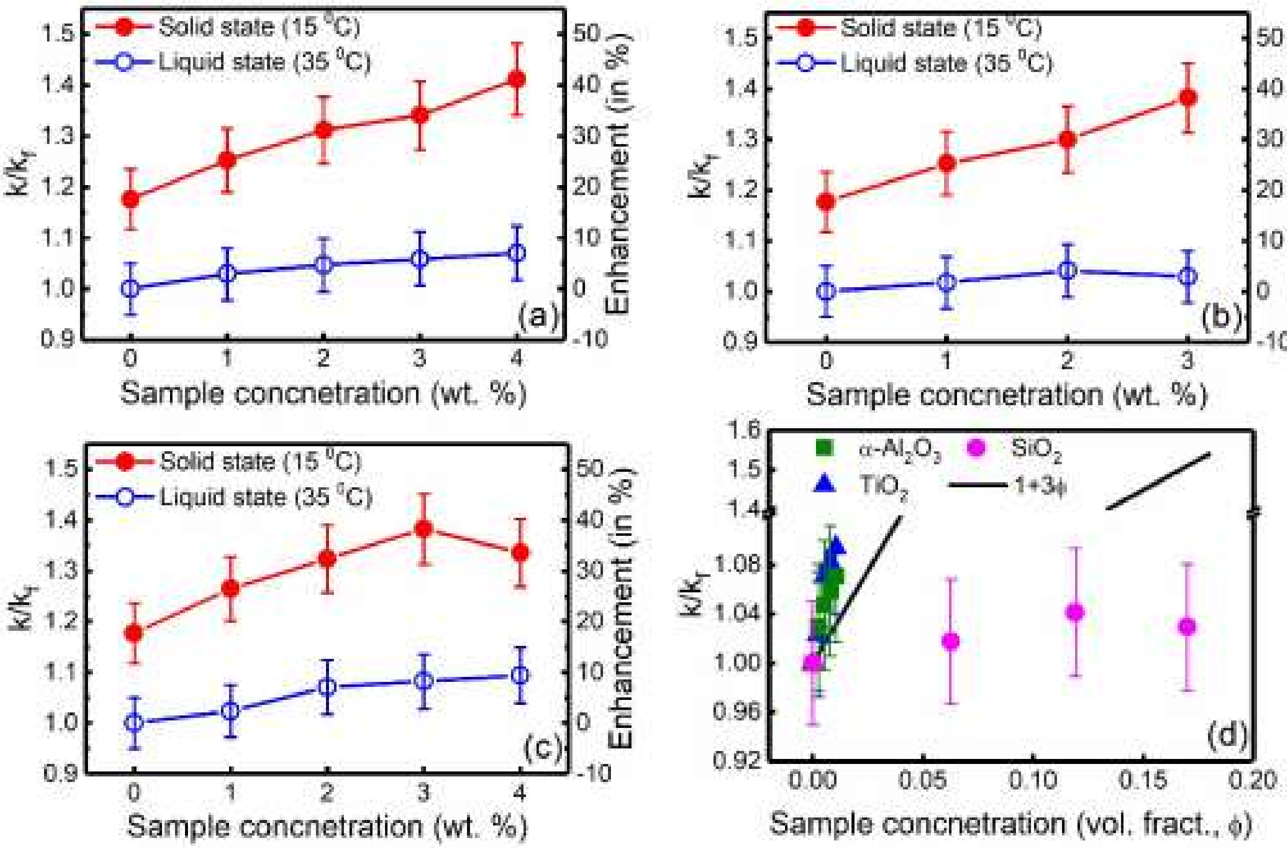

Figure 4.10 Variation of k/k_f and % enhancement in thermal conductivity in the solid (T = 15 ^{0}C) and liquid (T = 35 ^{0}C) state for the PCM loaded with different concentrations of (a) α-Al_2O_3, (b) SiO_2 and (c) TiO_2. (d) k/k_f as a function of concentration (in volume fraction) for PCM loaded with α-Al_2O_3, SiO_2 and TiO_2 in the liquid state. The theoretical curve (effective medium theory) for k/k_f variation is also shown.

Formation of such large aggregates caused a decrease in thermal conductivity of the PCM loaded with 4 wt. % of TiO_2 as seen in **Fig. 4.10c**. This can be explained on the basis of fractal morphologies of the nano-inclusions aggregates, which is embedded within a sphere of radius R_g (radius of gyration) and consisted of a backbone (a quasi-continuous network of nano-inclusions spanning the entire sphere) and randomly placed nanoparticles which are known as dead-ends [341]. Effective thermal transport occurs via the backbone, due to its connectivity, and in larger aggregates the number of dead-ends increases, which does not necessarily contribute to an enhancement in thermal conductivity. Moreover, such large aggregates are prone to sedimentation due to gravitational force, resulting in a decrease in the thermal conductivity at higher concentrations [38]. Similar decrease in thermal conductivity for higher concentration of graphite loading was reported by Zheng et al. [387] for hexadecane based PCM.

It must be noted in this regard that the thermal conductivity enhancement (in solid state) of PCM loaded with 3 wt. % of α-Al_2O_3, SiO_2 and TiO_2 were ~ 34.1, 38.2 and 38.2 %, respectively. The bulk thermal conductivity of α-Al_2O_3, SiO_2 and TiO_2 are ~ 35, 1.4 and 15 W/mK, respectively [38]. This clearly shows that though the bulk thermal conductivity was the highest for α-Al_2O_3, thermal conductivity enhancements were higher for the PCM loaded with SiO_2 and TiO_2 nano-inclusions. This is in agreement with the classical effective medium theory where the thermal conductivity in dispersions is primarily dependent on the effective concentration of the dispersed phase and not on the bulk thermal conductivity of the suspended particles [231]. **Fig. 4.10d** shows the variation of k/k_f of the nano-inclusion loaded PCM, in the liquid state, as a function of concentration (in volume fraction) of the nano-inclusions. The theoretical plot for effective medium theory is also shown in **Fig. 4.10d**. For α-Al_2O_3 and TiO_2, the experimentally measured k/k_f values were higher than the theoretically expected values, which indicated the presence of aggregates in these systems [289]. On the other hand, for PCM loaded with SiO_2, the experimentally measured k/k_f values were found to be systematically lower than the theoretically calculated values.

To obtain insight into the microstructural evolution of the PCM loaded with nano-inclusions, phase contrast optical microscopy was carried out and the results are shown in **Fig. 4.11** for the PCM loaded with different concentrations of α-Al_2O_3. **Figs. 4.11a-d** show the phase contrast images of the PCM loaded with 1, 2, 3 and 4 wt. % of α-Al_2O_3, respectively, in the liquid state. These images were obtained after sonicating the samples for 10 minutes. The evolution of the aggregates with increasing concentration of the nano-inclusions is evident from **Figs. 4.11a-d**. With increasing concentration of the nano-inclusion, aggregate size increased and inter-aggregate spacing decreased. Nevertheless, the aggregates were well dispersed and no large-scale sedimentation was observed. **Figs. 4.11e-h** show the phase contrast images of the PCM loaded with 1, 2, 3 and 4 wt. % of α-Al_2O_3, respectively, in the solid state. These images were obtained at ~ 20 ^{0}C, i.e. well below the freezing point and corresponded to region-III in **Fig. 4.5**. The needle like microstructure of the phenol-water system can be clearly seen from the phase contrast images. The presence of nano-inclusions at the grain boundaries were also clearly discernible. It was further observed that the aggregate size increased with the concentration of α-Al_2O_3. These aggregates formed a network of percolating structure for efficient heat transfer, resulting in an enhanced thermal conductivity [387].

Figure 4.12a shows a topography image (2 μm × 2 μm), obtained from atomic force microscopy (AFM), for 1 wt. % α-Al_2O_3 loaded in phenol. The topography image was obtained by drop-casting the liquid samples, after 10 minutes of sonication, on a freshly cleaved mica surface and dried *in situ* at 22 ^{0}C. The aggregates of α-Al_2O_3 were clearly discernible from the topography image. **Fig. 4.12b** shows the 3d image of **Fig. 4.12a**, where the presence of the aggregates was clearly seen. Grain analysis was performed using a

Gaussian Kernel of 5th order and **Fig. 4.12c** shows the grain distribution superimposed on the topography image. **Fig. 4.12d** shows the topography image (5 µm × 5 µm) for 4 wt. % α-Al_2O_3 loaded in phenol, where the presence of larger aggregates was clearly discernible. **Fig. 4.12e** shows an enlarged view (2 µm × 2 µm) of a section of **Fig. 4.12d** (marked by the rectangle), which clearly indicated the presence of larger aggregates for higher concentration of nano-inclusions. It can be further seen from **Fig. 4.12e** that the aggregates were closely packed in this case, which resulted in a more efficient heat transfer through the network of percolating structure. This was also confirmed from grain analysis, which is shown in **Fig. 4.12f**. It is evident from **Fig. 4.12f** that the contact area between the closely packed larger aggregates was higher, which resulted in a decreased thermal barrier resistance, thereby aiding in efficient heat transfer [342].

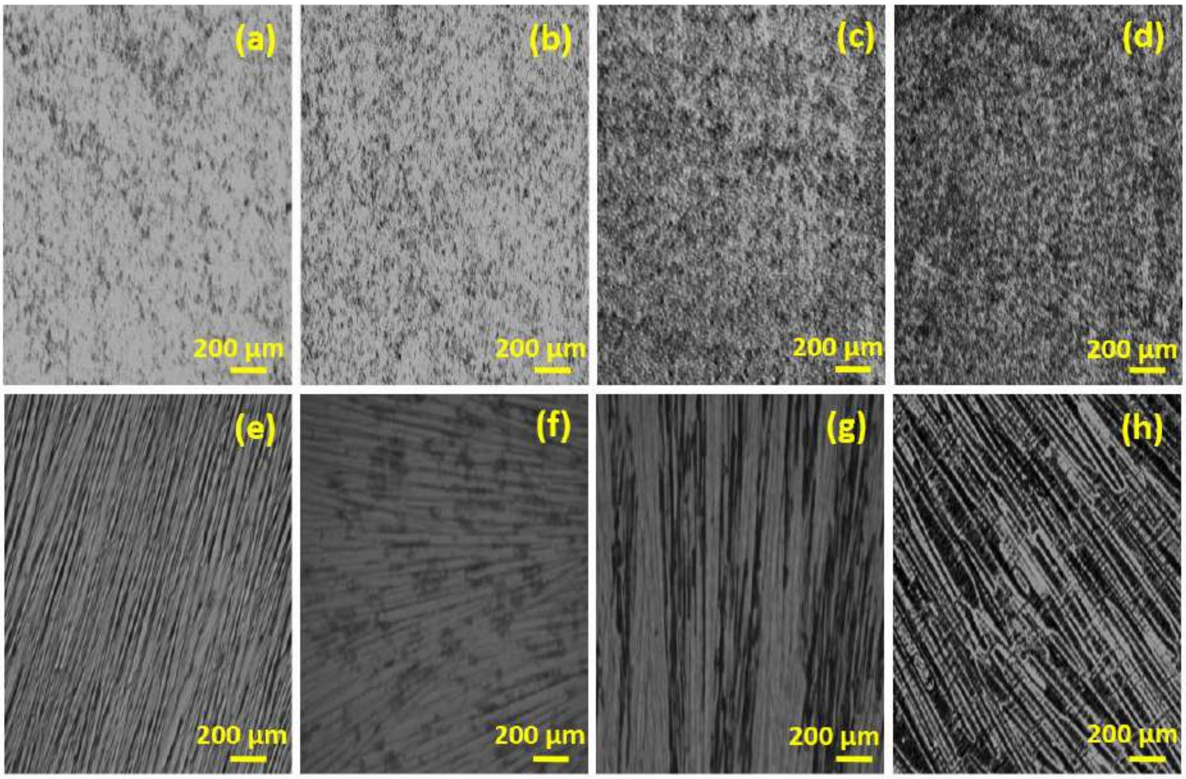

Figure 4.11 Optical phase contrast microscopy images of the PCM loaded with 1, 2, 3 and 4 wt. % of α-Al_2O_3, in the (a-d) liquid and (e-h) solid states, respectively.

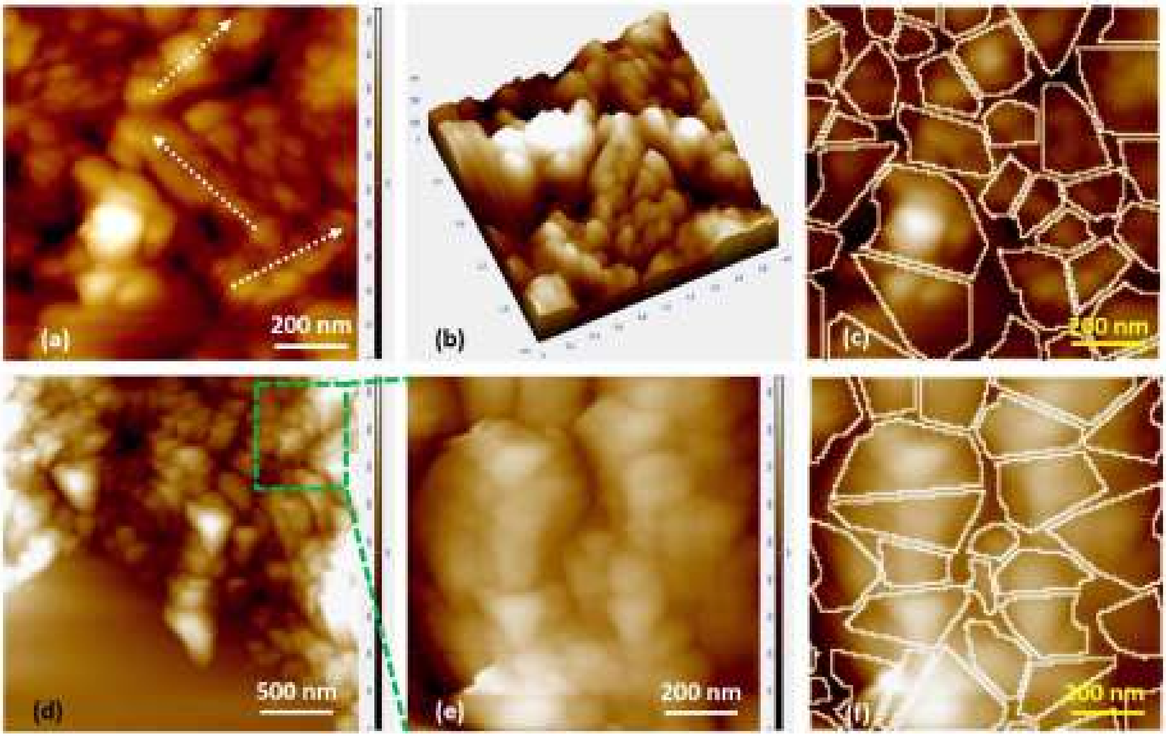

Figure 4.12 (a) Topography image (2 μm × 2 μm), obtained from atomic force microscopy (AFM), for 1 wt. % α-Al$_2$O$_3$ loaded in phenol. The high thermal conductivity percolation paths are indicated by the white arrows. (b) 3d image of (a). (c) Grain distribution (obtained using 5th order Gaussian kernel) superimposed on the topography image (a). (d) Topography image (5 μm × 5 μm) for 4 wt. % α-Al$_2$O$_3$ loaded in phenol. (e) A magnified view (2 μm × 2 μm) of a section (marked by the green rectangle) of (d). (f) Grain distribution (obtained using 5th order Gaussian kernel) superimposed on the topography image (e).

The repeatability tests (thermal cycling) for the PCM loaded with 4 and 3 wt. % of α-Al$_2$O$_3$ and SiO$_2$ are shown in **Figs. 4.13a-b**, respectively. During thermal cycling, thermal conductivity measurements were done at a temperature well above the freezing point (T = 35 ^{0}C) and then the sample was frozen to a temperature (15 ^{0}C) well below the freezing point and the thermal conductivity measurements were repeated several times. Though the freezing and melting cycles were perfectly symmetrical for the PCM (see **Fig. 4.4b**), some deviations were observed for the PCM loaded with nano-inclusions, especially in the solid state. In the case of α-Al$_2$O$_3$, the thermal conductivity enhancements in the liquid state were ~ 6.5, 2.9, 1.8 and 1.2 % after 1st, 2nd, 3rd and 4th cycle, respectively. On the other hand, thermal conductivity enhancements in the solid state were ~ 35.9, 31.8, 30.6 and 29.4 % after 1st, 2nd, 3rd and 4th cycle, respectively. In the case of SiO_2 loaded PCM, thermal conductivity enhancements in the liquid state were ~ 5.9, 2.4, 1.8 and 1.8 % after 1st, 2nd, 3rd and 4th cycle, respectively, whereas, thermal conductivity enhancements in the solid state were ~ 33.5, 26.5, 24.7 and 23.5 % after 1st, 2nd, 3rd and 4th cycle, respectively. It can be seen from **Fig. 4.13** that thermal conductivity decreased slightly in both the cases after repeated freezing-melting cycles which was attributed to the agglomeration of nano-inclusions after several thermal cycles and changes in thermal barrier resistance [231]. Studies show a negative thermal conductivity enhancement for positive Kapitza length due to weak solid-fluid interaction [45, 473]. The acoustic mismatch model for long wavelength phonons predicts a lowering of interfacial heat flux (directly proportional to thermal barrier conductance) with increasing domain size for larger aggregates [442]. On the other hand, diffuse mismatch model for high frequency phonons predicts an increased scattering from the interfaces due to physical roughness [443], which increases with the aggregate size, thereby increasing the thermal barrier resistance for larger aggregates. Hence, phonon scattering at the grain boundaries and aggregate interfaces leads to the degradation of thermal conductivity due to the formation of larger aggregates after a few thermal cycles [476].

Figures 4.14a-c show the variation in thermal conductivity enhancement after addition of 0.02 and 0.04 wt. % of CBNP to the PCM loaded with 4 wt. % of α-Al_2O_3, 3 wt. % of SiO_2 and 3 wt. % of TiO_2, respectively, in the solid state. For ease of comparison, thermal conductivity enhancement of the PCM (without any nano-inclusions) in the solid state is also shown. For α-Al_2O_3, the thermal conductivity enhancement was ~ 41.2 % for the PCM loaded with 4 wt. % of α-Al_2O_3 and addition of 0.02 and 0.04 wt. % CBNP caused an increase in thermal conductivity enhancement to ~ 44.7 and 45.9 %, respectively.

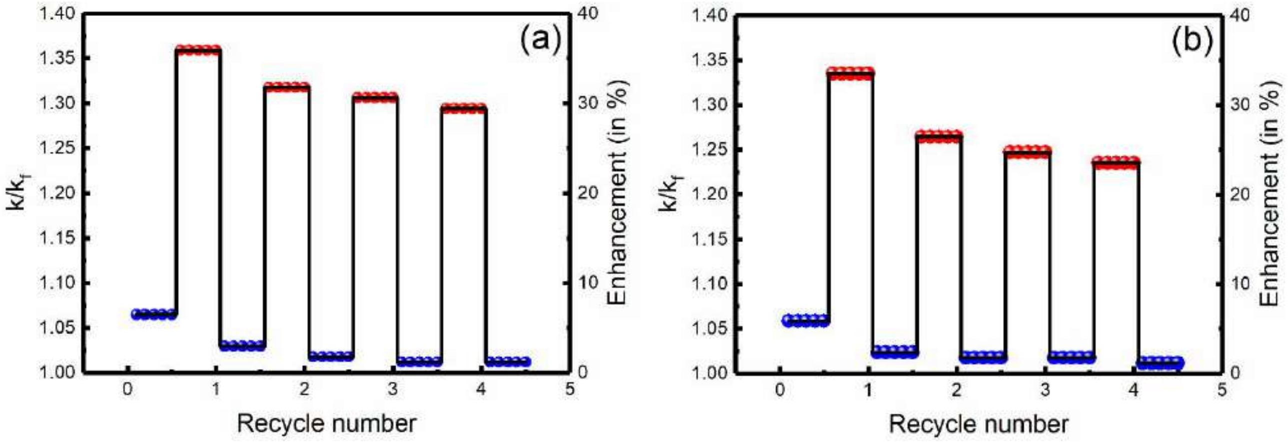

Figure 4.13 Variation of k/k_f and % enhancement in thermal conductivity during repeatability tests (thermal cycling) for the PCM loaded with (a) 4 wt. % of α-Al_2O_3 and (b) 3 wt. % of SiO_2.

In the case of SiO_2, the thermal conductivity enhancement was ~ 38.2 % for PCM loaded with 3 wt. % of SiO_2 and addition of 0.02 and 0.04 wt. % CBNP resulted in further increase of thermal conductivity enhancement to ~ 41.7 and 45.3 %, respectively. On the other hand, thermal conductivity enhancement was ~ 38.2 % for the PCM loaded with 3 wt. % of TiO_2 and with addition of 0.02 wt. % of CBNP thermal conductivity enhancement initially increased to ~ 41.2 % and then decreased to ~ 39.4 % for addition of 0.04 wt. % CBNP. It has been reported that CBNP primarily consist of aggregates and agglomerates (aciniform structure: grape like) of the primary particles (nodules) [407] and **Fig. 4.14d** schematically shows the primary particle (in red) and aggregates of CBNP. Due to the formation of aggregates, addition of CBNP to the PCM resulted in formation of additional high thermal conductivity percolation path, which caused further enhancement of thermal conductivity. It has been reported that addition of CBNP fills up the free volume and reduces inter-aggregate (of nano-inclusions) gaps thereby enhancing the conductive trajectories [431]. Leong and Chung [477] reported higher thermal conductivity for thermal paste containing CBNP dispersions which was attributed to the compressibility of CBNP aggregates that acts as high conductivity volume filling agents. For nano-inclusion loaded PCM, even in the presence of aggregates, thermal conductivity enhancement through the percolating network is limited due to the thermal barrier resistance at aggregate/PCM or aggregate/aggregate interfaces [432]. A study shows that even in the case of direct aggregate/aggregate interfaces, the heat transfer is limited due to phonon mismatch at the interfacial curvature (also seen from AFM images, see **Fig. 4.12**) [433]. Smaller aggregates of CBNP acts as volume filling agents and enhances the heat transfer through the percolating network due to improved aggregate/aggregate and aggregate/PCM interactions [431, 432]. Wu et al. [236] reported a substantial increase in thermal conductivity of carbon black/octadecane PCM which was attributed to the low fractal dimension of CBNP.

Our results show that addition of CBNP resulted in a synergistic increase in thermal conductivity of the PCM loaded with α-Al_2O_3 and SiO_2. In the case of PCM loaded with 3 wt. % of TiO_2, addition of addition of 0.04 wt. % of CBNP caused a decrease in thermal conductivity which was attributed to the formation of larger aggregates, which were not well dispersed. The synergistic effect (s) of CBNP addition was quantified by estimating the difference between the k/k_f values: $s = [(k/k_f)_{n\text{-}PCM+CBNP}-(k/k_f)_{n\text{-}PCM}] \times 100$ %, where $(k/k_f)_{n\text{-}PCM+CBNP}$ and $(k/kf)_{n\text{-}PCM}$ indicate the k/k_f values of the PCM loaded with nano-inclusions and CBNP and PCM loaded with nano-inclusions only, respectively. The values of s were ~ 3.53 and 4.71 % for 0.02 and 0.04 wt. % of CBNP addition, respectively, to the PCM loaded with 4 wt. % of α-Al_2O_3. In the case of PCM loaded with 3 wt. % of SiO_2, the values of s were ~ 3.53 and 7.06 % for 0.02 and 0.04 wt. % of CBNP addition, respectively. On the other hand, in the case of PCM loaded with 3 wt. % of TiO_2, s was ~ 2.94 % for 0.02 wt. % of CBNP addition which reduced to 1.18 % for 0.04 wt. % of CBNP addition due to higher aggregation probability of TiO_2.

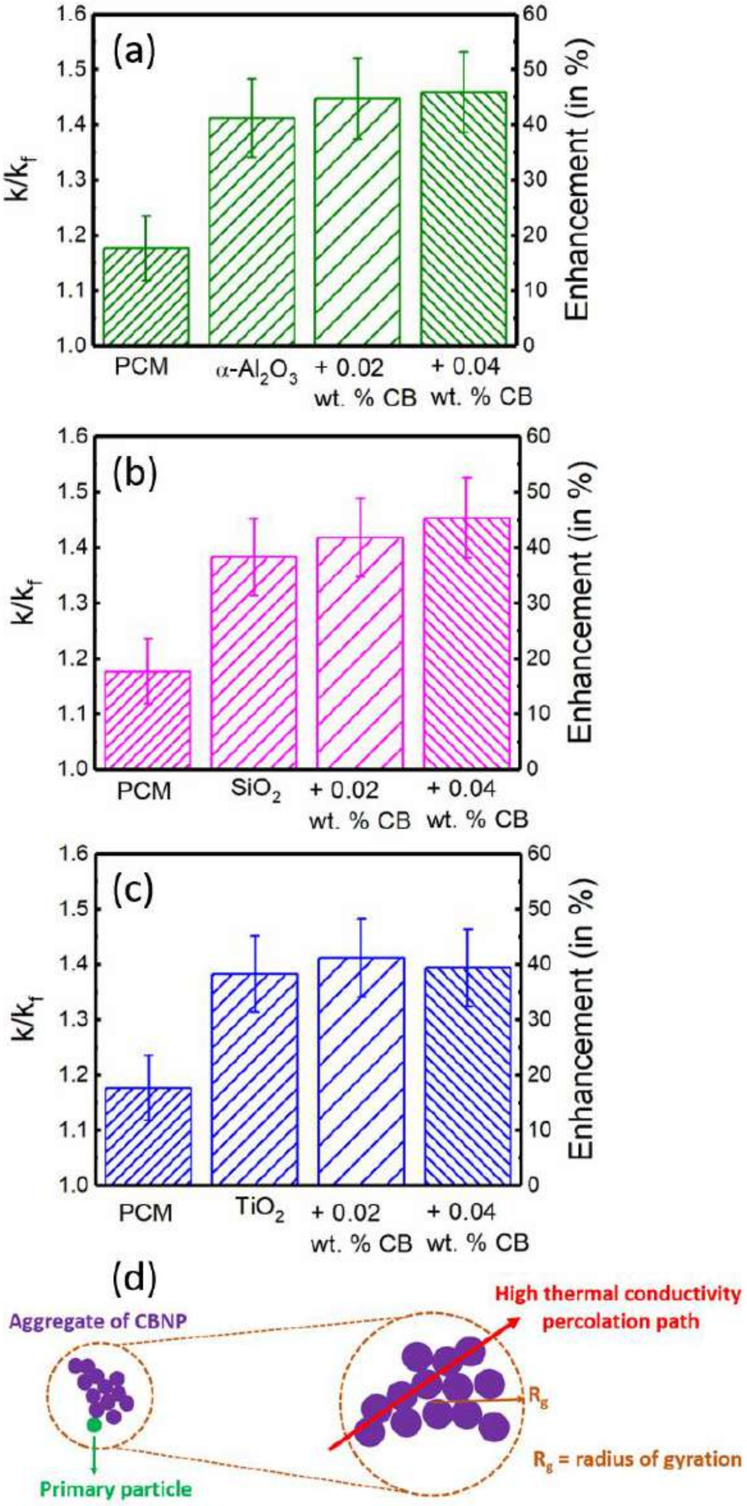

Figure 4.14 Variation of k/k$_f$ and % enhancement in thermal conductivity on addition of 0.02 and 0.04 wt. % of CBNP to the PCM loaded with (a) 4 wt. % of Al_2O_3, (b) 3 wt. % of SiO_2 and (c) 3 wt. % of TiO_2. (d) Schematic illustration of the primary particle and aggregates of CBNP. The high thermal conductivity percolation path is also indicated in the figure.

Figure 4.15a shows the temperature rise as a function of time for the PCM loaded with 1, 2 and 3 wt. % of α-Al_2O_3. Here the sample was initially placed in a recirculating water bath at 14 ^{0}C and thereafter heated at a rate of ~ 1-1.5 ^{0}C/minute. The sample temperature was monitored as a function of time using a platinum resistance thermometer. It can be clearly seen that the sample temperature increased linearly with time and below the phase transition region, the rate of temperature rise was the lowest for the PCM and increased with the concentration of the nano-inclusions. The higher rates of temperature rise for the nano-inclusion loaded PCM was due to the enhancement in thermal conductivity and **Fig. 4.15b** shows the variation of k/k_f as a function of melting rate ratio (normalized with respect to the melting rate of the PCM). It was observed that k/k_f increased linearly with the melting rate ratio. The slope and adjusted R^2 for the linear regression analysis were ~ 0.45 ± 0.05 and 0.97, respectively. It was also observed from **Fig. 4.15b** that the melting rates were ~ 13, 31 and 33 % higher (as compared to the melting rate of the PCM) with 1, 2 and 3 wt. % of α-Al_2O_3 loading, which was higher than the previously reported value of 27% increase in melting rate for nano Al_2O_3 (10 wt. %) loaded paraffin wax [469]. This shows the superior efficacy of the α-Al_2O_3 loaded phenol-water PCM for efficient heat transfer at a faster rate, which is advantageous for fabrication of efficient PCM based components. **Fig. 4.15c** shows the temperature variation as a function of time for the PCM loaded with 1, 2 and 3 wt. % of SiO_2, where it was observed that the melting rate increased with the concentration of the nano-inclusion. **Fig. 4.15d** shows the variation of k/k_f as a function of melting rate ratio for the SiO_2 loaded PCM, where it was observed that k/k_f linearly increased with the melting rate ratio. The adjusted R^2 and slope of the linear regression analysis were ~ 0.85 and 0.5 ± 0.1, respectively. **Figs. 4.15e-f** show the similar analyses for the PCM loaded with 1, 2 and 3 wt. % of TiO_2 and the slope and adjusted R^2 for the linear regression analysis (**Fig. 4.15f**) were ~ 0.7 ± 0.1 and 0.9, respectively. **Fig. 4.15** clearly shows that the rate of temperature rise is directly correlated with the nano-inclusion assisted enhancement in thermal conductivity of the PCM and shows the efficacy of nano-inclusion loaded phenol-water based PCM for room temperature thermal energy storage with faster heating/cooling rates.

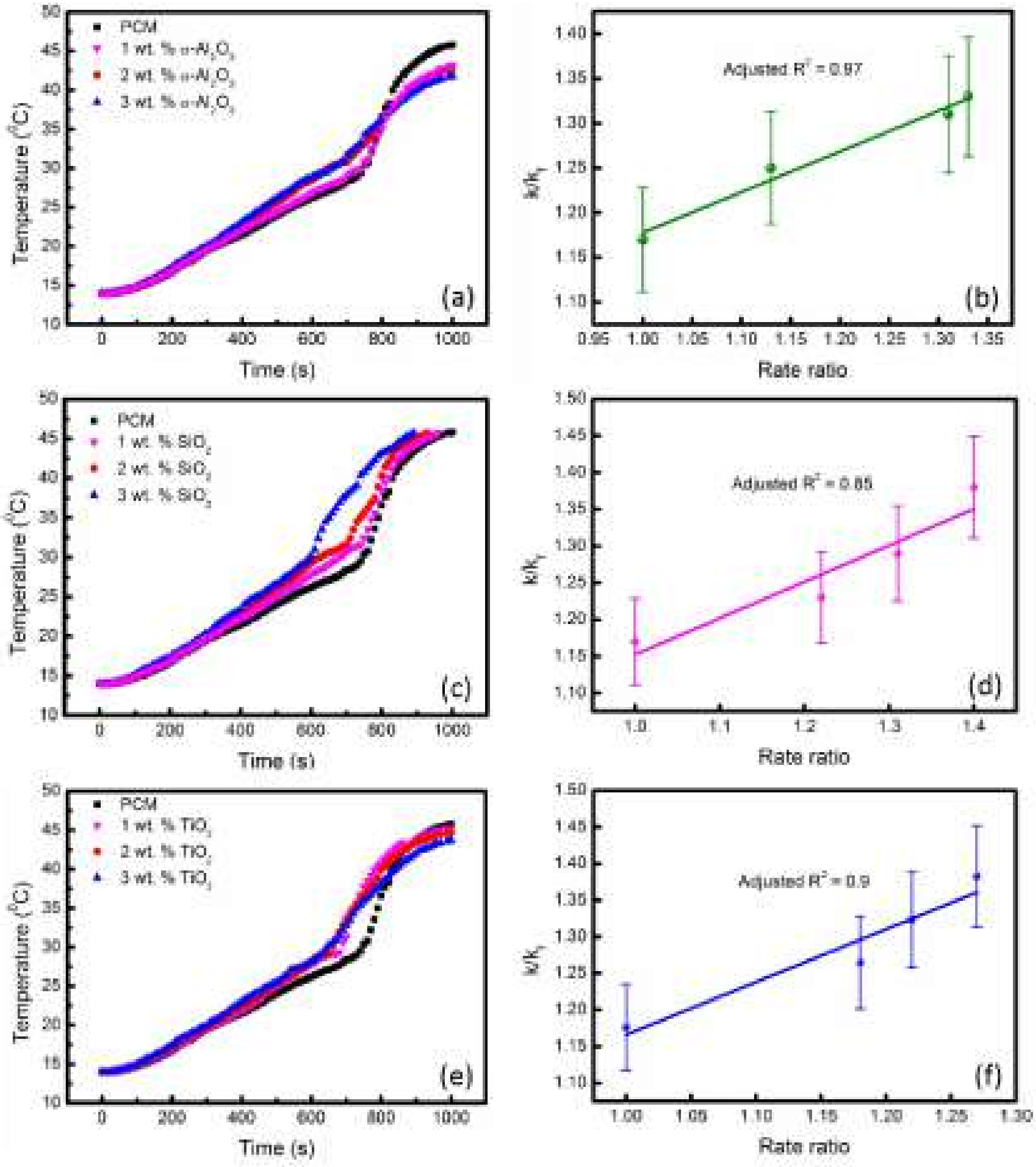

Figure 4.15 (a) Temperature rise as a function of time for the PCM loaded with 1, 2 and 3 wt. % of α-Al_2O_3. (b) Variation of k/k$_f$ as a function of melting rate ratio (normalized with respect to the melting rate of the PCM) in the case of α-Al_2O_3 loaded PCM. The data is fitted with linear regression analysis. (c) Temperature rise as a function of time for the PCM loaded with 1, 2 and 3 wt. % of SiO_2. (d) Variation of k/k$_f$ as a function of melting rate ratio in the case of SiO_2 loaded PCM. The data is fitted with linear regression analysis. (e) Temperature rise as a function of time for the PCM loaded with 1, 2 and 3 wt. % of TiO_2. (f) Variation of k/k$_f$ as a function of melting rate ratio in the case of TiO_2 loaded PCM. The data is fitted with linear regression analysis.

4.3 Tuning phase transition temperature of palmitic acid based PCMs and nano-inclusion assisted thermal conductivity enhancement

Palmitic acid has been chosen as the phase change material, owing to its several beneficial properties such as, high latent heat of phase change, low supercooling, non-toxicity, non-corrosiveness, smaller volume changes during solid-liquid phase transition and repeatable thermal properties even after consecutive thermal cycles [124, 276, 478]. Additionally, palmitic acid is derived from raw vegetables and animal sources, which is environment friendly [276]. Earlier studies on palmitic acid based PCMs, loaded with various types of metallic and carbon based nano-inclusions have shown improved thermal stability, significant thermal conductivity enhancements and usability in practical applications [60, 70, 219, 247, 479, 480]. On the other hand, Lee et al. [481] proposed a PCM consisting of anhydrous and hydrated palmitic acid/camphene solid dispersions with high latent heat and specific heat. The major objectives of the present study are twofold, viz. (1) to achieve significant thermal conductivity enhancement in a PCM using a comparatively cheaper carbon-based nano-inclusions with lower density and (2) to experimentally probe the aggregation dynamics and cluster formation, during liquid solid phase transition of nano-inclusion loaded PCMs.

4.3.1 Tuning of phase transition temperature and characterization of the PCM

The palmitic acid (PA)-dimethyl formamide (DMF) weight ratio was varied to tune the phase transition temperatures of the PA-DMF composite PCMs. Four different PA-DMF composite PCMs were prepared by adding 16.6, 27.4, 50.5 and 59.4 wt. % of DMF in PA. DMF (liquid at room temperature) was added in the required proportion to pristine PA in the liquid state (temperature maintained at 65 ± 1 ^{0}C). Thereafter, the mixtures were subjected to magnetic stirring for 1200 s at 62 ± 1 ^{0}C, followed by water bath sonication for 600 s at T = 60 ± 1, 50 ± 1, 40 ± 1 and 35 ± 1 ^{0}C for composite PCMs with 16.6, 27.4, 50.5 and 59.4 wt. % of DMF. The water bath temperature was kept constant at ~ 5 ^{0}C higher than the corresponding melting point (subsequently discussed) of the composite PCMs for proper mixing. The composite PCMs were subjected to differential scanning calorimetry (DSC) studies to ascertain the phase transition temperature and latent heat values. DSC studies were carried out in an argon environment with a heating rate of 3 ^{0}C/minute. For DSC measurements, the errors associated with the peak phase transition temperature, onset temperature and latent heat values were ~ ± 0.1 ^{0}C, ± 0.5 ^{0}C and 0.4 kJ/kg, respectively. The phase transition temperatures of the composite PCMs were also estimated in a non-contact way using infrared thermography (IRT) during melting. The samples were collected in a glass vial and placed inside a beaker, which was, in turn, immersed within a recirculating water bath with controllable temperature. The initial temperature of the samples was maintained at ~ 20 ± 1 ^{0}C and the water bath temperature was allowed to rise, during which the rise in PCM temperature was mapped over the top surface using a FLIR SC5000 series infrared camera, placed vertically above the samples at a distance of ~ 0.35 m. The phase transition temperatures were estimated from the changes in slopes of the temperature-time curves. Further, variation of temperature dependent refractive indices (at a wavelength of ~ 589.3 nm) of the PA-DMF composite PCMs were measured during the melting and freezing cycles, to estimate the phase transition temperatures. Refractive index measurements were performed using J357 automatic refractometer. To probe the complex formation between PA and DMF, the composite PCM with 50.5 wt. % DMF was subjected to Fourier transform infrared spectroscopy (FTIR), under a wavenumber range of 900-3600 cm^{-1}. FTIR spectroscopy was carried out in the attenuated total reflection (ATR) mode, using a zinc selenide crystal.

4.3.2 Preparation of nano-inclusion loaded PCMs

For thermal energy storage applications close to outdoor ambient temperature (~ 35 ^{0}C), the composite PCM with 50.5 wt. % DMF (peak melting temperature ~ 36 ^{0}C) was chosen as the

PCM in the present study and further experiments were performed on this composition upon loading with four different nano-inclusions of varied concentrations. The nano-inclusions were dispersed in the continuous phase of the PCM, in the liquid phase, by water bath sonication with bath temperature maintained at ~ 45 ± 1 ^{0}C. The sonication time was increased with increasing loading concentration to ensure thorough and homogenous distribution of the loaded nano-inclusions. For GNP, MWCNT and α-Al_2O_3 nano-inclusions, six different loading concentrations were used, viz., 0.004, 0.007, 0.01, 0.0125, 0.0150 and 0.02 volume fraction. The sonication time was varied from 900 to 1200 s, in steps of 300 s for the above-mentioned loading concentrations. For CBNP, nine different loading concentrations were used, viz., 0.004, 0.007, 0.01, 0.0125, 0.0150, 0.02, 0.03, 0.04 and 0.05 volume fraction. The sonication time was suitably varied from 900 to 3300 s in the case of CBNP nano-inclusions. To probe microscale aggregation and cluster formation, optical phase contrast microscopy was carried out at 10X magnification using an inverted phase contrast microscope (Carl Zeiss) in the liquid and solid states of the PCM with or without nano-inclusion loading. Additionally, real-time video was acquired for the PCM loaded with 0.02 vol. fraction of CBNP during freezing. Thermal conductivity measurements were carried out using a KD2 probe, as discussed in the 2nd chapter.

4.3.3 Theoretical and FTIR analysis of PA-DMF composites

To understand the complex formation between PA and DMF, density functional theory (DFT) based calculations were performed, using Gaussian 09 software package [482]. Further, frequency calculations were also performed to confirm the presence of hydrogen bonding in the PA/DMF composite PCMs. The individual molecules (PA and DMF) and PA-DMF complex were optimized at B3LYP/6-31g(d) level [483, 484]. Frequency calculations were carried out on the optimized geometries to confirm that the structures correspond to their ground states by obtaining all real vibration frequencies. The interaction energy was calculated using the supermolecular approach [485, 486], where interaction energy = energy of PA-DMF complex- (energy of isolated PA + energy of isolated DMF). **Figs. 4.16a-c** show the optimized structures of isolated PA, DMF and PA-DMF complex, respectively. Different conformations and orientations were evaluated using chemical intuition for the prediction of PA-DMF complex and the most stable energy minimized conformer is shown in **Fig. 4.16c**. **Table 4.3** shows the selected bond parameters, where it can be seen that the C=O bonds of PA and DMF were elongated from 1.211 to 1.221Å and 1.220 to 1.236Å, respectively, upon complex formation with DMF. On the other hand, for PA, the elongation of O-H bond was from 0.975 to 1.002Å after complex formation. These changes indicated that the PA-DMF complex was stabilized by hydrogen bond formation. Two key hydrogen bonding interactions (O-H---O and C-H---O) were present in PA-DMF complex, as shown in **Fig. 4.16c**. The bond distance and bond angle for O-H---O was found to be 1.71Å and ~ 180^0, respectively, which were well within the limits of hydrogen bond interactions. On the other hand, the bond distance and bond angle for C-H---O interaction were 2.301Å and ~ 120^0, respectively. This shows that the PA-DMF complex was stabilized by a strong hydrogen bond (O-H---O) and a weak C-H---O interaction. The calculated interaction energy was found to be ~ -13.74kJ/mol, where the negative sign indicated that the formation of PA-DMF complex was energetically favoured. Further, the IR frequencies of C=O and O-H bonds were calculated theoretically, where it was observed that stretching frequencies were reduced upon complex formation, which was due to the elongation of the bond lengths in the PA-DMF composite PCMs. The results obtained from DFT based calculations were experimentally verified using FTIR spectroscopy.

Figure 4.17a shows the FTIR spectra of DMF, PA and PA-DMF composite PCM, where all the major absorption bands were indexed and **Table 4.4** shows the detailed descriptions [453, 487, 488]. **Fig. 4.17b** shows the magnified view of a region (1600-1800 cm^{-1}) of **Fig. 4.17a**, where the shifts in the stretching frequencies, upon complex formation, are clearly discernible.

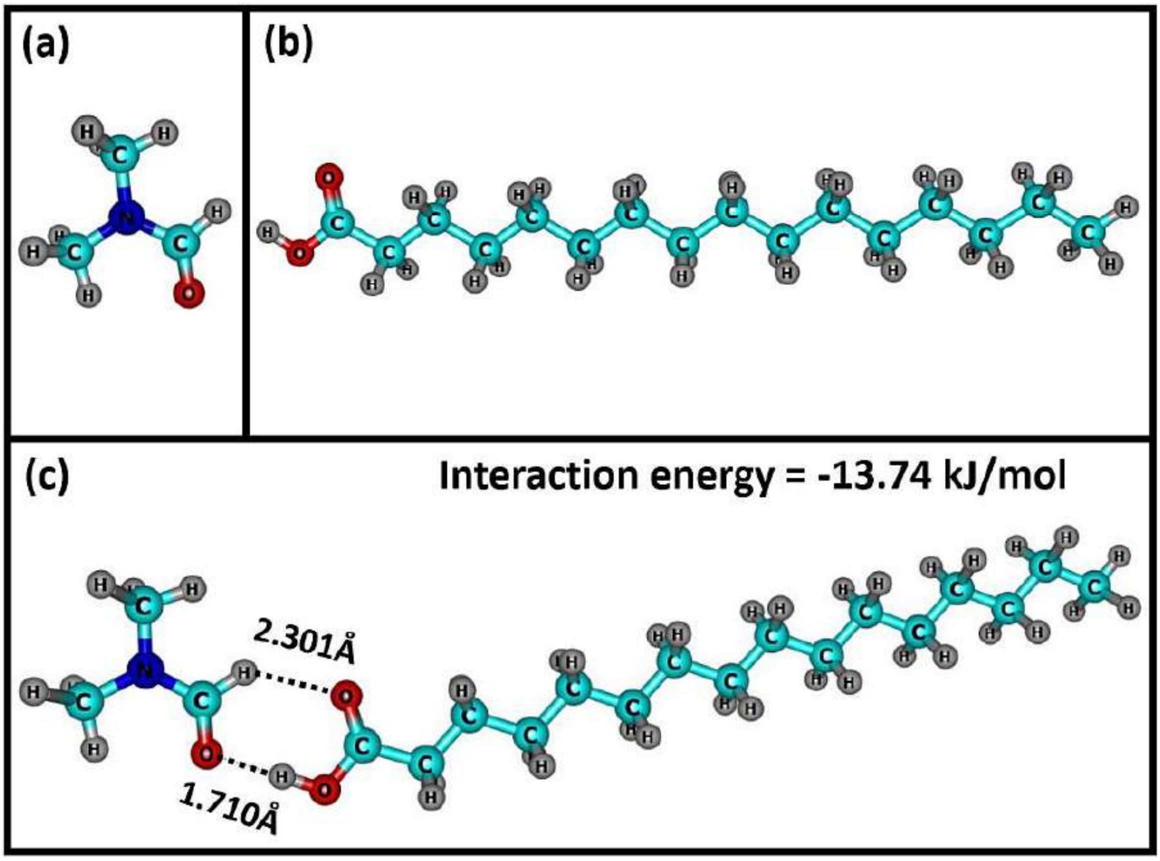

Figure 4.16 The optimized molecular structures of (a) isolated PA, (b) DMF and (c) PA-DMF complex. The presence of O-H---O and C-H---O hydrogen bonds, in PA-DMF complex, is also shown in (c). The bond lengths and interaction energy, upon complex formation are also indicated.

Table 4.3 Selected bond parameters of optimized geometries of isolated PA, isolated DMF and PA-DMF complex, obtained from DFT calculations.

Molecule	Type of bond	In isolated state (Å)	In PA-DMF complex (Å)
PA	C=O	1.211	1.221
	C-O	1.359	1.334
	O-H	0.975	1.002
DMF	C=O	1.220	1.236
	C-H	1.108	1.099
	N-C	1.366	1.351

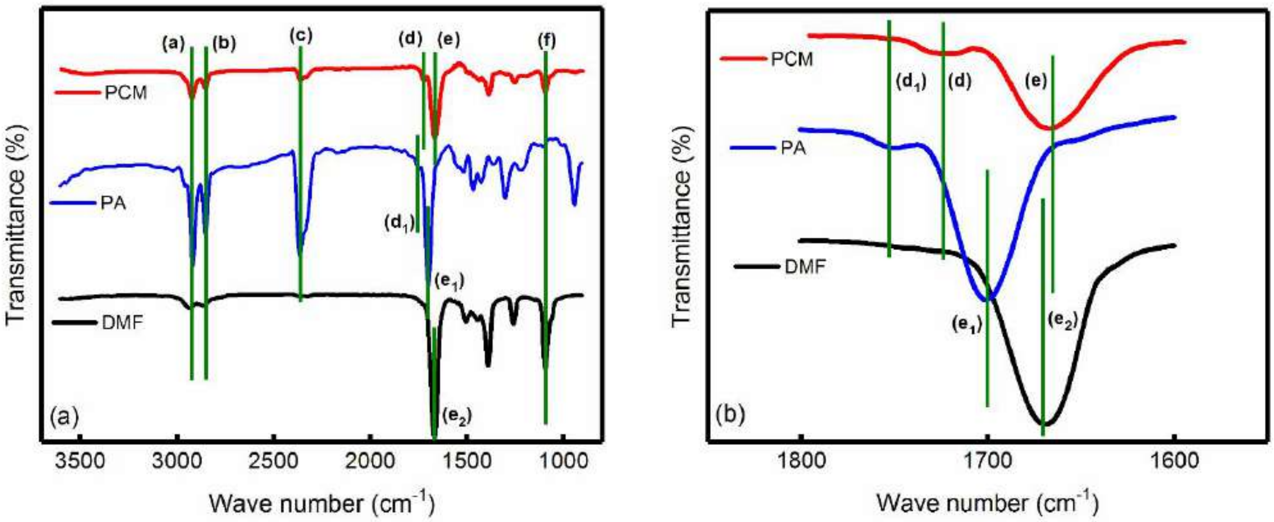

Figure 4.17 (a) FTIR spectra of DMF, PA and PA-DMF composite PCM. The major absorption bands are indexed and Table 4.4, in text, shows the detailed descriptions. (b) Magnified view of a region (1600-1800 cm^{-1}) of (a), where the shifts in the stretching frequencies, upon complex formation, are clearly discernible.

The stretching frequency of C=O bond in DMF (legend: e$_2$) shifted from 1677 to 1666 cm^{-1} after complex formation. Similarly, the stretching frequency of C=O bond of isolated PA (legend: e$_1$) reduced from 1700 to 1666 cm^{-1} in the PA-DMF complex. Additionally, the C=O stretching frequency of monomer hydrogen bonded molecule also decreased from 1753 (for isolated PA) to 1724 cm^{-1} after complex formation. The reduction in various stretching frequencies were attributed to the increase bond lengths, as seen from DFT calculations. For confirming the reduction in O-H stretching frequency, additional FTIR experiments were performed on pellets, made by thorough mixing of isolated PA and PA-DMF composite PCMs with KBr, followed by hard pressing. The recorded FTIR spectra (shown in **Fig. 4.18**, in the supplementary information) indicated that O-H stretching frequency shifted from 3614 to 3463 cm^{-1} upon complex formation, which was in agreement with the predictions made from DFT calculations. The FTIR data along with the DFT calculations indicated the formation of a stable PA-DMF complex, which was essential for ensuring repeatable thermal response during thermal energy storage applications.

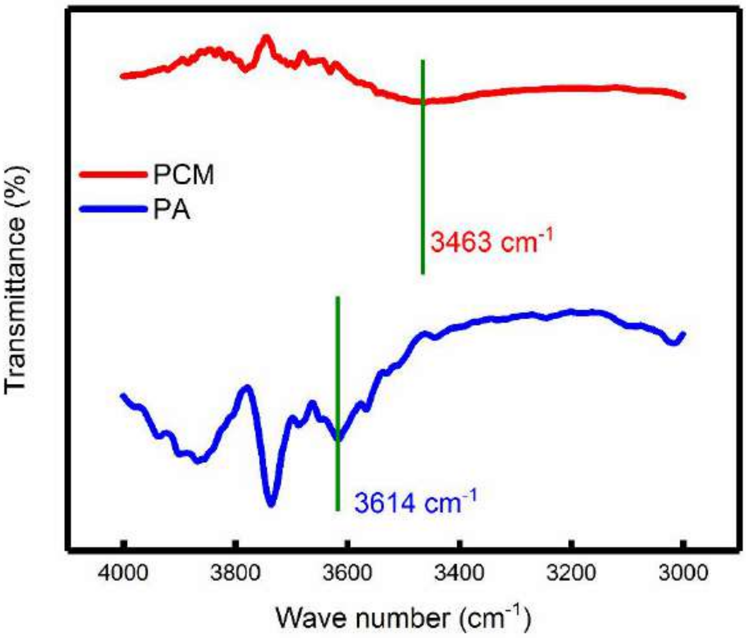

Figure 4.18 FTIR spectra indicating that O-H stretching frequency diminished from 3614 cm^{-1} to 3463 cm^{-1} upon PA-DMF complex formation.

Table 4.4 Major absorption bands, observed in FTIR spectra.

Legend	Wave number (cm^{-1})	Description	Reference
(a)	2925	Symmetrical stretching of $–CH_3$	[487]
(b)	2851	Symmetrical stretching of $–CH_2$	[487]
(c)	2362	C=O stretching from atmospheric CO_2	[215]
(d)	1724	C=O stretching of monomer hydrogen bonded molecule in PCM	this study
(d_1)	1753	C=O stretching of monomer hydrogen bonded molecule in PA	[453]
(e)	1666	C=O stretching of dimer hydrogen bonded molecule in PCM	this study
(e_1)	1700	C=O stretching of dimer hydrogen bonded molecule in PA	[487]
(e_2)	1677	C=O stretching of DMF	[488]
(f)	1091	C-N stretching vibration in DMF	[488]

4.3.4 Thermo-physical characterization of PA-DMF PCMs with tunable phase transition temperatures

Figures 4.19a-c show the variation of temperature dependent refractive indices (RI) for PA, 27.4 wt. % DMF + PA and 50.5 wt. % DMF + PA, respectively, during melting and freezing cycles. It can be seen from **Figs. 4.19a-c** that RI changed abruptly during solidification or melting, which was attributed to the discontinuous changes in sample density during first order phase transition. The phase transition regions are encircled in brown in **Figs. 4.19a-c**. Similar results were obtained for refractive index measurements, as a function of temperature, for 16.6 wt. % DMF + PA and 59.4 wt. % DMF + PA, respectively. From RI measurements, melting temperatures were estimated as ~ 59.0 ± 0.6, 49.0 ± 0.5, 47.0 ± 0.5, 40.0 ± 0.4 and 30.0 ± 0.3 ^{0}C for PA, 16.6 wt. % DMF + PA, 27.4 wt. % DMF + PA, 50.5 wt. % DMF + PA and 59.4 wt. % DMF + PA, respectively. The corresponding solidification temperatures were ~ 57.0 ± 0.6, 45.0 ± 0.5, 43.0 ± 0.4, 38.0 ± 0.4 and 26.0 ± 0.3 ^{0}C, respectively. **Figs. 4.19d-e**

show typical photographs of PA in the liquid and solid states, respectively. It can be clearly seen from **Fig. 4.19e** that the transparency of PA in solid state is significantly lower, which resulted in a higher refractive index change during liquid-solid phase transition, as seen from **Fig. 4.19a** (refractive index discontinuously varied by ~ 9.3 %). On the other hand, **Figs. 4.19f-g** show the typical photographs of 50.5 wt. % DMF + PA in the molten and frozen states, respectively. It was evident that the change in optical density was much lower in this case, as compared to pristine PA. This resulted in a comparatively lower change in refractive index for the composite PCM across liquid-solid phase transition, as can be seen from **Fig. 4.19c** (refractive index discontinuously varied by ~ 0.2 %).

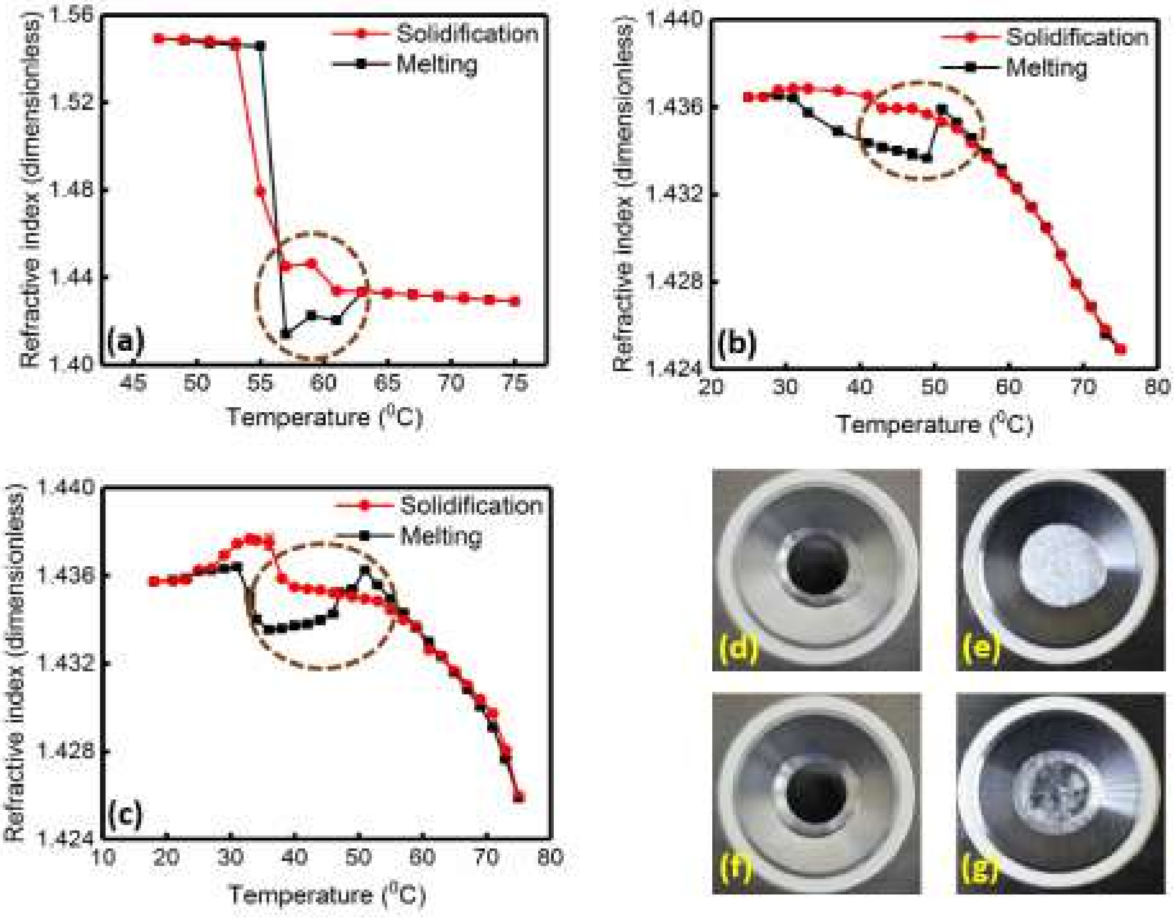

Figure 4.19 Variation of temperature dependent refractive indices, during freezing and melting, for (a) PA, (b) 27.4 wt. % DMF + PA and (c) 50.5 wt. % DMF + PA. Typical photographs of PA in the (d) liquid and (e) solid states. Typical photographs of 50.5 wt. % DMF + PA in the (f) liquid and (g) solid states.

Figure 4.20a shows temperature evolution during melting, recorded by infrared thermography, for PA and PA-DMF composites with various concentrations of DMF. It is evident from **Fig. 4.20a** that the solid-liquid phase transitions were associated with regions of distinct slope change in the temperature-time curves. The regions of slope change were encircled in **Fig. 4.20a** for ease of representation. From these curves, the melting temperatures were evaluated as 61.1 ± 0.6, 51.8 ± 0.5, 41.6 ± 0.4, 30.0 ± 0.3 and 28.0 ± 0.3 ^{0}C for PA, 16.6 wt. % DMF + PA, 27.4 wt. % DMF + PA, 50.5 wt. % DMF + PA and 59.4 wt. % DMF + PA, respectively. These values were close to the phase transition temperatures obtained from the variation of refractive indices (see **Figs. 4.19a-c**). **Figs. 4.20b-c** show the typical infrared images of PA and 50.5 wt. % DMF + PA, respectively at time t = 548 s, along with the temperature scales. The location of the sample and water baths are indicated by the green and blue arrows, respectively, in the infrared images. On the other hand, the black arrow represents the glass beaker, which appeared to be at a lower temperature (pseudo colour back), as glass is not transparent to infrared waves. The average temperature over the entire sample surface was utilized for obtaining the temperature evolution curves (as shown in **Fig. 4.20a**). Thus, infrared thermography-based technique provided an alternate way for rapid and non-contact determination of phase transition temperatures. However, to obtain better insights into the variation of latent heat values and phase transition temperatures, differential scanning calorimetry studies were carried out as discussed below.

Figure 4.21 shows the heat flow curves, obtained from DSC studies, for PA and PA-DMF composite PCMs with various concentrations of DMF. The phase transition peaks were clearly discernible and the onset (T^O) and peak melting temperatures (T^P), for different PCM compositions, are marked in **Fig. 4.21**.

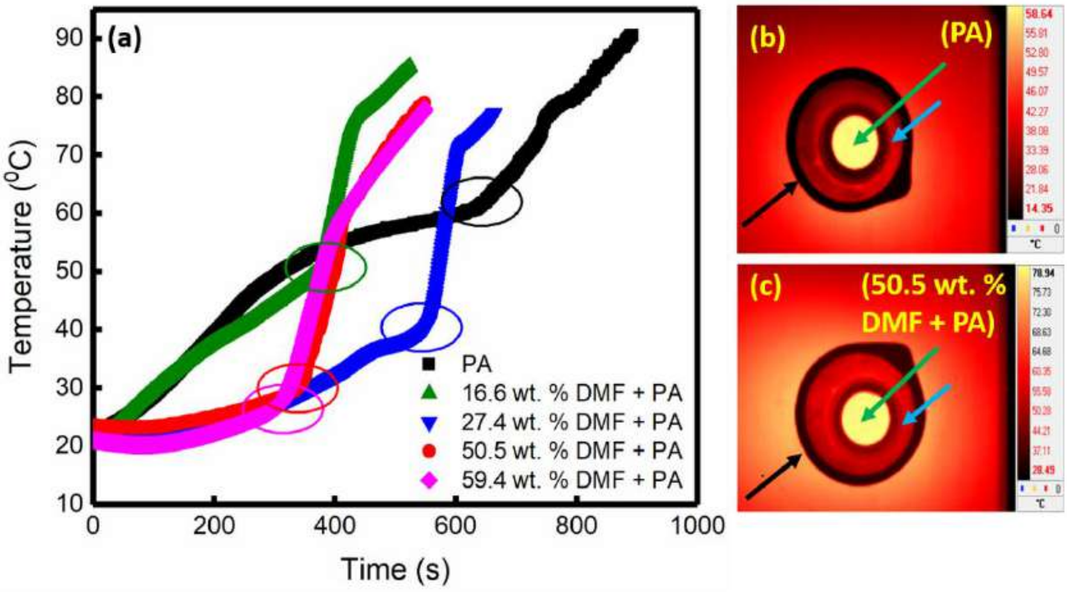

Figure 4.20 Temperature evolution during melting, recorded by infrared thermography, for PA and PA-DMF composites with various concentrations of DMF. The solid-liquid phase transitions were associated with regions of distinct slope change in the temperature-time curves, which are encircled for ease of representation. Typical infrared images of (b) PA and (c) 50.5 wt. % DMF + PA, respectively at time t = 548 s. The temperature scale bars are also shown. The green, blue and black arrows indicate the location of the sample, water bath and glass beaker, respectively. The glass beaker appears to be at a lower temperature (pseudo colour back), as glass is not transparent to infrared waves.

The T_O indicates the beginning of the melting process and is obtained from the intersection of the base line and extrapolated tangent from the point of maximum slope on the leading side [412]. The phase transition temperatures were characterized by the peak melting temperatures [489]. The latent heat values were estimated from the area under the peak by numerical integration. The peak melting temperatures, onset temperatures and latent heat values for PA and PA-DMF composite PCMs with various concentrations of DMF are listed in **Table 4.5**.

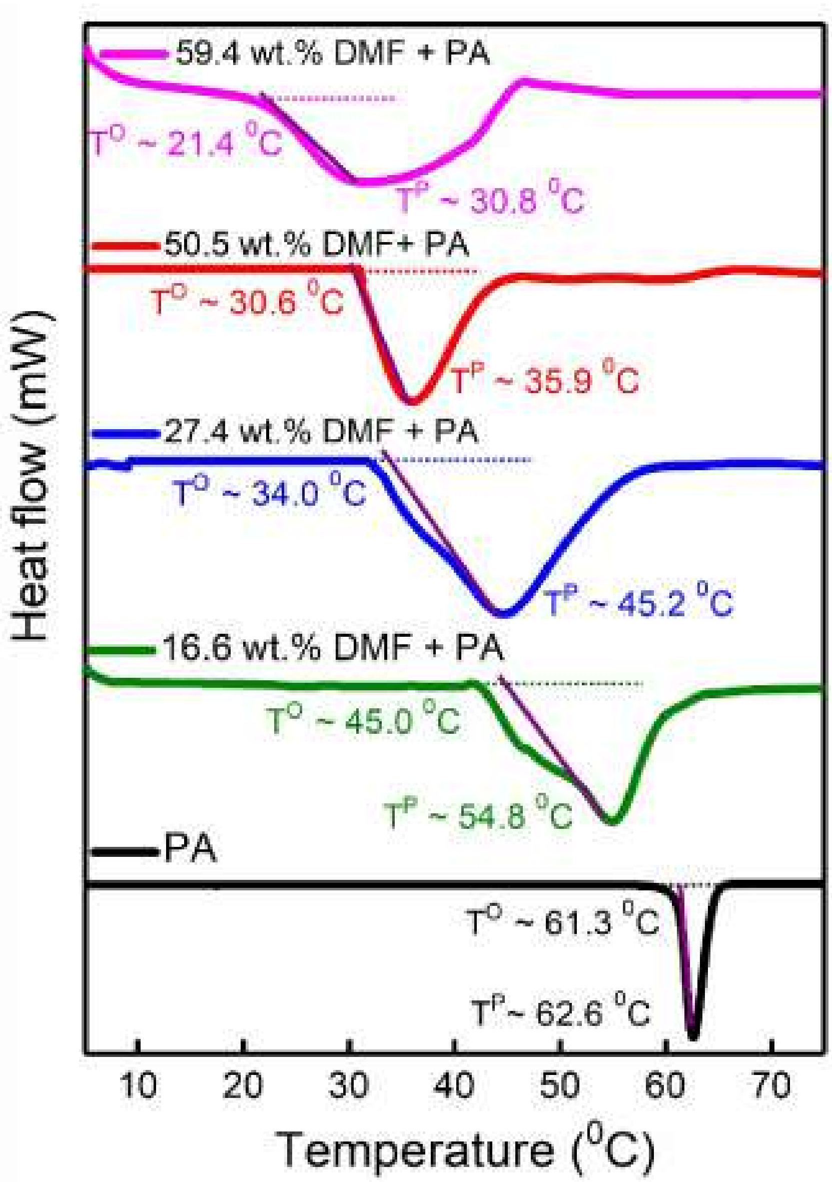

Figure 4.21 Heat flow curves, obtained from DSC studies, for PA and PA-DMF composite PCMs with various concentrations of DMF. The peak melting temperatures (T^P) and onset temperatures (T^O) are indicated in the figure.

In the case of pristine PA, the peak melting temperature was found to be ~ 62.6 ± 0.1 ^{0}C, which was in good agreement with values (~ 61.7 - 62.4 ^{0}C) reported by Sari and Karaipekli [276], Wang et al. [60, 479] and Mehrali et al. [480]. **Fig. 4.21** and **Table 4.5** indicated that the peak melting temperatures and onset temperatures decreased with increasing DMF concentrations.

Table 4.5 Peak melting temperature, onset temperature and latent heat of PA and PA-DMF composite PCMs, with various DMF concentrations.

Material	Onset temperature (T^{O}) (^{0}C) (± 0.5 ^{0}C)	Peak melting temperature (T^{P}) (^{0}C) (±0.1 ^{0}C)	Latent heat (kJ/kg) (± 0.4 kJ/kg)
PA	61.3	62.6	171.0
16.6 wt. % DMF + PA	45.0	54.8	108.0
27.4 wt. % DMF + PA	34.0	45.2	73.0
50.5 wt. % DMF + PA	30.6	35.9	25.0
59.4 wt. % DMF + PA	21.4	30.8	13.5

Vapour pressure of a mixture changes proportionally with the concentration of solute [215, 463] and hence, the depression in phase transition temperature of PA-DMF composite PCMs was found to increase with increasing DMF concentration. **Fig. 4.22a** shows the variation of melting temperature, obtained from DSC, refractive index and infrared thermography experiments, as a function of DMF concentration, where it can be seen that melting temperature decreased with increasing DMF concentration. It can be further seen from **Fig. 4.22a** that the data obtained from the above-mentioned three techniques were in good agreement. In the case of pristine PA, the latent heat of melting was found to be ~ 171.0 ± 0.4 kJ/kg, which was slightly lower than the values (173.7-202.0 kJ/kg) reported in literature [219, 490, 491]. It has been reported that such small variations in latent heat does not significantly affect the applicability of organic PCMs for thermal energy storage [492]. It can be further seen from **Table 4.5** that latent heat decreased with increasing DMF concentration, which is shown graphically in **Fig. 4.22b**. This was attributed to the lower heat of fusion of DMF (~ 110 kJ/kg) and presence of interaction between DMF and PA, as shown from DFT calculations (**Fig. 4.16**) and FTIR spectra (**Fig. 4.17**) of PA-DMF composite PCM.

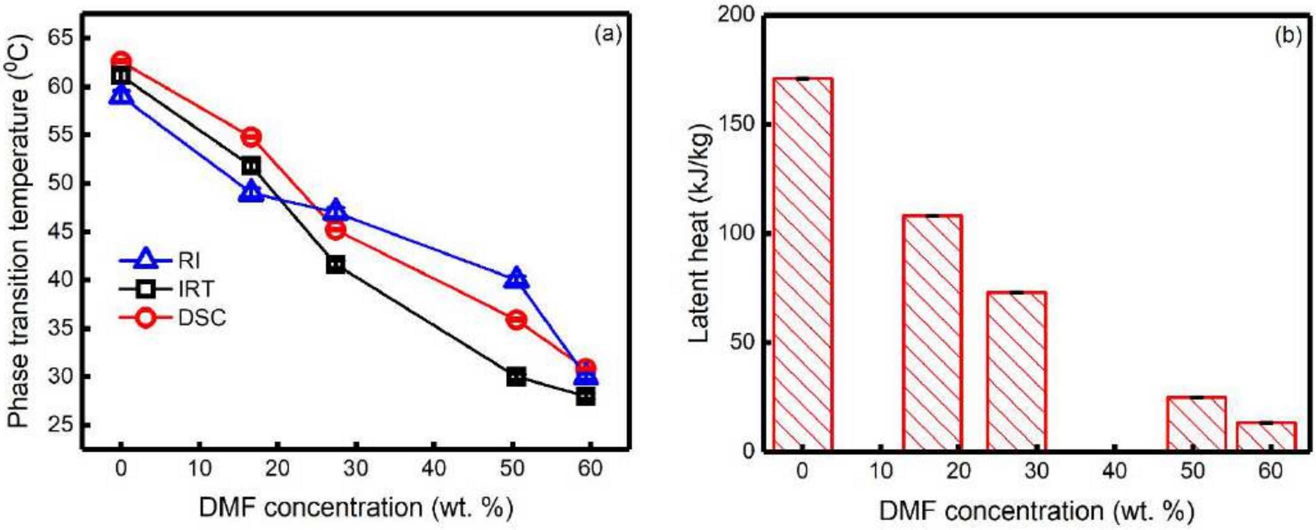

Figure 4.22 Variation of melting temperature, for the PA-DMF composite PCMs, obtained from DSC, RI and IRT experiments, as a function of DMF concentration. (b) Bar chart showing the variation of latent heat for the PA-DMF composite PCMs, as a function of DMF concentration.

Figure 4.23a shows the variation of thermal conductivity in the liquid and solid phases, for pristine PA and PA-DMF composite PCMs with increasing DMF concentration. The thermal conductivity of pristine PA in the liquid state was found to be ~ 0.151 ± 0.002 W/mK. **Fig. 4.23a** indicated that thermal conductivity of the composite PCMs increased monotonically in the liquid state due to the slightly higher thermal conductivity of pure DMF (~ 0.186 ± 0.002 W/mK). In the solid state, on the other hand, thermal conductivity of PA-DMF composite PCM initially increased with DMF concentration and attained a maximum for 50.5 wt. % DMF + PA and decreased thereafter. The initial increase in thermal conductivity with DMF concentration was due to the higher thermal conductivity of DMF. The freezing point of pure DMF is ~ -60.4 ^{0}C and hence, with increasing DMF concentration (especially beyond 50.5 wt. %), the nanocrystalline structure of the composite PCM matrix in solid state, is less orderly due to large mismatch between the freezing points of PA and DMF, which resulted in a decreases of the composite PCM with higher DMF concentration. In the present study, the highest thermal conductivity for 50.5 wt. % DMF + PA was found to be ~ 0.196 ± 0.002 W/mK. Owing to its higher thermal conductivity in the solid state and peak phase transition temperature ~ 36 ^{0}C, this combination was chosen as PCM in the present study.

Figure 4.23b shows the variation of k/k_f and thermal conductivity enhancement (in %) of the PCM, as a function of temperature. Here, k_f indicates the thermal conductivity of the PCM in the liquid state ($k_f \sim 0.162 \pm 0.002$ W/mK), whereas, k is the temperature dependent thermal conductivity. The percentage enhancement in thermal conductivity was calculated as $[(k-k_f)/k_f] \times 100$ %. It can be seen from **Fig. 4.23b** that the variation of k/k_f is divided into three distinct regimes (also indicated in **Fig. 4.23b**). In region-I (for T> 34 ^{0}C), the PCM was in the liquid state. For, 27 ^{0}C<T<34 ^{0}C, the PCM undergoes liquid-solid phase transition and this region is indicated as region-II. For T< 27 ^{0}C, the PCM is macroscopically in the solid state and this region is indicated as region-III. It is evident from **Fig. 4.23b** that thermal conductivity did not enhance significantly in the liquid state, whereas thermal conductivity enhanced by ~ 109 % and ~ 21 % in the phase transition region and solid state (15 ^{0}C), respectively. The higher thermal conductivity in the solid state is due to the presence of orderly and closely packed nanocrystalline microstructure, which aids in phonon mediated efficient heat conduction [216]. Babaei et al. [493] carried out simulations based on molecular dynamics and confirmed the presence of such nano-crystalline structure with regular molecular arrangement during freezing of PCMs. However, thermal conductivity enhancement is the highest in the phase transition region, which is attributed to the accelerated molecular vibration due to an increase in matrix temperature, just before melting [60]. In the liquid state, thermal conductivity enhancement is insignificant due to the lack of orderly microstructure, that severely attenuate phonon propagation [215]. The **inset in Fig. 4.23b** shows an optical phase contrast micrograph of the PCM in the frozen condition, where the formation of brush like microstructures (with several spikes) can be clearly seen. Such anisotropic microstructure has been also reported for n-hexadecane and phenol based PCMs in the solid state [215, 216, 237, 387]. Similarly, for pristine PA, thermal conductivity enhancements in the solid state and phase transition regions were ~ 15.3 % and 187 %, respectively. **Fig. 4.23c** shows the variations of k/k_f and thermal conductivity enhancement (in %) for the PCM, without any nano-inclusion, during consecutive thermal cycling. In the liquid state ($T = 47\ ^0C$), k/k_f was ~ 1 and increased up to ~ 1.21 in the solid state (i.e. ~ 21% enhancement ion thermal conductivity). Further, thermal conductivity enhancements were found to be perfectly reversible even after four thermal cycles, indicating superior thermal stability of the PCM, which is essential for practical thermal energy storage applications. α-Al_2O_3, GNP, MWCNT and CBNP nano-inclusions were added to the PCM and before proceeding with thermal conductivity measurements, nano-inclusion loaded PCMs were subjected to FTIR spectroscopy to ascertain possible chemical interactions. The FTIR spectra of the nano-inclusion loaded PCMs are shown in **Fig. 4.24**. For comparison, the FTIR spectra of the pristine PCM is also shown in the figure. It is evident from **Fig. 4.24** that all major absorption (as shown in **Table 4.4**) bands remain unaltered upon loading with various nano-inclusions. This confirmed the lack of any chemical interactions between the nano-inclusions and the PCM host matrix [49, 494].

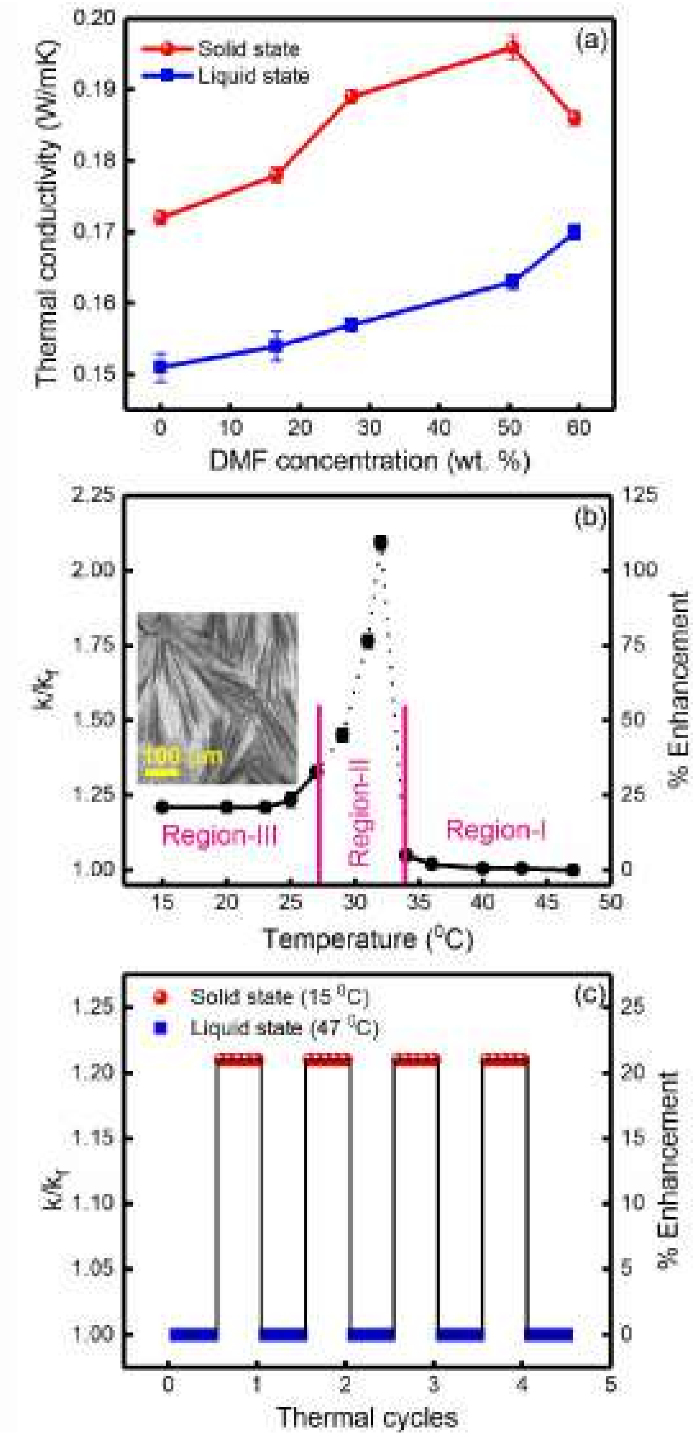

Figure 4.23 (a) Variation of thermal conductivity in the liquid and solid phases for pristine PA and PA-DMF composite PCMs with increasing DMF concentration. (b) Variation of k/k$_f$ and percentage enhancement in thermal conductivity of the PCM (50.5 wt. % DMF + PA), as a function of temperature. (Inset) Optical phase contrast micrograph of the PCM in the frozen condition. (c) Variations of k/k$_f$ and percentage enhancement in thermal conductivity of the PCM, without any nano-inclusion, during consecutive thermal cycling.

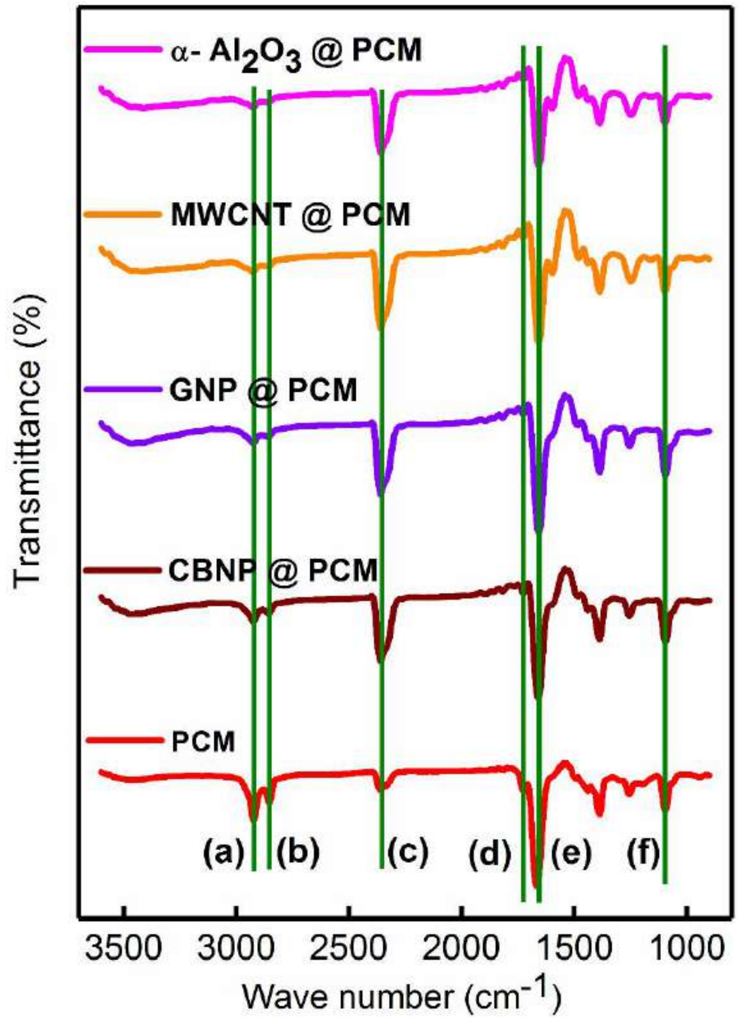

Figure 4.24 FTIR spectra of the PCM loaded with α-Al_2O_3, GNP, MWCNT and CBNP nano-inclusions. For comparison, the FTIR spectra of pristine PCM is also shown in the figure. All the major absorption bands are indexed and described in Table 4.4.

4.3.5 Thermal conductivity enhancement upon loading with different nano-inclusions

Figures 4.25a-d show the variations in k/k_f and thermal conductivity enhancement (in %), as a function of temperature, for the PCM loaded with varied concentrations of α-Al_2O_3, GNP, MWCNT and CBNP nano-inclusions, respectively. The variations of k/k_f for the pristine PCM are also shown in the figures for comparison. It is evident from **Figs. 4.25a-d** that the variations in k/k_f can be clearly divided into three distinct regimes, viz. region I, II and III, corresponding to the liquid state, phase transition region and solid state, respectively. **Fig. 4.25a** shows that, in the liquid state, thermal conductivity enhanced by ~ 6.6, 8.4, 11.1, 12.3, 13.6 and 14.2 % for the PCM loaded with 0.004, 0.007, 0.01, 0.0125, 0.015 and 0.02 vol. fraction of α-Al_2O_3, respectively. On the other hand, thermal conductivity enhancements in the solid state were ~ 26.5, 29.4, 34.6, 36.1, 37.0 and 40.7 % for α-Al_2O_3 loading concentrations of 0.004, 0.007, 0.01, 0.125, 0.015 and 0.02 vol. fraction, respectively. This clearly shows that thermal conductivity enhancements were significantly higher in the solid state, which was due to two different phenomena, viz. formation of nano-crystalline orderly structure in the solid state with higher heat transfer efficiency and formation of a network of percolating structures of the nano-inclusions during freezing that increases the efficiency of phonon mediated heat conduction [342, 387]. However, **Fig. 4.25a** clearly shows that the thermal conductivity enhancements were the highest in the phase transition region, which was attributed to the accelerated molecular vibration due to an increase in matrix temperature, just before melting. In the phase transition region thermal conductivity enhancements were ~ 153.1, 156.2, 160.5, 165.4, 150.0 and 154.3 % for the PCM loaded with 0.004, 0.007, 0.01, 0.125, 0.015 and 0.02 vol. fraction of α-Al_2O_3, respectively.

Figure 4.25b shows that the thermal conductivity enhancements in the liquid states were ~ 7.4, 11.1, 14.2, 16.1, 17.3 and 19.1 % for the PCM loaded with 0.004, 0.007, 0.01, 0.0125, 0.015 and 0.02 vol. fraction of GNP, respectively. For a similar variation in loading concentration, thermal conductivity enhancements in the phase transition region were ~ 116.1, 122.2, 134.6, 140.7, 143.8 and 140.7 %, respectively. On the other hand, thermal conductivity enhancements in the solid state were ~ 27.8, 32.7, 38.9, 43.2, 46.3 and 48.8 % for the PCM loaded with 0.004, 0.007, 0.01, 0.0125, 0.015 and 0.02 vol. fraction of GNP, respectively. **Fig. 4.25c** shows that the thermal conductivity enhancements in the phase transition region were ~ 140.7, 148.1, 156.2, 159.3, 165.4, 166.7 % for loading concentrations of 0.004, 0.007, 0.01, 0.0125, 0.015 and 0.02 vol. fraction, respectively. For similar loading concentrations, thermal conductivity enhancement in the liquid states were ~ 9.8, 12.3, 14.2, 14.8, 15.4 and 14.8 %, respectively. On the other hand, in region-III (solid state), thermal conductivity enhancements were ~ 27.2, 29.0, 33.3, 35.8, 41.9 and 34.6 % for the PCM loaded with 0.004, 0.007, 0.01, 0.0125, 0.015 and 0.02 vol. fraction of MWCNT, respectively. **Fig. 4.25d** shows that the liquid state thermal conductivity enhanced by ~ 3.7, 4.9, 6.8, 7.4, 8.6, 9.3, 9.8, 9.9 and 11.1 % for the PCM loaded with 0.004, 0.007, 0.01, 0.0125, 0.015, 0.02, 0.03, 0.04 and 0.05 vol. fraction of CBNP, respectively. In the phase transition region, the corresponding values of thermal conductivity enhancements were ~ 116.1, 127.2, 134.6, 140.7, 143.8, 146.9, 150.0, 153.1, and 146.9 %, respectively. Thermal conductivity enhancements in the solid state were ~ 29.0, 33.9, 38.3, 42.6, 45.7, 51.2, 58.6, 64.2 and 67.2 % for CBNP loading concentrations of 0.004, 0.007, 0.01, 0.0125, 0.015, 0.02, 0.03, 0.04 and 0.05 vol. fraction, respectively.

Figures 4.26a-d show the variation of k/k_f and thermal conductivity enhancement (in %) in the liquid state as a function of loading concentration (in vol. % = $\phi \times 100$ %, ϕ being vol. fract.) for the α-Al_2O_3, GNP, MWCNT and CBNP loaded PCMs, respectively. It can be seen from **Figs. 4.26a-d** that thermal conductivity generally enhanced with increasing concentration of the nano-inclusions, however at higher loading concentration, thermal conductivity enhancements showed saturation tendency. In fact, thermal conductivity slightly decreased for the PCM loaded with 2 vol. % of MWCNT. **Figs. 4.26a-d** also shows the theoretical curves for thermal conductivity enhancements obtained from Hamilton-Crosser (HC) and classical Maxwell-Garnett (MG) models [38, 366], where it can be observed that the experimental data were significantly higher than those calculated from classical models, which indicated the presence of aggregates in the liquid state [215, 289]. It can be further seen that the difference between the theoretical and experimental data was comparatively lower for HC model, which was due to the incorporation of particle shape factor (~ 3 and 6 for spherical α-Al_2O_3 nanoparticles and MWCNT, GNP and CBNP nano-inclusions, respectively) in the calculations.

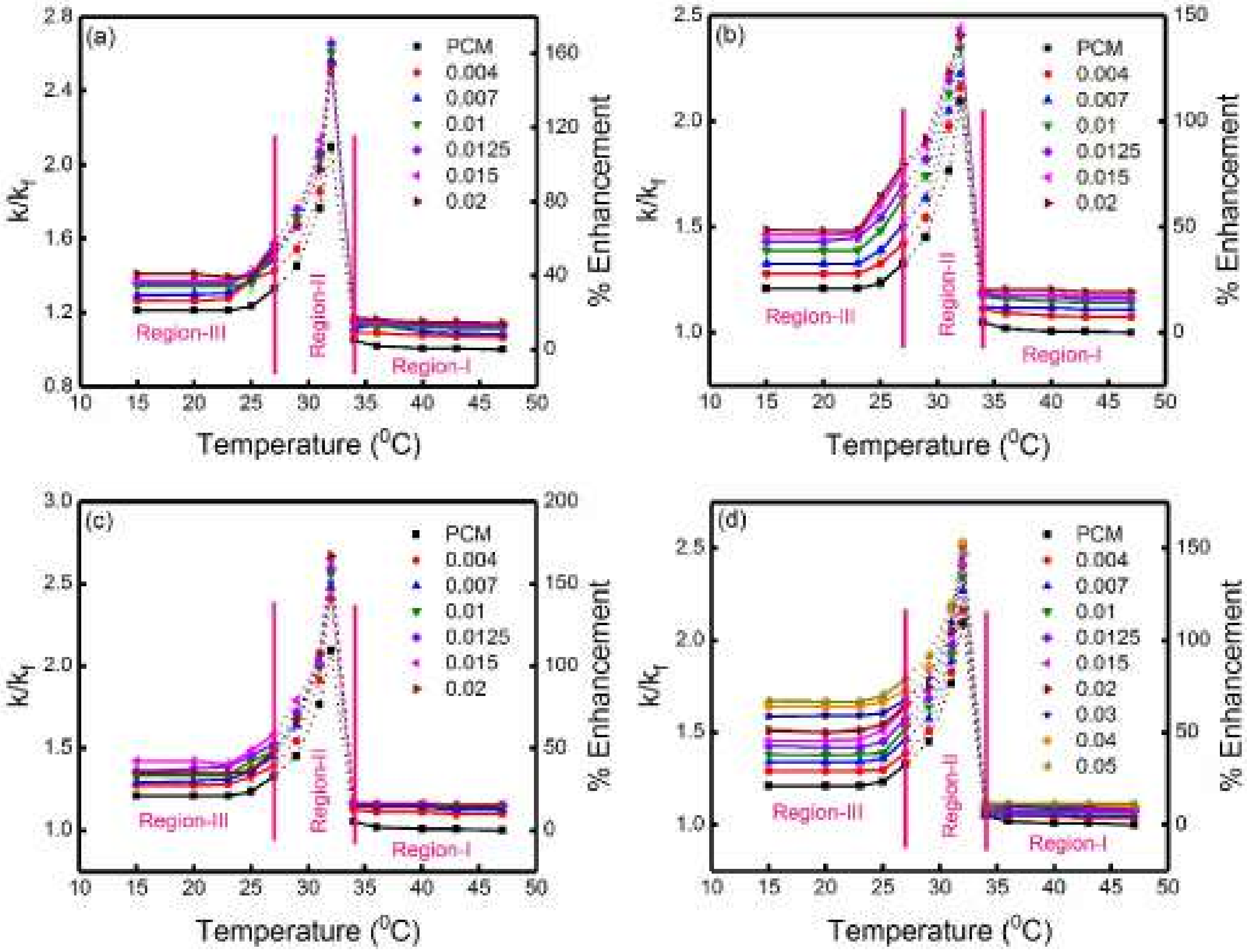

Figure 4.25 Variations in k/k_f and thermal conductivity enhancement (in %), as a function of temperature, for the PCM loaded with various concentrations of (a) α-Al_2O_3, (b) GNP, (c) MWCNT and (d) CBNP nano-inclusions. The variations of k/k_f for the pristine PCM are also shown in the figures for comparison.

The nano-inclusions form aggregate in the liquid state under van-der Waal's interaction and with increasing loading concentrations the aggregate size grows (within the realm of well-dispersed aggregates), leading to an increase in thermal conductivity enhancement [342]. It has been reported that such aggregates are fractal in nature and consist of a quasi-continuous backbone and randomly placed dead-ends, which does not effectively contribute towards thermal conductivity enhancements [341].

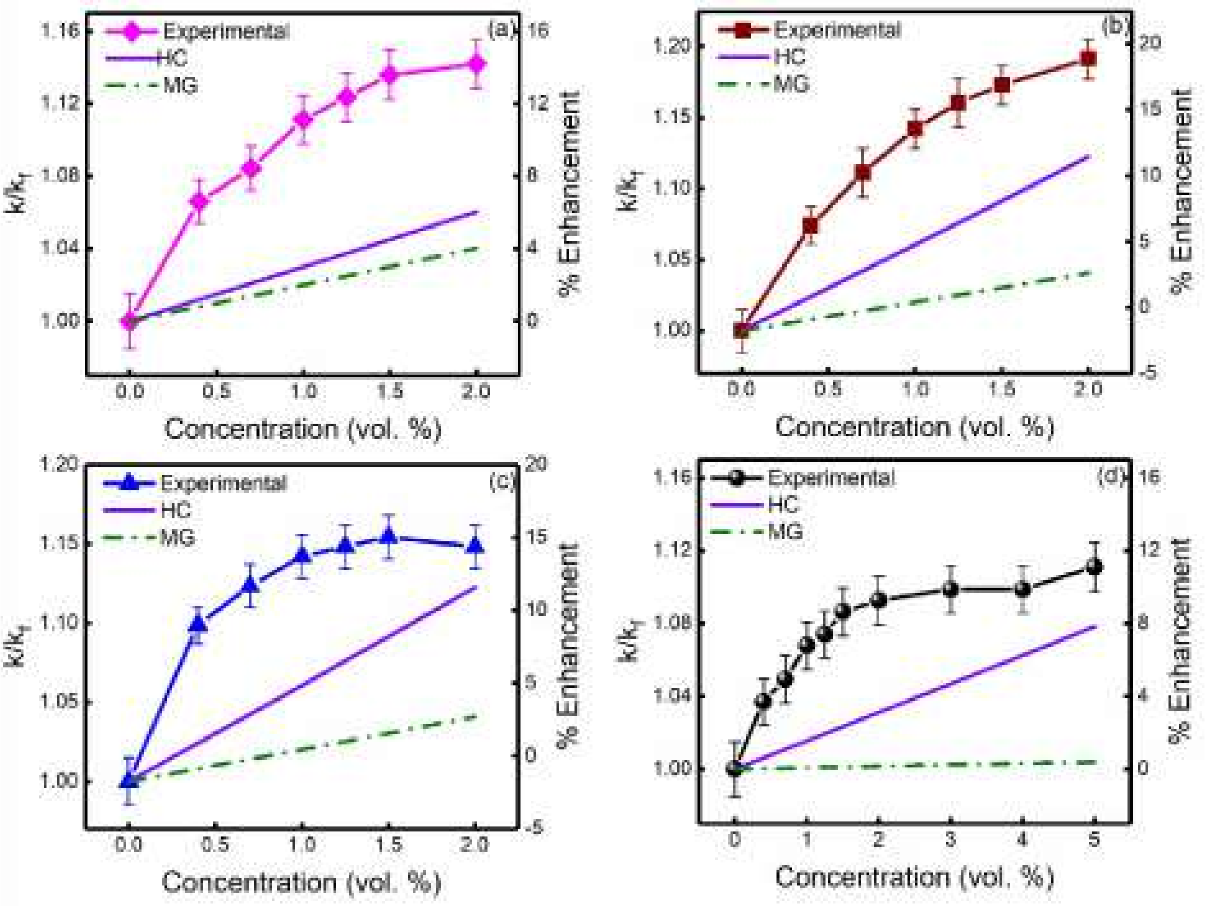

Figure 4.26 Variations in k/k_f and thermal conductivity enhancement (in %) in the liquid state, as a function of loading concentration, for the PCM loaded with various concentrations of (a) α-Al_2O_3, (b) GNP, (c) MWCNT and (d) CBNP. The theoretical curves for thermal conductivity enhancements, obtained from Hamilton-Crosser (HC) and classical Maxwell-Garnett (MG) models, are also shown in the corresponding figures.

With further increase in loading concentration, the number of such randomly placed dead-ends increases. In addition, such larger aggregates phase separated due to sedimentation. Hence, thermal conductivity enhancements showed saturation tendency or decreasing trend at higher loading concentrations. **Figs. 4.27a-d** show the variation in k/k_f and thermal conductivity enhancement (in %) in the solid state, as a function of concentration (in vol. % = $\phi \times 100$ %, ϕ being vol. fract.), for the PCM loaded with α-Al_2O_3, GNP, MWCNT and CBNP nano-inclusions, respectively. It can be seen from **Fig. 4.27** that for the PCM loaded with α-Al_2O_3, GNP and CBNP nano-inclusions, k/k_f progressively increased with loading concentrations. With increase in loading concentration, larger nano-inclusion aggregates are formed that causes the thermal conductivity to enhance in the solid state. To probe the increase in aggregate size, optical phase contrast microscopy imaging was carried out in the liquid and solid states for the PCM loaded with 0.004, 0.007 and 0.015 vol. fraction of CBNP nano-inclusions and **Figs. 4.28a-f** show the corresponding photo-micrographs. The increase in aggregate size and reduced inter-aggregate spacing are clearly discernible from **Fig. 4.28**, at higher particle loading. Such larger aggregates enhanced the phonon mediated percolative heat transfer [238], augmented the near-field radiative heat transfer due to reduced inter-inclusion spacing [419] and reduced the thermal barrier resistance [237]. All of these factors contributed towards the enhanced thermal conductivity of the nano-inclusion loaded PCMs, in the solid state, with increasing particle loading. Further, the formation of inter-connected percolation pathways is also clearly discernible from the microscopy images obtained in the solid state (**Figs. 4.28d-f**), which was due to the squeezing of the nano-inclusions during freezing of the PCM, as subsequently discussed. However, for the PCM loaded with MWCNT, thermal conductivity decreased at the highest loading concentration of 2 vol. % (**Fig. 4.27c**). This was attributed to the formation of larger aggregates that phase separated at higher concentration and did not contribute to the thermal conductivity enhancement. It must be noted that for the PCM loaded with MWCNT, thermal conductivity also showed a decreasing trend at the highest loading concentration in the liquid state (see **Fig. 4.26c**).

Enhancement of thermal conductivity, obtained in the present study, is comparable or higher than the values reported in literature for PA based PCMs loaded with various metallic or carbon based nano-inclusions. A few representative values for PA based PCMs are shown in **Table 4.6** along with the nature and concentrations of the nano-inclusions added to the PCM host matrix [54, 60, 69, 70, 247, 276, 479, 490, 491].

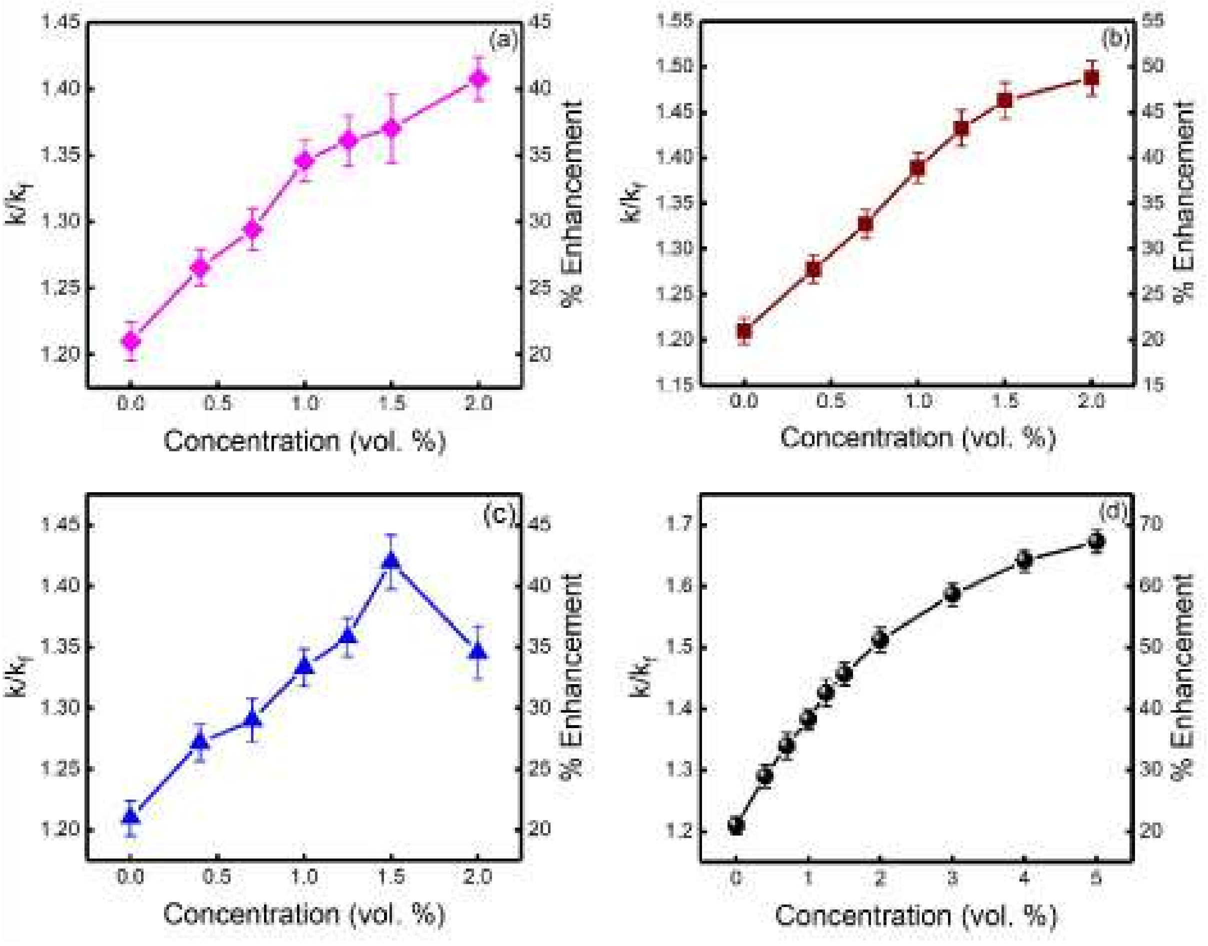

Figure 4.27 Variation in k/k$_f$ and thermal conductivity enhancement (in %) in the solid state, as a function of concentration, for the PCM loaded with (a) α-Al_2O_3, (b) GNP, (c) MWCNT and (d) CBNP nano-inclusions.

It can be seen from **Table 4.6** that thermal conductivity enhancements, in the solid state, were ~ 80.0, 65, 76.5 % for PA based PCMs loaded with 5 wt. % of TiO2, 7 wt. % of MWCNT and 10 wt. % of expanded graphite, respectively [54, 69, 276]. On the other hand, in the present study, the highest thermal conductivity enhancement in the solid state was obtained as

~ 67.3 %, which is comparable to or higher than most of the earlier reported values (see **Table 4.6**).

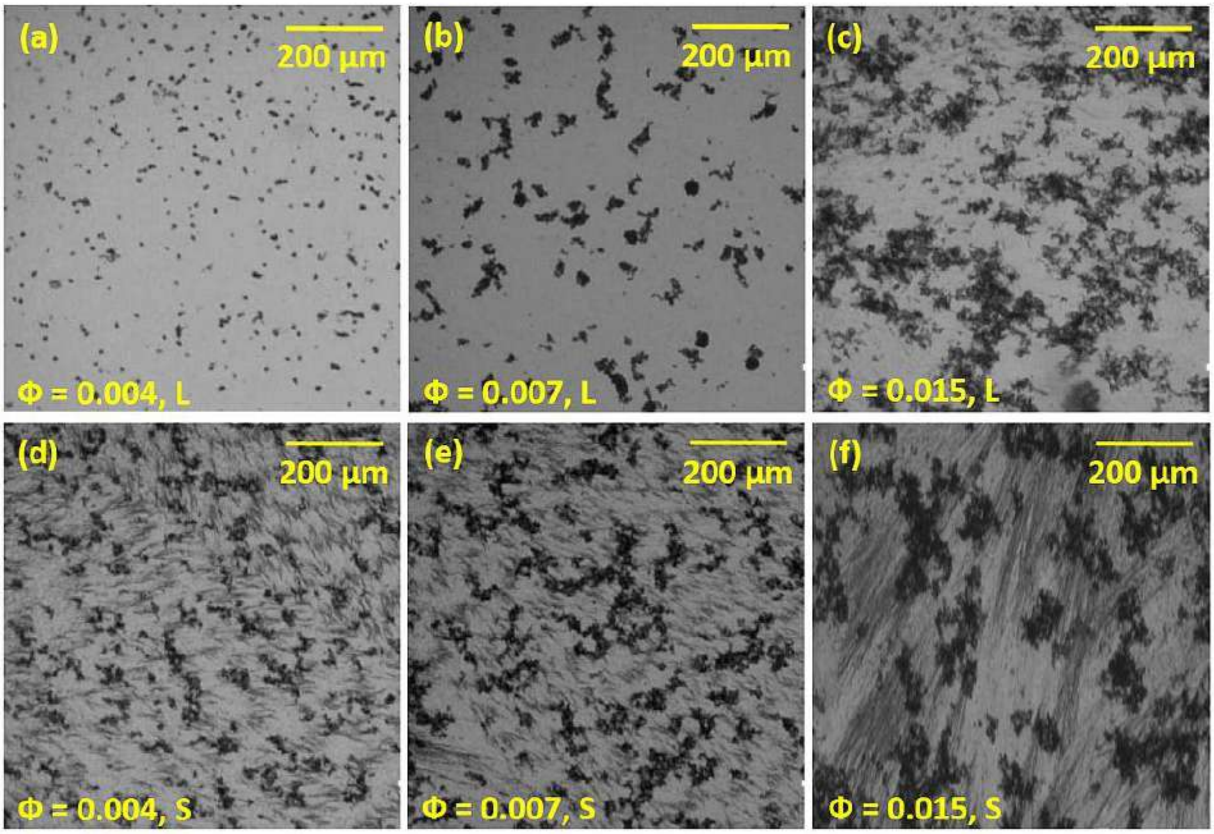

Figure 4.28 Optical phase contrast microscopy images of the PCM loaded with various concentrations (in vol. fractions, ϕ) of CBNP nano-inclusions in the liquid (L) and solid (S) states. (a) $\phi = 0.004$ in L, (b) $\phi = 0.007$ in L, (c) $\phi = 0.015$ in L, (d) $\phi = 0.004$ in S, (e) $\phi = 0.007$ in S and (f) $\phi = 0.015$ in S.

In the literature, higher thermal conductivity enhancement has been reported for PA based PCM loaded with larger concentrations of carbon-based or metallic nano-inclusions. This increases the operational cost of the PCM based LTES. On the other hand, in the present study, significantly high thermal conductivity enhancement has been achieved using CBNP nano-inclusions at lower loading concentrations (0.6 wt. %). Moreover, CBNP is comparatively cheaper (typical cost of research grade CBNP, MWCNT, SWCNT and graphene oxide are ~ < \$1/g, \$5/g, \$75/g and \$100/g, respectively [495]), thereby making the PCM systems financially more viable. Further, low density of CBNP nano-inclusions (density of CBNP, graphite and aluminum are ~ 0.1, 2.3 and 2.7 g/cc, respectively) does not increase the weight of the CBNP loaded PCM, which is advantageous for industrial applications.

Table 4.6 Representative values of thermal conductivity enhancement in the solid state for PA based PCMs loaded with various nano-inclusions

Nano-inclusions		Thermal conductivity enhancement in solid state (in %)	Year	Reference
Name	Concentration in wt. % (vol. fract.)			
MWCNT (surface functionalized)	1.0 wt. % 2.0 wt. % 5.0 wt. %	~ 10 ~ 33 ~ 56	2008	[479]
MWCNT	5.0 wt. %	~ 26.3	2009	[491]
Expanded graphite	10.0 wt. %	~ 76.5	2009	[276]
MWCNT (modified by mechano-chemical reaction)	1.5 (0.01)	~ 52	2010	[70]
MWCNT	1.0 wt. %	~ 46.0	2010	[60]
MWCNT (oxidized)	7.0 wt. %	~ 65.0	2012	[69]
TiO_2	0.5 wt. % 1.0 wt. % 3.0 wt. % 5.0 wt. %	~ 12.7 ~ 20.6 ~ 46.6 ~ 80.0	2016	[54]
CuO nanoparticles (SDBS capped)	0.1 wt. % 0.2 wt. % 0.3 wt. %	~ 19.9 ~ 45.6 ~ 66.1	2018	[247]
α-Al_2O_3 GNP MWCNT CBNP CBNP	8.5 (0.02) 4.9 (0.02) 2.9 (0.02) 0.2 (0.02) 0.6 (0.05)	~ 40.7 ~ 48.8 ~ 34.6 ~ 51.2 ~ 67.2	2019	**Present study**

In the present study, CBNP nano-inclusions were used in the as-received condition without any cumbersome sample preparation steps. This clearly shows the efficacy of CBNP nano-inclusions for enhancing the thermal conductivity of organic PCMs. Nevertheless, a few studies reported extremely higher thermal conductivity enhancements (~ 390 % and 238 %) for shape stabilized PA based PCMs loaded with 10 wt. % GNP and 7.9 wt. % polyaniline and exfoliated graphite nanoplatelets, respectively, where the higher thermal conductivity enhancements were attributed to very high in-plane thermal conductivity of the nano-inclusions [59, 496]. However, such PCMs require extensive sample preparation (like vacuum impregnation) that significantly increases the operational cost.

Figures 4.29a-d show the variations of k/k_f and thermal conductivity enhancement (in %) during repeated thermal cycling for the PCMs loaded with α-Al_2O_3, GNP, MWCNT and CBNP nano-inclusions, respectively. For thermal cycling, five independent measurements were performed in the molten condition (47 ^{0}C) and then the PCMs were allowed to freeze and measurements were repeated in the frozen state (15 ^{0}C). For the pristine PCM, thermal conductivity enhancements were found to be perfectly reversible, during thermal cycling (see **Fig. 4.23c**), whereas for the nano-inclusions loaded PCMs, some irreversibility was observed. For the PCMs loaded with α-Al_2O_3, GNP, MWCNT and CBNP nano-inclusions, thermal conductivity enhancements in the solid states were ~ 33.7, 37.4, 32.5, 38.0; 25.8, 28.8, 25.8, 31.9; 22.7, 25.2, 23.3, 27.6 and 21.5, 24.5, 22.1, 22.7 % after first, second, third and fourth cycles, respectively. This was attributed to the irreversible aggregation dynamics of the nano-inclusions. After subsequent freezing and melting cycles, the aggregates of nano-inclusions (formed due to van der Waal's interaction) do not re-disperse reversibly, leading to the variations in the thermal conductivity enhancements [237]. Moreover, the aggregates grow in size, during consecutive thermal cycles, which increases the phonon scattering at the rough interfaces. It has been reported that for weak-solid fluid interaction, a positive Kapitza length leads to a negative thermal conductivity enhancement [45]. Hence, the k/k_f values were found to be irreversible for the nano-inclusion loaded PCMs, after successive thermal cycles.

However, the degree of irreversibility (mismatch between k/k_f values between two successive thermal cycles) was found to decrease progressively with increasing number of thermal cycles, which was beneficial for practical applications.

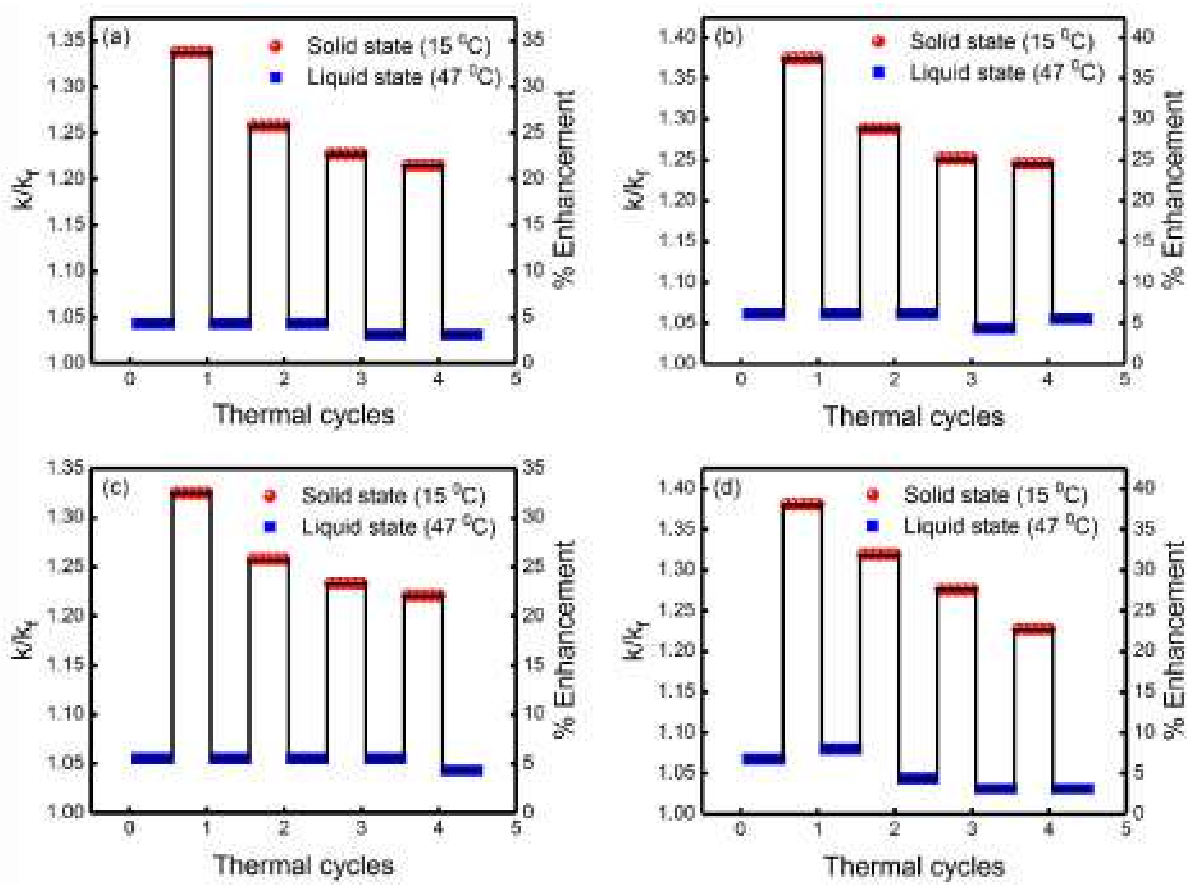

Figure 4.29 Variations in k/k_f and thermal conductivity enhancement (in %) during repeated thermal cycling for the PCMs loaded with (a) α-Al_2O_3, (b) GNP, (c) MWCNT and (d) CBNP nano-inclusions.

4.3.6 Nano-inclusion aided thermal conductivity enhancement: microscopic observation of aggregation phenomena

Thermal conductivity enhancement in nanofluids, in general, has been a topic of intense scientific scrutiny and various theoretical models have been proposed to explain the experimental data sets, viz. clustering, micro-convection and Brownian motion, ballistic heat transfer, interfacial layer and several modifications of classical Maxwell theories [38, 50, 346, 362, 363]. Among these theories, however, nanoparticle clustering and associated percolative heat transfer is the most widely accepted theory that shows significant agreement with most of the experimental data sets [341, 342, 346, 362, 385, 386]. Similarly, thermal conductivity enhancement in nano-inclusions loaded PCMs has also been studied extensively, primarily from the applications point of view. However, there exist considerable debate on the microscopic mechanism of thermal conductivity enhancement and the aggregation effects are not well understood, especially near the phase transition regime and in the solid state. It has been hypothesized that during freezing, solidification induced stress fields are generated within the PCM host matrix. The stress fields drive the nano-inclusions towards each other or towards the grain boundaries leading to the formation of a network of percolating structures, which is favourable to enhanced heat transfer [237, 387, 395]. Internal stress measurements in frozen hexadecane, using pressure-sensitive films, confirmed uneven and anisotropic stress distribution, which aided in the formation of percolating structures [387]. Squeezing of the nano-inclusions leads to improved contact between them, which results in a decrease of thermal barrier resistance (or Kapitza resistance), ultimately causing an enhancement of phonon mediated heat transfer [234, 342]. Enhanced percolative heat transfer has also been observed in stable graphite dispersions [238]. Moreover, it has been recently reported that substantially lower inter-inclusion distance leads to an augmentation of near-field radiative heat transfer, which also contributes to the to the total enhancement of thermal conductivity in nano-inclusion loaded PCMs [419].

The nano-inclusion aggregates are fractal in nature and consist of a quasi-continuous backbone of closely attached nano-inclusions, which span the volume defined by the radii of gyration of the aggregates and randomly distributed dead-ends [342]. The aggregation dynamics influence the heat transfer phenomena and the resultant thermal conductivity enhancement in nano-enhanced PCM is due to triple homogenization effects, proposed by Prasher and Evans [341]. In the first level, dead-ends are homogenized with the continuous medium and thereafter the backbone is superimposed in the second level to obtain effective cluster thermal conductivity. These clusters are finally homogenized with the host matrix to obtain the effective thermal conductivity of the nano-inclusion loaded PCMs. The detailed theoretical calculations for the three-level homogenization model can be found elsewhere [216, 341, 342, 421].

This has been the most widely accepted mechanism of nano-inclusion aided thermal conductivity enhancement of PCM and a plethora of scientific studies have been based on this theoretical framework [9, 15, 38, 65, 83, 234, 497, 498]. Nevertheless, there has been no direct observational proof towards solidification induced cluster formation in nano-inclusion loaded PCM. In this study, direct experimental evidence is provided for cluster formation during solidification, using real-time phase contrast optical microscopy video. **Fig. 4.30** shows a few snapshots from the real-time video microscopy multimedia field, where solidification induced cluster formation is shown. The propagation of the solidification wave-fronts was clearly discernible from **Fig. 4.30b** (indicated by the dashed arrows in magenta). These solidification fronts represented the solidification induced stress fields in the PCM host matrix, which squeezed the nano-inclusions to form larger aggregates. From **Figs. 4.30a-b** the formation of an interconnected cluster can be seen. In **Fig. 4.30a**, the clusters were well separated, whereas in **Fig. 4.30b**, the clusters appeared interconnected, due to the solidification induced stress field (indicated by the solid arrows in red). Similarly, **Figs. 4.30e-g** (70-90 s) show the formation of another interconnected cluster (encircled by the solid line in light blue). **Figs. 4.30i-k** (103-110 s) show a dynamic event, where a small nano-cluster can be found to travel towards a larger cluster and eventually attach to it (indicated by the solid arrows in orange). It must be noted that this dynamic event occurred within a time span of ~ 7 s. Formation of such larger cluster is energetically favourable and leads to the formation of a larger network of percolating structures. On the other hand, the central large cluster became more tightly bound and interconnected with other smaller clusters (**see Figs. 4.30e, h & l**, encircled by dashed line in deep blue). The lower thermal barrier resistance in these tightly bound clusters (because of improved aggregate/aggregate contact) augment phonon mediated heat transfer through the percolation network, eventually spanning over the entire host matrix.

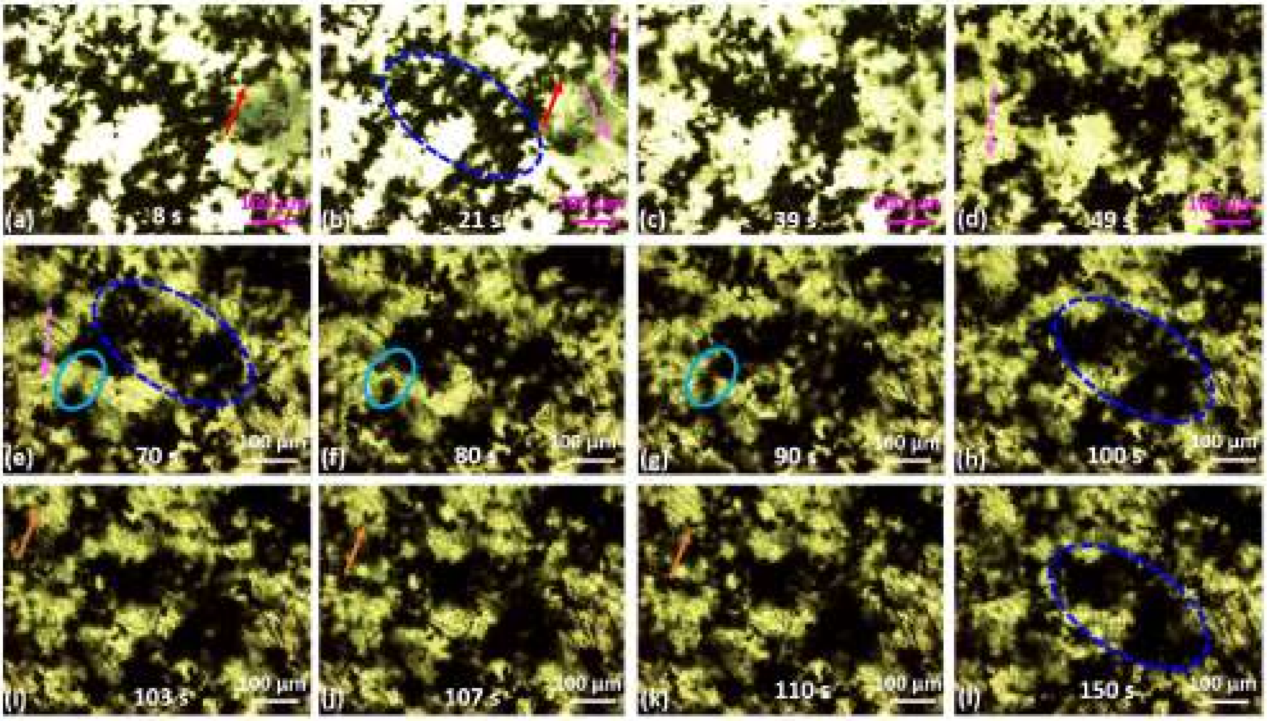

Figure 4.30 A few time-stamped snapshots from the phase contrast optical microscopy video analysis, during solidification of the PCM loaded with 0.02 vol. fraction of CBNP nano-inclusions. The time stamps are: (a) 8 s, (b) 21 s, (c) 39 s, (d) 49 s, (e) 70 s, (f) 80 s, (g) 90 s, (h) 100 s, (i) 103 s, (j) 107 s, (k) 110 s and (l) 150 s. The dashed arrows in magenta, in (b, d and e), indicate the solidification wave fronts which represented solidification induced stress fields in the PCM host matrix. The solid red arrows in (a-b) show the formation of an interconnected cluster. The solid encircling in light blue, in (e-g), shows formation of another inter-connected cluster. The dashed encircling in deep blue, in (b, e, h and l), shows the formation of more closely packed cluster. The solid arrows in orange, in (i-k) show a dynamic event, where a smaller cluster gets attached to a larger cluster during freezing.

Based on these observations, the mechanism of formation of percolation network is schematically shown in **Fig. 4.31a**. At first, the nano-inclusion are isolated and no percolative network exist (box-1 in **Fig. 4.31a**). Thereafter, the nano-inclusions grow in size and also moves towards each other due to the solidification stress fields, eventually forming percolation contacts with each other (box-2 in **Fig. 4.31a**). The growth in aggregate size is energetically favourable, as surface energy is minimized during the process (due to a decrease in surface-to-volume ratio) [385]. The **inset of Fig. 4.31a** shows the schematic of a percolation contact between two nano-inclusions. The phonon mediated heat transfer is severely attenuated in the entrapped liquid layer in-between the nano-inclusions. However, as the nano-inclusions are squeezed towards each other, due to solidification induced stress fields, the entrapped liquid layer is eventually expelled during solidification leading to an improved aggregate/aggregate contact with lower thermal barrier resistance. Such percolation contacts are favourable for efficient heat transfer with significantly less interfacial phonon scattering. Finally, a quasi-2d percolating network is formed (box-3 in **Fig. 4.31a**), spanning over the entire PCM host matrix, that resulted in a significant enhancement in thermal conductivity for the nano-inclusion loaded PCM.

Figure 4.31b shows a bar chart comparing the k/k_f and percentage enhancement in thermal conductivity of the PCM loaded with 0.02 vol. fraction of α-Al_2O_3, GNP, MWCNT and CBNP nano-inclusions, in the solid state. The highest thermal conductivity enhancement was obtained for the PCM loaded with CBNP nano-inclusions, followed by GNP, α-Al2O3 and MWCNT loading (in the decreasing order). However, the bulk thermal conductivity was the highest for MWCNT (~ 6600 W/mK) followed by GNP (~ 3000 W/mk), α-Al_2O_3 (~ 35 W/mK) and CBNP (~ 0.182 W/mK) [38]. This clearly showed effective thermal conductivity enhancements in nano-inclusion loaded PCMs is not significantly influenced by the bulk thermal conductivities of the nano-inclusions and several other factors like nature of fractal structures, aggregation dynamics and variation in Kaptiza resistance play a more prominent role [216, 434].

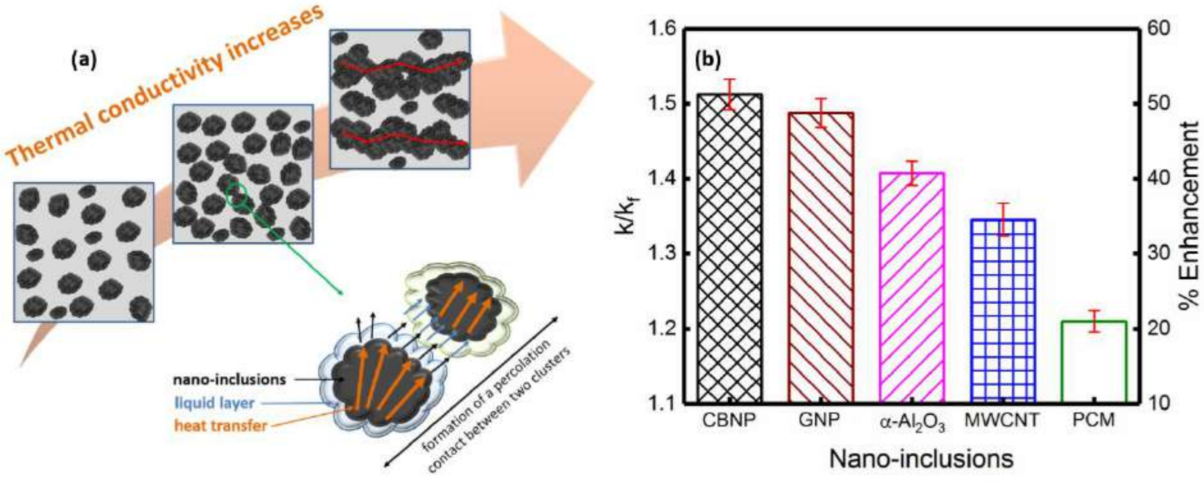

Figure 4.31 (a) Schematic representation of the formation of percolation network in nano-inclusion loaded PCM. (Inset) Schematic showing the formation of a percolation contact between two nano-inclusions aggregates. The phonon mediated heat transfer is severely attenuated in the entrapped liquid layer in-between the nano-inclusions. The entrapped liquid layer is eventually expelled during freezing of the PCM due to solidification induced stress field, leading to efficient percolative heat transfer. (b) Bar chart comparing the k/k_f of the PCM loaded with α-Al_2O_3, GNP, MWCNT and CBNP nano-inclusions, in the solid state. The percentage enhancement in thermal conductivity is also shown in the figure. The loading concentration was kept constant at 0.02 vol. fraction.

Molecular dynamics based studies reported a comparatively weaker bonding between the MWCNT and PCM matrix [499], which caused a higher tube/tube and tube/PCM matrix thermal barrier resistance leading to a comparatively lower thermal conductivity enhancements for the PCMs loaded with MWCNT [70]. On the other hand, GNP forms larger 2D networks of percolation pathways [65] and act as nucleation sites, during freezing of the PCM, leading to a stronger GNP/PCM matrix bonding [430]. Moreover, lower thermal barrier resistance of GNP also aided in the observed higher thermal conductivity enhancement for the GNP loaded PCM. However, the highest thermal conductivity enhancement was obtained for the PCM loaded with CBNP nano-inclusions due to low fractal dimension of the CBNP aggregates, coupled with excellent compressibility and volume filling capacity [236, 477]. CBNP forms grape-like (aciniform) aggregates of primary carbon black nanoparticles, which are called nodules [407]. The smaller aggregate size and excellent volume filling capacity are favourable to the formation of the quasi-2D network of percolation pathways, during freezing of the PCM, with reduced inter-aggregate gaps that is beneficial for phonon mediated heat transfer [431]. Thermal conductivity contrast of ~ 3.3 was reported for octadecane based PCM loaded with ~ 0.12 vol. fraction of CBNP, where the higher thermal conductivity enhancement was attributed to the formation of a fractal network of CBNP nano-inclusions, spanning over the entire PCM matrix [236]. This was in agreement with the microscopic observations made in the present study (**Fig. 4.30**), where a quasi-continuous network of CBNP, spanning over the entire PCM matrix, was seen. In general, nano-inclusion aided enhancement in thermal conductivity is limited due to phonon scattering at the interfaces (aggregate/aggregate and aggregate/matrix) [432]. CBNP nano-inclusions, on the other hand formed closely packed aggregates with augmented aggregate/matrix bonding and improved aggregate/aggregate contact that reduced the thermal barrier resistance and increased phonon coupling along the percolative trajectories of CBNP. This is in agreement with the predications of acoustic mismatch and diffuse mismatch models of scattering for the high and low wavelength phonons, respectively [442, 443]. Hence, CBNP loaded PCM exhibited the highest thermal conductivity enhancement in the solid state, as observed from **Fig. 4.31b**. This study shows the efficacy of cheaper CBNP nano-inclusions to achieve higher thermal conductivity enhancement in a PCM host matrix that is comparable to the other alternatives, which are either costly or requires extensive sample preparations.

4.4 Summary and conclusions

Thermal conductivity enhancement was studied across first order liquid-solid phase transition in phenol-water system incorporated with four different nano-inclusions, viz. α-Al_2O_3, SiO_2, hydrophobic SiO_2 and TiO_2. The phase transition temperature of the phenol-water system was tuned by adjusting the phenol-water ratio. Incorporation of nano-inclusions to the PCM caused an enhancement in thermal conductivity which was more prominent in the solid state. This was attributed to the formation of nano-crystalline needle like microstructure, during freezing, which was confirmed from optical phase contrast microscopy. Formation of needle like microstructures during freezing squeezed the nano-inclusions towards the grain boundaries, thereby forming a network of high thermal conducting percolating pathways, which caused an enhancement in thermal conductivity. With α-Al_2O_3, SiO_2 and hydrophobic SiO_2 inclusions, thermal conductivity enhancement increased with concentration due to the formation of larger aggregates at higher concentrations. Atomic force microscopy images confirmed increased contact area between the closely packed larger aggregates at higher concentrations, which resulted in a decreased interfacial resistance, thereby aiding in efficient heat transfer. Thermal conductivity enhancement for the PCM incorporated with hydrophobic SiO_2 was found to be lower, as compared to the PCM loaded with hydrophilic SiO_2, which was attributed to the higher interfacial resistance of the hydrophobic nano-inclusion/PCM interface. On the other hand, in the case of TiO_2 nano-inclusions, thermal conductivity enhancement increased up to a certain concentration (3 wt. %) and beyond that, it decreased, possibly due to the higher aggregation probability of TiO_2. Addition of 0.02 and 0.04 wt. % of CBNP increased the thermal conductivity enhancement to 44.7 and 45.9 %, 41.7 and 45.3 % for PCM loaded with 4 wt. % of α-Al_2O_3 and 3 wt. % of SiO_2, respectively. The synergetic enhancement was attributed to the fractal nature of the CBNP aggregates, which acts as volume filling agents, increasing the efficiency of the thermal trajectories. Experimental results demonstrated the possibility of nano-inclusion assisted enhancement in thermal conductivity in phenol-water system (PCM) with tunable phase transition temperature for room temperature thermal energy storage applications, like thermo-regulation of buildings, domestic refrigeration or cooling and reversible thermal switches.

Thermal conductivity enhancement across the first order liquid-solid phase transition was studied for palmitic acid (PA)-di-methyl formamide (DMF) based organic phase change material (PCM), loaded with various concentrations of α-Al_2O_3, GNP, MWCNT and CBNP nano-inclusions. The phase transition temperature was tuned from ~ 61 to 31 ^{0}C by tuning the PA-to-DMF ratio. DFT based theoretical studies were carried out to understand the PA-DMF complex formation and the same was verified using FTIR spectroscopy. DSC studies were carried out to probe the variations in phase transition temperature and latent heat values with increasing DMF concentration. PA-DMF composite PCM with 50.5 wt. % DMF was chosen due to its higher thermal conductivity in the solid state and phase transition temperature ~ 36 ^{0}C, which is ideal for various practical applications. Studies revealed large thermal conductivity enhancement in the solid state and phase transition region, due to the presence of nano-crystalline microstructure, in the solid state, decorated with quasi-2D percolation network of the nano-inclusions, in the solid state. Obtained results indicated that significant thermal conductivity enhancement was achieved using CBNP nano-inclusions (~ 67 and 153 % in the solid state and phase transition regions, respectively at a loading concentration of 0.05 vol. fraction), as compared to various other metallic and carbon based nano-inclusions. The reduced cost and low density of CBNP nano-inclusions are beneficial for practical applications, as it reduces the operational cost. The excellent volume filling capacity and low fractal dimension of CBNP resulted in the formation of more closely bound aggregates with improved aggregate/aggregate contacts, which reduced the thermal barrier resistance leading to enhanced heat transfer along the percolation networks. Aggregation dynamics and formation of such percolation network was probed using optical phase contrast microscopy, where for the first time, direct experimental evidence was provided for solidification induced cluster formation during liquid-solid phase transition of nano-inclusions loaded PCMs. This study clearly shows the efficacy of CBNP nano-inclusions as an alternate agent for efficient thermal conductivity enhancement in PCMs without increasing the cost and loading density. It is envisaged that CBNP nano-inclusions will provide further impetus towards various practical applications involving nano-enhanced PCM based thermal energy storage.

Chapter 5

Carbon black nano powder assisted enhancement in thermal conductivity and photo thermal conversion in paraffin wax and lauric acid-based phase change materials

Chapter 5

Carbon black nano powder assisted enhancement in thermal conductivity and photo thermal conversion in paraffin wax and lauric acid-based phase change materials

5.1 Introduction

In today's world low carbon energy policies and rapid industrialization drive the research and development of green energy materials and technology. Nano-inclusion loaded organic phase change materials (PCMs) are being developed as efficient agents for latent heat thermal energy storage (LHTES) [1, 500], intermediate thermal energy storage for solar applications and waste heat recovery [156], thereby playing a monumental role in reducing fossil fuel consumption and carbon foot print [144]. Though higher thermal conductivity has been reported for PCMs loaded with various metallic oxides, multi-walled or single-walled carbon nano-tubes and graphene nanoplatelets, higher cost of these nano-inclusions (cost of research grade multiwalled, single walled and graphene oxide are ~ \$5/g, \$75/g and \$100/g, respectively [495]) remains an issue. Carbon black nanopowder (CBNP), on the other hand, is significantly cheaper (< \$1/g) and has shown high thermal contact conductance in thermal pastes [477]. CBNP loaded nanofluids have also shown superior photo-thermal capability [501]. Though room temperature electrical and thermal regulation in oleic acid coated carbon black nanopowder loaded octadecane has been reported earlier by Wu et al. [236], the underlying phenomena for thermal conductivity enhancement was not studied in depth. Moreover, the effect of uncoated CBNP on enhancements of thermal conductivity and photo-thermal conversion in paraffin wax (PW) and lauric acid (LA) based PCMs need to be probed experimentally.

5.2 CBNP aided enhancement in thermal conductivity and photo-thermal conversion in paraffin wax based PCMs

Paraffin wax (PW) is a mixture of saturated hydrocarbons (n-alkanes), with a melting temperature of 45-65 ^{0}C and superior wetting properties [502]. PW is one of the most widely used organic PCMs due to its high latent heat of fusion, enhanced thermal stability and repeatability, low vapour pressure during melting, chemical inertness, reduced lower supercooling requirements, ease of use, environment friendliness and comparatively lower cost [1, 58, 286, 428]. Recently, Pavithra et al. [503] reported ~ 25 % higher overall heat transfer efficiency for co-dispersion of nanostructured magnesium-lined PW and magnesium oxide hybrid nanofluid. PW based organic PCM has been proposed for battery thermal management system (BTMS) of Li-ion [212] batteries for electric or hybrid vehicles, which are more energy efficient and poised to reduce global pollution levels by manifolds. Nevertheless, low thermal conductivity of pristine PW reduces the heat transfer rate, thereby increasing the charging/discharging time and hence, nano-inclusion assisted enhancement of PW based PCMs has attracted considerable interest from fundamental as well as applications points of view [212, 214, 241, 242, 502, 504, 505]. In the present study, thermal conductivity enhancement of a PW based PCM, upon loading with various concentrations of CBNP, is probed systematically. The phase transition temperature of PW is also tuned by adding required amount of hexadecane (HD) and CBNP assisted enhancement of thermal conductivity is also investigated for the composite PCM (PW-HD). Consecutive thermal cycling are performed to study the stability of the CBNP loaded PCM and optical phase contrast microscopy is carried out to understand the role of microscale aggregation on thermal conductivity enhancement in the solid state, which is analyzed using a logarithmic model proposed by Agari & Uno [390]. Photo-thermal conversion efficiency of the CBNP loaded PW based PCM is also studied experimentally, in a non-contact way, using infrared thermography.

5.2.1 Preparation of CBNP loaded PCMs

The average sizes of the CBNP nano-inclusions were found to be ~ 29 ± 1 and ~ 31 ± 1 nm from SEM and AFM studies, respectively (details provided in chapter 2). Here, paraffin wax (PW) and binary mixture of paraffin wax-hexadecane (PW-HD) were used as PCMs. PW was used in as-received condition, whereas PW-HD was prepared by mixing 9 mL of HD in 6 mL of PW. While maintain the temperature of PW at ~ 70 ± 2 ^{0}C, HD was slowly added in the liquid state. Thereafter, the mixture of PW and HD was subjected to magnetic stirring for 25 minutes at a fixed temperature of ~ 65 ± 2 ^{0}C. This was followed by a water bath sonication for 15 minutes at ~ 55 ± 2 ^{0}C. The binary mixture was then allowed to cool at room temperature to form PW-HD based PCM. Five different concentrations (0.5, 1.0, 1.5, 2.0 and 2.5 wt. %) of CBNP were directly dispersed in the PW or PW-HD PCMs in the liquid state (sample temperature higher than the corresponding melting points) and thereafter, subjected to water bath sonication for 30 minutes with bath temperature maintained at 65 ± 2 and 55 ± 2 ^{0}C for PW and PW-HD, respectively, to prepare the CBNP loaded PCMs. The nano-inclusions (CBNP) were physically added to the PCMs and hence, chemical properties of the host matrices were left unchanged. To confirm the absence of any chemical reactions, FTIR spectroscopy was carried out in the attenuated total reflection mode. Additionally, for reference, FTIR spectra of CBNP was also acquired from transparent pellets, prepared by hard pressing after thorough mixing with KBr (1.5 wt. %).

The phase transition temperatures and latent heat values of the PCMs, with or without CBNP loading, were determined from differential scanning calorimetry (DSC) studies under argon atmosphere with a heating rate of 3 ^{0}C/minute. The phase transition temperatures of the PW and PW-HD based PCMs were also approximately estimated from the variation of temperature dependent refractive index. Optical phase contrast microscopy (Carl Zeiss equipped with 10X & 40X objectives) was carried out on the PCMs, with or without CBNP loading, to study the effect of aggregation at microscale. The microstructure of the pristine PCMs were also studied by atomic force microscopy (AFM), using a commercial silicon tip with ~ 10 nm bending radius. For AFM, pristine PCMs (in molten state at temperatures above their corresponding melting point) were drop casted on thoroughly cleaned glass substrates and thereafter allowed to freeze *in situ*. Thermal conductivity measurements were carried out using a KD2 probe (details provided in chapter 2).

Experiments were carried out to study the photo-thermal conversion efficiency of the PW based PCM loaded with various concentrations of CBNP, where the samples were exposed to an artificial solar spectrum using two 1 kW halogen lamps, working at 50 % efficiency. The halogen lamps were placed at 45 ^{0} from the hypothetical straight line passing through the centre of the sample holder on either side. The sample-to-lamp distance was fixed at ~ 0.15 m throughout the experiments. The rise in sample temperature was remotely monitored using a FLIR SC5000 infrared camera, positioned vertically above the sample at a distance of ~ 0.35 m. For comparison, experiments were also performed on the PCMs without any CBNP loading. All experiments were repeated thrice and the average values of temperature rise were considered for further data analysis.

5.2.2 Thermo-physical characterization of PW and PW-HD PCMs

Figures 5.1a-c shows the FTIR spectra of the PW and PW-HD based PCMs, with and without CBNP loading. For comparison, FTIR spectra of pure HD and CBNP are also shown in the corresponding figures. The major absorption bands are indexed in **Figs. 5.1a-c** and **Table 5.1** shows the relevant details [68, 216, 411]. FTIR spectra clearly showed that in the cases of PCMs loaded with CBNP, the major absorption bands were neither shifted, nor any new bands were discernible, which indicated the absence of any chemical reactions between CBNP and the PCMs [215, 216].

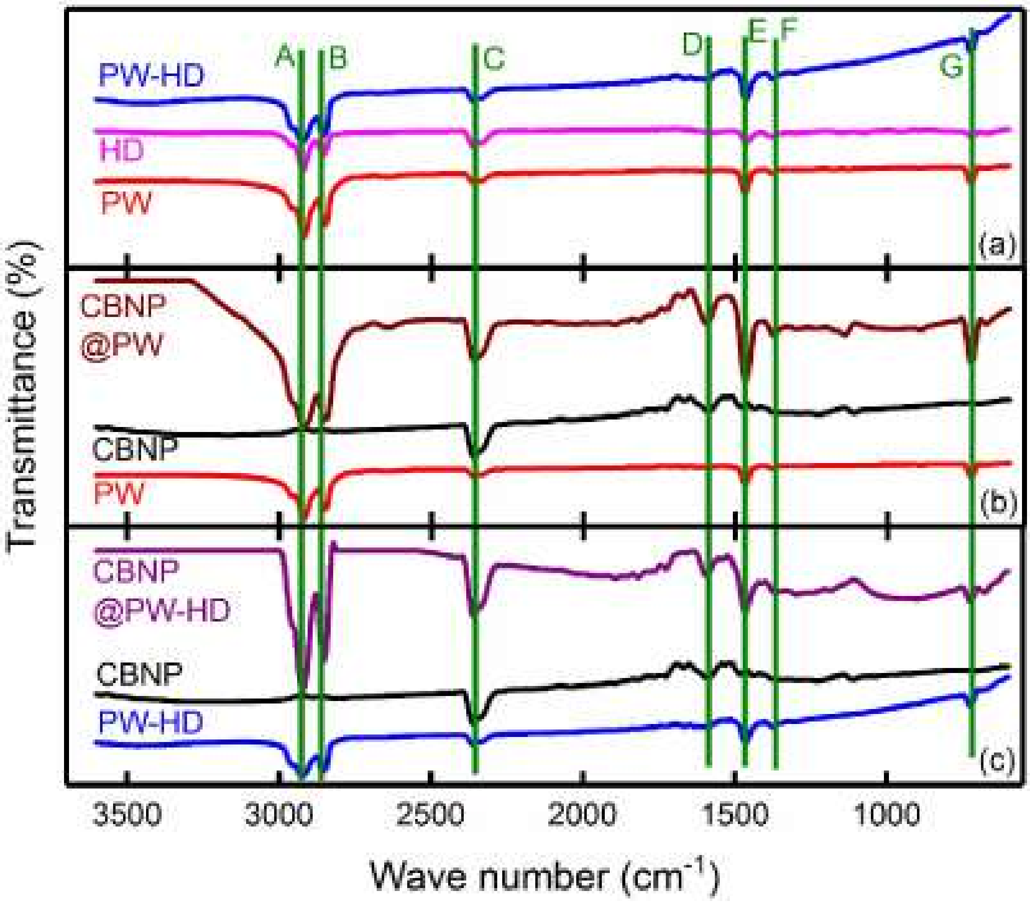

Figure 5.1 Fourier transform infrared (FTIR) spectra of (a) pristine PW, HD and PW-HD; (b) pristine PW, CBNP and CBNP loaded PW; (c) pristine PW-HD, CBNP and CBNP loaded PW-HD. The major absorption bands are indexed and Table 5.1 shows the detailed descriptions.

Figures 5.2a-b show the variation of k/k_f during consecutive thermal cycling of PW and PW-HD based PCMs, respectively, without any CBNP loading. During thermal cycling, a series of thermal conductivity measurements were performed in the liquid state, followed by another set of measurements in the solid state.

Table 5.1 Major absorption bands indicated in the FTIR spectra.

Legends	Wave number (cm^{-1})	Description	Reference
A	2921	Asymmetric C-H stretch of CH_2	[216, 411]
B	2852	Symmetric C-H stretch of CH_2	[216, 411]
C	2360	C=O stretching from atmospheric CO_2	[215, 216]
D	1588	Symmetric C=C aromatic stretching (not present for pristine PW and PW-HD)	[68]
E	1463	Asymmetric $–CH_3$ bending	[216, 411]
F	1378	Symmetric $–CH_3$ bending	[216]
G	719	C-H rocking vibration of long chain alkanes	[411]

Here, k and k_f signify the temperature dependent variable thermal conductivity and thermal conductivity values of the PCMs in the liquid state (at 65 and 50 ^{0}C for PW and PW-HD), respectively. For PW, the thermal conductivity in the liquid state was found to be ~ 0.155 ± 0.001 W/mK, which was in agreement with the values reported by Wang et al. [58, 245]. On the other hand, in the case of PW-HD, thermal conductivity in the liquid state was ~ 0.146 ± 0.001 W/mK, which was slightly lower than that of pure PW. This was attributed to the presence of HD, which has lower thermal conductivity of ~ 0.140 ± 0.002 W/mK [216]. In the solid state, thermal conductivity values were ~ 0.274 ± 0.003 and 0.237 ± 0.002 W/mK for PW and PW-HD, respectively. Presence of nanocrystalline structures in the solid state aids in phonon mediated heat transfer, leading to a higher thermal conductivity, which is also confirmed by molecular dynamics simulation [493]. **Figs. 5.2a-b** also show the percentage enhancement in thermal conductivity. For PW, k/k_f was ~ 1 in the liquid state, which increased up to ~ 1.764 in the solid state (i.e. ~ 76.4 % enhancement of thermal conductivity in the solid state). Similarly, for PW-HD, thermal conductivity enhanced by ~ 62% after freezing. It can be further seen from **Figs. 5.2a-b** that the thermal responses were reversible for the PCMs, even after four consecutive melting/freezing cycles. This indicated superior thermal stability of PW and PW-HD based PCMs, which is desirable for practical applications. **Figs. 5.2c-d** show the optical phase contrast images of pristine PW and PW-HD, respectively, in the solid state. Formation of needle like structures due to anisotropic growth of HD during freezing [387] were clearly discernible for PW-HD (**Fig. 5.2d**). On the contrary, pure PW showed flaky microstructure, with nearly isotropic growth. This was also confirmed from AFM topography image (50 µm × 50 µm) of pristine PW, shown in **Fig. 5.2e**. On the other hand, the presence of anisotropic growth can be clearly seen from the AFM topography image (50 µm × 50 µm) of PW-HD, shown in **Fig. 5.2f**. It can be further seen from **Fig. 5.2f** that the presence of PW in the host matrix of PW-HD based PCMs leads to a distribution of isotropic and anisotropic microstructures, where the isotropic regions are predominantly located in-between the needle like structures.

Figure 5.3a-b show the heat flow curves during melting of PW and PW-HD based PCMs, respectively, loaded with various concentrations of CBNP. It can be seen from **Fig. 5.3a** that for PW based PCMs, two distinct phase transformations were present. The smaller peaks at lower temperature (~ 45 ^{0}C) signified solid-solid phase transformation, whereas the major peaks at higher temperature (~ 60 ^{0}C) indicated solid-liquid phase transformation. Around ~ 45 ^{0}C, PW undergoes a solid-solid phase transformation, where the layered low temperature structure (monoclinic) transforms to a high temperature homogenous FCC structure with higher symmetry [506]. It has been reported that PW with chain length below 25 shows two solid-solid phase transitions, whereas for PW with chain length higher than 32, solid-solid phase transition is indistinguishable [507]. Hence, the average chain length of PW, used in the present study, was estimated as ~ 25-32. The presence of C-H rocking vibration in the FTIR spectra at ~ 719 cm^{-1} (**Fig. 5.1**) also confirmed the presence of long carbon chains.

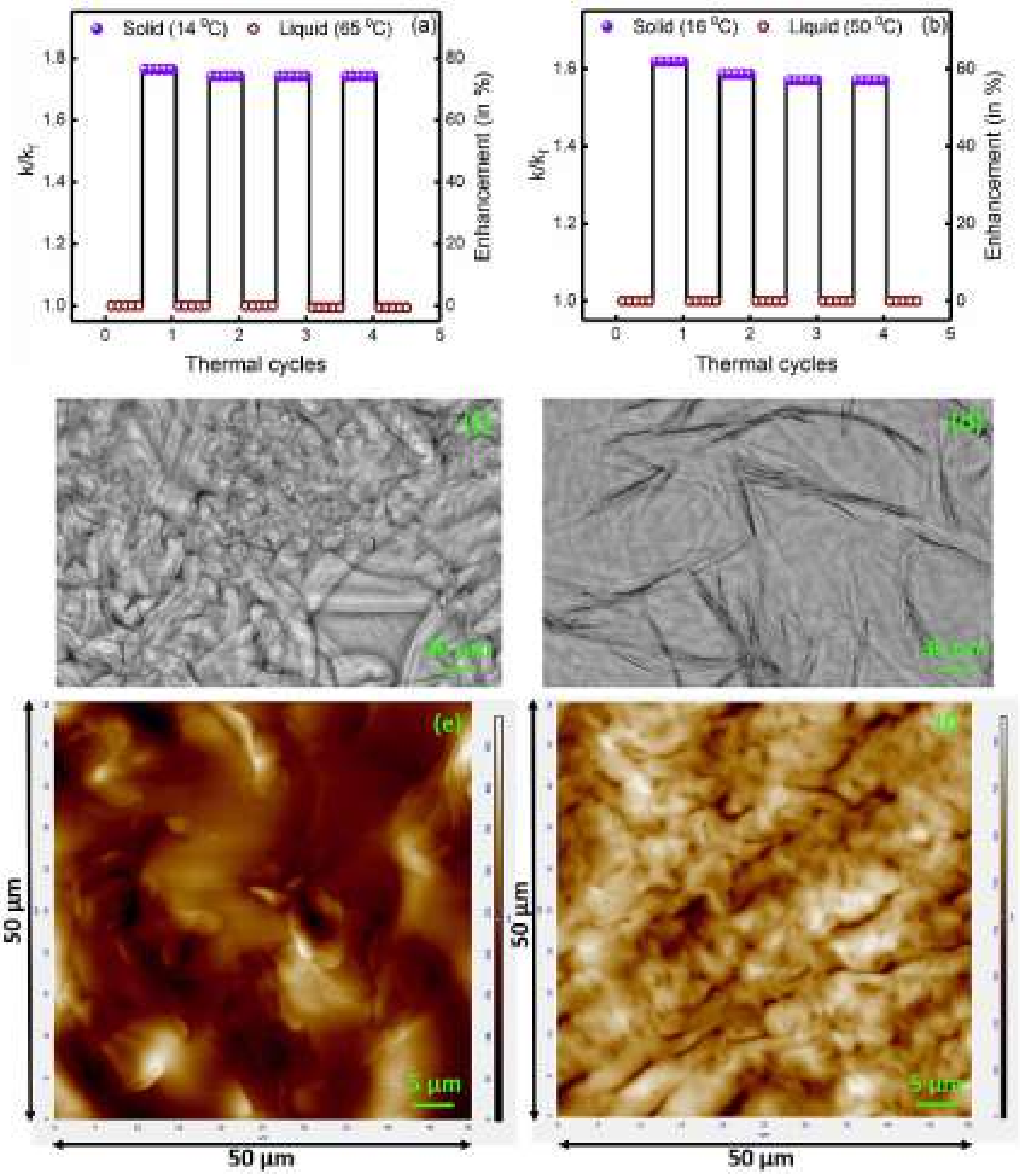

Figure 5.2 Variation of k/k$_f$ and percentage enhancement in thermal conductivity during consecutive thermal cycling of (a) PW and (b) PW-HD based PCMs, without any CBNP loading. Optical phase contrast microscopy (10X) images of pristine (c) PW and (d) PW-HD, in the solid state. AFM topography image (50 µm × 50 µm) of pristine (e) PW and (f) PW-HD.

On further raising the temperature, the PW molecules absorbed thermal energy to overcome the intermolecular forces, subsequently leading to solid-liquid phase transformation. The solid-solid and solid-liquid phase transformation temperatures for PW, obtained in the present study, were found to be in good agreement with those reported by Lin et al. [239], Sari and

Karaipekli [274] and Yu et al [508]. **Tables 5.2 & 5.3** show the onset, endset and peak phase transformation temperatures along with latent heat values for solid-solid and solid-liquid phase transformations, respectively for PW based PCMs with varying concentration of CBNP loading. On the other hand, **Fig. 5.3b** shows a single peak (around ~ 45^{0}C) indicating solid-liquid phase transformation for PW-HD based PCMs loaded with different concentrations of CBNP and **Table 5.4** shows the corresponding onset, endset and peak phase transformation temperatures along with the latent heat values.

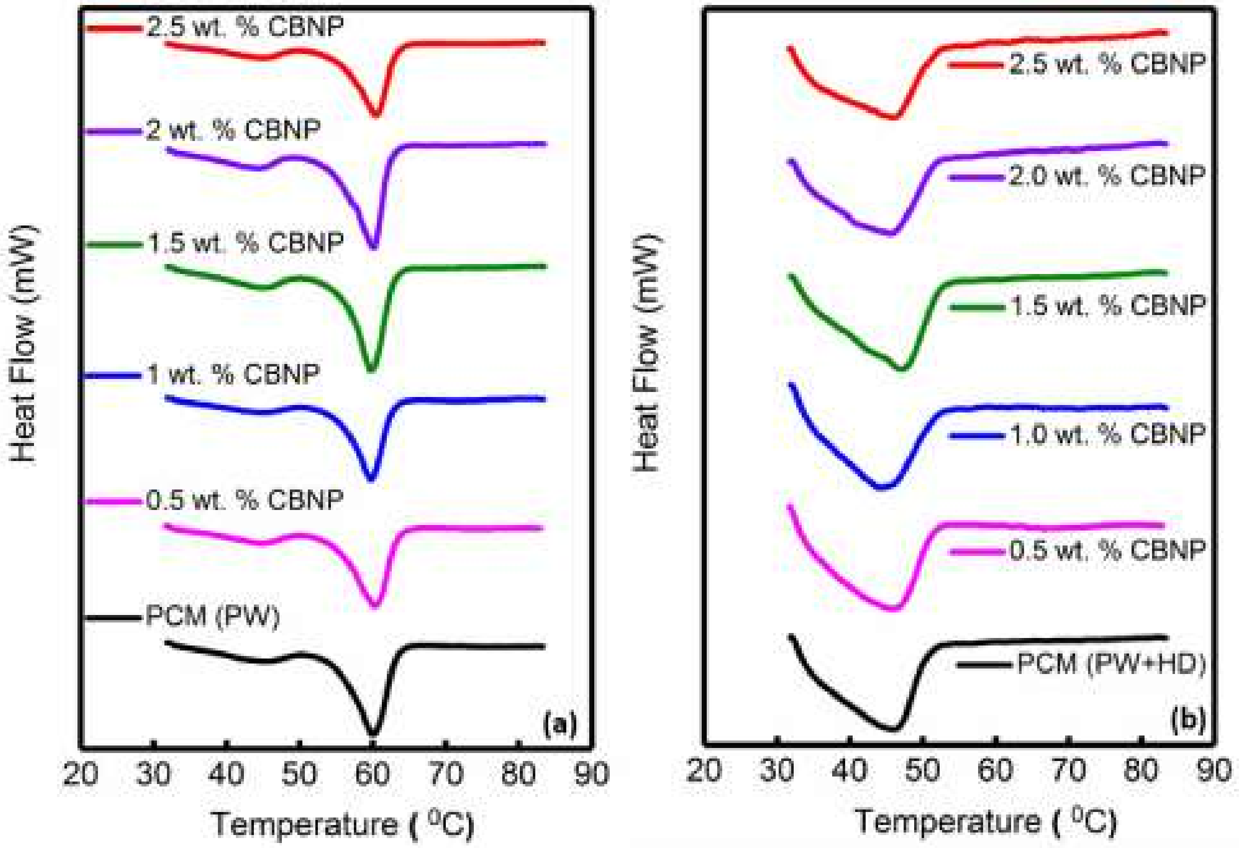

Figure 5.3 Heat flow curves during melting of (a) PW and (b) PW-HD based PCMs, loaded with various concentrations of CBNP.

Table 5.2 Thermal properties of solid-solid phase transformation of PW based PCMs.

CBNP concentration (wt. %)	Onset temperature (^{0}C) (±0.2 ^{0}C)	Endset temperature (^{0}C) (±0.2 ^{0}C)	Peak phase transformation temperature (^{0}C) (±0.2 ^{0}C)	Latent heat (kJ/kg)
0	33.9	49.2	45.6	11.83
0.5	33.3	47.2	45.2	13.19
1.0	39.8	48.9	44.5	11.82
1.5	41.3	48.4	45.5	8.76
2.0	38.5	47.8	44.4	14.92
2.5	38.5	48.6	45.1	14.96

Table 5.3 Thermal properties of solid-liquid phase transformation of PW based PCMs.

CBNP concentration (wt. %)	Onset temperature (^{0}C) (±0.2 ^{0}C)	Endset temperature (^{0}C) (±0.2 ^{0}C)	Peak phase transformation temperature (^{0}C) (±0.2 ^{0}C)	Latent heat (kJ/kg)
0	55.5	63.3	60.1	125.85
0.5	55.2	63.3	60.3	123.49
1.0	55.7	62.7	59.7	124.49
1.5	55.9	62.9	59.8	124.10
2.0	55.5	62.3	60.1	121.30
2.5	55.4	63.1	60.4	120.14

Table 5.4 Thermal properties of solid-liquid phase transformation of PW-HD based PCMs.

CBNP concentration (wt. %)	Onset temperature (^{0}C) (±0.2 ^{0}C)	Endset temperature (^{0}C) (±0.2 ^{0}C)	Peak phase transformation temperature (^{0}C) (±0.2 ^{0}C)	Latent heat (kJ/kg)
0	32.8	50.4	45.9	44.89
0.5	33.3	51.2	45.2	42.91
1.0	33.6	51.6	44.2	40.93
1.5	34.2	52.2	45.5	41.60
2.0	33.4	51.4	45.6	41.28
2.5	33.6	51.1	46.1	41.89

Figure 5.4a shows the variations of peak phase transformation temperature and latent heat, as a function of CBNP loading, during solid-liquid phase transformation of PW based PCMs. It can be seen from **Fig. 5.4a** that the peak temperatures did not vary significantly with increasing CBNP loading. In the present study, the latent heat of melting was obtained as ~ 126 kJ/kg for pristine PW. For PW with short chains (< 15), a higher latent heat value of ~ 184-200 kJ/kg was reported in literature [239, 241]. On the other hand, for PW with chain length ~ 19-36, Wang et al. [58] and Ukrainczyk et al. [509] reported latent heat values around ~ 140-147 kJ/kg. In the present study, a slightly lower value of latent heat was obtained for pristine PW, which was attributed to the variation in chain length (average chain length of ~ 25-32). It can be further seen from **Fig. 5.4a** that the latent heat decreased slightly with increasing CBNP concentration, which was also confirmed from **Table 5.3**. Interaction of host matrix with the loaded nano-inclusions leads to an increase in latent heat, whereas increasing nano-inclusion concentration, in general, causes the overall system latent heat to reduce, as the nano-inclusions do not contribute towards latent heat storage [58, 244]. CBNP nano-inclusions in PW form fractal clusters (as confirmed by phase contrast optical microscopy and discussed subsequently), which grow in size with increasing loading fractions, leading to the dominance of the second factor over the former, resulting in a net decrease in latent heat with increasing CBNP loading. This is in agreement with the earlier observations made by Lin et al. [239], Wang et al. [245] and Fang et al. [244] for PW or other long chain n-alkanes, loaded with metallic or carbon based nano-inclusions. **Fig. 5.4b** shows the variations of peak phase transformation temperature and latent heat, as a function of CBNP loading, during solid-liquid phase transformation of PW-HD based PCMs. It can be seen that the peak temperatures did not vary significantly with increasing CBNP loading, whereas latent heat decreased for higher loading fractions. These were in agreement with the observations made for PW based PCMs.

Figure 5.4c shows the variation of refractive indices of PW and PW-HD based PCMs, without any CBNP loading, during melting and solidification cycles. The refractive index of a medium is defined as the ratio of velocity of light in vacuum to the velocity of light in that medium and hence, refractive indices were higher in the solid states for PW and PW-HD. As sample temperature decreased, for a fixed physical state (solid or liquid), refractive index was found to increase, which was attributed to the reduction of velocity of light in the medium due to an increase in sample density. The sudden jump in refractive indices during solidification or melting (encircled in red and black for PW and PW-HD, respectively in **Fig. 5.4c**) indicated the discontinuous variations in sample density across the first order liquid-solid phase transformations. During freezing, refractive index discontinuously increased by ~ 5.8 and 6.7 % for PW and PW-HD, respectively. From refractive index measurements, the melting and freezing temperatures were found to be ~ 58.9 and 53.1 ^{0}C; 44.9 and 30.1 ^{0}C for PW and PW-HD, respectively, which were in good agreement with the data obtained from DSC (~ 60.1 and 45.9 ^{0}C for PW and PW-HD, respectively).

Figure 5.4c shows a super cooling requirement of ~ 5 ^{0}C for PW based PCMs, which was lower than the typical value (~ 8 ^{0}C), reported by Wu et al. [214] for MWCNT and GNP loaded PW. A narrower supercooling requirement, as obtained in the present study, makes energy recovery easier during practical applications. On the other hand, it can be seen from **Fig. 5.4c** that for PW-HD based PCMs, liquid-solid phase transformation occurs over a wider range (differences between the onset and endset temperatures were ~ 7.8 and 17.6 ^{0}C for PW and PW-HD, respectively), which was also indicated by the larger widths of the heat flow curves for PW-HD based PCMs (**Fig. 5.3b**). **Figs. 5.4d-e** show typical photographs of PW in the liquid and solid states, respectively. **Figs. 5.4f-g** show the typical photographs of PW-HD in the liquid and solid states, respectively.

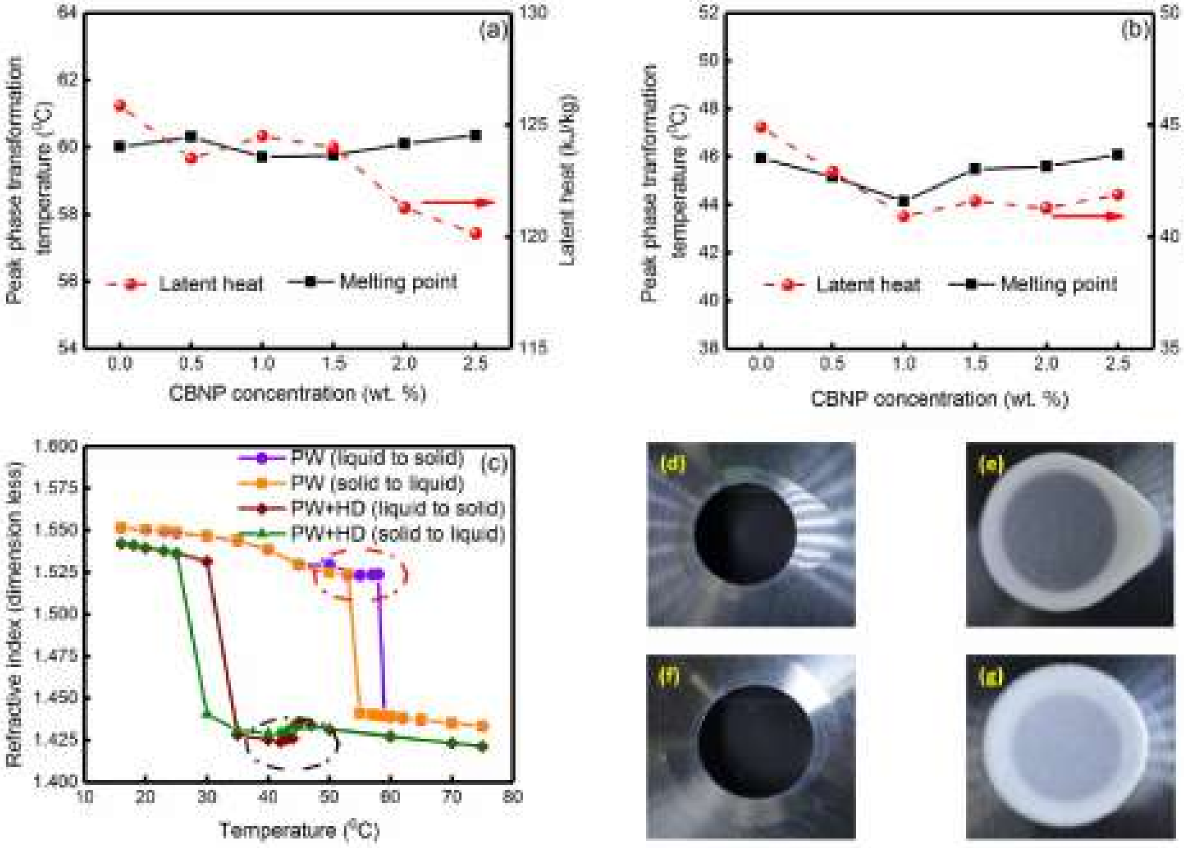

Figure 5.4 Variations of peak phase transformation temperature and latent heat, as a function of CBNP loading, during solid-liquid phase transformation of (a) PW and (b) PW-HD based PCMs. (c) Variation of refractive indices of PW and PW-HD based PCMs, without any CBNP loading, during melting and solidification cycles. Typical photographs of pristine PW in (d) liquid and (e) solid states. Typical photographs of pristine PW-HD in (f) liquid and (g) solid states.

Infrared thermography (IRT) based non-contact temperature mapping was performed to probe the variations in surface temperature distribution, during freezing of PW and PW-HD based PCMs, without CBNP loading. The samples were initially thermally acclimatized above ~ 85 ^{0}C (in the liquid state) and thereafter placed inside a re-circulating water bath, which was maintained at a constant temperature of ~ 37 (± 0.1) ^{0}C. The water bath was provided with a top opening to ensure un-interrupted field of view for the infrared camera. **Figs. 5.5a-j** show the typical infrared images for PW, during freezing, at time t = 0, 100, 200, 300, 400, 600, 1000, 1200, 1500 and 1800 s, respectively. **Figs. 5.5k-t** show the typical infrared images for PW-HD, during freezing, at time t = 0, 100, 200, 300, 400, 600, 1000, 1200, 1500 and 1800 s, respectively. For easy interpretation, pseudo colour coded temperature scales were provided along with the infrared images. The decrease in sample temperature, during freezing is evident from the infrared images. It can be further seen from **Fig. 5.5** that sample temperature initially decreased at a faster rate (up to 100 s), whereas for t = 1000-1800 s, the rate of temperature decay was significantly slower.

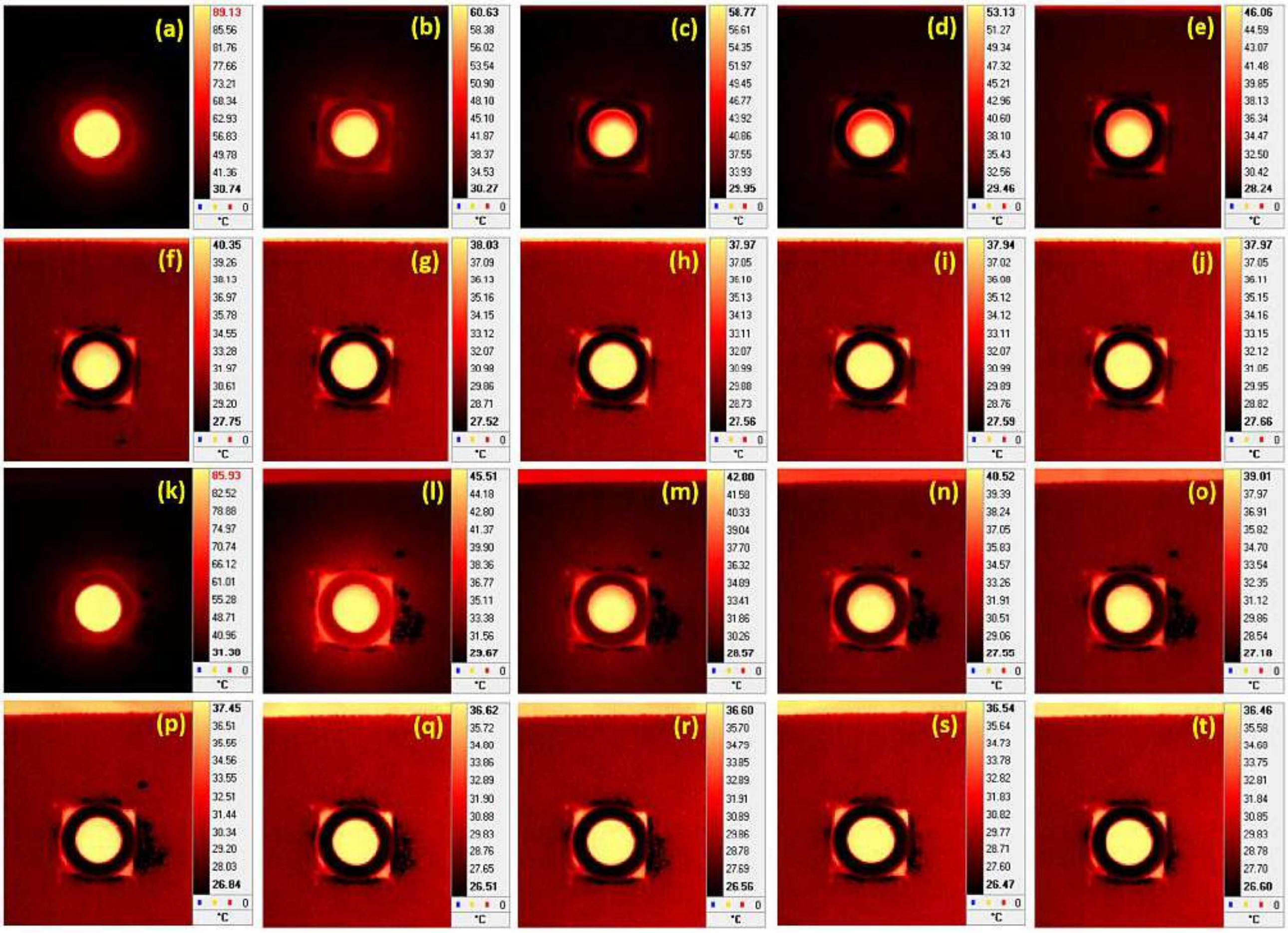

Figure 5.5 Typical infrared images for PW, during freezing, at time t = (a) 0, (b) 100, (c) 200, (d) 300, (e) 400, (f) 600, (g) 1000, (h) 1200, (i) 1500 and (j) 1800 s. Typical infrared images for PW-HD, during freezing, at time t = (k) 0, (l) 100, (m) 200, (n) 300, (o) 400, (p) 600, (q) 1000, (r) 1200, (s) 1500 and (t) 1800 s. For easy interpretation, pseudo colour coded temperature scales were provided along with the infrared images.

For quantitative analyses, circular regions of interest were considered, excluding the edge pixels, and spatial averaging was performed over several pixel locations, within the regions of interest, to obtain the temporal variation in average temperature. The variations of sample temperature as a function of time for PW and PW-HD based PCMs, without any CBNP loading are shown in **Fig. 5.6**. For comparison, the cooling curve for de-ionized water is also shown in **Fig. 5.6**. In the case of de-ionized water, a rapid and exponential fall in sample temperature was observed and the reference temperature was attained after ~ 550 (± 20) s. On the other hand, for PW and PW-HD, phase transitions occurred near the corresponding freezing points (encircled in **Fig. 5.6**) and hence, reference temperature was attained at significantly higher time scales (~ 1100 ± 20 and 1000 ± 20 s for PW and PW-HD, respectively).

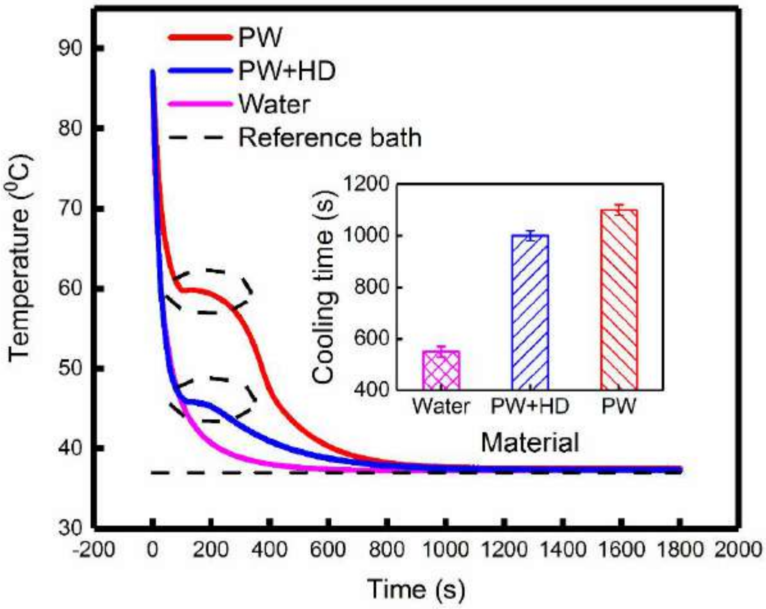

Figure 5.6 IRT based variation of sample temperature, as a function of time, for PW and PW-HD based PCMs, without any CBNP loading, during cooling. For comparison, the temperature decay curve for de-ionized water is also shown in the figure. The reference temperature of ~ 37 ^{0}C is indicated by the dashed horizontal line. The phase transformation regions for PW and PW-HD are encircled in black. (Inset) Bar chart comparing the cooling time (i.e. the time required to attain the reference temperature of 37 ^{0}C) for de-ionized water, PW and PW-HD.

The **inset of Fig. 5.6** shows a bar chart comparing the cooling time (i.e. the time required to attain the reference temperature of 37 ^{0}C) for de-ionized water, PW and PW-HD. The cooling time was significantly higher for PW and PW-HD based PCMs, as compared to de-ionized water, which was attributed to the latent heat storage during first order liquid-solid phase transformations in the PCMs. The gain in cooling time was estimated from the differences in time required to reach the reference temperature and the gain in cooling time was found to ~ 82 and 100 % for PW-HD and PW, respectively, which is immensely beneficial for practical thermal energy storage applications. These values were comparable to that reported by Rao and Zhang [510], where the efficacy of PW based PCMs for battery thermal management was studied and ~ 100 % enhancement in cooling time, as compared to air, was reported for PW loaded with 20 wt. % modified natural graphite. Further, the phase transformation temperatures were estimated from the IRT based cooling curves using a differential data analysis technique and the phase transformation temperatures were estimated as 59.8 ± 0.2 and 45.8 ± 0.1 ^{0}C for PW and PW-HD, respectively, which were found to correspond well with the values obtained from DSC. This study clearly shows the adaptability and accuracy of IRT based remote temperature mapping, during liquid-solid phase transitions in organic PCMs, to estimate the phase transition temperature and gain in cooling time in a rapid and non-contact way.

5.2.3 CBNP assisted enhancement in thermal conductivity of PW-based PCMs

Figure 5.7a shows the temperature dependent variation of k/k_f and percentage (%) enhancement in thermal conductivity for PW based PCMs loaded with various concentration of CBNP. For comparison, the variation of k/k_f for PW, without any CBNP loading, is also shown in **Fig. 5.7a**. Here, k and k_f indicate the temperature dependent thermal conductivity and thermal conductivity of virgin PW in the liquid state ($k_f \sim 0.155 \pm 0.001$ W/mK at 65 ^{0}C), respectively. As evident from **Fig. 5.7a**, the variation of k/k_f can be divided into three regions, viz., region I, II and III. In region-I, for temperature above 60 ^{0}C, the samples were in the liquid state. On the other hand, for 30 ^{0}C <T<60 ^{0}C, the samples underwent solid-liquid phase transformations (region-II). Transient hot wire based thermal conductivity measurements were found to be prone to experimental errors in this region and hence, k/k_f values for region-II were not included in **Fig. 5.7a**. On the other hand, in region-III, for temperature below 30 ^{0}C, the samples were in the solid state. **Fig. 5.7a** shows that thermal conductivity enhancements were negligible in region-I (liquid state) and the average values of thermal conductivity enhancements were ~ 1.7, 3, 4.3, 8.2 and 9.4 % for 0.5, 1.0, 1.5, 2.0 and 2.5 wt. % CBNP loading, respectively. On the other hand, the PCMs showed significantly higher thermal conductivity values in the solid state due to the formation of crystalline structure in PW, after freezing, that enhanced phonon mediated heat transfer [237, 387]. For Virgin PW, thermal conductivity enhanced by ~ 76.4 % after solidification (at ~ 14 ^{0}C). It was further observed that thermal conductivity enhancements increased with CBNP loading and the average values of thermal conductivity enhancements in solid state were ~ 80.3, 84.8, 97.6, 128.5 and 135 % for 0.5, 1.0, 1.5, 2.0 and 2.5 wt. % CBNP loading, respectively.

Figure 5.7b shows the temperature dependent variation of k/k_f and % enhancement in thermal conductivity for PW-HD based PCMs loaded with various concentration of CBNP. For comparison, **Fig. 5.7b** also shows the variation of k/k_f for virgin PW-HD. Here, k_f indicates the thermal conductivity of virgin PW-HD in the liquid state ($k_f \sim 0.146 \pm 0.001$ W/mK at 50 ^{0}C). Similar to the observations made for PW based PCMs (**Fig. 5.7a**), the variation of k/k_f in the case of PW-HD based PCMs can also be divided into regions-I, II and III, corresponding to the liquid, phase transformation and solid states, respectively.

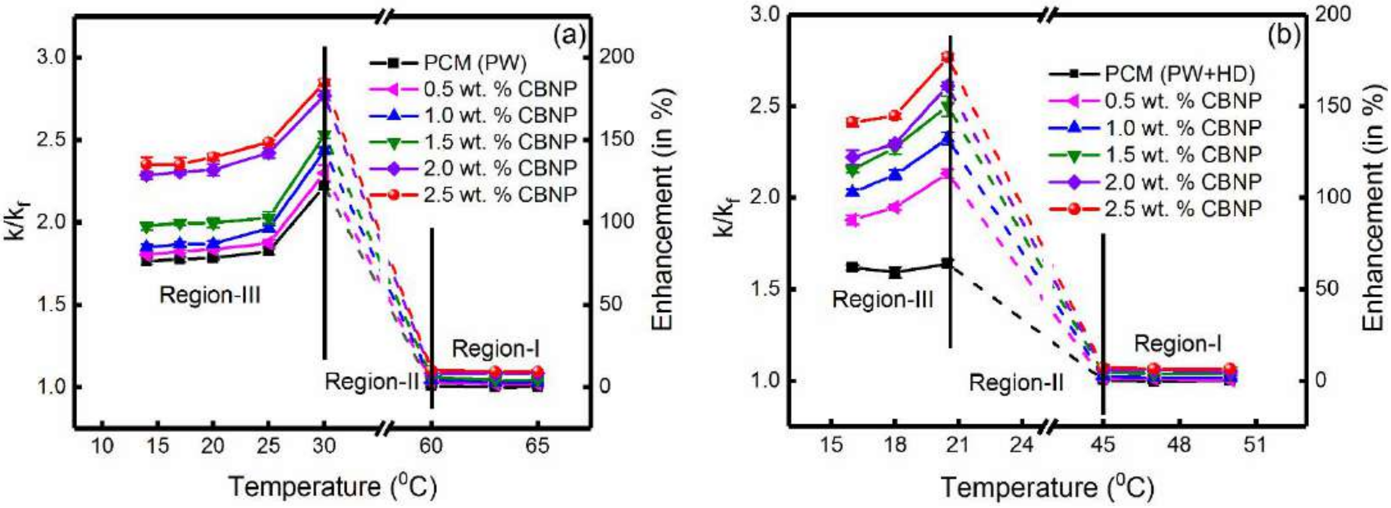

Figure 5.7 Variation of k/k_f and percentage enhancement in thermal conductivity, as a function of temperature, for (a) PW and (b) PW-HD based PCMs loaded with various concentration of CBNP. The variation of k/k_f can be divided into three distinct regions, viz., region-I, II and III, which corresponded to the liquid state, phase transformation region and solid state, respectively.

For T> 45 ^{0}C, the samples were in the liquid state and average values of thermal conductivity enhancements were ~ 0.5, 1.8, 3.9, 4.9 and 6.6 % for 0.5, 1.0, 1.5, 2.0 and 2.5 wt. % CBNP loading, respectively. **Fig. 5.7b** further shows that thermal conductivity values were significantly higher in the solid state (region-III) and for virgin PW-HD thermal conductivity enhanced by ~ 62 % after solidification (at 16 ^{0}C). In the solid state, thermal conductivity enhancements were ~ 87.9, 102.9, 115.3, 122.1 and 141.1 % for 0.5, 1.0, 1.5, 2.0 and 2.5 wt. % CBNP loading, respectively. **Figs. 5.7a-b** show that thermal conductivity enhancements reduced slightly with decreasing temperature in the solid state, which was due to the microstructural changes in the host matrices, where larger crystallites are converted to smaller ones, probably due to the stress fields developed during solidification. Such phenomena were also earlier observed for hexadecane and phenol based PCMs [215, 216].

In nano-inclusion loaded PCMs, the nano-inclusions are pushed towards the inter-crystallite regions during liquid-solid phase transformations, thereby forming a network of clusters/ aggregates along the grain boundaries [215, 216, 231]. Internal stress field, generated during crystallization, pushes the nano-inclusions towards inter-crystallite regions, leading to an increase in surficial contact and lowering of interfacial thermal barrier resistance (Kapitza resistance) [237, 387]. The percolating heat transfer through the network of nano-inclusion clusters causes an overall enhancement in thermal conductivity [238, 342]. Moreover, lower interparticle spacing, under the action of internal stress fields, also augments the near-field radiative heat transfer, thereby enhancing the thermal conductivity of the PCMs loaded with CBNP nano-inclusions [419]. **Figs. 5.8a-b** show the optical phase contrast microscopy images of CBNP loaded (at 0.5 wt. %) PW and PW-HD based PCMs, respectively, in the solid state, where the clusters of CBNP are clearly discernible. Additionally, **Fig. 5.8b** shows the presence of needle like microstructure for PW-HD. A magnified view of a region of **Fig. 5.8a** is shown in **Fig. 5.8c**, where the formation of percolating heat transfer pathways can be clearly visualized. Such network of nano-clusters enhances the effective thermal conductivity by reducing interfacial phonon scattering and thermal barrier resistance and augmenting the near-field radiative heat transfer [216]. **Fig. 5.8d** shows the magnified view (40X) of a single large cluster of CBNP nano-inclusions in PW-HD, where the presence of needle like microstructure in the host matrix is clearly discernible. Strong anisotropic growth kinetics have been reported earlier for HD [216, 237, 387] and these needle like structures were attributed to the incorporation of HD in the host matrix of PW-HD based PCMs. **Figs. 5.8e-f** show the optical phase contrast images of PW and PW-HD based PCMs, respectively, loaded with 2.0 wt. % CBNP, where the presence of quasi-2D network of CBNP nano-inclusions can be clearly seen. It can be also seen from **Figs. 5.8e-f** that for higher loading fractions of CBNP, larger network of percolating structures formed within the PCMs, eventually spanning over the entire host matrices, which resulted in a progressively increasing enhancement in thermal conductivity for larger loading fractions.

In the present study, the maximum thermal conductivity enhancements with 2.5 % CBNP loading were ~ 135 and 141 % for PW and PW-HD based PCMs, respectively, which were substantially larger than most of the earlier values reported in literature using metallic or carbon based nano-inclusion [58, 214, 239-241, 243, 245, 246, 504, 508]. A few representative thermal conductivity enhancement values for PW based PCMs, along with the nature and concentrations of the loaded nano-inclusions are shown in **Table 5.5**.

Table 5.5 Enhancement in thermal conductivity for PW based PCMs using various nano-inclusions. MWCNT, GNP and CNF indicate multiwalled carbon nanotubes, graphene nanoplatelets and carbon nanofibers, respectively.

Nano-inclusions		Enhancement in thermal conductivity in solid state (in %)	Year	Reference
Name	Concentration (wt. %)			
TiO_2	7.0	~ 16.6-17.0	2014	[58]
Cu-nanoparticles	2.0	~ 46.3	2016	[239]
Copper oxide nanoparticles	10.0	~ 12.2	2012	[240]
SiO_2	10.0 (along with ~ 2 wt. % of expanded graphite)	~ 98.7	2018	[241]
functionalized MWCNT	10.0	~ 86.7	2014	[246]
MWCNT	2.0	~ 35.0-40.0	2009	[245]
CNF	4.0	~ 30.0-33.0	2005	[243]
graphene aerogel encapsulating PW (core-shell like structure)	-	~ 32.4 %	2015	[504]
GNP	3.0	~ 50.0	2016	[214]
MWCNT	3.0	~ 18.0		
GNP	4.0	~ 93.3	2013	[508]
CNF	4.0	~ 20.0		
MWCNT	4.0	~ 20.0		
CBNP@PW	**2.5**	**~ 135.0**	2019	**Present study**
CBNP@PW-HD	**2.5**	**~ 141.1**		

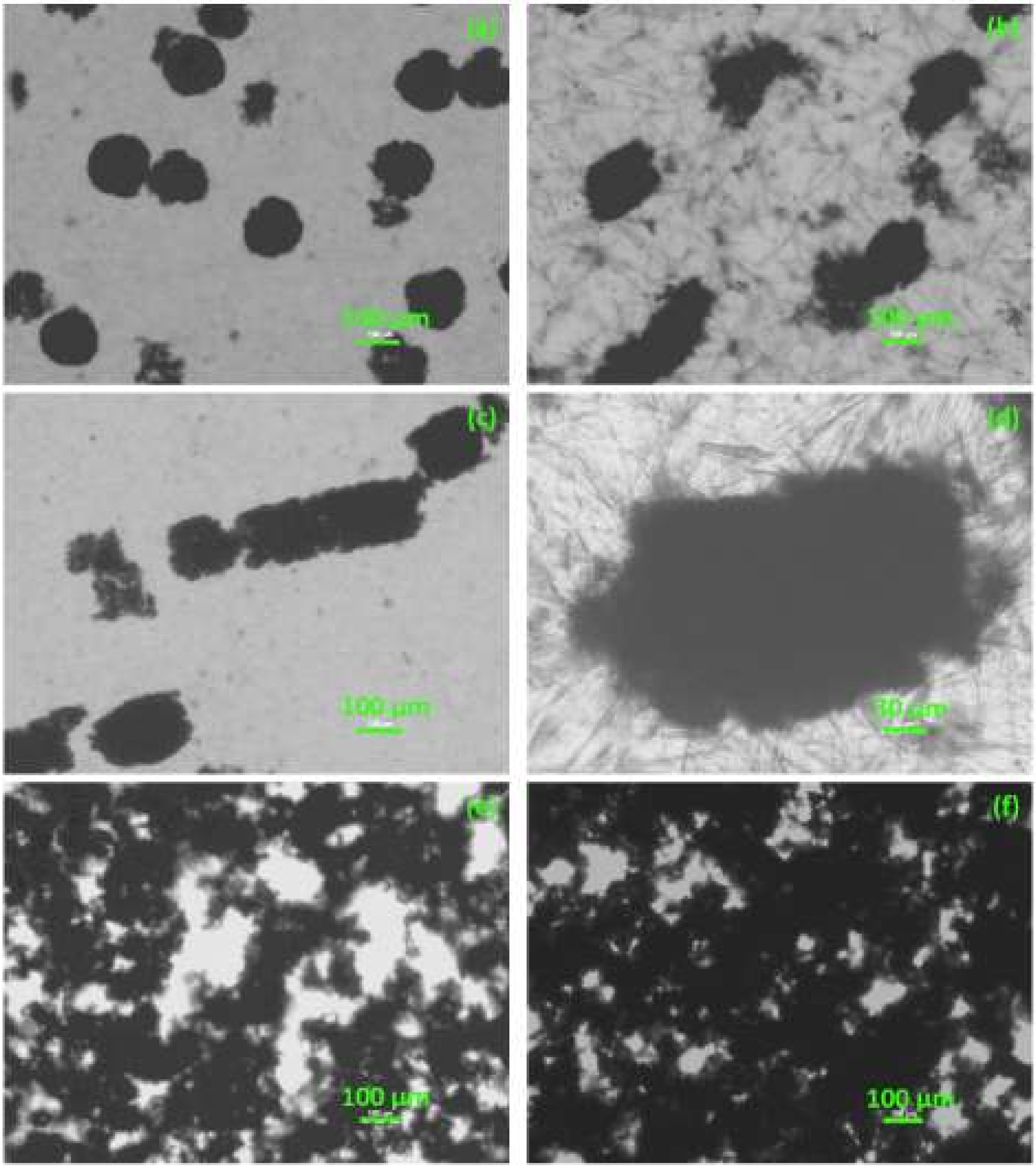

Figure 5.8 Optical phase contrast microscopy (10X) images of (a) PW and (b) PW-HD based PCMs, in the solid state, loaded with 0.5 wt. % CBNP. (c) Magnified view (10X) of a region of (a), where the formation of percolating heat transfer pathways can be clearly visualized. (d) Magnified view (40X) of a single large cluster of CBNP nano-inclusions in PW-HD, from (b). Here, the presence of needle like microstructure in the host matrix is clearly discernible. Optical phase contrast microscopy (10X) images of (e) PW and (f) PW-HD based PCMs, loaded with 2.0 wt. % CBNP. Here, the presence of quasi-2D network of CBNP nano-inclusions can be clearly seen. For higher loading fractions of CBNP, larger network of percolating structures formed within the PCMs, eventually spanning over the entire host matrices.

It can be seen from **Table 5.5** that ~ 98.7 % enhancement in thermal conductivity was obtained for SiO_2 nanoparticle loaded PW with 4 times higher loading concentrations (~ 10 wt. %), as compared to 2.5 wt. % CBNP loading used in the present study. Nevertheless, very high thermal conductivity enhancement in PW based PCMs loaded with carbon coated aluminum nanoparticles (~ 206.5 % enhancement in thermal conductivity for 4 wt. % loading) [212] and exfoliated graphite nanoplatelets of ~ 15 μm lateral size and ~ 10 nm thickness have been reported earlier [505]. The higher thermal conductivity enhancements obtained in these studies were attributed to the high bulk thermal conductivity of aluminum (~ 226 W/mK) or high in-plane thermal conductivity of graphite (~ 3000 W/mK). Nevertheless, these metallic or graphite based nano-inclusions are costly, requires surface capping for enhancing thermal stability and involves lengthy sample preparation steps (like in-plane or through plane milling or casting), which make them less economically viable. On the other hand, ~ 135 % enhancement in thermal conductivity was achieved in the present study using extremely cheap CBNP nano-inclusions with low loading concentration (2.5 wt. %) and without any lengthy sample preparation steps, which make these nano-enhanced PCMs economically viable and does not increase the weight of the PCM host matrices due to low density of CBNP (density of CBNP is ~ 0.1 g/cc as compared to ~ 2.7 g/cc and ~ 2.26 g/cc for aluminum and graphite, respectively).

It is reported that CBNP forms aciniform shaped aggregates of primary carbon black particles (nodules) [407]. The high thermal conductivity of CBNP dispersions in thermal paste is attributed to its excellent compressibility and volume filling capacity [477]. It is suggested that the high volume filling capacity and smaller aggregate sizes aids in the formation of percolation networks with reduced inter-aggregate gaps in PCM loaded with CBNP, after solidification, which results in larger thermal conductivity enhancements [431]. Wu et al. [236] reported a thermal conductivity contrast of ~ 3.3 in octadecane based PCM loaded with

1.25 % volume fraction of CBNP, where the low fractal dimensions of CBNP clusters caused an enhancement in thermal conductivity. Thermal conductivity enhancements in such nano-inclusion loaded organic PCM is restricted due to phonon scattering at inter-aggregate and aggregate-matrix interfaces [432, 433]. Low fractal dimension of CBNP leads to the formation of close-packed nano-inclusion aggregates with enhanced aggregate-PCM interactions and improved inter-aggregate contacts, leading to reduced thermal barrier resistance and improved phonon coupling along the conduction pathways, as predicted from acoustic and diffuse mismatch models for low and high frequency phonons, respectively [442, 443]. This explains the observed large thermal conductivity enhancements for the PW and PW-HD based PCMs loaded with various concentrations of CBNP. It can be further observed from **Table 5.5** that for similar loading fractions, thermal conductivity enhancements were significantly higher for PW based PCMs loaded with GNP (~ 50-93.3 %), as compared to those loaded with MWCNT or CNF (~ 20-40 %). This was attributed to the larger Kaptiza resistance of MWCNT and CNF, as compared to GNP [65], which also forms quasi-2D and fractal networks of nano-inclusions [342], similar to the networks formed by CBNP nano-inclusions. Among various nano-inclusions shown in **Table 5.5**, the highest thermal conductivity enhancement was observed for CBNP loading, that too with the lowest loading concentrations.

Thermal conductivity enhancements for PW and PW-HD based PCMs were found to increase with CBNP loading, both in liquid and solid states and these variations were studied in detail to probe the role of agglomeration on thermal conductivity enhancement. **Figs. 5.9a-b** show the variations of k/k_f and % enhancement in thermal conductivity, as a function of CBNP concentration (in vol. % = $\phi \times 100$ %, ϕ being vol. fract.), for PW and PW-HD based PCMs, respectively, in the liquid state. For PW based PCMs, thermal conductivity enhancements increased from ~ 1.7 to ~ 9.4 %, when CBNP loading was varied from 0.5 to 2.5 wt. %. On the other hand, for PW-HD based PCMs, thermal conductivity enhancements increased from ~ 0.5 to ~ 6.6 % for similar variation in CBNP loading. **Figs. 5.9a-b** also show the theoretical curves for thermal conductivity enhancements, which were obtained from Hamilton-Crosser [366] model considering a particle shape factor of 6 and classical Maxwell-Garnett model. It can be seen from **Figs. 5.9a-b** that the experimentally obtained k/k_f values were systematically higher than those predicted by classical Maxwell-Garnett, which indicated the presence of aggregates, formed due to weak van der Waal's interactions, in the liquid state [215, 289]. Such aggregates resulted in an augmentation of thermal conductivity due to improved physical contact of the nano-inclusions with each other within an aggregate, with dimension (indicated by its radius of gyration) significantly larger than the individual nano-inclusions [215, 342]. Moreover, these aggregates grow in size with increasing loading concentration leading to a progressive enhancement in thermal conductivity. It can be further seen from **Figs. 5.9a-b** that the theoretical estimations were better for data obtained from the Hamilton-Crosser model, which was due to the incorporation of particle shape factors in these calculations. Classical effective medium theory is strictly valid for spherical particles [511], whereas the shape of the CBNP aggregates were fractal in nature. Further, the mismatch between the experimental and theoretical data increased with CBNP concentration in both the cases, which was attributed to the increasing size of the aggregates and enhanced liquid layering in the vicinity of the nano-clusters [511, 512].

On the other hand, the enhancement of thermal conductivity in the solid state was analyzed using a logarithmic heat conduction model proposed by Agari and Uno [390], which takes into account the heat transfer through a percolation network of nano-inclusions in a host matrix at medium to high loading concentrations.

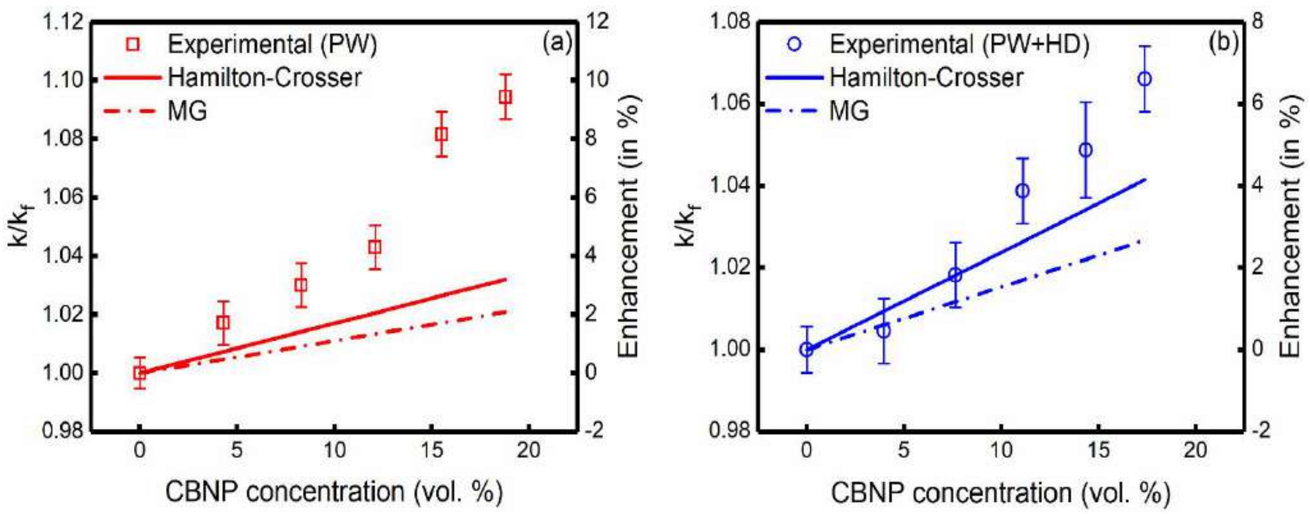

Figure 5.9 Variation of k/k_f and percentage enhancement in thermal conductivity of (a) PW and (b) PW-HD based PCMs, in the liquid state, as a function of CBNP concentration. The theoretical curves for thermal conductivity enhancements, obtained from Hamilton-Crosser (HC) and classical Maxwell-Garnett (MG) models are also shown in the corresponding figures.

The effective thermal conductivity of the CBNP loaded PCMs are the highest for parallel mode of heat transfer, whereas series mode of heat transfer leads to the minimum effective thermal conductivity. The effective thermal conductivity (k) in parallel mode can be expressed as $k = \phi k_{CB} + (1-\phi)k_f$, where ϕ, k_{CB} and k_f indicate the loading concentration in volume fraction, thermal conductivity of CBNP nano-inclusions and host matrices (PW or PW-HD in solid state), respectively. On the other hand, effective thermal conductivity in the series mode is expressed as $\frac{1}{k} = \frac{\phi}{k_{CB}} + \frac{(1-\phi)}{k_f}$. Assuming both modes of heat transfer occur in real scenario, a generalized effective thermal conductivity was proposed by Agari and Uno, which is indicated by the following equation [390].

$$k^n = \phi(k_{CB})^n + (1-\phi)(k_f)^n \tag{5.1}$$

Here, n is an exponent and for n = 1 or -1, the heat transfer modes are purely parallel or series in nature, respectively. To account for the effects of percolative heat transfer through the network of nano-inclusions, changes in crystallinity of the host matrices upon loading with nano-inclusions and liquid-layering in the vicinity of the nano-inclusions, Eq. 5.1 was further modified to incorporate the empirical constants (β_1 and β_2) and is expressed by the following equation [390].

$$k^n = \phi (k_{CB})^{\beta_1 n} + (1-\phi)(\beta_2 k_f)^n \qquad (5.2)$$

Here, the empirical constant β_1 indicates the ease of forming of quasi-2D network of nano-inclusions and in-turn, corresponds to the percolation heat transfer efficiency [513]. A high value of β_1 (~ 1) indicates superior percolation heat transfer through the networks of nano-inclusions. On the other hand, the empirical constant β_2 indicates the nano-inclusions mediated changes of the thermo-physical properties of the host matrices, like crystallinity [390], enhanced orientational ordering in the vicinity of nano-inclusions-PCM interfaces [65] and nano-inclusion induced nucleation during freezing [430]. Performing natural logarithm on both sides of Eq. 5.2, resulted in a linear variation of ln(k) with loading concentration, which is indicated by the following equation [390].

$$\ln(k) = \phi \beta_1 \ln(k_{CB}) + (1-\phi)\ln(\beta_2 k_f) \qquad (5.3)$$

The empirical constants β_1 and β_2 were determined from linear regression analyses. **Figs. 5.10a-b** show the variations of ln(k) as a function of CBNP loading concentration (in vol. %) for PW and PW-HD based PCMs, respectively.

The linear regression analyses, based on Eq. 5.3, are also shown in the corresponding figures. The R^2 values were found to be ~ 0.89 and 0.97 for PW and PW-HD, respectively. The empirical constant β_1 was found to be ~ 1.0, in both the cases, which indicated efficient percolative heat transfer through the fractal network of CBNP nano-inclusions. It must be noted in this regard, that the value of β_2 was found to be ~ 30 % higher for PW-HD based PCMs, which might be due to the strong anisotropic growth kinetics of HD during freezing [387].

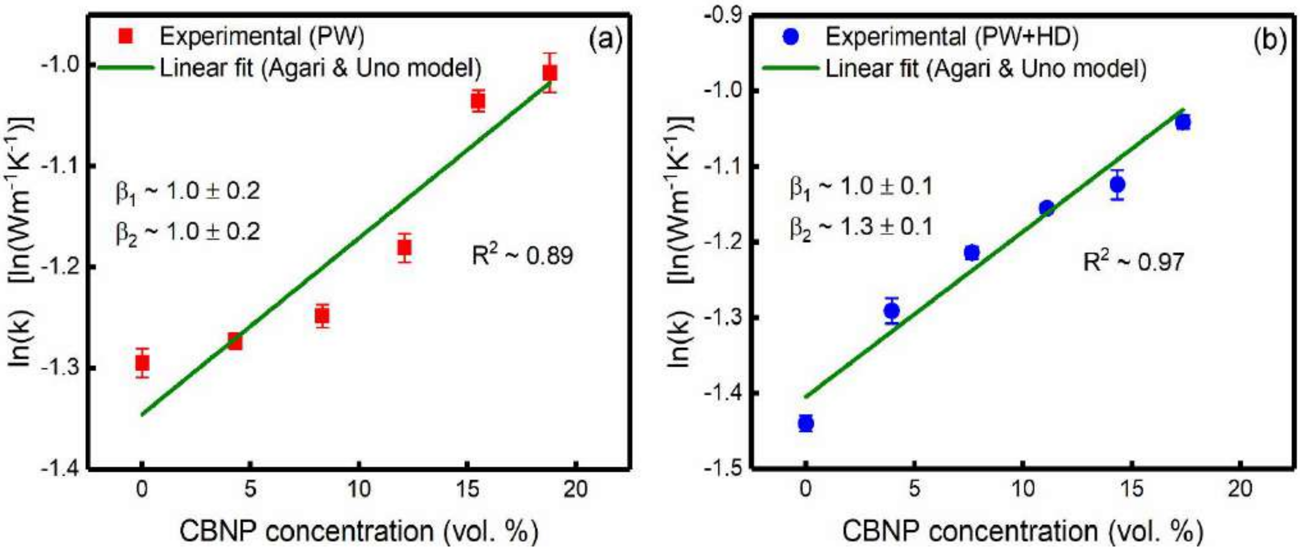

Figure 5.10 Variation of ln(k) as a function of CBNP loading concentration (in volume fraction) for (a) PW and (b) PW-HD based PCMs, in the solid state. The linear regression analyses, obtained from Eq. 4, following Agari & Uno model, are also shown in the corresponding figures. The values of the empirical constants (β_1 & β_2) were estimated from the linear regression analyses.

This was also discernible from the atomic force and optical phase contras microscopy images. For theoretical calculations, the thermal conductivity of CBNP (k_{CB}) was considered as ~ 0.182 W/mK [514]. Though this value is higher than the liquid state thermal conductivities of PW and PW-HD; thermal conductivities of the pristine PCMs were higher in the solid state. Nevertheless, it must be noted in this regard, during freezing of the nano-inclusion loaded PCMs, solidification induced internal stress field compresses the CBNP nano-inclusions leading to a higher thermal conductivity in the solid state [514].

Figures 5.11a-b show the thermal cycling of PW and PW-HD based PCMs, respectively, loaded with 1.5 wt. % of CBNP. In the case of PW based PCM, thermal conductivity enhancements in the solid state were ~ 91.4, 79.0, 74.1 and 71.6 % after 1st, 2nd, 3rd and 4th thermal cycles, respectively. On the other hand, for PW-HD, thermal conductivity enhancements in the solid state were ~ 117.1, 92.8, 67.8 and 57.9 % after 1st, 2nd, 3rd and 4th thermal cycles, respectively. Due to irreversible aggregation dynamics of the nano-inclusion clusters, thermal conductivity enhancements in solid state decreased with increasing number of thermal cycles (as seen from **Figs. 5.11a-b**) [216, 515]. Moreover, weak interactions between nano-inclusions and host matrices leads to negative thermal conductivity enhancements for positive Kapitza length, which also results in the variation of thermal conductivity enhancements during thermal cycling [231]. It must be noted in this regard that after repeated freezing/melting cycles, the aggregates of CBNP grow in size, which increases the surface roughness leading to higher diffused phonon scattering at the interfaces, which also contributes to the lowering of thermal conductivity [443]. **Figs. 5.11c-d** show the heat flow curves for PW and PW-HD based PCMs, respectively, without any CBNP loading in the virgin condition as well as after 100 thermal cycles. It can be clearly seen from **Figs. 5.11c-d** that phase transformation characteristics remain almost similar for the PCMs, even after 100 thermal cycles. The **inset of Fig. 5.11c** show the variations of peak phase transformation temperature and latent heat after 100 cycles for PW. It can be clearly seen that peak phase transition temperature and latent heat remained almost constant (peak temperature increased from ~ 60.0 ^{0}C to ~ 60.1 ^{0}C after 100 cycles and latent heat slightly decreased from ~ 125.9 kJ/kg to ~ 123.3 kJ/kg after 100 thermal cycles). Similarly, from the **inset of Fig. 5.11d** it can be seen that for PW-HD, the variations in peak phase transformation temperature and latent heat were negligible (peak phase transformation temperature increased from ~ 45.9 ^{0}C to ~ 46.1 ^{0}C after 100 cycles and latent heat decreased from ~ 44.9 kJ/kg to ~ 44.1 kJ/kg after 100 cycles). The decrease in latent heat was only ~ 2.1 and 1.8 % for PW and PW-HD, respectively, even after 100 thermal cycles, which shows the efficacy of these PCMs for practical applications in latent heat thermal energy storage systems.

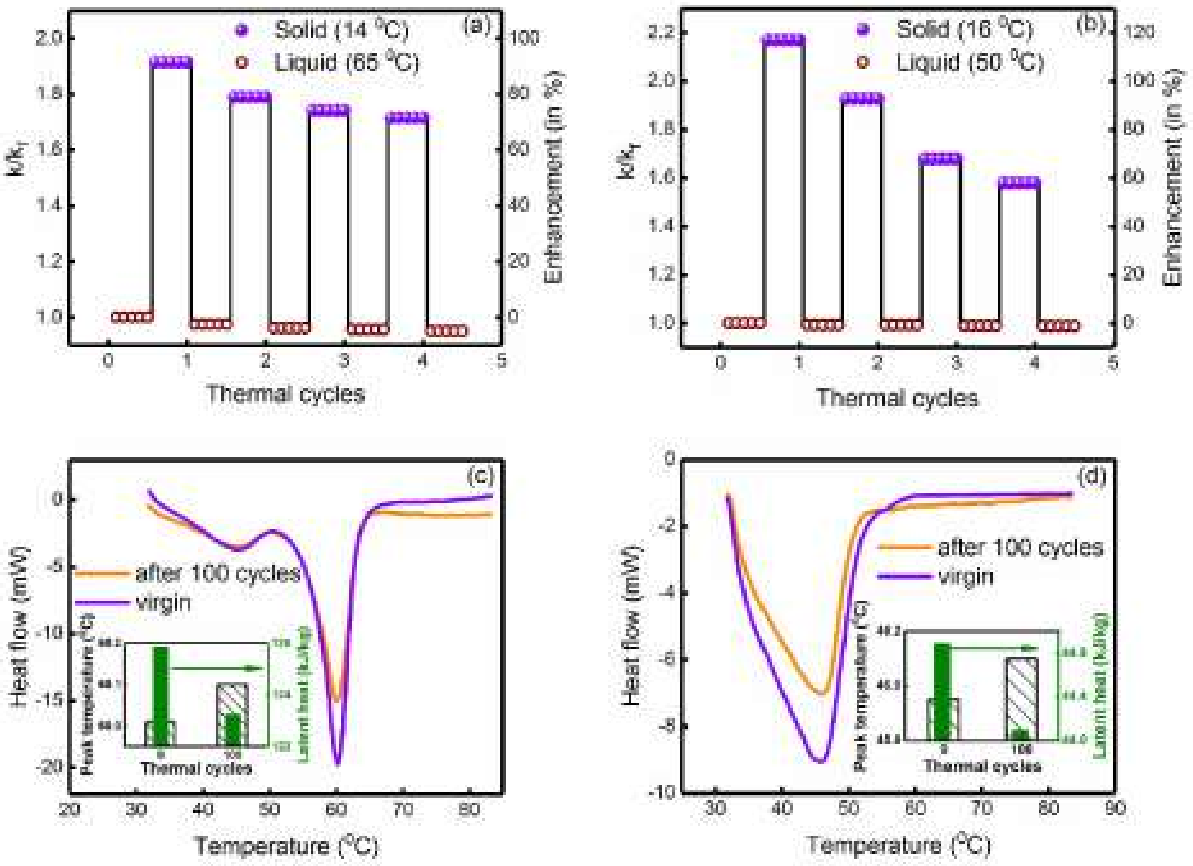

Figure 5.11 Variation of k/k$_f$ and percentage enhancement in thermal conductivity during repeated thermal cycling of (a) PW and (b) PW-HD based PCMs, loaded with 1.5 wt. % of CBNP. Heat flow curves for (c) PW and (d) PW-HD based PCMs, without any CBNP loading, in the virgin condition as well as after 100 thermal cycles. (Inset of c and d) Bar chart comparing the variations of peak phase transformation temperature and latent heat values between the virgin condition and after 100 thermal cycles for PW and PW-HD based PCMs, respectively.

5.2.4 CBNP assisted enhancement in photo-thermal conversion of PW-based PCMs

Photo-thermal conversion is of immense practical importance for efficient utilization of solar energy in the form of direct solar absorbing working fluids or intermediate storage of solar energy using direct solar absorbing PCMs [47, 516]. CBNP is a non-selective solar absorber over a wide range of solar spectrum (~ 0.25-2.5 μm) and has been reported to exhibit superior solar absorption properties and volumetric heating efficiency, when incorporated in a host matrix, as compared to other nanoparticles [516, 517]. Here, we study the photo-thermal conversion efficiency of CBNP loaded PW based PCMs and **Fig. 5.12a** shows the variation in temperature rise, as a function of time, for the PW based PCMs loaded with various concentrations of CBNP. Here, the samples were initially thermally acclimatized at ~ 20 (± 1) ^{0}C for 5 minutes and thereafter, exposed to the artificial solar spectrum using two 1kW halogen lamps working at 50% efficiency. Infrared thermography was used for non-contact measurement of the rise in sample temperature and it can be seen from **Fig. 5.12a** that sample temperature monotonically increased with time upon exposure to the solar spectrum. It can be further seen from **Fig. 5.12a** that the rate of temperature rise was larger for higher CBNP loading. The observations were in agreement with the temperature rise curves earlier reported for aqueous nanofluid containing CBNP nano-inclusions [47].

The photo-thermal conversion efficiency was quantitatively estimated from the initial rate of temperature rise under adiabatic limit, ($\left.\frac{dT}{dt}\right|_{t\to 0}$), which was estimated from linear regression analyses of the temperature rise curves. **Fig. 5.12b** shows the variation of initial rates of temperature rise and maximum temperature rise (ΔT_{max}) at t = 700 s, as a function of CBNP concentrations. It can be seen from **Fig. 5.12b** that the rates of temperature rise and ΔT_{max} increased linearly with CBNP concentration (linear fits are also shown in the figure). The R^2 values were ~ 0.97 in both the cases. The observed linear increase in photo-thermal conversion efficiency with increasing CBNP loading was found to be in agreement with the measurements reported by Zeiny et al. [516] for CBNP based nanofluids. **Fig. 5.12c** shows a bar chart comparing the % enhancement in photo-thermal conversion efficiency as a function of CBNP loading for the PW based PCMs. The % enhancements in photo-thermal conversion efficiency were ~ 6.5, 24.5, 49.7, 66.5 and 84.3 % for 0.5, 1.0, 1.5, 2.0 and 2.5 wt. % CBNP loading, respectively.

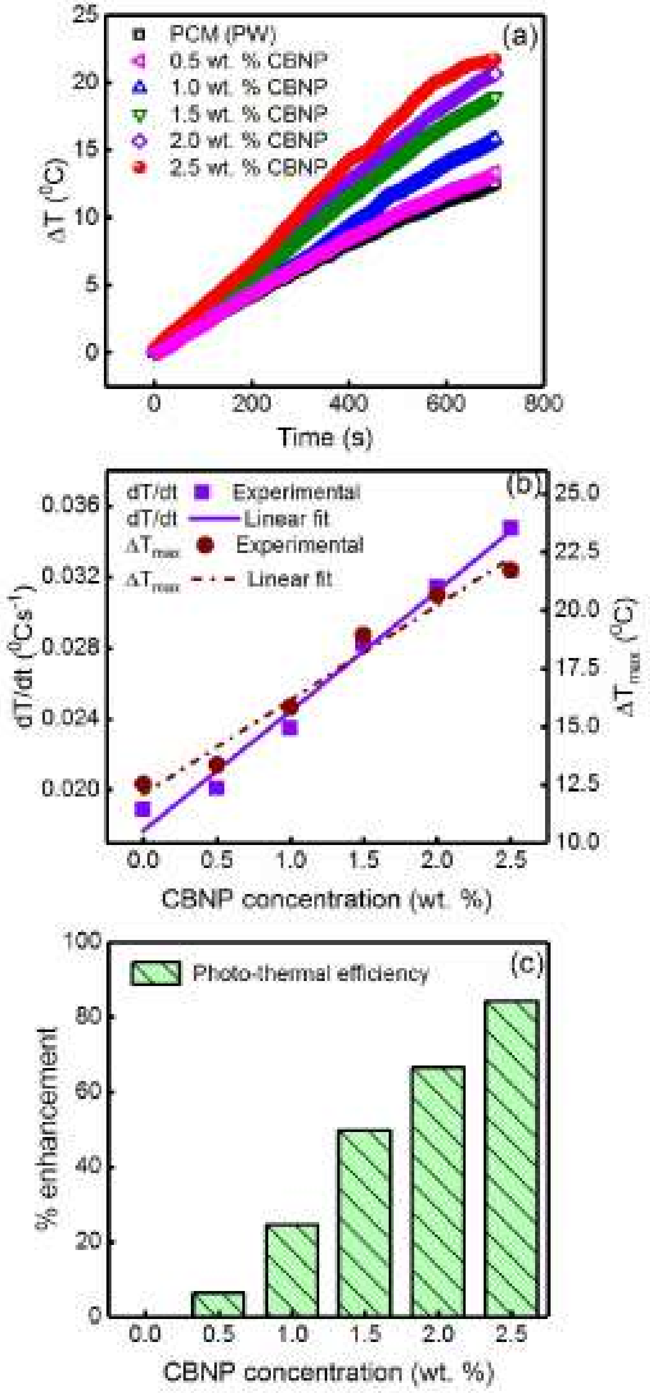

Figure 5.12 (a) Variation in temperature rise, as a function of time, for the PW based PCMs loaded with various concentrations of CBNP during photo-thermal studies. (b) Variation of initial rates of temperature rise and maximum temperature rise (ΔT_{max}) at t = 700 s, as a function of CBNP loading for the PW based PCMs. The linear regression analyses are also shown in the figure. (c) A bar chart comparing the percentage enhancement in photo-thermal conversion efficiency as a function of CBNP loading for the PW based PCMs.

The total extinction coefficient (σ_{eff}) of the nano-enhanced PCM is the sum-total of the extinction coefficients of the host matrix (PCM) and the dispersed nano-inclusions (CBNP), i.e. $\sigma_{eff} = \sigma_{matrix} + \sigma_{CBNP}$. The extinction coefficient of the host matrix is independent of the CBNP loading concentration and can be expressed as $\sigma_{matrix} = 4\pi\lambda^{-1}k_{matrix}$, where λ and k_{matrix} indicate incident wavelength and complex component of the refractive index of the host matrix [518]. On the other hand, the extinction coefficient of the CBNP nano-inclusions are dependent on the scattering (Q_S) and absorption (Q_A) efficiencies of the dispersed nano-inclusions and can be expressed as $\sigma_{CBNP} = 1.5\phi(Q_S + Q_A)/D$, where ϕ and D indicate loading concentration and typical nano-inclusion dimension, respectively [519]. This shows that the total extinction coefficient increases with CBNP loading, thereby enhancing the photo-thermal conversion efficiency.

CBNP forms aciniform shaped aggregates and the size of these aggregates increases with loading concentrations, as seen from the optical phase contrast microscopy images. (**Figs. 5.8e-f**). Such micron sized aggregates result in Mie scattering of the incident solar radiation and the total extinction ($Q_E = Q_S + Q_A$) efficiency is expressed by the following equation [520].

$$Q_E = \frac{2}{(\pi D/\lambda)^2}\sum_{n=1}^{\infty}(2n+1)\Re(a_n + b_n) \tag{5.4}$$

Here, a_n and b_n are Mie scattering coefficients (electric and magnetic, respectively [520]) and earlier studies show that for fixed values of incident wavelength and dielectric constant, the Mie extinction efficiency of carbon nanospheres increases with the dimension of the nano-inclusions [521]. This results in intense multiple scattering and augmented absorption of the incident solar radiation in the PW based PCMs loaded with higher concentrations of CBNP nano-inclusions, leading to enhanced photo-thermal conversion efficiency.

5.3 CBNP aided enhancement in thermal conductivity and photo-thermal conversion in lauric acid-based PCMs

Here, lauric acid (LA) was chosen as the PCM due to its solid-liquid phase transition temperature (~ 45 ^{0}C), which is ideal for various applications in building thermoregulation, textile industries, hot water pipe lines, waste heat recovery and solar-thermal applications [90, 281, 522]. Earlier studies, reported thermal conductivity enhancements in LA based PCMs loaded with various types of nano-inclusions, viz. expanded perlite [282], single walled carbon nano horns [250], activated carbon, graphene nanoplatelets [65], expanded vermiculite [284], modified sepiolite [283], carbonized wood [523] and silicon dioxide [249]. Nevertheless, lengthy and time-consuming sample preparation steps (like vacuum impregnation or wet chemical methods) and high cost of these nano-inclusions render them less cost effective for rapid large-scale adaptation. This calls for the development of cheaper PCMs loaded with alternate nano-inclusions. Intermediate storage of solar energy using solar absorbing PCMs is essential for effective utilization and load redistribution of solar-thermal energy applications [47]. This is also immensely beneficial from environmental aspect to minimize energy wastage [516]. It is envisaged that high thermal conductivity coupled with enhanced photo-thermal conversion efficiency of such alternate nano-inclusions will pave the way for designing portable solar-thermal battery packs that are immensely helpful for practical applications. Towards this objective, here, the suitability of carbon black nano powder (CBNP) as a low-cost alternate nano-inclusion for LA based PCMs was studied. To arrest the leakage and associated material loss, LA based form-stable PCM with good load bearing capacity was demonstrated.

5.3.1 Preparation of nano-inclusion loaded PCMs

CBNP nano-inclusions were dispersed in the liquid PCM, under water bath sonication with bath temperature maintained at ~ 55 ± 2 ^{0}C (i.e. above the solid-liquid phase transition temperature of LA, which is typically around ~ 45 ^{0}C). In the case of CBNP nano-inclusions, 8 different loading concentrations were used, viz. 0.5, 1.0, 1.5, 2.0, 2.5, 3.0, 3.5 and 4.0 wt. %. The corresponding sonication times were 1200, 1500, 1800, 2100, 2400, 2700, 3000 and 3300 s, respectively. The sonication time was increased for higher loading concentrations to ensure homogenous dispersion of the nano-inclusions within the PCM. After thorough mixing, the nano-inclusion loaded PCMs were solidified under natural cooling (environmental temperature kept constant at 22 ± 1 ^{0}C). To confirm the absence of any chemical reactions, FTIR spectroscopy was performed. To study the effect of aggregation on thermal conductivity enhancement of the nano-inclusion loaded PCMs, optical phase contrast microscopy imaging was carried out, in the solid state, using a Carl Zeiss inverted microscope equipped with a 10X objective. Additionally, to probe the aggregation dynamics at micro-scale, real-time optical phase contrast video-microscopy was carried out during freezing of the PCM loaded with 1 wt. % of CBNP nano-inclusions. Differential scanning calorimetry (DSC) studies were carried out under an inert atmosphere of argon gas (heating rate of ~ 3 ^{0}C per minute) to quantify the phase transition temperature and latent heat of the pristine or nano-inclusion loaded PCMs. The peak phase transition temperatures, onset and endset temperatures and the associated latent heat values were evaluated from the heat flow curves, with measurement accuracies of ± 0.1 ^{0}C, ± 0.5 ^{0}C and 0.4 kJ/kg, respectively. The phase transition temperatures were also evaluated from refractive index and IRT-based measurements. For IRT based experiments, the samples were initially thermally acclimatized at 75 ^{0}C and then placed within a recirculating water bath with bath temperature fixed at ~ 20 ± 0.1 ^{0}C. The recirculating water bath was equipped with a top opening that ensured unobstructed field of view for the infrared camera, which was positioned at ~ 0.35 m vertically above the samples. Thermal conductivity and photo-thermal conversion were measured using a KD2 probe and infrared thermography-based non-contact temperature measurement, respectively (details provided in chapter 2).

5.3.2 Thermo-physical properties of the nano-inclusion loaded PCMs

Figure 5.13 shows the FTIR spectra of the pristine PCM and the PCM loaded with CBNP nano-inclusion, where all the major absorption bands are indexed. Detailed descriptions of the absorption bands are provided in **Table 5.6** [68, 217, 248, 249, 524]. It can be seen from **Fig. 5.13** that the absorption bands remained unchanged after loading the PCMs with CBNP nano-inclusions and no new absorption bands were observed. This indicated that no chemical reactions occurred between the nano-inclusions and the PCM host matrix [62, 142, 220].

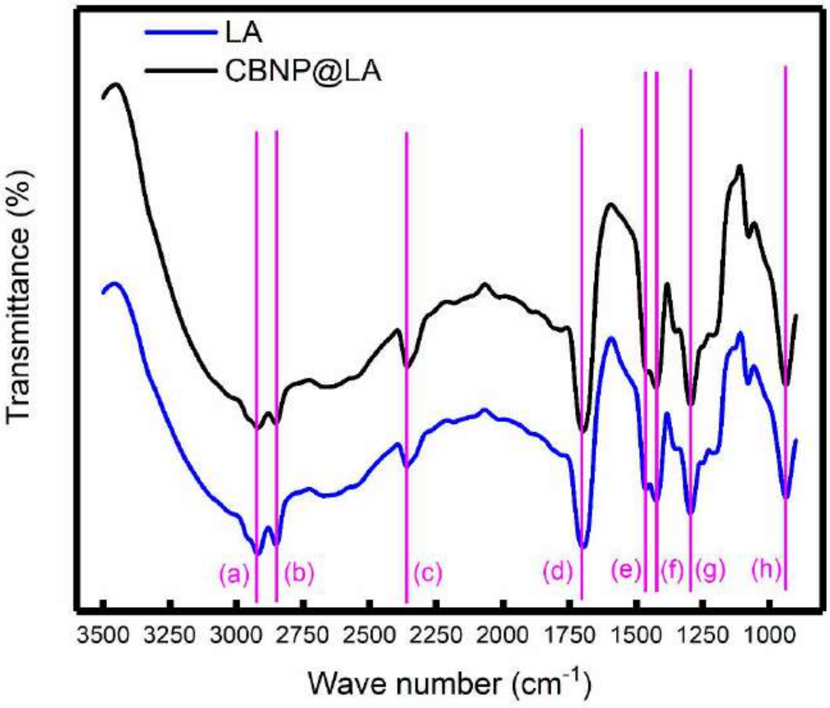

Figure 5.13 FTIR spectra of the CBNP a loaded PCM, where all the major absorption bands are indexed and detailed descriptions are provided in Table 5.6. For comparison, the FTIR spectra of the pristine PCM, without any nano-inclusions, are also shown.

Table 5.6 Detailed description of the major absorption bands observed in the FTIR spectra of the PCMs, with or without nano-inclusion loading.

Legend	Wave number (cm^{-1})	Description	Reference
(a)	2926	Stretching vibrations of $-CH_3$ group	[68, 249]
(b)	2850	Stretching vibrations of $-CH_2$ group	[68, 249]
(c)	2358	C-O stretching vibration from atmospheric CO_2	[217]
(d)	1707	Stretching vibration of C=O (carbonyl group)	[68]
(e)	1470	$-CH_2$ scissor vibration	[524]
(f)	1424	$-CH_3$ asymmetric deformation vibration	[524]
(g)	1298	In-plane bending vibration of O-H (hydroxyl group)	[248]
(h)	937	Out-of-plane bending vibration of O-H (hydroxyl group)	[248]

Figure 5.14a shows the heat flow curves for the PCMs loaded with varied concentrations of CBNP nano-inclusions. The heat flow curves for the pristine LA is also shown the figure for comparison. It can be seen from **Fig. 5.14a** that the heat flow curves consisted of single endotherms, indicating the first order solid-liquid phase transitions. The onset (T^O) and endset (T^E) temperatures indicted the beginning and completion of the phase transition process, which were determined from the intersections of the extrapolated tangents from points of maximum slopes of the leading and trailing edges, respectively, with the base line [412]. The latent heat values were determined from the areas under the heat flow curves. Additionally, the latent heat values were calculated for the nano-inclusion loaded PCMs, using the formula: $\Delta H_{PCM} = \varepsilon \times \Delta H_{LA}$, where ΔH_{PCM}, ΔH_{LA} and ε indicate the calculated latent heat of the nano-inclusion loaded PCMs, experimentally determined latent heat for pristine LA and mass percentage of the host matrix in the nano-inclusion loaded PCMs, respectively [523]. The peak phase transition temperature (T^P), T^O, T^E and latent heat values (experimental and theoretical) are listed in **Table 5.7** for the PCMs loaded with various concentrations of CBNP nano-inclusions. In the present study, the peak phase transition temperature for pristine LA was found to be ~ 45.4 ± 0.1 ^{0}C, which was found to be in agreement with the earlier reported

values of 44.0 - 46.8 ^{0}C [249, 250, 525]. **Fig. 5.14b** shows the variations of T^{O}, T^{P} and T^{E} for the PCMs loaded with various concentrations of CBNP nano-inclusions. It is evident from **Figs. 5.14b** and **Table 5.7** that the phase transition temperature did not vary significantly with increasing loading concentrations, which indicated the absence of any strong interactions between the nano-inclusions and the PCM host matrix [249]. Similar results were earlier reported for paraffin wax based PCMs loading with various concentrations of CBNP nano-inclusions [217]. In the present study, the latent heat of melting for pristine LA was found to be 151.6 ± 0.4 kJ/kg, which was in agreement with the earlier reported values of 142-159 kJ/kg [250, 281, 282]. **Figs. 5.14c** shows the variations of experimental and calculated latent heat values with increasing loading of CBNP nano-inclusions.

Table 5.7 Onset temperature, peak phase transition temperature, endset temperature and latent heat values for the PCMs loaded with various concentrations of CBNP nano-inclusions.

CBNP concentration (wt. %)	T^{O} (^{0}C) (± 0.5 ^{0}C)	T^{P} (^{0}C) (± 0.1 ^{0}C)	T^{E} (^{0}C) (± 0.5 ^{0}C)	Latent heat (kJ/kg) (± 0.4 kJ/kg) (experimental)	Latent heat (kJ/kg) (calculated)
0	43.8	45.4	48.4	151.6	-
1	43.8	45.8	48.5	149.5	150.1
2	43.7	45.5	48.4	142.6	148.6
3	43.7	45.2	48.9	139.0	147.1
4	43.7	45.3	49.3	138.5	145.5

Figure 5.14c clearly shows that latent heat decreased at higher loading. In the absence of any significant interaction between the nano-inclusions and the PCM host matrix (as confirmed from FTIR spectroscopy), increasing loading of nano-inclusions leads to a decrease in latent heat as the mass percentage of PCM is decreased progressively and only the PCM matrix absorb or release heat during phase transition and the nano-inclusion do not contribute towards latent heat storage [58, 217, 249]. Similar decreasing trends in latent heat values for

higher loading were earlier reported by Chen et al. [248] for LA-activated carbon composite PCMs; Fu et al. [281] for LA-diatomite composite PCMs; Sari et al. [282] for LA–expanded perlite composite PCMs and Shen et al. [283] for LA-modified sepiolite composite PCMs.

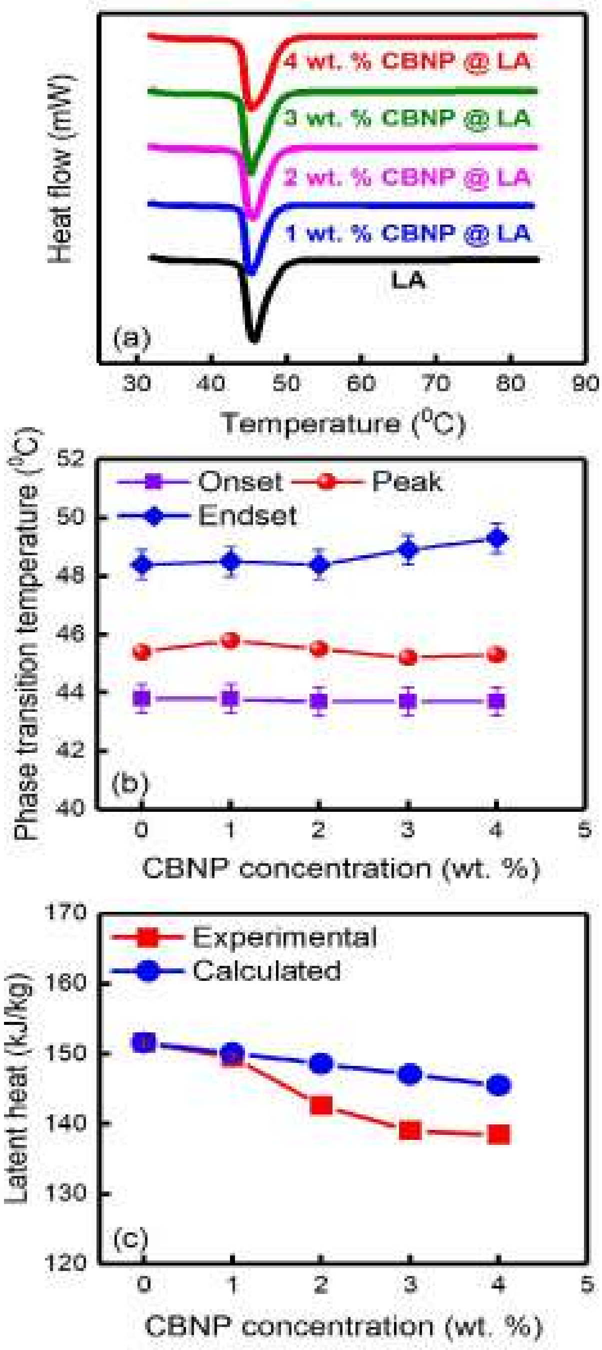

Figure 5.14 (a) Heat flow curves of the CBNP loaded LA-based PCMs. For comparison, heat flow curve of the pristine LA is also shown. (b) Variation of onset, peak and endset temperature as a function of CBNP loading. (c) Variation of experimental and calculated latent heat as a function of CBNP loading.

Figure 5.15a shows the temperature dependence of the refractive index for pristine LA, during melting and solidification. Refractive index was lower in the liquid state and with decrease in temperature, refractive index increased due to an increase in medium density. The phase transition region (encircled in **Fig. 5.15a**) was associated with a sudden change in refractive index due to the discontinuous change in medium density during first order liquid-solid phase transition. From refractive index measurements, the phase transition temperature for pristine LA was estimated as ~ 44 ± 0.5 ^{0}C. Further, the refractive index at T = 40 ^{0}C, were ~ 1.4335 and 1.43315 during solidification and melting, respectively. These values were in good agreement with the earlier reported value of ~ 1.4319 at T = 40 ^{0}C, for pure LA [526]. The **insets of Fig. 5.15a** show the typical photographs of LA in the solid and liquid states.

Non-contact temperature mapping using infrared thermography (IRT) was carried out to probe the cooling curve of pristine LA and **Figs. 5.15b-c** show the typical infrared images, along with the pseudo-colour coded temperature scales, for LA at time t = 0 and 500 s, respectively. The infrared images showed a clear decrease in sample temperature with time. Quantitative measurements were carried out by performing spatial averaging over several pixels, excluding the edge pixels. **Fig. 5.15d** show the average temperature decay during natural cooling, when the sample was immersed in a recirculating water bath maintained at ~ 20 ± 0.1 ^{0}C (indicated by the black horizontal base line in **Fig. 5.15d**). The region of highest slope change was identified from differential analysis of the IRT-based temperature decay curve and the phase transition temperature was estimated at 46.2 ± 0.5 ^{0}C. The sample temperature dropped from the initial value of ~ 75 ^{0}C to ~ 46.2 ^{0}C within 117 s and thereafter, the sample temperature remained constant during completion of the phase transition for ~ 800 s. The phase transition region was associated with the nearly flat region of the temperature-time curve in **Fig. 5.15d** and beyond this, the sample temperature again decreased, ultimately attaining the surrounding water-bath temperature.

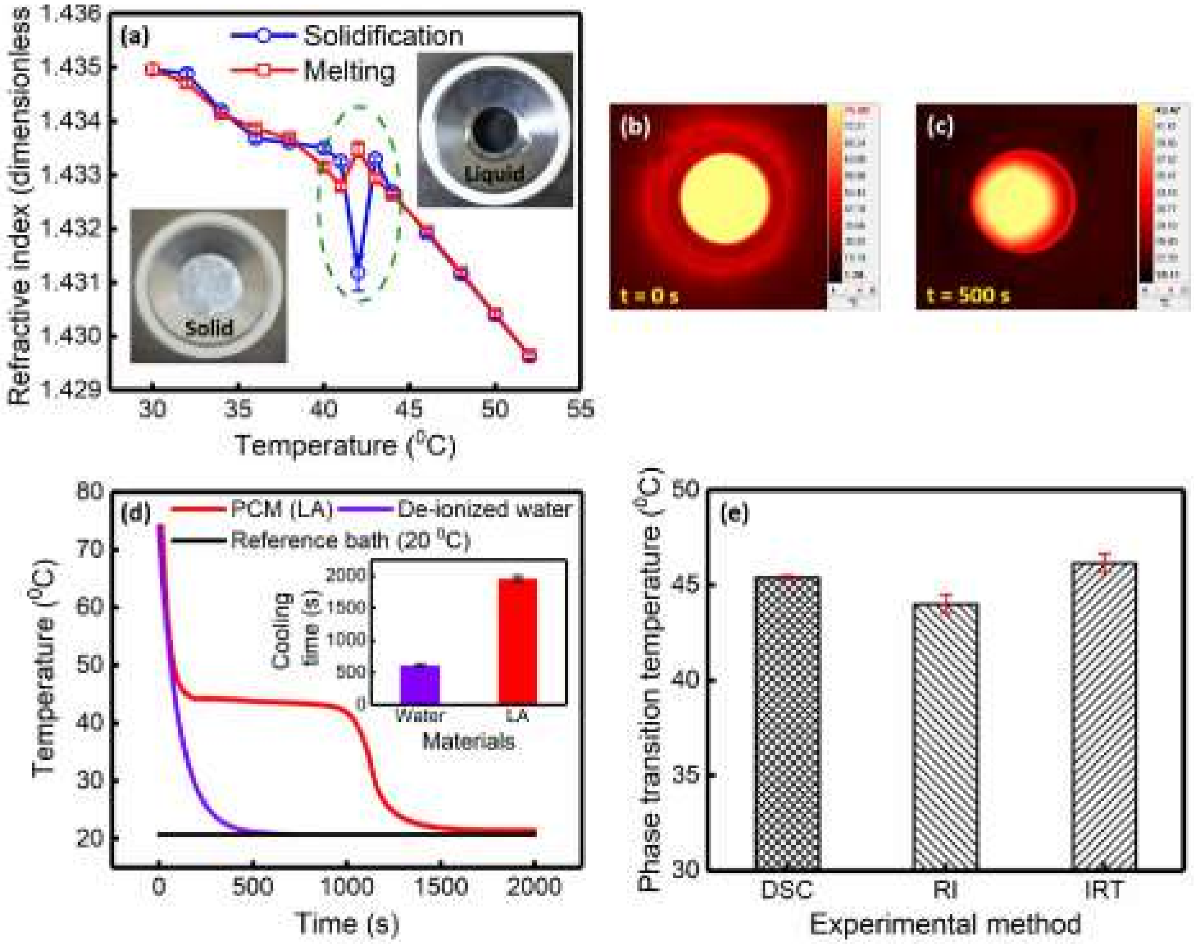

Figure 5.15 (a) Variation of the refractive index as a function of temperature for pristine LA, during melting and solidification. The phase transition region is indicated in the figure. (Insets) Typical photographs of LA in the solid and liquid states. Typical infrared images for LA during cooling, when placed within a temperature-controlled water bath at time t = (b) 0 and (c) 500 s. The pseudo colour coded temperature scales are also shown. (d) Average temperature decay, during natural cooling, obtained from infrared thermography. For comparison, the temperature decay curve for de-ionized water is also shown. The horizontal line indicates the water bath temperature. (Inset) Bar chart comparing the cooling times for de-ionized water and LA. (e) Bar chart comparing the phase transition temperatures for pristine LA, estimated from three different experimental techniques, viz. differential scanning calorimetry (DSC), refractive index (RI) measurement and infrared thermography (IRT) based temperature mapping.

For comparison, **Fig. 5.15d** also shows the temperature decay for de-ionized water, where temperature decayed exponentially to attain the surrounding water bath temperature at an earlier time scale. The **inset of Fig. 5.15d** shows a bar chart comparing the cooling times for de-ionized water and LA. Here, cooling time was defined as the time required to attain the temperature of water bath (with a relaxation of ± 0.5 ^{0}C). The cooling times for de-ionized water and pristine LA were 610 ± 25 and 1960 ± 40 s, respectively. This indicated ~ 221 % gain in cooling time for pristine LA, which is immensely advantageous for thermal energy storage applications. **Fig. 5.15e** show a bar chart comparing the phase transition temperatures for pristine LA, estimated from three different experimental techniques, viz. DSC, refractive index (RI) measurement and IRT based temperature mapping. It can be seen from **Fig. 5.15e** that the phase transition temperatures determined from the above-mentioned three methods were in agreement with each other.

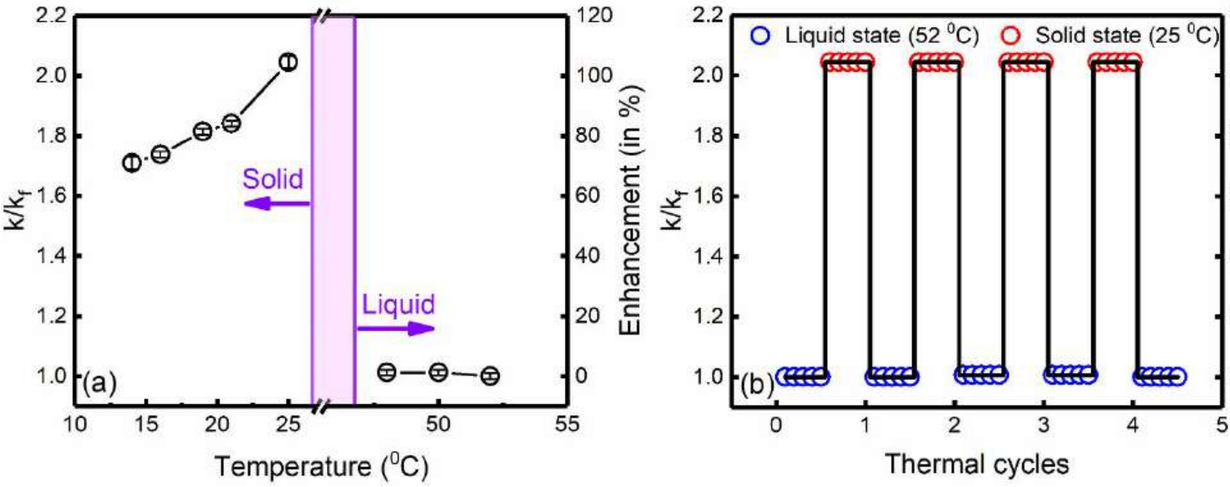

Figure 5.16 (a) Variation of k/k$_f$ and percentage enhancement in thermal conductivity as a function of temperature for pristine LA. Here, k and k$_f$ indicate temperature dependent thermal conductivity and thermal conductivity of LA in the liquid state (at T = 52 ^{0}C), respectively. The variation of k/k$_f$ was divided into two distinct regions, viz. liquid and solid states (as indicated in the figure). The shaded region in the figure indicate the phase transition region. (b) Variations in k/k$_f$ and percentage enhancement in thermal conductivity in the liquid (T = 52 ^{0}C) and solid (T = 25 ^{0}C) states for pristine LA, during consecutive melting/freezing cycles (thermal cycles).

Figure 5.16a shows the temperature dependent variations of k/k_f in the case of pristine LA, where k and k_f indicated measured thermal conductivity and thermal conductivity of pristine LA in the liquid state (at T = 52 ^{0}C), respectively. In the present study, k_f was found to be ~ 0.140 ± 0.001 W/mK, which was in agreement with the earlier reported values [527]. **Fig. 5.16a** also shows the percentage enhancement in thermal conductivity, as a function of temperature. The variation of k/k_f was divided into two distinct regions, viz. liquid and solid states (as indicated in **Fig. 5.16a**). On the other hand, the purple shaded region in **Fig. 5.16a** indicated the phase transition region, where thermal conductivity measurements were not performed because of instabilities due to thermal fluctuations. It can be seen from **Fig. 5.16a** that k/k_f values were lower in the liquid state and significant thermal conductivity enhancement was observed in the solid state. In the solid state, thermal conductivity for pristine LA were ~ 0.287 ± 0.002 and 0.240 ± 0.002 W/mk at T = 25 and 14 ^{0}C, respectively. These values were in good agreement with earlier reported values of 0.215-0.280 W/mK [65, 68]. With decrease in sample temperature, LA undergoes first order liquid-solid phase transition (at ~ 45 ^{0}C) and form nano-crystalline structure after freezing, which aides in phonon mediated heat transfer in the solid state [215, 216]. Formation of regular crystalline structure in LA, after freezing, was experimentally confirmed from X-ray diffraction, where sharp Bragg reflection peaks, corresponding to the monoclinic structure of solidified LA crystals, were observed [281, 528]. Molecular dynamics based simulation studies also confirmed higher thermal conductivity in the solidified PCMs, due to the presence of nanocrystalline structures [493]. Harish et al. [250] also reported similar thermal conductivity enhancements in LA based PCMs, after solidification. **Fig. 5.16a** further indicated a slight decrease in solid state thermal conductivity at lower temperature, which was attributed to the stress field induced conversion of larger crystallites to finer ones [387]. Presence of such smaller crystallites increases the phonon scattering at the grain boundaries, which can result in a decrease in thermal conductivity in the solid state with decreasing sample temperature. Similar phenomena were also observed in other crystal forming organic PCMs, like phenol-water system, n-hexadecane and paraffin wax [215-217, 237, 387, 395]. On the other hand, absence of phonon mediated heat transfer in the liquid state resulted in the lower thermal conductivity, as observed in **Fig. 5.16a** [215]. **Fig. 5.16b** shows the variations in k/k_f and percentage enhancement in thermal conductivity during consecutive thermal cycling for pristine LA. It was observed from **Fig. 5.16b** that the k/k_f values were ~ 1.0 and 2.05 in the liquid and solid states, respectively, indicating ~ 105 % enhancement in thermal conductivity in the solid state for pristine LA, which was attributed to the high phonon-mediated heat conduction efficiency in the solid state. **Fig. 5.16b** clearly shows the superior reversibility and stability of thermal conductivity enhancements during consecutive thermal cycles for the LA-based PCMs, which are advantageous for practical applications in thermal energy storage.

5.3.3 CBNP assisted enhancement of thermal conductivity in LA-based PCMs

Figure 5.17 shows the temperature dependent variations of k/k_f and thermal conductivity enhancement (in %) for the CBNP loaded PCMs, with varying particle loading. The variations of k/k_f were divided into the liquid and solid regions and the purple shaded regions in **Fig. 5.17** indicated the phase transition region. For comparison, variations of k/k_f in the case of pristine LA are also shown in the figure. **Fig. 5.17** clearly showed that the variation of k/k_f were not significant in the liquid state, whereas large thermal conductivity enhancements were observed in the solid state, i.e. at temperatures well below the phase transition point. In the case of CBNP loaded PCMs, thermal conductivity enhancements in the liquid state (T = 52 ^{0}C) were ~ 3.6, 5.5, 9.0, 11.2, 13.3, 15.4, 16.9, 17.6 % for loading concentrations of 0.5, 1.0, 1.5, 2.0, 2.5, 3.0, 3.5 and 4.0 wt. %, respectively. **Fig. 5.17** further shows that the thermal conductivity enhancements in the solid state (T = 25 ^{0}C) were ~ 132.8, 140.1, 143.0, 160.1, 163.7, 174.3 and 195.0 and 167.2 % for the PCMs loaded with 0.5, 1.0, 1.5, 2.0, 2.5, 3.0, 3.5 and 4.0 wt. % CBNP nano-inclusions, respectively.

For nano-inclusion loaded PCMs, the inclusions are squeezed towards the grain boundaries during freezing, predominantly due to the solidification induced stress fields [237, 387]. Existence of inhomogeneous distribution of internal stress fields in frozen hexadecane has been experimentally demonstrated [387]. The internal stress fields drive the nano-inclusions towards the intercrystallite spacing, which leads to the development of a quasi-2D percolating network of nano-inclusions with significantly superior thermal conductivity [238, 342]. Solidification induced stress field improves the surficial contacts between the nano-inclusions, thereby reducing interfacial phonon scattering and Kapitza resistance (i.e. thermal contact resistance) that causes an enhancement in phonon mediated conductive heat transfer through the network of nano-inclusions [234].

Further, the internal stress field induced aggregation reduces the interparticle spacing that results in the improvement of near-field radiative heat transfer, which provides further impetus to the effective heat transfer properties of the nano-inclusion loaded PCMs [419]. Formation of such nano-inclusion aggregates and subsequent development of percolating network was experimentally observed using optical phase contrast video microscopy. **Figs. 5.18a-l** show a few typical still micrographs, extracted from a time stamped video file, corresponding to t = 0, 5, 10, 15, 17, 19, 21, 23, 25, 30, 35 and 40 s, respectively. **Figures 5.18a-c** show the photomicrographs corresponding to the liquid state of the PCM (sample temperature ~ 50.5 ± 0.1 ^{0}C), where the CBNP nano-inclusions are clearly seen. In the present study, CBNP nano-inclusions were used without any surface modification and hence, on dispersion in the liquid PCM, loosely bound aggregates were formed due to van der Waal's interaction, as seen from **Figs. 5.18a-c**.

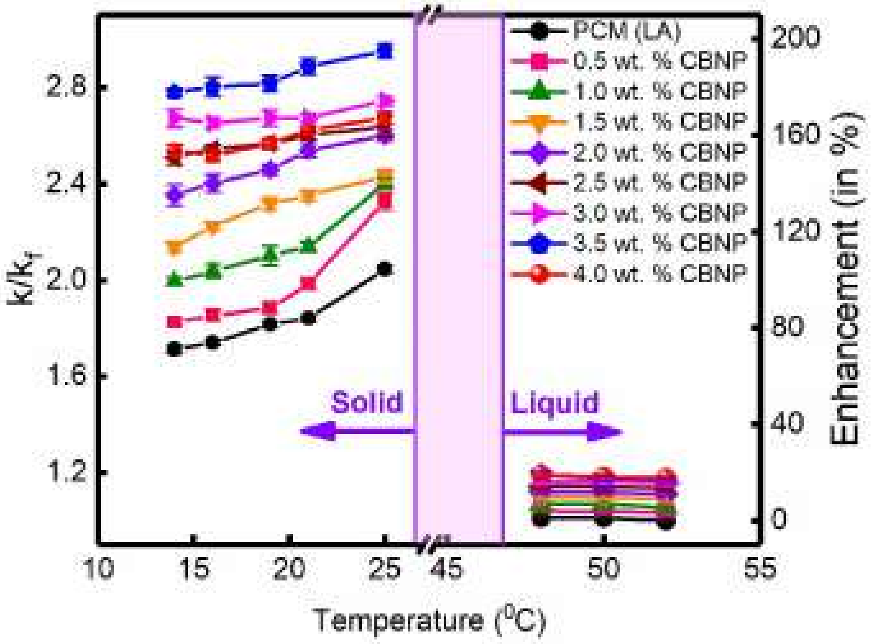

Figure 5.17 Variations of k/k$_f$ and percentage enhancement in thermal conductivity, as a function of temperature, for the LA based PCMs loaded with various concentrations of CBNP nano-inclusions. The variation of k/k$_f$ was divided into two regions, viz. liquid and solid states and the shaded regions indicated the phase transition region. For comparison, variation of k/k$_f$ in the case of pristine LA is also shown.

At time t = 10 s, the sample stage (peltier controlled) was allowed to cool to ~ 43.0 ± 0.1 ^{0}C at a cooling rate of 1.5 ^{0}C/minute and thereafter, the sample temperature was maintained at 43.0 ± 0.1 ^{0}C up to 40 s for completion of the freezing process. **Fig. 5.18d** (at t = 15 s) shows the commencement of the freezing process and the solidification wave fronts were clearly visible (indicated by the brown arrows). These wave fronts represented the internal stress fields, which initiated micro-scale movement of the nano-inclusions. **Figs. 5.18e-i** show the formation of nano-inclusion aggregates during freezing. The red dashed elliptical regions in **Figs. 5.18e, j and l** show the consolidation of a tightly bound aggregate which resulted in improved aggregate-aggregate surficial contacts, thereby reducing interfacial phonon scattering.

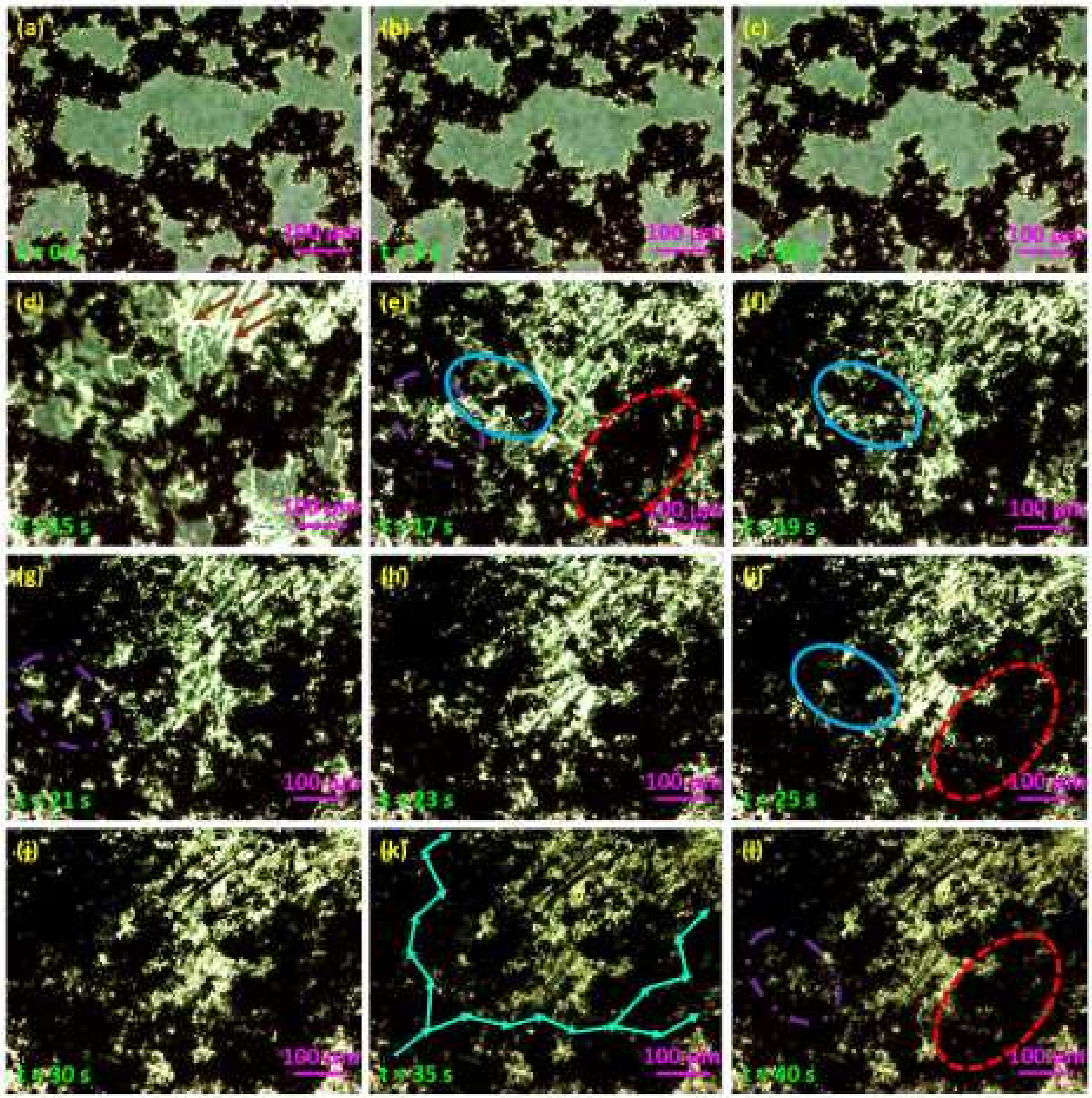

Figure 5.18 A few typical still micrographs, extracted from the real-time optical phase contrast video microscopy (multimedia file SV1.avi in the supplementary information), corresponding to t = (a) 0, (b) 5, (c) 10, (d) 15, (e) 17, (f) 19, (g) 21, (h) 23, (i) 25, (j) 30, (k) 35 and (l) 40 s. Formation of nano-inclusion clusters and percolating network are evident from the images and the legends are explained in the text. A typical percolating heat transfer path is schematically shown by the zig-zag arrows in (k).

Similarly, the indigo coloured elliptical regions in **Figs. 5.18e, f and j** show the development of a large aggregate of nano-inclusion, with progressively reduced interparticle spacing. On the other hand, the violet coloured elliptical regions in **Figs. 5.18e, g and l** show the internal stress induced merging of two smaller nano-inclusion aggregate to form a comparatively larger aggregate, which is energetically favourable due to the lowering of surface-to-volume ratio [385]. The optical phase contrast video microscopy-based studies experimentally confirmed the micro-scale aggregation phenomena during solidification of the PCMs that resulted in the formation of quasi-2d network of nano-inclusions with high percolation heat transfer efficiency (schematically shown in **Fig. 5.18k**). Thermal conductivity enhancement in nano-inclusion loaded PCMs is primarily due to three level homogenizations of the clusters with the host matrices [216, 341, 342]. The effective thermal conductivity of the nano-inclusion aggregates (consisting of a quasi-continuous back-bone and randomly placed dead-ends) are due to the second level homogenization of the back-bone network with the dead-ends homogenized (first level) with the PCM host matrix. Finally, a third level homogenization of the nano-inclusion aggregates with the PCM host matrix leads to the enhanced thermal conductivity of the nano-enhanced PCM [341]. The above hypothesis is the most widely accepted one for explaining the nano-inclusion aided thermal conductivity enhancement in organic PCMs [9, 65, 497] and the time-stamped video microscopy-based studies provided direct experimental evidence for the same.

Figure 5.19 shows the changes in k/k_f and percentage enhancement in thermal conductivity in the liquid state, as a function of nano-inclusion concentration (in vol. % = $\phi \times 100$ %, ϕ being vol. fract.), for the LA-based PCMs loaded with CBNP nano-inclusions. It can be seen from **Fig. 5.19** that thermal conductivity enhancement increased with loading concentration. For CBNP loaded PCMs, thermal conductivity enhancement increased from ~ 3.6 % to 17.6 %, when the loading concentration was varied from 0.5 wt. % ($\phi = 0.042$) to 4.0 wt. % ($\phi = 0.268$). With increasing loading, a greater number of aggregates are formed and these aggregates grow in size, leading to improved contact between the nano-inclusions within an aggregate, as the radius of gyration of the aggregates are significantly larger than the dimensions of individual nano-inclusions [342]. This caused the thermal conductivity to enhance with increasing loading concentration. **Figs 5.19** also shows the theoretical thermal conductivity enhancement curves, obtained from the classical Maxwell-Garnet (MG) [364] and Hamilton-Crosser (HC) [366] models. It is evident from **Fig. 5.19** that the experimental data were systematically higher than the theoretically estimated thermal conductivity values, which indicated the formation of nano-inclusion aggregates in the liquid state due to van der Waal's interaction [289]. It must be further noted from **Fig. 5.19** that the mismatch between the theoretical and experimental data were less significant for the calculations based on HC model, which was attributed to the incorporation of particle shape factors into the calculations [38]. Formation of larger sized aggregates with enhanced liquid layering around the nano-inclusions caused the deviations between the experimental and theoretical data to increase at higher loading concentrations, as observed from **Fig. 5.19**, for the PCMs loaded with CBNP nano-inclusions [512].

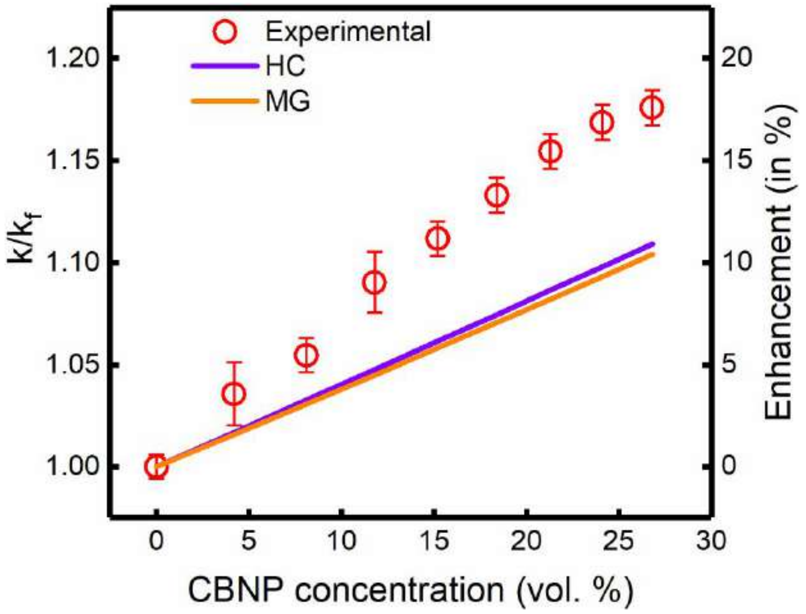

Figure 5.19 Variations of k/k$_f$ and percentage enhancement in thermal conductivity in the liquid state, as a function of concentration (in vol. fraction, ϕ), for the LA-based PCMs loaded with CBNP nano-inclusions. The theoretical thermal conductivity enhancement curves obtained from the classical Maxwell-Garnet (MG) and Hamilton-Crosser (HC) models are also shown.

The variations of k/k_f and percentage enhancement in thermal conductivity in the solid state, as a function of loading for CBNP nano-inclusions is shown in **Fig. 5.20**. For the PCMs loaded with CBNP nano-inclusions, thermal conductivity enhancements increased from ~ 132.8 % to 195.0 %, when the loading was increased from 0.5 to 3.5 wt. %. However, at the highest loading concentration of 4.0 wt. %, thermal conductivity enhancement decreased to ~ 167.2 %, which was attributed to the increased phonon scattering due to the formation of larger nano-clusters, which were not well dispersed and prone to sedimentation, as subsequently discussed. It can be seen from **Fig. 5.20** that in the cases of the PCMs loaded with CBNP nano-inclusions, k/k_f increased linearly with loading concentration up to 3.5 wt. %. The linear regression analysis (Adj. $R^2 \sim 0.96$) is also shown in **Fig. 5.20**. Harish et al. [65] reported a linear increase of k/k_f with increasing loading concentration, in the solid state, for LA based PCMs loaded with graphene nanoplatelets, which formed quasi-2D fractal network during freezing, similar to the percolation network formed by the CBNP nano-inclusions.

Prasher et al. [342] reported that thermal conductivity of nanofluid initially increases with aggregate size due to the formation of a percolating network and thereby, attains an optimal value for the well-dispersed aggregates, beyond which, thermal conductivity decreases for larger aggregates. Similar decrease in thermal conductivity enhancements for higher loading has been experimentally demonstrated for various organic PCMs, including n-hexadecane, paraffin wax and phenol-water systems [215-217, 237]. As described earlier, the nano-inclusion aggregates consisted of a nearly continuous back-bone and randomly placed dead-ends [341]. Thermal conductivity enhancement is primarily aided by the effective percolating heat transfer through the back-bone networks and the dead-ends, whose average population increases with aggregate size, did not contribute effectively towards thermal conductivity enhancement.

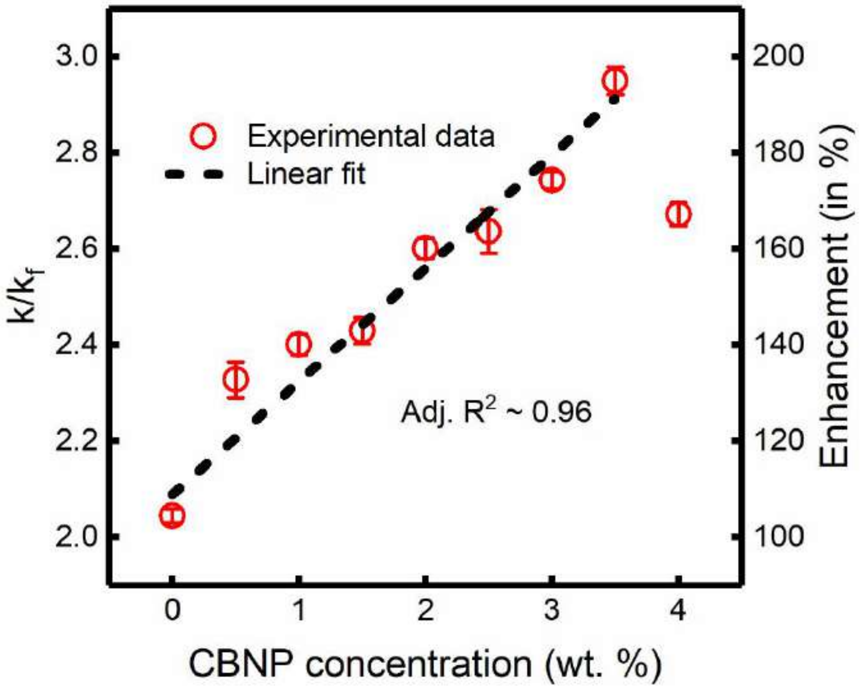

Figure 5.20 Variations of k/k$_f$ and percentage enhancement in thermal conductivity in the solid state, as a function of concentration (in wt. %), for the PCMs loaded with CBNP nano-inclusions. For the CBNP loaded PCMs, thermal conductivity enhancements increased linearly with concentration and the linear regression analysis (Adj. $R^2 \sim 0.96$) is shown in the figure.

This resulted in the near saturation or decrease in thermal conductivity at higher loading concentrations, for the PCMs loaded with CBNP nano-inclusions. Additionally, as these nano-aggregates grow in size, surface roughness increases leading to enhanced phonon scattering from the aggregate/aggregate and aggregate/PCM interfaces, as predicted from diffuse mismatch model of phonon scattering [443], resulting in a negative thermal conductivity enhancement at higher loading.

To probe the microstructural evolution and to obtain insight into the microscale aggregation phenomena, optical phase contrast microscopy was performed and **Fig. 5.21** shows a few typical images for the CBNP loaded PCMs, respectively, where particle loading was varied. **Figs. 5.21a-f** show the phase contrast microscopy images of pristine PCM and PCMs loaded with 0.5, 1.5, 2.5, 3.5 and 4 wt. % CBNP nano-inclusions, respectively, in the solid state. The evolution of the microstructure with increasing loading is evident from the phase contrast microscopy images. With increasing loading concentration, the size of the aggregates increased progressively with decreasing inter-aggregate spacing. During solidification, the nano-inclusions are driven towards the inter-crystallite spacing and forms "nano-rich" regions [65], that subsequently forms a quasi-2D percolating network spanning over the entire host matrix, as seen from the optical phase contrast microscopy images. Further, the needle like microstructure of the solidified PCM host matrix is clearly discernible from the phase contrast microscopy images (**Fig. 5.21a**). Formation of such needle like microstructure during solidification of pristine LA has been earlier reported using scanning electron microscopy [65]. It was observed that the needle like microstructure is largely retained during freezing of the LA based PCMs loaded with varying concentrations of nano-inclusions (**Figs. 5.21b-f**).

In the present study, the highest thermal conductivity enhancement of ~ 195% was achieved for 3.5 wt. % CBNP loading. The higher thermal conductivity enhancement for CBNP loading was attributed to its high compressibility, excellent volume filling capability and fractal nature of the aggregates [236, 477]. CBNP forms aciniform aggregates consisting of primary nodules of carbon black nanoparticles [407]. The low fractal dimension of CBNP aggregates leads to the formation of percolating networks with improved aggregate-aggregate and aggregate-PCM interfacial interactions, that reduces interfacial phonon scattering and Kapitza resistance [431, 432]. This is expected to give rise to the high thermal conductivity enhancements in the cases of the PCMs loaded with CBNP nano-inclusions. **Table 5.8** shows a few thermal conductivity enhancement values from literature for LA based PCMs loaded with various types of nano-inclusions along with the corresponding loading concentrations [65, 248, 250, 282-284, 523]. It is evident from **Table 5.8** that the highest thermal conductivity enhancements achieved in the present study (i.e. ~ 195 and 178 % for CBNP and MWCNT loaded PCMs, respectively) were substantially higher than those obtained using other types of carbon based nano-inclusions.

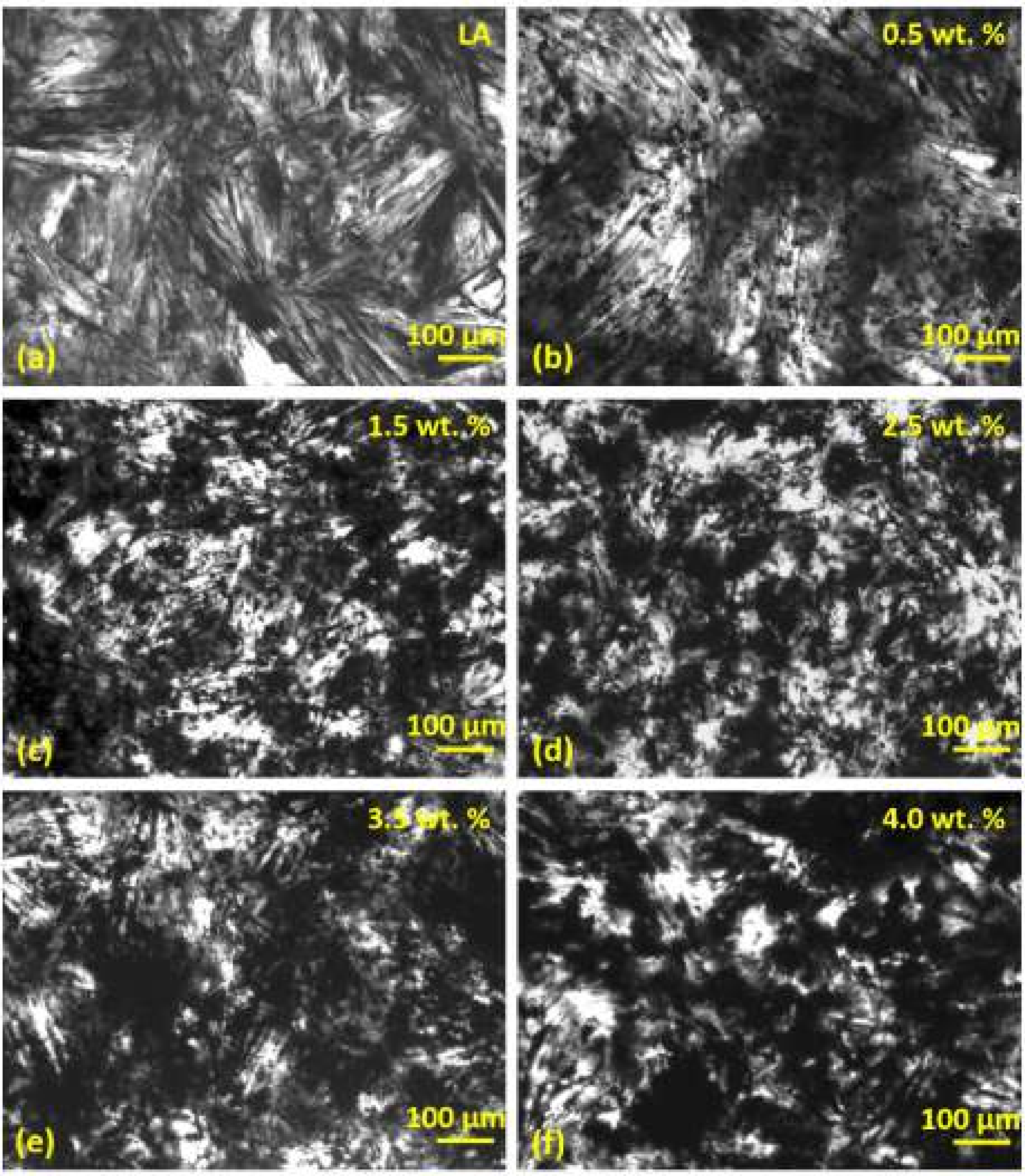

Figure 5.21 Optical phase contrast microscopy images of the (a) pristine PCM and PCMs loaded with (b) 0.5, (c) 1.5, (d) 2.5, (e) 3.5 and (f) 4 wt. % CBNP nano-inclusions, in the solid state.

Table 5.8 Enhancement in thermal conductivity (in the solid state) for LA based PCMs upon loading with different nano-inclusions. SWCNH, CBNP and MWCNT indicate Single walled carbon nano horn, carbon black nano powder and multiwalled carbon nanotubes, respectively.

Nano-inclusion	Concentration	Thermal conductivity enhancement in solid state	Year	Reference
Expanded perlite	10 wt. %	86 %	2009	[282]
Activated carbon	100 g LA + 300 g activated carbon	57 %	2012	[248]
SWCNH	2 vol. %	37 %	2015	[250]
Graphene nanoplatelets	1 vol. %	127 %	2015	[65]
Expanded vermiculite	10 wt. %	78 %	2016	[284]
Modified sepiolite	40 wt. %	79 %	2017	[283]
Porous deep carbonized wood Porous shallow carbonized wood	~ 19 wt. %	-6 % -20 %	2019	[523]
CBNP	**3.5 wt. %**	**~ 195 %**	**2019**	**Present study**
MWCNT	**3.5 wt. %**	**~ 178 %**	**2019**	**Present study**

However, Feng et al. [68] reported ~ 257 % enhancement in thermal conductivity for LA encapsulated within single walled carbon nanotubes (SWCNT). Nevertheless, in the present study, CBNP and MWCNT nano-inclusions were used without any chemical treatment or complicated sample preparation steps, like vacuum impregnation or encapsulation, which makes the process ideal for rapid industrial adaptation. Further, it can be seen from **Table 5.8** that the loading concentrations were significantly lower in the present case, as compared to the other cases. This is found to be advantageous from storage efficiency as well as economical points of view, as lower concentration of nano-inclusion is favourable for higher latent heat during phase transition and lower cost, respectively. High thermal conductivity enhancement along with low density (~ 0.1 g/cc) and low cost of CBNP nano-inclusions are immensely beneficial for practical applications in thermal energy storage systems.

Superior thermal stability and repeatable thermal responses of the nano-inclusion loaded PCMs are essential for practical thermal energy storage applications. To probe the thermal stability of the PCMs, with or without nano-inclusion loading, differential scanning calorimetry studies were carried out after 100 successive thermal cycles. **Figs. 5.22a-b** show the heat flow curves in the virgin condition and after 100 thermal cycles for the pristine PCM and PCMs loaded with 2 wt. % of CBNP nano-inclusions, respectively. It can be clearly seen from **Figs. 5.22a-b** that the heat flow curves are single endotherms in all the cases, indicating a prominent first order solid-liquid phase transitions without any secondary transitions. The peak phase transition temperatures and latent heat values were computed from the heat flow curves and the numerical values are shown in **Table 5.9**.

Table 5.9 Peak phase transition temperature and latent heat values for the PCMs (with or without loading with CBNP nano-inclusions) in the virgin condition and after 100 thermal cycles.

PCM material	Peak phase transition temperature (^{0}C) (± 0.1 ^{0}C)		Latent heat (kJ/kg) (± 0.4 kJ/kg)	
	Virgin condition	After 100 cycles	Virgin condition	After 100 cycles
LA	45.4	44.8	151.6	146.9
2 wt. % CBNP @ LA	45.5	44.9	142.6	139.6

It can be seen from **Table 5.9** that the peak phase transition temperature remained unchanged even after 100 thermal cycles, indicating excellent thermal stability of LA based PCMs loaded with CBNP and MWCNT nano-inclusions. Using thermogravimetric analyses, it has been reported that LA based PCMs remain thermally stable up to ~ 150 ^{0}C [281]. **Table 5.9** also showed a slight decrease in latent heat values after 100 thermal cycles (~ 3.1 and 2.1 % for the pristine PCM and PCMs loaded with 2 wt. % of CBNP nano-inclusions, respectively).

This showed excellent heat storage capacity of the LA based PCMs even after repeated thermal cycles, indicating its suitability for industrial applications.

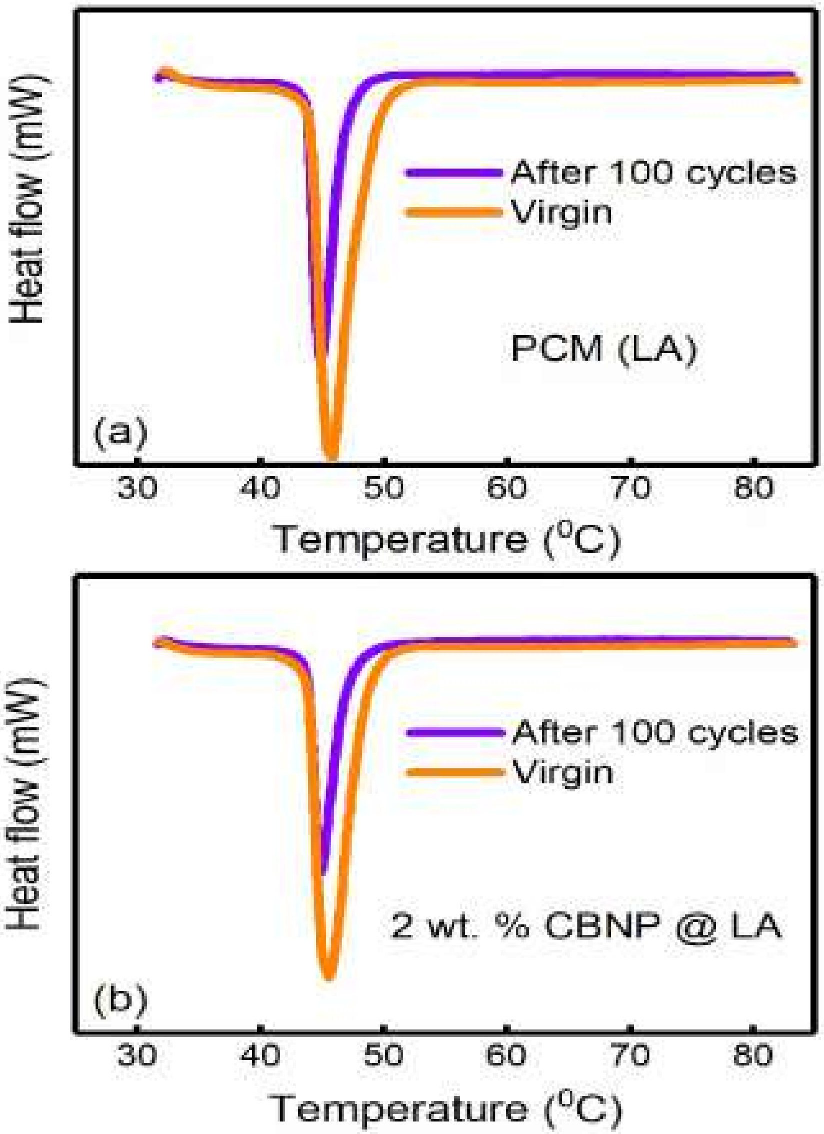

Figure 5.22 Heat flow curves in the virgin condition and after 100 thermal cycles for the (a) pristine PCM and (b) PCMs loaded with 2 wt. % of CBNP nano-inclusions. The peak phase transition temperature and latent heat values were computed from the heat flow curves and the numerical values are shown in Table 5.9.

5.3.4 Arresting material leakage: LA-based form-stable PCM

To arrest material leakage, during solid-liquid phase transition, 25 wt. % chalk powder ($CaCO_3$) was added to LA to fabricate form-stable PCM. The conventional and form-stable PCMs were placed on a hot-plate maintained at 50 ^{0}C, i.e. ~ 5 ^{0}C higher than the melting point) and leakage testing was performed. **Figs. 5.23a-b** show the typical photographs of the conventional and form-stable PCM loaded with 3.5 wt. % CBNP nano-inclusions, respectively at time t = 0 s. **Figs. 5.23c & e** show the photographs of the conventional PCM at time t = 60 and 300 s, respectively. **Figs. 5.23d & f** show the typical photographs of the form-stable PCM at time t = 60 and 100 s, respectively. It can be clearly seen from **Figs. 5.23a-f** that significant leakage occurred from the conventional PCM, whereas material leakage was minimal for the form-stable PCM. This was attributed to the capillary effect of the porous structure of $CaCO_3$, which retained the liquid LA within the exo-structure and prevented leakage [248]. **Fig. 5.23g** show the side views of the conventional (left) and form-stable (right) PCMs at time t = 300 s, where substantial leakage was seen from the conventional PCM. The form-stable PCM, on the other hand, showed nearly zero leakage.

Figure 5.23h show the heat flow curves for the conventional and form-stable PCMs. The peak phase transition temperatures were ~ 45.4 and 45.7 ^{0}C for the conventional and form-stable PCMs, respectively. On the other hand, latent heat values were ~ 151.6 and 119.9 kJ/kg for the conventional and form-stable PCMs, respectively. This indicated ~ 21 % decrease in latent heat on addition of 25 wt. % $CaCO_3$ to the PCM host matrix, which did not contribute to the latent heat storage. Nevertheless, the obtained latent heat value was high enough for industrial applications [492]. Load bearing capacity of the form-stable PCMs were verified by placing two lead bricks of mass 3.5 kg each and **Figs. 5.23i-j** show the typical photographs. It was observed that the form-stable PCM retained its shape even after subjecting to 7 kg load.

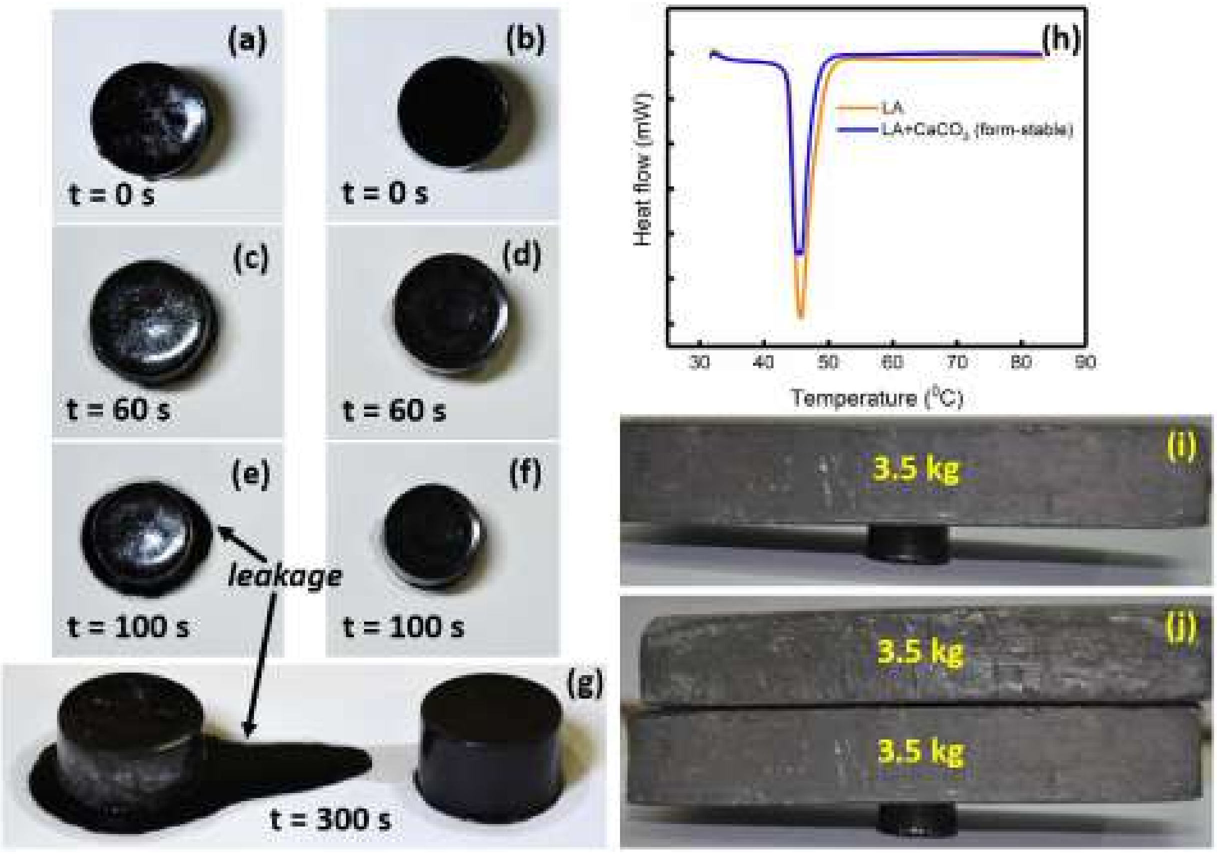

Figure 5.23 Typical photographs of the (a) conventional and (b) form-stable PCMs at time t = 0 s, when placed on a hot plate maintained at ~50 ^{0}C. Typical photographs of (c) conventional and (d) form-stable PCMs at time t = 60 s. Typical photographs of (e) conventional and (f) form-stable PCMs at time t = 100 s. (g) Side view of the conventional (left) and form-stable (right) PCMs at time t = 300 s. (h) Heat flow curves of the conventional and form-stable PCMs. Load bearing capacity of the form-stable PCM under (i) 3.5 kg and (j) 7.0 kg loads.

5.3.5 CBNP assisted enhancement of photo-thermal conversion in LA-based PCMs

To probe the photo-thermal conversion efficiency of the LA based PCMs loaded with CBNP nano-inclusion, experiments were performed in the present study, where the nano-inclusion loaded PCMs were exposed to artificial solar irradiation using two 1 kW halogen lamps and non-contact temperature measurement was performed using infrared thermography. The experimental protocol and a typical photograph of the experimental set-up is described in chapter 2. **Figs. 5.24a-b** show typical infrared images of the PCM loaded with 3.5 wt. % CBNP nano-inclusions for time t = 100 and 500 s. It can be clearly seen from the infrared images that temperature of the nano-inclusion loaded PCMs increased with time, under irradiation from the halogen lamps. Mean temperature was determined from spatial averaging over several pixel locations and **Fig. 5.24c** shows the typical heating and subsequent cooling curves for the PCM loaded with 3.5 wt. % of CBNP nano-inclusions. Initially the sample was thermally acclimatized at T = 20 (±1) ^{0}C and thereafter, exposed to the artificial solar irradiation for 515 s followed by natural cooling up to 2530 s. The sample temperature increased monotonically during the heating stage and CBNP nano-inclusions aided in the conversion of solar energy to thermal energy, which was then stored within the PCM. When the artificial solar irradiation was switched off, the sample temperature started to decrease and showed a wide plateau region near the phase transition point (~ 45 ^{0}C), where thermal energy was extracted from the PCM. The freezing process was completed after ~ 1200 s and the temperature of the solidified PCM is found to decrease rapidly and finally attained the surrounding temperature (~ 20 ^{0}C) in ~ 1500 s. This study clearly demonstrates the photo-thermal conversion capability of CBNP loaded PCMs. **Fig. 5.24d** shows the temperature rise ($\Delta T = T - 20$ ^{0}C) curves for the PCM loaded with 1, 2, 3 and 3.5 wt. % CBNP nano-inclusions. For comparison, temperature rise curve for the pristine PCM, without any nano-inclusion loading, is also shown in the figure. The shaded region in **Fig. 5.24d** indicates the phase transition region. For the CBNP loaded PCMs, temperature rise was measured up to 515 s, whereas for the pristine PCM, temperature rise was measured up to 600 s to allow for the completion of the phase transition.

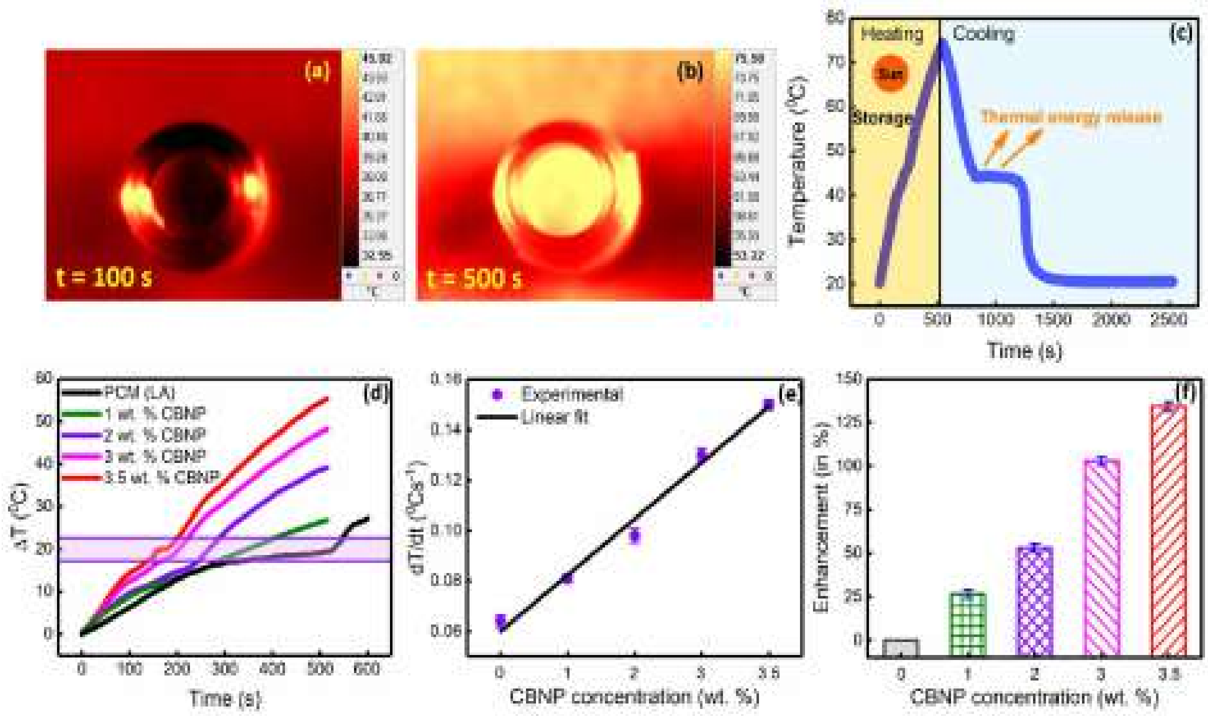

Figure 5.24 Typical infrared images of the PCM loaded with 3.5 wt. % CBNP nano-inclusion at time t = (a) 100 and (b) 500 s during the heating stage, under artificial solar light irradiation. (c) Typical photo-thermal heating and subsequent natural cooling curves for the PCM loaded with 3.5 wt. % of CBNP nano-inclusions. (d) Temperature rise ($\Delta T = T - 20\ ^0C$) curves for the PCM loaded with 1, 2, 3 and 3.5 wt. % CBNP nano-inclusions. For comparison, temperature rise curve for the pristine PCM, without any nano-inclusion loading, is also shown. The shaded region indicates the phase transition region. (e) The initial rates of temperature rise as a function of CBNP loading. (f) Bar chart showing the percentage enhancement in photo-thermal conversion efficiency as a function of CBNP loading concentration.

It can be seen from **Fig. 5.24d** that the initial rates of temperature increase and the maximum increase in sample temperature, during a given time duration, were larger at higher loading concentrations. These observations were in agreement with the temperature rise curves reported earlier for paraffin wax based PCMs and aqueous nanofluids loaded with CBNP nano-inclusions [47, 217]. The maximum temperature rise at 515 s were ~ 19.4 ± 0.2, 26.8 ± 0.3, 39.1 ± 0.4, 48.1 ± 0.5 and 55.4 ± 0.5 ^{0}C for the pristine PCM and PCMs loaded with 1, 2, 3 and 3.5 wt. % of CBNP nano-inclusions, respectively. The initial rates of temperature rise under adiabatic limit indicated the efficiency of photo-thermal conversion and ($\left.\frac{dT}{dt}\right|_{t\to 0}$) values were experimentally determined from linear regression analyses of the temperature rise curves [217]. **Fig. 5.24e** show the initial rates of temperature rise as a function of CBNP loading. It was observed from **Fig. 5.24e** that photo-thermal conversion efficiency increased with CBNP loading. The initial rates of temperature rise were ~ 0.064 ± 0.003, 0.081 ± 0.002, 0.098 ± 0.003, 0.130 ± 0.003 and 0.150 ± 0.002 $^0Cs^{-1}$ for the pristine PCM and PCMs loaded with 1, 2, 3 and 3.5 wt. % CBNP nano-inclusions, respectively. The photo-thermal conversion efficiency was found to increase linearly with CBNP loading concentration and the linear regression analysis is also shown in **Fig. 5.24e**. The adj. R^2 was found to be ~ 0.99, indicating good agreement with the linear model. The linear increase in photo-thermal conversion efficiency was found to be in agreement with earlier measurements reported for paraffin wax based PCMs and nanofluids loaded with CBNP nano-inclusions [217, 516]. **Fig. 5.24f** shows a bar-chart comparing the enhancement in photo-thermal conversion (in %), as a function of CBNP loading concentration, where it can be seen that photo-thermal conversion efficiency enhanced with increasing CBNP loading. The enhancements in photo-thermal conversion efficiency were ~ 26.6 ± 2.5, 53.1 ± 2.5, 103.1 ± 2.6 and 134.4 ± 2.5 % for the PCMs loaded with 1, 2, 3 and 3.5 wt. % of CBNP nano-inclusion.

The extinction coefficient of the nano-inclusion loaded PCM is independent of particle concentration and varies with the wavelength of the incident radiation and complex refractive index of the PCM matrix [518]. On the other hand, extinction efficiency (Q_{CBNP}) of the CBNP nano-inclusions is the sum total of the absorption (Q_{A-CBNP}) and scattering (Q_{S-CBNP}) efficiencies [519, 520]. For a constant value of the medium dielectric constant and incident wavelength, the Mie extinction efficiency increases with the size of the carbon nano-spheres [521]. Optical phase contrast microscopy images clearly indicated an increase in the aggregate size with increasing CBNP nano-inclusions (see **Figs. 5.21a-f**), which resulted in intense multiple Mie scattering of the incident solar radiation, leading to an augmentation of the extinction efficiency within the nano-inclusion loaded PCMs. The absorbed solar energy was subsequently converted to thermal energy that caused an enhancement of photo-thermal conversion efficiency with increasing CBNP loading, as observed from **Fig. 5.24f**.

5.4 Summary and conclusions

Thermal conductivity enhancements during liquid-solid phase transitions in paraffin wax (PW), binary mixture of paraffin wax and hexadecane (PW-HD) and lauric acid loaded with various concentrations of carbon black nanopowder (CBNP) of primary size ~ 30 nm were experimentally studied. Differential scanning calorimetry studies showed that the liquid-solid phase transition temperatures (and the associated latent heat values) for PW and PW-HD based PCMs are ~ 60.1 and 45.9 ^{0}C (125.85 and 44.89 kJ/kg), respectively. It was further observed, that peak phase transition temperature remained almost constant, whereas latent heat decreased slightly for the PCMs incorporated with increasing concentrations of CBNP, which was attributed to the exclusion of significant volume of host matrix on higher loading. Similarly, for CBNP loaded lauric acid based PCMs, differential scanning calorimetry results also indicated that the phase transition temperature remained almost constant with increasing CBNP loading. On the other hand, latent heat values decreased slightly, which was attributed to the reduction in LA concentration. Differential scanning calorimetry further revealed that the phase transition temperature of pristine lauric acid was ~ 45.4 ± 0.1 ^{0}C and the associated latent heat value was ~ 151.6 ± 0.4 kJ/kg. Phase transition temperatures were also evaluated using the refractive index measurement and infrared thermography (IRT) based non-contact temperature monitoring, where it was observed that the phase transition temperature obtained from the above-mentioned three methods were in good agreement with each other.

Upon incorporation of CBNP in the host matrices, an enhancement in thermal conductivity was observed, which was more significant in the solid state. The maximum thermal conductivity enhancements with 2.5 wt. % CBNP loading were ~ 135 and 141 % for PW and PW-HD based PCMs, respectively, which were found to be significantly higher than the earlier reported values achieved by incorporating various carbon based and metallic nano-fillers. Similarly, for CBNP loaded lauric acid based PCMs, the maximum thermal conductivity enhancements was ~195 % for a loading concentration of 3.5 wt. %, which was found to be significantly higher than the earlier values reported in literature. The higher thermal conductivity enhancement was attributed to the efficient percolating heat transfer through the quasi-2D networks of CBNP nano-inclusions, formed during freezing of the host matrices. The lower primary nodule size, high compressibility and volume filling capacity of CBNP resulted in the formation of more closely packed aggregates with improved aggregate-aggregate and aggregate-PCM contacts, which aided in lowering the thermal barrier resistance, thereby augmenting phonon mediated heat conduction and near-field radiative heat transfer efficiency, which caused an overall enhancement in thermal conductivity of the nano-inclusion loaded PCMs. Time-stamped optical phase contrast video microscopy provided direct experimental proof for the formation of such percolation network within the PCM host matrix during liquid-solid phase transition. For the paraffin wax based PCMs, the thermal conductivity enhancement in the solid state was comparable to the theoretically obtained values from logarithmic heat conduction model, which further confirmed the percolative heat transfer. On the other hand, experimental finings indicated that, in the solid state, thermal conductivity enhancement increased linearly with particle concentration for the CBNP loaded lauric acid-based PCMs.

Infrared thermography based non-contact temperature monitoring was performed to estimate the gain in cooling time and obtained results indicated ~ 82 and 100 % gain in cooling time for PW and PW-HD based PCMs, respectively. The enhancements in heat transfer rates, in the solid state showed a reduction in charging time by ~ 17.3 and 16.2 % for PW and PW-HD based PCMs, respectively, loaded with 2.5 wt. % CBNP. The cooling time was also estimated for the LA based PCM and it was observed that the gain in cooling time was ~ 221 %. Repeated thermal cycling showed good thermal stability of the PCMs, with or without nano-inclusions. It was further observed that the CBNP loaded PCMs showed negligible degradation in latent heat after 100 thermal cycles. The latent heat values were found to decrease by ~ 2.1, 1.8 and 2.1 % for PW, PW-HD, and lauric acid-based CPMs, respectively, after 100 thermal cycles.

Further, an increase in photo-thermal conversion efficiency with increasing CBNP loading was observed, which was attributed to the enhancement in total extinction coefficient of the incident solar radiation due to intense Mie scattering by the micron sized clusters of CBNP. The maximum enhancement in photo-thermal conversion efficiency of PW based PCM loaded with 2.5 wt. % CBNP was ~ 84 %. For the LA based PCM loaded with 3.5 wt. % CBNP nano-inclusions, the maximum enhancement in photo-thermal conversion was ~ 134 %.

Addition of porous calcium carbonate (25 wt. %) to the lauric acid-based PCM host matrix arrested the leakage during phase transition. The form-stable PCMs showed negligible leakage up to 300 s when subjected to a constant temperature of ~ 50 ^{0}C (i.e. 5 ^{0}C higher than the melting temperature). However, the latent heat is found to have decreased by ~ 21 % in the form-stable PCMs, with a good load bearing capacity of ~ 7 kg.

High thermal conductivity of the CBNP loaded paraffin wax and lauric acid-based PCMs, low density of CBNP, one-step sample preparation without any functionalization or encapsulation steps, abundant availability and low cost of CBNP and the host matrix, make CBNP loaded paraffin wax and lauric acid-based PCMs economically viable candidates for practical thermal energy storage systems. Moreover, superior thermal and chemical stability, combined with high latent heat, thermal conductivity and photo-thermal conversion efficiency of CBNP loaded PCMs may pave the way for fabrication of portable, low cost and self –sustainable solar-thermal battery packs.

Chapter 6

Development of binary form-stable PCM using palmitic acid and n-hexadecane

Chapter 6 Development of binary form-stable PCM using palmitic acid and n-hexadecane

6.1 Introduction

Material loss due to leakage during phase transition of organic phase change materials (PCMs) have been one of the primary challenges for gainfully employing such materials in real-life applications. On solid-liquid phase transition, the liquid constituents of a PCM assembly posses several technical problems, viz. leakage from the container, increased pressure on the container leading to bulging or rupture, undesired direct contact with the environment, sedimentation of nano-inclusions leading to phase separation, non-congruent phase transition during the successive thermal cycles and progressively increasing loss of latent heat storing PCM matrix due to non-reversibility of freezing/melting process of the entire PCM matrix [1, 4]. To overcome the difficulties associated with leakages, form-stable PCMs are being developed using various methods [219, 220]. Form-stability in PCMs is primarily achieved by two techniques, viz, micro-encapsulation and preparation of shape-stable PCM fabrication [1]. Microencapsulation cab be achieved by various chemical methods, viz. coacervation [254-256], suspension polymerization for non-polar PCMs [257], emulsion polymerization [258, 259], polycondensation [260-262] and polyaddition [263]. Though it is possible to prepare microencapsulated PCMs with desired size distribution, shell thickness and morphology, the involved chemical processes are comparably complex and time consuming [1]. Alternatively shape-stable PCMs have been prepared by impregnating a graphite or polymer matrices [1]. However, the latent heat of such shape stable PCMs were slightly lower than the latent heat values of pristine fatty acids [1]. In general, it is observed that latent heat proportionally decreases with increasing concentration of the supporting material [1, 4]. This calls for further studies on development of form-stable PCMs with higher latent heat energy storage capability. Moreover, the phase transition temperature needs to be tuned within 15-25 ^{0}C for various room temperature applications.

With this objective, binary shape-stable PCMs were developed using palmitic acid (PA) and n-hexadecane (HD), with a phase transition temperature in the range of 14-19 ^{0}C, without compromising the latent heat value. Upon loading with various concentrations of carbon black nano powder (CBNP), the shape-stable PCM showed significant enhancement in thermal conductivity.

6.2 Preparation of shape-stable PCM and loading with CBNP nano-inclusions

Biphasic mixture of hexadecane and palmitic acid (24 wt. % PA/HD composition) was prepared by mixing 3.5 ml of HD in 1ml of PA. While mixing, the temperature of PA was maintained at ~ 65 ± 2 ^{0}C and HD was slowly added in the liquid state with magnetic stirring for 20 minutes. This was followed by a water bath sonication for 20 min at ~ 48 ± 2 °C. Finally, the mixture was allowed to cool at ~ 15 ± 2 ^{0}C for preparing the shape-stable PCMs. The phase transition temperature and latent heat values were estimated from differential scanning calorimetry studies. Further for thermal conductivity enhancement, carbon black nanopowder (CBNP) of size ~ 30 nm, was added to the shape stable PCM. The CBNP nano-inclusion was dispersed in the continuous phase of the PCMs, in the liquid phase, by water bath sonication with bath temperature maintained at ~ 65 ± 2 ^{0}C. Thereafter the PCM was rapidly cooled at ~ 15 ± 2 ^{0}C for solidification. Five different loading concentrations were used, viz. 0.005, 0.01, 0.05, 0.075 and 0.1 wt. %. The water bath sonication time was increased from 20 to 50 minutes for higher CBNP loading to ensure thorough and homogenous distribution of the CBNP nano-inclusions within the PCM host matrix. Thermal conductivity enhancements were measured using a KD2 probe (detailed description provided in chapter 2). To probe microscale aggregation phenomena optical phase contrast microscopy was carried out at 10X magnification using an inverted phase contrast microscope (Carl Zeiss) in the liquid and solid states of the PCMs with or without nano-inclusion loading.

6.3 Thermo-physical properties of the shape-stable PCMs

Figure 6.1 shows the Fourier transform infrared (FTIR) spectra of the palmitic acid, hexadecane and PA-HD shape-stable PCM, where all the major absorption bands are indexed and **Table 6.1** shows the details [215, 216, 276, 411, 487]. It can be seen from Fig. 6.1 that the shape-stable PCM showed all the absorption bands of the individual components. This indicated the absence of any chemical reactions between the constituent elements and the shape-stable PCM was formed due physical mixture of palmitic acid and hexadecane.

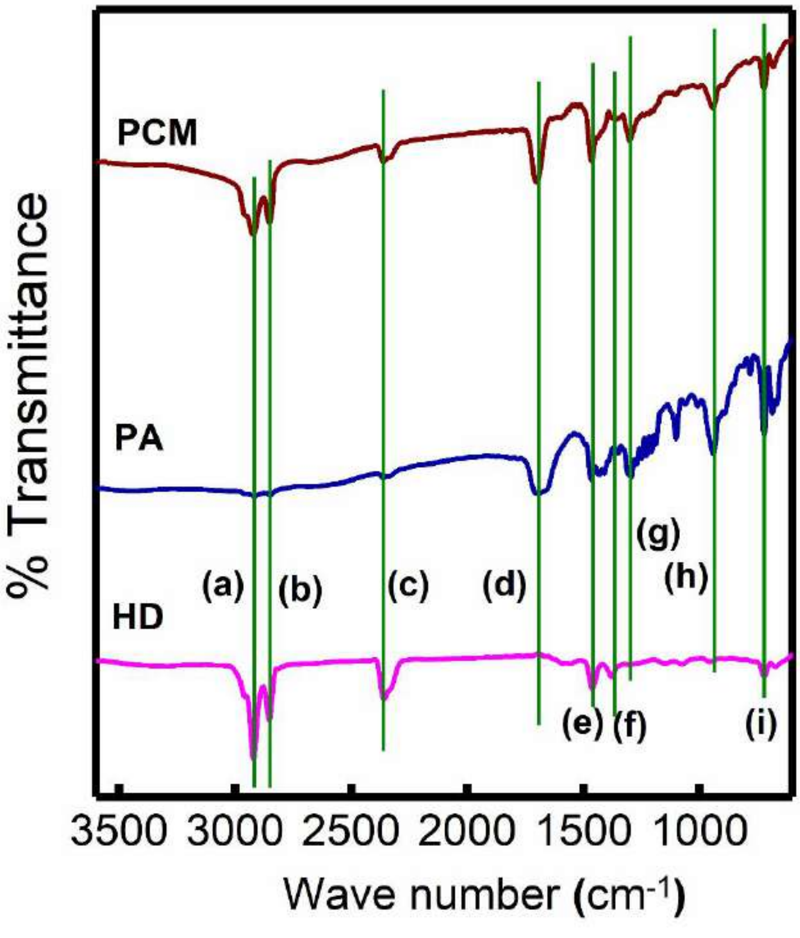

Figure 6.1 FTIR spectra of palmitic acid (PA), n-hexadecane (HD) and shape-stable PCM. All the major absorption bands are indexed and Table 6.1 shows the details.

Table 6.1 Detailed description of the FTIR absorption bands.

Legend	Wave number (cm^{-1})	Description	Reference
(a)	2925	Asymmetrical C-H stretch of CH_2 group	[216, 411]
(b)	2843	Symmetrical C-H stretch of CH_2 group	[216, 411]
(c)	2351	C=O stretching from atmospheric CO_2	[215, 216]
(d)	1700	C = O stretching vibration	[487]
(e)	1463	Asymmetric -CH_3 bending	[216, 411]
(f)	1370	Symmetric -CH_3 bending	[216]
(g)	1300	In plane bending of O – H (hydroxyl group)	[487]
(h)	937	Out of plane bending of O – H (hydroxyl group)	[276]
(i)	725	C-H rocking vibration of long chain alkanes	[411]

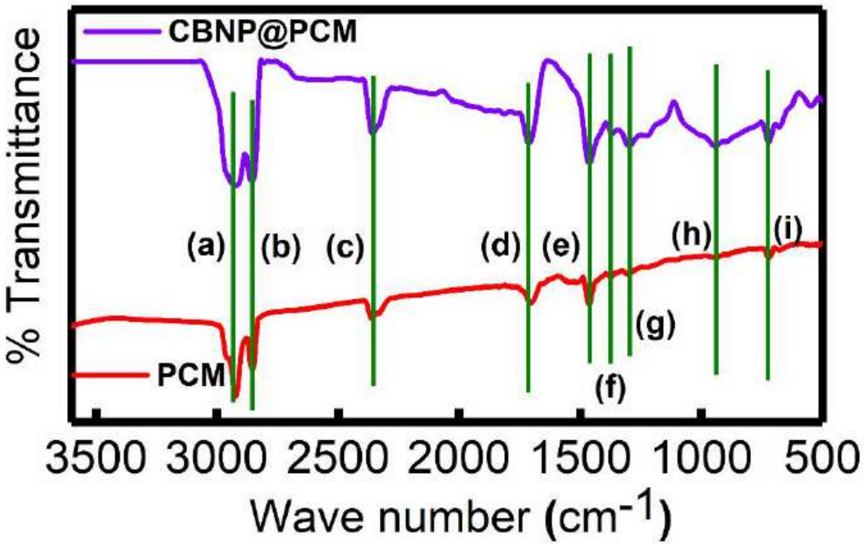

Figure 6.2 FTIR spectra of the PA-HD shape-stable PCM loaded with carbon black nanopowder (CBNP). For comparison, the spectra of the pristine PCM is also shown in the figure. All the major absorption bands are indexed and Table 6.1 shows the details.

Figure 6.2 shows the FTIR spectra of the carbon black nanopowder (CBNP) loaded shape-stable PCM. For comparison the spectra for the pristine shape-stable PCM is also shown in **Fig. 6.2**. The major absorption bands are indexed and described in **Table 6.1**, where it can be seen that the absorption bands were neither shifted, nor any new absorption bands were observed. This showed the absence of any chemical reaction between the CBNP nano-inclusions and the PCM host matrix [214, 235, 455].

Figures 6.3a-b show the heat flow curves for n-hexadecane and palmitic acid, respectively. It can be seen from **Figs. 6.3a-b** that the heat flow curves consisted of pairs of single endotherm/exotherm, indicating the solid-liquid phase transition in the corresponding materials. The melting and solidification temperatures for n-hexadecane were found to be ~ 19.3 and 14.5 ^{0}C, respectively. The corresponding latent heat values for the melting and freezing were ~ 241.4 and 238.6 kJ/kg, respectively. On the other hand, the melting and solidification temperatures for palmitic acid were ~ 62.5 and 58.5 ^{0}C, respectively. The corresponding latent heat values were ~ 222.4 and 220.2 kJ/kg, respectively. The latent heat and phase transition temperature values were in agreement with the earlier values reported in literature [216, 218, 219, 237, 387, 428, 490, 491].

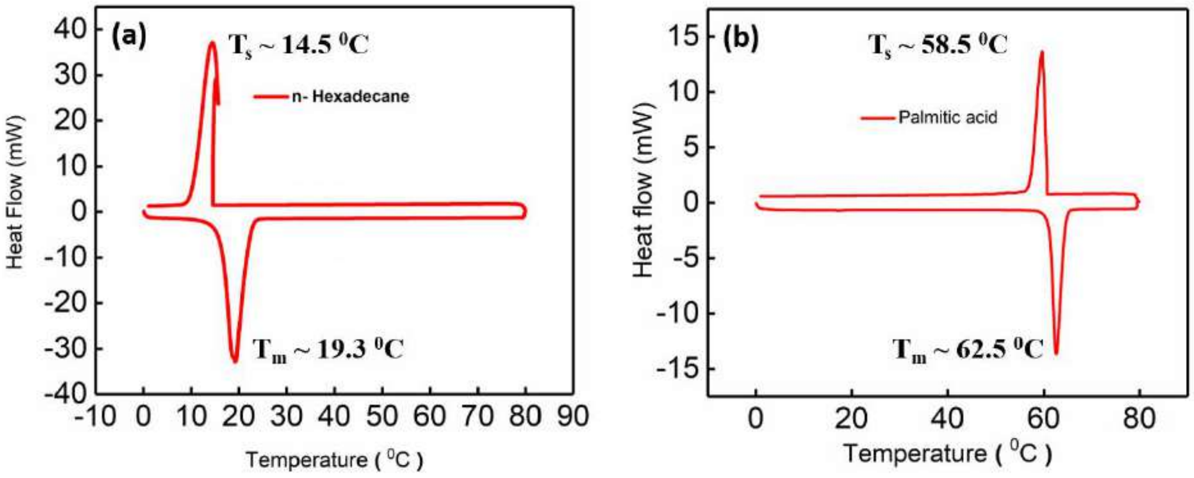

Figure 6.3 Heat flow curves for (a) n-hexadecane and (b) palmitic acid, obtained from differential scanning calorimetry studies.

Figure 6.4 shows the heat flow curve for PA-HD shape-stable PCM. It can be seen from **Fig. 6.4** that the shape stable PCM showed two distinct phase transformation in the temperature range of 0-80 ^{0}C. The smaller peaks indicated the melting of palmitic acid, which was shifted to 45.2 ^{0}C from 62.5 ^{0}C (in the case of pure palmitic acid). The corresponding solidification temperature was shifted to ~ 42 ^{0}C from 58.5 ^{0}C (in the case of pure palmitic acid). In the case of shape-stable PCM, the melting and solidification temperatures corresponding to the solid-liquid phase transition of palmitic acid were depressed by ~ 27.7 and 28.2 %, respectively, which was attributed to the presence of hexadecane (with significantly lower phase transition temperature) within the PCM host matrix. On the other hand, the larger peaks in **Fig. 6.4** signified the solid-liquid phase transition of hexadecane and the corresponding melting and freezing points were ~ 19 and 14 ^{0}C, respectively, which were very close to the melting and solidification temperatures (~ 19.3 and 14.5 ^{0}C, respectively) of pure hexadecane (**Fig. 6.3a**). The latent heat values were estimated from the area under the heat flow curves. In the case of shape-stable PCM, latent heat values corresponding to the melting and solidification process of palmitic acid were ~ 26.8 and 29.2 kJ/kg, respectively. These values were ~ 88 and 86.7 % lower than the corresponding latent heat values in the pure palmitic acid. For the phase transition corresponding to the melting of hexadecane, within the matrix of shape-stable PCM, the melting and solidification latent heat values were ~ 140 and 157 kJ/kg, respectively. Though these values were ~ 42 and 34.2 % lower than the corresponding values for pure hexadecane, the latent heat values were sufficiently higher for industrial applications [492]. **Table 6.2** shows a few shape stable PCMs along with their melting and solidification temperatures and latent heat values [282, 529-535]. It can be seen from **Table 6.2** that the shape-stable PA-HD binary PCM, prepared in the present study showed very high latent heat values as compared to the data available in the literature.

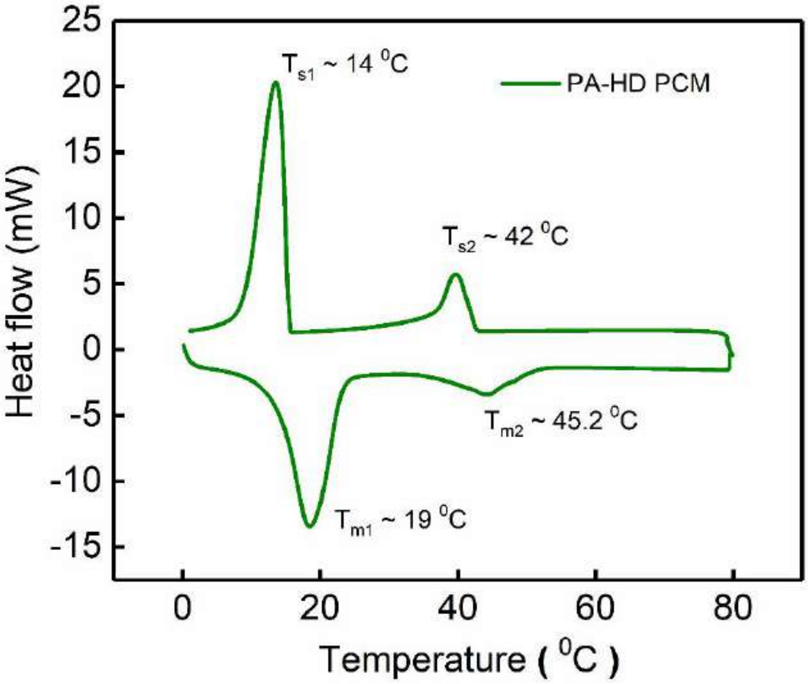

Figure 6.4 Heat flow curve for the shape-stable PA-HD PCM, obtained from differential scanning calorimetry studies.

6.4 CBNP assisted thermal conductivity enhancement in shape-stable PCM

Figure 6.5 shows the variation of k/k_f and percentage enhancement in thermal conductivity for the shape-stable PCM loaded with various concentrations of CBNP nano-inclusions. For comparison, the variation for pristine PCM is also shown in the figure. It can be seen from **Fig. 6.5** that the variation of k/k_f can be divided into 5 regions. For T> 43 ^{0}C, the sample was macroscopically in the liquid state and this was indicated as region-I. For 36 ^{0}C < T < 43 ^{0}C, the sample underwent a phase transition corresponding to the freezing of palmitic acid. This region was indicated as region-II in **Fig. 6.5**. The region corresponding to 20 ^{0}C < T < 36 ^{0}C was indicated as region-III, which was the intermediate region between the phase transitions, where the sample was macroscopically in solid state. Region-IV indicated the first phase transition, corresponding to the freezing of hexadecane (for 12 ^{0}C < T < 20 ^{0}C). In region-V (for T < 12 ^{0}C), the sample was in the solid state.

Table 6.2 Latent heat and phase transition temperature of a few shape-stable PCMs.

PCM	**Melting temperature (^{0}C)**	**Melting latent heat (kJ/kg)**	**Solidification temperature (^{0}C)**	**Solidification latent heat (kJ/kg)**	**Reference**
n-octadecane-polystyrene/expanded graphite	~ 29.62 ~ 29.73 ~ 29.81	~ 45.97 ~ 72.38 ~ 80.20	~ 25.78 ~ 25.81 ~ 26.24	~ 43.85 ~ 67.46 ~ 75.16	[529]
Hexadecane olefin block copolymer	~ 16.6	~ 148	~ 4.8	-	[530]
Lauric-stearic acid/gypsum	~ 34.0	~ 50.3	-	-	[531]
Paraffin/silica ceramic	~ 56.3	~165.2	-	-	[532]
Lauric acid/expanded perlite	~ 44.1	~ 93.4	~ 40.9	~94.8	[282]
Palmitic acid castor oil form-stable PCM	~ 66.57	~ 141.2	~ 54.32	~ 137.1	[533]
Octadecane encapsulated within a carbonate shell	~ 28.22 ~ 29.19	~ 67.91 ~ 84.37	~ 19.83 ~ 20.07	~ 65.32 ~ 82.15	[534]
Hexadecane microencapsulated within phenolic resin shell	~ 17.29 ~ 18.23	~ 98.08 ~ 85.29	~ 3.91 ~ 3.99	~ 96.49 ~ 86.05	[535]
Palmitic acid-hexadecane shape-stable binary PCM	~ 19.0	~ 140	~ 14	~ 157	Present study

It can be seen from **Fig. 6.5** that thermal conductivity enhanced upon loading with CBNP nano-inclusions. It was further observed that the enhancements in thermal conductivity were more prominent in the solid state, which was attributed to the formation of closely packed nano-crystalline structures [237, 387], as discussed earlier in chapters 3-5. It can be further seen from **Fig. 6.5**, that in the liquid region (region-I), thermal conductivity enhanced by ~

1.54, 5.38, 7.69, 6.15 and 10.0 % for CBNP loading concentrations of 0.005, 0.01, 0.05, 0.075 and 0.1 wt. %, respectively.

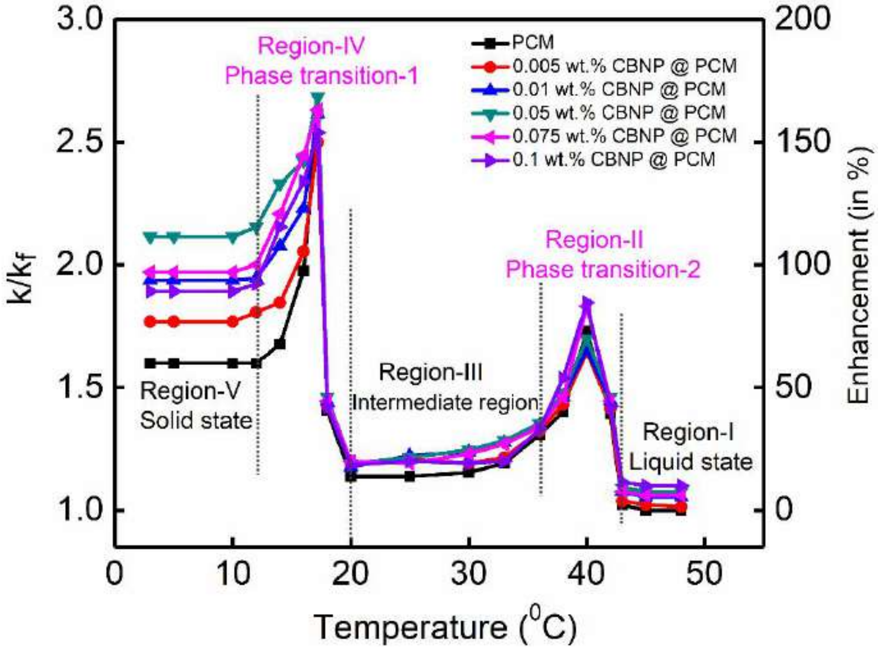

Figure 6.5 Variation of k/k$_f$ and percentage enhancement in thermal conductivity of the shape-stable PCM, upon loading with various concentrations of CBNP nano-inclusions. For comparison, the variation for pristine PCM is also shown in the figure.

In the region-II (phase transition corresponding to palmitic acid), CBNP loading of 0.005, 0.01, 0.05, 0.075 and 0.1 wt. % caused thermal conductivity enhancements of ~ 64.6, 65.4, 70.0, 83.1 and 84.6 %, respectively. In region-III, thermal conductivity enhancements decreased slightly and for an intermediate temperature of T = 30 ^{0}C, the enhancements in thermal conductivity were ~ 19.2, 23.8, 24.6, 23.1 and 19.2 % for CBNP loading concentrations of 0.005, 0.01, 0.05, 0.075 and 0.1 wt. %, respectively. In region-IV (phase transition corresponding to hexadecane), thermal conductivity enhanced by ~ 150.0, 161.5, 168.5, 163.1 and 153.8 % for the shape-stable PCMs loaded with 0.005, 0.01, 0.05, 0.075 and 0.1 wt. % of CBNP nano-inclusions, respectively. In region-V, at T = 3 ^{0}C for shape-stable

PCMs loaded with 0.005,0.01, 0.05, 0.075 and 0.1 wt. % of CBNP nano-inclusions, thermal conductivity enhancements were ~ 76.9, 93.8, 115.4, 96.9 and 89.2 %, respectively.

During, freezing the nano-inclusions are pushed towards the intercrystallite spacing, thereby forming a percolation network with high heat transfer efficiency, which ultimately leads to an enhancement in thermal conductivity of the nano-inclusion loaded PCMs [215-218, 237, 387]. CBNP nano-inclusions form aciniform aggregates with very small primary nodule sizes [407]. This enables formation of more tightly bound aggregates with augmented surficial coupling along the percolation network [217, 218]. Superior compressibility and volume filling capacity of CBNP nano-inclusions were also found to be beneficial towards thermal conductivity enhancement of the nano-inclusion loaded PCMs [236, 431, 477]. The thermal conductivity enhancement mechanism and synergistic effects of incorporation of CBNP nano-inclusions, within the PCM host matrices, were discussed in detail in chapter 5.

Figures 6.6a-f show optical phase contrast microscopy images of the shape-stable PCM in pristine condition and PCMs loaded with 0.005, 0.01, 0.05, 0.075 and 0.01 wt. % of CBNP nano-inclusions, respectively. The phase contrast images were acquired in the solid state. **Fig. 6.6a** shows the presence of needle like microstructures within he PCM host matrix, which is typical for hexadecane based PCMs [237, 387]. It can be seen from **Figs. 6.6b-f** that the aggregate size increased and interaggregate spacing decreased with increasing CBNP nano-inclusions. Percolation heat transfer through a network of such tightly bound CBNP nano-clusters leads to an enhancement in thermal conductivity. The presence of needle like microstructure in the PCM host matrix was also evident after 0.1 wt. % CBNP loading (**Fig. 6.6f**).

Figure 6.7 shows the variation of k/k_f and percentage enhancement in thermal conductivity of the shape-stable PCM, as a function of CBNP loading in the solid (T = 10 ^{0}C) and liquid (T = 48 ^{0}C) states, respectively.

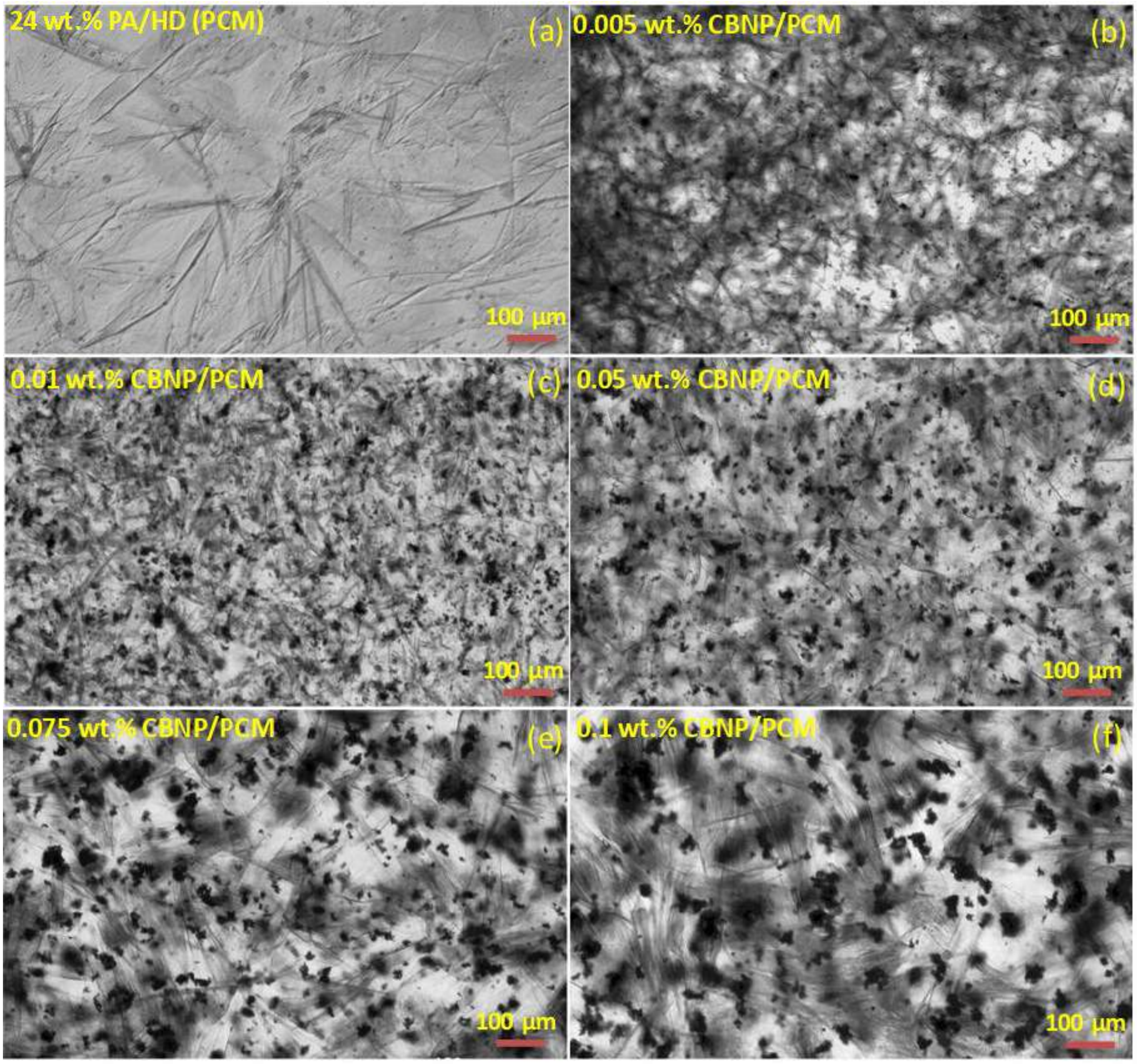

Figure 6.6 Optical phase contrast microscopy images of (a) pristine shape-stable PCM; and PCMs loaded with (b) 0.005, (c) 0.01, (d) 0.05, (e) 0.075 and (f) 0.1 wt. % CBNP nano-inclusions. The phase contrast images were acquired in the solid state.

It can be seen from **Fig. 6.7** that thermal conductivity enhancements were substantially higher in the solid state, which was in agreement with our earlier observations (**Fig. 6.5**). In the liquid state, thermal conductivity enhanced from 1.54 % to 10.0 % when CBNP loading was increased from 0.005 to 0.1 wt. %. On the other hand, in the solid state, thermal conductivity enhancement increased from 76.9 to 89.2 %, when CBNP loading was increased from 0.005 to 0.1 wt. %.

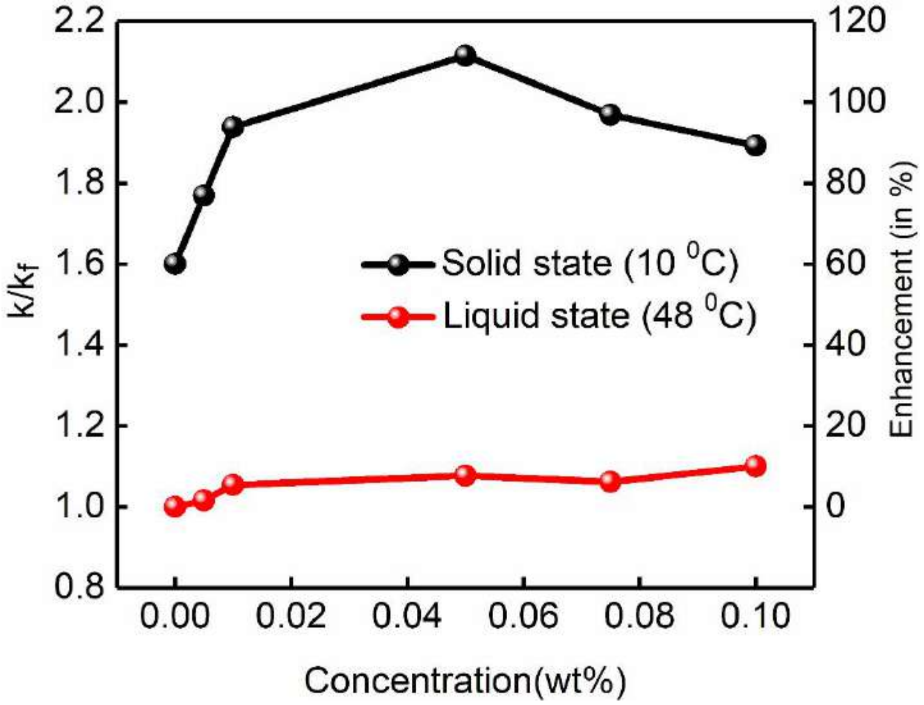

Figure 6.7 Variation of k/k$_f$ and percentage enhancement in thermal conductivity as a function of CBNP loading for the shape-stable PA-HD binary PCM.

It can be further seen from **Fig. 6.7**, that thermal conductivity enhancement was not monotonic in the solid state, i.e. initially thermal conductivity enhancement increased with CBNP loading up to an optimal concentration and beyond that it decreased. With increase in CBNP loading the aggregate size increased leading to a more compact and tightly bound percolation path within the PCM host matrix that resulted in the initial increase in thermal conductivity enhancements [217, 236]. However, at higher loading, beyond the optimal concentration, the clusters grow in size and are not well dispersed, which caused a decrease in thermal conductivity enhancement [218, 342], as seen in **Fig. 6.7**. Similar decrease in thermal conductivity at higher loading concentrations were earlier reported for palmitic acid based PCMs loaded with multi-walled carbon nanotubes [218], hexadecane based PCMs loaded with graphene nanoplatelets [387] and hexadecane based PCMs loaded with carbon nanotubes [237]. Further, for larger sized aggregates at higher CBNP loading, the surface roughness increased, which resulted in an increase in phonon scattering from the aggregate/aggregate and aggregate/PCM matrix interfaces leading to a decrease in effective thermal conductivity enhancement [215, 217]. In the present study, the maximum enhancement in thermal conductivity was found to be ~ 115.4 % for a CBNP loading of 0.05 wt. % (optimal concentration).

6.5 Shape-stability of the PA-HD binary PCM loaded with CBNP nano-inclusions

To probe the shape-stability of the PA-HD binary PCM, experiments were performed, where the shape stable PCM in pristine condition and after loading with 0.1 wt.% CBNP nano-inclusions were exposed to a steady temperature of T ~ 30 ^{0}C, i.e. in the intermediate region (region-III) in **Fig. 6.5**. This environmental temperature was chosen in such a way, that it was higher than the phase transition temperature of hexadecane and lower than the phase-transition temperature of palmitic acid. Time-stamped optical images were acquired to probe the melting and subsequent material leakage. **Fig. 6.8** shows the optical images for the shape stability studies. For comparison, similar experiment was also performed for pure hexadecane and the results are shown in **Fig. 6.8**. It can be seen from **Figs. 6.8a-e** that pure hexadecane progressively melted with time when exposed to an environmental temperature of T ~ 30 ^{0}C. The optical images clearly showed the melting and subsequent material leakage. On the other hand, no such macroscopic melting and material leakage was discernible in the case of the PA-HD binary shape stable PCM, with or without CBNP loading (**Figs. 6.8f-j**). This confirmed the shape-stability of the PA-HD binary PCM.

When exposed to an environmental temperature of T ~ 30 ^{0}C, the hexadecane melts within the PCM host matrix, but it remained confined within the solid structure of palmitic acid, whose melting point was ~ 42-45 ^{0}C. Hence, the prepared PA-HD binary PCM exhibited excellent shape-stability within a temperature a range of 3-30 ^{0}C, which is highly beneficial for various practical applications like domestic refrigeration, building thermo-regulation and room-temperature thermal energy storage.

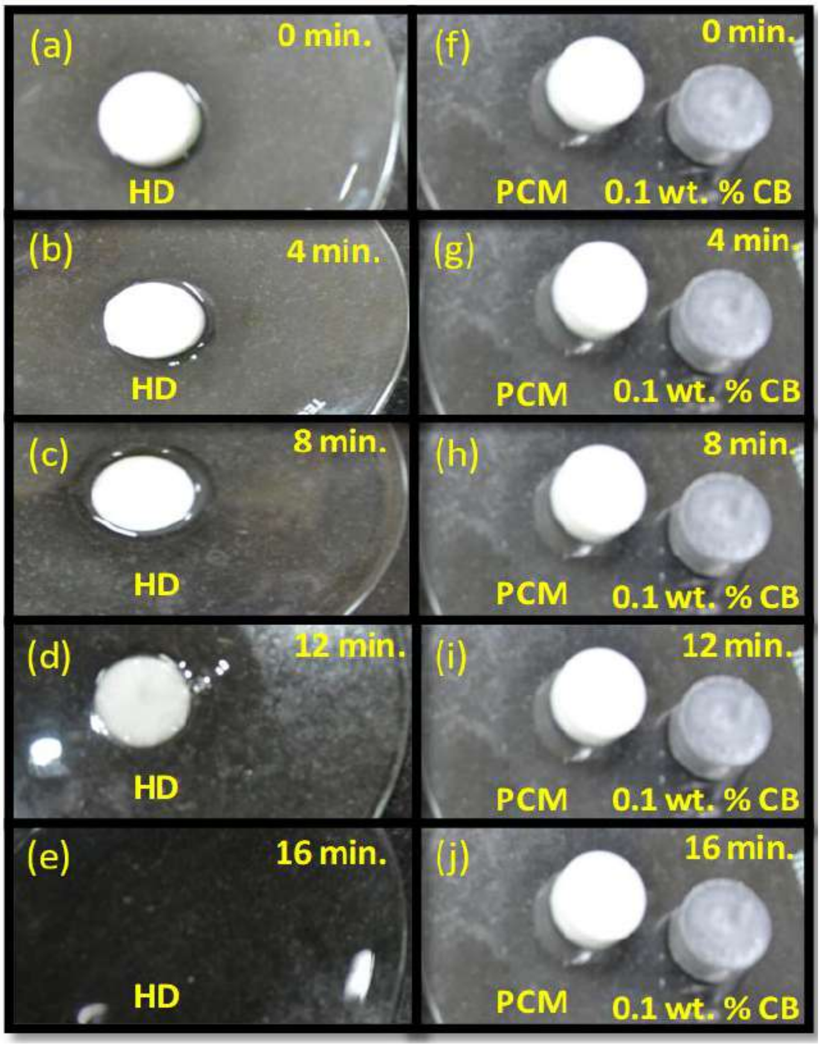

Figure 6.8 Testing of shape-stability of PA-HD binary PCM. Typical images of pure hexadecane PCM, maintained at T ~ 30 ^{0}C, at time t = (a) 0, (b) 4, (c) 8, (d) 12 and (e) 16 minutes. Material leakage is evident from the pure hexadecane PCM. Typical images of PA-HD binary shape-stable PCM in the pristine condition and upon loading with 0.1 wt. % carbon black nanopowder (CBNP, in short CB in the figures), maintained at T = 30 ^{0}C, at time t = (f) 0, (g) 4, (h) 8, (i) 12 and (j) 16 minutes. No material leakage was discernible in the case of the shape-stable PCM.

6.6 Summary and conclusions

Biphasic mixture of hexadecane and palmitic acid (24 wt. % PA/HD composition) was prepared by mixing 3.5 ml of HD in 1ml of PA. The binary PCM showed two distinct phase transitions at T ~ 14-19 ^{0}C (corresponding to the phase transition of hexadecane) and at T ~ 42-45 ^{0}C (corresponding to the phase transition of palmitic acid). Further the melting and solidification latent heat values corresponding to the hexadecane phase transition were ~ 140 and 157 kJ/kg, respectively, which were found to be among the highest in literature for shape-stable PCMs. Upon loading with carbon black nanopowder (CBNP), the shape stable PCM showed significant enhancement in thermal conductivity, which was more prominent in the solid state. In the solid state, thermal conductivity enhancement increased from 76.9 to 89.2 %, when CBNP loading was increased from 0.005 to 0.1 wt. %. Further, thermal conductivity enhancement in the solid state initially increased with CBNP loading up to an optimum concentration and beyond that it decreased due to the formation of larger sized aggregates. The optimum concentration in the present case was found to be ~ 0.05 wt. % and the maximum enhancement in thermal conductivity was ~ 115.4 %. The PA-HD binary PCM showed excellent shape-stability up to 30 ^{0}C and no material leakage was discernible. For temperature beyond 19 ^{0}C, the hexadecane component melted but remained confined within the solid structure of palmitic acid, which showed a solid-liquid phase transition around 42-45 ^{0}C. The high thermal conductivity enhancement, augmented shape stability over a temperature range of 3-30 ^{0}C and extremely high latent heat storage capacity make CBNP nano-inclusion loaded PA-HD binary shape-stable PCMs ideal candidates for various practical applications, domestic refrigeration, building thermo-regulation and room-temperature thermal energy storage.

Chapter 7

Conclusions and recommendations for future work

Chapter 7 Conclusions and recommendations for future work

7.1 Summary and conclusions

Effective conservation, storage and management of renewable energy sources and energy harvesting are essential to close the gap between the supply and demand of energy. In this context, intermediate storage of solar energy, waste heat recovery from industrial processes and thermoregulation in buildings using latent heat thermal energy storage system is one of the most prudent approaches. In spite of immense industrial benefits of thermal energy storage using organic phase change materails (PCMs), inherently low thermal conductivity and material leakage during phase transition are the two major drawbacks of such PCMs. In this thesis, concentrated efforts are made to probe the role of surface functionalization of nano-inclusions, particle loading, cluster formation and nature of nano-inclusions on thermal conductivity enahncment in PCMs. Also photo-thermal conversion efficiency and shape-stability of PCMs were demonstrated. The major conclusions are summarized below.

Thermal conductivity enhancements across the liquid-solid phase transition of hexadecane-based PCM, incorporated with six different nano-inclusions, viz. CBNP, NiNP, CuNP, AgNW, MWCNT and GNP were systematically probed. Incorporation of nano-inclusions caused a significant enhancement in thermal conductivity of the PCMs in the solid state, due to the formation of nano-crystalline phase on solidification, consisting of needle like microstructure, which was confirmed from optical phase contrast microscopy. In the solid state, the nano-inclusions were squeezed towards the inter-crystallite grain boundaries, forming a quasi 2D network of percolating structures with high thermal transport efficiency due to the enhancement of phonon mediated heat transfer and near-field radiative heat transfer along the thermal trajectories. For the PCM loaded with CBNP, CuNP, MWCNT and GNP nano-inclusions, thermal conductivity enhancements increased with concentration of the nano-inclusions due to the formation of larger-sized aggregates with improved conduction path. On the other hand, for the PCM loaded with NiNP and AgNW, thermal conductivity decreased at higher concentrations of the nano-inclusions, due to the formation of larger aggregates, which were prone to sedimentation. Among the carbon-based nano-inclusions, the highest enhancement in thermal conductivity was obtained for the PCM loaded with CBNP nano-inclusions, which was attributed to the low fractal dimensions and volume filling capacity of CBNP aggregates with efficient phonon coupling. In the case of metallic nano-inclusions, the highest thermal conductivity enhancement was obtained for the PCM loaded with AgNW nano-inclusions, which was attributed to the large aspect ratio of AgNW. Experimental findings indicated that surface functionalization of the GNP nano-inclusions with oleic acid resulted in better thermal stability of the nano-inclusion loaded PCM, without significant reduction in thermal conductivity, which is beneficial for practical applications. The carboxylic group of oleic acid was bound to the nano-inclusions, whereas, the long aliphatic chain was extended into the non-polar matrix of hexadecane (PCM), thereby providing additional steric stability, that prevented formation of large and unstable aggregates, at higher loading concentration or after repeated thermal cycling, which was also confirmed from optical phase contrast microscopy images. Increased interfacial thermal resistance, for the surface functionalized nano-inclusions, was also studied theoretically and the theoretical and experimental results were found to be in good agreement.

The phase transition temperature of the phenol-water system was tuned by adjusting the phenol-water ratio. Incorporation of α-Al_2O_3, SiO_2, hydrophobic SiO_2 and TiO_2 nano-inclusions to the PCM caused an enhancement in thermal conductivity. With α-Al_2O_3, SiO_2 and hydrophobic SiO_2 inclusions, thermal conductivity enhancement increased with concentration due to the formation of larger aggregates at higher concentrations. Atomic force microscopy images confirmed increased contact area between the closely packed larger aggregates at higher concentrations, which resulted in a decreased interfacial resistance, thereby aiding in efficient heat transfer. Thermal conductivity enhancement for the PCM incorporated with hydrophobic SiO_2 was found to be lower, as compared to the PCM loaded with hydrophilic SiO_2, which was attributed to the higher interfacial resistance of the hydrophobic nano-inclusion/PCM interface. On the other hand, in the case of TiO_2 nano-inclusions, thermal conductivity enhancement increased up to a certain concentration (3 wt. %) and beyond that, it decreased, possibly due to the higher aggregation probability of TiO_2. Addition of 0.02 and 0.04 wt. % of CBNP increased the thermal conductivity enhancement to 44.7 and 45.9 %, 41.7 and 45.3 % for PCM loaded with 4 wt. % of α-Al_2O_3 and 3 wt. % of SiO_2, respectively. The synergetic enhancement was attributed to the fractal nature of the CBNP aggregates, which acts as volume filling agents, increasing the efficiency of the thermal trajectories. The phase transition temperature of palmitic acid (PA)-di-methyl formamide (DMF)-based PCM was tuned from ~ 61 to 31 ^{0}C by varying the PA-to-DMF ratio. DFT based theoretical studies were carried out to understand the PA-DMF complex formation and the same was verified using FTIR spectroscopy. DSC studies were carried out to probe the variations in phase transition temperature and latent heat values with increasing DMF concentration. PA-DMF composite PCM with 50.5 wt. % DMF was chosen due to its higher thermal conductivity in the solid state and phase transition temperature ~ 36 ^{0}C, which is ideal for various practical applications. Studies revealed large thermal conductivity enhancement in the solid state and phase transition region upon loading with of α-Al_2O_3, GNP, MWCNT and CBNP nano-inclusions. Obtained results indicated that significant thermal conductivity enhancement was achieved using CBNP nano-inclusions (~ 67 and 153 % in the solid state and phase transition regions, respectively at a loading concentration of 0.05 vol. fraction), as compared to various other metallic and carbon based nano-inclusions. Aggregation dynamics and formation of such percolation network was probed using optical phase contrast microscopy, where for the first time, direct experimental evidence was provided for solidification induced cluster formation during liquid-solid phase transition of nano-inclusions loaded PCMs.

Thermal conductivity enhancements during liquid-solid phase transitions in paraffin wax (PW), binary mixture of paraffin wax and hexadecane (PW-HD) and lauric acid loaded with various concentrations of carbon black nanopowder (CBNP) of primary size ~ 30 nm were experimentally studied. Differential scanning calorimetry studies showed that the liquid-solid phase transition temperatures (and the associated latent heat values) for PW and PW-HD based PCMs are ~ 60.1 and 45.9 ^{0}C (125.85 and 44.89 kJ/kg), respectively. It was further observed, that peak phase transition temperature remained almost constant, whereas latent heat decreased slightly for the PCMs incorporated with increasing concentrations of CBNP, which was attributed to the exclusion of significant volume of host matrix on higher loading. Similarly, for CBNP loaded lauric acid based PCMs, differential scanning calorimetry results also indicated that the phase transition temperature remained almost constant with increasing CBNP loading. On the other hand, latent heat values decreased slightly, which was attributed to the reduction in LA concentration. Differential scanning calorimetry further revealed that the phase transition temperature of pristine lauric acid was ~ 45.4 ± 0.1 ^{0}C and the associated latent heat value was ~ 151.6 ± 0.4 kJ/kg. Phase transition temperatures were also evaluated using the refractive index measurement and infrared thermography (IRT) based non-contact temperature monitoring, where it was observed that the phase transition temperature obtained from the above-mentioned three methods were in good agreement with each other.

Upon incorporation of CBNP in the host matrices, an enhancement in thermal conductivity was observed, which was more significant in the solid state. The maximum thermal conductivity enhancements with 2.5 wt. % CBNP loading were ~ 135 and 141 % for PW and PW-HD based PCMs, respectively, which were found to be significantly higher than the earlier reported values achieved by incorporating various carbon based and metallic nano-fillers. Similarly, for CBNP loaded lauric acid based PCMs, the maximum thermal conductivity enhancements was ~195 % for a loading concentration of 3.5 wt. %, which was found to be significantly higher than the earlier values reported in literature. The higher thermal conductivity enhancement was attributed to the efficient percolating heat transfer through the quasi-2D networks of CBNP nano-inclusions, formed during freezing of the host matrices. The lower primary nodule size, high compressibility and volume filling capacity of CBNP resulted in the formation of more closely packed aggregates with improved aggregate-aggregate and aggregate-PCM contacts, which aided in lowering the thermal barrier resistance, thereby augmenting phonon mediated heat conduction and near-field radiative heat transfer efficiency, which caused an overall enhancement in thermal conductivity of the nano-inclusion loaded PCMs. For the paraffin wax based PCMs, the thermal conductivity enhancement in the solid state was comparable to the theoretically obtained values from logarithmic heat conduction model, which further confirmed the percolative heat transfer. On the other hand, experimental finings indicated that, in the solid state, thermal conductivity enhancement increased linearly with particle concentration for the CBNP loaded lauric acid-based PCMs. Infrared thermography based non-contact temperature monitoring was performed to estimate the gain in cooling time and obtained results indicated ~ 82 and 100 % gain in cooling time for PW and PW-HD based PCMs, respectively. The enhancements in heat transfer rates, in the solid state showed a reduction in charging time by ~ 17.3 and 16.2 % for PW and PW-HD based PCMs, respectively, loaded with 2.5 wt. % CBNP. The cooling time was also estimated for the LA based PCM and it was observed that the gain in cooling time was ~ 221 %. Repeated thermal cycling showed good thermal stability of the PCMs, with or without nano-inclusions. It was further observed that the CBNP loaded PCMs showed negligible degradation in latent heat after 100 thermal cycles. The latent heat values were found to decrease by ~ 2.1, 1.8 and 2.1 % for PW, PW-HD, and lauric acid-based CPMs, respectively, after 100 thermal cycles. Further, an increase in photo-thermal conversion efficiency with increasing CBNP loading was observed, which was attributed to the enhancement in total extinction coefficient of the incident solar radiation due to intense Mie scattering by the micron sized clusters of CBNP. The maximum enhancement in photo-thermal conversion efficiency of PW based PCM loaded with 2.5 wt. % CBNP was ~ 84 %. For the LA based PCM loaded with 3.5 wt. % CBNP nano-inclusions, the maximum enhancement in photo-thermal conversion was ~ 134 %.

Addition of porous calcium carbonate (25 wt. %) to the lauric acid-based PCM host matrix arrested the leakage during phase transition. The form-stable PCMs showed negligible leakage up to 300 s when subjected to a constant temperature of ~ 50 ^{0}C (i.e. 5 ^{0}C higher than the melting temperature). However, the latent heat is found to have decreased by ~ 21 % in the form-stable PCMs, with a good load bearing capacity of ~ 7 kg. Biphasic mixture of hexadecane and palmitic acid (24 wt. % PA/HD composition) was prepared by mixing 3.5 ml of HD in 1ml of PA. The binary PCM showed two distinct phase transitions at T ~ 14-19 ^{0}C (corresponding to the phase transition of hexadecane) and at T ~ 42-45 ^{0}C (corresponding to the phase transition of palmitic acid). Further the melting and solidification latent heat values corresponding to the hexadecane phase transition were ~ 140 and 157 kJ/kg, respectively, which were found to be among the highest in literature for shape-stable PCMs. Upon loading with carbon black nanopowder (CBNP), the shape stable PCM showed significant enhancement in thermal conductivity, which was more prominent in the solid state. In the solid state, thermal conductivity enhancement increased from 76.9 to 89.2 %, when CBNP loading was increased from 0.005 to 0.1 wt. %. Further, thermal conductivity enhancement in the solid state initially increased with CBNP loading up to an optimum concentration and beyond that it decreased due to the formation of larger sized aggregates. The optimum concentration in the present case was found to be ~ 0.05 wt. % and the maximum enhancement in thermal conductivity was ~ 115.4 %. The PA-HD binary PCM showed excellent shape-stability up to 30 ^{0}C and no material leakage was discernible. For temperature beyond 19 ^{0}C, the hexadecane component melted but remained confined within the solid structure of palmitic acid, which showed a solid-liquid phase transition around 42-45 ^{0}C. The high thermal conductivity enhancement, augmented shape stability over a temperature range of 3-30 ^{0}C and extremely high latent heat storage capacity make CBNP nano-inclusion loaded PA-HD binary shape-stable PCMs ideal candidates for various practical applications, domestic refrigeration, building thermo-regulation and room-temperature thermal energy storage.

The key findings of the thesis are summarized below.

- During solidification of the PCMs, the nano-inclusions are squeezed towards the inter-crystallite regions, forming "nano-rich" aggregates along the grain boundaries. Solidification induced stress fields result in the formation of a quasi-2D network of such tightly bound aggregates with high phonon mediated heat conduction efficiency. Improved surficial contact also reduces thermal barrier resistance, which is beneficial for heat transfer. Further, close proximity of the nano-inclusions also augments the near-field radiative heat transfer. All of these ultimately results in the enhancement of heat transfer efficiency of the nano-inclusion loaded PCMs.
- Surface functionalization of the nano-inclusions resulted in better long-term thermal stability of the nano-enhanced PCMs, without significant reduction in thermal conductivity enhancement. The theoretical values of interfacial thermal resistance for the surface functionalized nano-inclusions was in agreement with the experimental findings.

- The phase transition temperatures of phenol-water and palmitic acid/di-methyl formamide mixtures were tuned to near room temperature by varying constituent ratios. The tuned PCMs were found to be thermally stable and exhibited significant thermal conductivity enhancement, upon loading with various nano-inclusions.
- Carbon black nano powder loaded paraffin wax and lauric acid based PCMs showed very high thermal conductivity enhancement. Superior volume filling capacity and fractal nature of CBNP aggregates aided in the formation of closely bound percolation network with reduced thermal barrier resistance, which resulted in the observed higher thermal conductivity enhancements.
- Carbon black nano-inclusion loaded PCMs showed significant enhancement in photo-thermal conversion, which further increased with particle loading due to augmented absorption of the incident light.
- Palmitic acid-hexadecane binary shape-stable PCM showed a phase transition ~ 14-19 ^{0}C with a latent heat value of ~ 140-157 kJ/kg. Enhanced thermal conductivity was observed for the shape-stable PCM loaded with various nano-inclusions.

7.2 Recommendations for future work

The following future works are recommended.

- Development of microencapsulated organic phase change materials (PCMs) with inorganic moities as shell and PCMs as core. Such microencapsulated PCMs offer several benefits, like form-stability, prohibition of direct contact between the PCM and the environment and augmented heat transfer area.
- Studies on the synergistic enhancement of thermal conductivity of PCMs loaded with multiple types of nano-inclusins and probing the underlying physical phenomena.

- Studies on the effects of morphology and aspect ratio of nano-inclusions on thermal conductivity enahcnment of PCMs.
- Fabriaction of pilot scale devices to assess the efficacy of latent heat thermal energy storage using nano-inclusion loaded PCMs.

List of References

[1] K. Pielichowska, K. Pielichowski, Phase change materials for thermal energy storage, Prog. Mater. Sci., 65 (2014) 67-123.

[2] A.B. Jaffe, R.N. Stavins, The energy-efficiency gap what does it mean?, Energ. Policy, 22 (1994) 804-810.

[3] G. Alva, Y. Lin, G. Fang, An overview of thermal energy storage systems, Energy, 144 (2018) 341-378.

[4] R.K. Sharma, P. Ganesan, V.V. Tyagi, H.S.C. Metselaar, S.C. Sandaran, Developments in organic solid–liquid phase change materials and their applications in thermal energy storage, Energy Convers. Manag., 95 (2015) 193–228.

[5] D. Liu, L. Xin-Feng, L. Bo, Z. Si-quan, X. Yan, Progress in thermochemical energy storage for concentrated solar power: a review, Int. J. Energy Res., 42 (2018) 4546-4561.

[6] S.S.M. Tehrani, Y. Shoraka, K. Nithyanandam, R.A. Taylor, Shell-and-tube or packed bed thermal energy storage systems integrated with a concentrated solar power: A techno-economic comparison of sensible and latent heat systems, Appl. Energy, 238 (2019) 887-910.

[7] P. Pardo, A. Deydier, Z. Anxionnaz-Minvielle, S. Rouge, M. Cabassud, P. Cognet, A review on high temperature thermochemical heat energy storage, Renew. Sustain. Energy Rev., 32 (2014) 591-610.

[8] L. Wei, C. Wei, D. Wang, Research and development of thermochemical energy storage based on hydrated salt, Refrig. Air Cond., 17 (2017) 14-21.

[9] L. Fan, J.M. Khodadadi, Thermal conductivity enhancement of phase change materials for thermal energy storage: A review, Renew. Sustain. Energy Rev., 15 (2011) 24–46.

[10] M.M. Farid, A.M. Khudhair, S.A.K. Razack, S. Al-Hallaj, A review on phase change energy storage: materials and applications, Energy Convers. Manag., 45 (2004) 1597-1615.

[11] A.S. Hariri, I.C. Ward, A review of thermal storage systems used in building applications, Build. Environ., 23 (1988) 1-10.

[12] S. Jegadheeswaran, S.D. Pohekar, Performance enhancement in latent heat thermal storage system: a review, Renew. Sustain. Energy Rev., 13 (2009) 2225-2244.

[13] S. Kamali, Review of free cooling system using phase change material for buildings, Energ. Buildings, 80 (2014) 131-136.

[14] A.M. Khudhair, M.M. Farid, A review on energy conservation in building applications with thermal storage by latent heat using phase change materials, Energy Convers. Manag., 45 (2004) 263-275.

[15] M.A. Kibria, M.R. Anisur, M.H. Mahfuz, R. Saidur, I.H.S.C. Metselaar, A review on thermophysical properties of nanoparticle dispersed phase change materials, Energy Convers. Manag., 95 (2015) 69–89.

[16] Z. Ling, Z. Zhang, G. Shi, X. Fang, L. Wang, X. Gao, Y. Fang, T. Xu, S. Wang, X. Liu, Review on thermal management systems using phase change materials for electronic components, Li-ion batteries and photovoltaic modules, Renew. Sustain. Energy Rev., 31 (2014) 427-438.

[17] M. Liu, W. Saman, F. Bruno, Review on storage materails and thermal performance enhancement techniques for high temperature phase change thermal storage systems, Renew. Sustain. Energy Rev., 16 (2012) 2118-2132.

[18] E.G. Roubaud, D.P. Osorio, C. Prieto, Review of commercial thermal energy storage in concentrated solar power plants: steam vs. molten salts, Renew. Sustain. Energy Rev., 80 (2017) 133-148.

[19] W. Sua, J. Darkwa, G. Kokogiannakis, Review of solid–liquid phase change materials and their encapsulation technologies, Renew. Sustain. Energy Rev., 48 (2015) 373–391.

[20] D. Zhou, C.Y. Zhao, Y. Tian, Review on thermal energy storage with phase change materials (PCMs) in building applications, Appl. Energ., 92 (2012) 593–605.

[21] S. Mondal, Phase change materials for smart textiles – an overview, Appl. Therm. Eng., 28 (2008) 1536-1550.

[22] H. Herrmann, D.W. Kearney, Survey of thermal energy storage for parabolic trough power plants, J. Sol. Energy Eng., 124 (2002) 145-152.

[23] E. Boysen, N. Boysen, Nanotechnology for Dummies, 2nd ed., Wiley Publishing Inc., New Jersey, 2011.

[24] E. Serrano, G. Rus, J. Garcıia-Martıinez, Nanotechnology for sustainable energy, Renew. Sustain. Energy Rev., 13 (2009) 2373-2384.

[25] F. Ramiro-Manzano, P. Atienzar, I. Rodriguez, F. Meseguer, H. Garciab, A. Corma, Apollony photonic sponge based photoelectrochemical solar cells, Chem. Commun, 3 (2007) 242-244.

[26] I. Rodriguez, F. Ramiro-Manzano, P. Atienzar, J.M. Martinez, F. Meseguer, H. Garciab, A. Corma, Solar energy harvesting in photoelectrochemical solar cells, J. Mater. Chem., 17 (2007) 3205-3209.

[27] L.A. Silva, S.Y. Ryu, J. Choi, W. Choi, M.R. Hoffmann, Photocatalytic hydrogen production with visible light over Pt-interlinked hybrid composites of cubic-phase and hexagonal-phase CdS, J. Phys. Chem. C, 112 (2008) 12069-12073.

[28] M. Ni, M.K.H. Leung, D.Y.C. Leung, K. Sumathy, A review and recent developments in photocatalytic water-splitting using for hydrogen production, Renew. Sustain. Energy Rev., 11 (2007) 401-425.

[29] C. Carpetis, W. Peschka, A study on hydrogen storage by use of cryoadsorbents, Int. J. Hydrogen Energy, 5 (1980) 539-554.

[30] C. Wang, M. Waje, X. Wang, J.M. Tang, R.C. Haddon, Y. Yan, Proton exchange membrane fuel cells with carbon nanotube based electrodes, Nano Lett., 4 (2004) 345-348.

[31] Y. Shao, J. Liu, Y. Wang, Y. Lin, Novel catalyst support materials for PEM fuel cells: current status and future prospects, J. Mater. Chem., 19 (2009) 46-59.

[32] C. Niu, E.K. Sichjel, R. Hoch, D. Hoi, H. Tennent, High power electrochemical capacitors based on carbon nanotube electrodes, Appl. Phys. Lett., 70 (1997) 1480-1482.

[33] A.G. Pandolfo, A.F. Hollenkamp, Carbon properties and their role in supercapacitors, J. Power Sources, 157 (2006) 11-27.

[34] P.G. Bruce, B. Scrosati, J.M. Tarascon, Nanomaterials for rechargeable lithium batteries, Angew. Chem. Int. Ed., 47 (2008) 2930-2946.

[35] M.S. Whittingham, Inorganic nanomaterials for batteries, Dalton Trans., 40 (2008) 5424-5431.

[36] S.A. Ahmed, M. Ozkaymak, A. Sozen, T. Menlik, A. Fahed, Improving car radiator performance by using TiO_2-water nanofluid, Eng. Sci. Technol. Int. J., 21 (2018) 996-1005.

[37] S.A. Angayarkanni, J. Philip, Role of adsorbing moieties on thermal conductivity and associated properties of nanofluids, J. Phys. Chem., 119 (2013) 9009-9019.

[38] S.A. Angayarkanni, J. Philip, Review on thermal properties of nanofluids: Recent developments, Adv. Colloid Interface Sci., 225 (2015) 146-176.

[39] W. Arshad, H.M. Ali, Graphene nanoplatelets nanofluids thermal and hydrodynamicperformance on integral fin heat sink, Int. J. Heat Mass Transfer., 107 (2017) 995-1001.

[40] M. Bahiraei, S. Heshmatian, Electronics cooling with nanofluids: a critical review, Energy Convers. Manag., 172 (2018) 438-456.

[41] J. Buongiorno, Convective Transport in Nanofluids, J. Heat Transfer, 128 (2006) 240-250.

[42] J. Buongiorno, D.C. Venerus, N. Prabhat, T. McKrell, J. Townsend, R. Christianson, Y.V. Tolmachev, P. Keblinski, L.-w. Hu, J.L. Alvarado, I.C. Bang, S.W. Bishnoi, M. Bonetti, F. Botz, A. Cecere, Y. Chang, G. Chen, H. Chen, S.J. Chung, M.K. Chyu, S.K. Das, R.D. Paola, Y. Ding, F. Dubois, G. Dzido, J. Eapen, W. Escher, D. Funfschilling, Q. Galand, J. Gao, P.E. Gharagozloo, K.E. Goodson, J.G. Gutierrez, H. Hong, M. Horton, K.S. Hwang, C.S. Iorio, S.P. Jang, A.B. Jarzebski, Y. Jiang, L. Jin, S. Kabelac, A. Kamath, M.A. Kedzierski, L.G. Kieng, C. Kim, J.-H. Kim, S. Kim, S.H. Lee, K.C. Leong, I. Manna, B. Michel, R. Ni, H.E. Patel, J. Philip, D. Poulikakos, C. Reynaud, R. Savino, P.K. Singh, P. Song, T. Sundararajan, E. Timofeeva, T. Tritcak, A.N. Turanov, S.V. Vaerenbergh, D. Wen, S. Witharana, C. Yang, W.-H. Yeh, X.-Z. Zhao, S.-Q. Zhou, A benchmark study on the thermal conductivity of nanofluids, J. Appl. Phys., 106 (2009) 094312.

[43] M. Chandrasekar, S. Suresh, A Review on the Mechanisms of Heat Transport in Nanofluids, Heat Transfer Eng., 30 (2009) 1136–1150.

[44] J.A. Eastman, S.U.S. Choi, S. Li, W. Yu, L.J. Thompson, Anomalously increased effective thermal conductivities of ethylene glycol-based nanofluids containing copper nanoparticles, Appl. Phys. Lett. , 78 (2001) 718-720.

[45] W. Evans, J. Fish, P. Keblinski, Role of Brownian motion hydrodynamics on nanofluid thermal conductivity, Appl. Phys. Lett., 88 (2006) 093116.

[46] M.N. Golubovic, H.D.M. Hettiarachchi, W.M. Worek, W.J. Minkowycz, Nanofluids and critical heat flux, experimental and analytical study, Appl. Therm. Eng., 29 (2009) 1281-1288.

[47] D. Han, Z. Meng, D. Wu, C. Zhang, H. Zhu, Thermal properties of carbon black aqueous nanofluids for solar absorption, Nanoscale Res. Lett., 6 (2011) 457.

[48] S. Harikrishnan, S. Kalaiselvam, Preparation and thermal characteristics of CuO–oleic acid nanofluids as a phase change material, Thermochim. Acta, 533 (2012) 46-55.

[49] S. Harikrishnan, S. Magesh, S. Kalaiselvam, Preparation and thermal energy storage behaviour of stearic acid–TiO_2 nanofluids as a phase change material for solar heating systems, Thermochim. Acta, 565 (2013) 137-145.

[50] J. Philip, P.D. Shima, B. Raj, Evidence for enhanced thermal conduction through percolating structures in nanaofluids, Nanotechnology, 19 (2008) 305706.

[51] P.D. Shima, J. Philip, Role of Thermal Conductivity of Dispersed Nanoparticles on Heat Transfer Properties of Nanofluid, Ind. Eng. Chem. Res., 53 (2014) 980-988.

[52] S. Lohrasbi, M. Sheikholeslami, D.D. Ganji, Discharging process expedition of NEPCM infin-assisted latent heat thermal energy storage system, J. Mol. Liq., 221 (2016) 833-841.

[53] M. Sheikholeslami, Solidification of NEPCM under the effect of magnetic field in a porous thermal energy storage enclosure using CuO nanoparticles, J. Mol. Liq., 263 (2018) 303-315.

[54] R.K. Sharma, P. Ganesan, V.V. Tyagi, H.S.C. Metselaar, S.C. Sandaran, Thermal properties and heat storage analysis of palmitic acid-TiO_2 composite as nano-enhanced organic phase change material (NEOPCM), Appl. Therm. Eng., 99 (2016) 1254-1262.

[55] M. Sheikholeslami, Numerical modeling of nano enhanced PCM solidification in an enclosure with metallic fin, J. Mol. Liq., 259 (2018) 424-438.

[56] S. Shenogin, L. Xue, R. Ozisik, P. Keblinski, Role of thermal boundary resistance on the heat flow in carbon-nanotube composites, J. Appl. Phys., 95 (2004) 8136-8144.

[57] K. Tumirah, M.Z. Hussein, Z. Zulkarnain, R. Rafeadah, Nano-encapsulated organic phase change material based on copolymer nanocomposites for thermal energy storage, Energy, 66 (2014) 881-890.

[58] J. Wang, H. Xie, Z. Guo, L. Guan, Y. Li, Improved thermal properties of paraffin wax by addition of TiO_2 nanoparticles, Appl. Therm. Eng., 73 (2014) 1541-1547.

[59] J. Wang, H. Xie, Z. Xin, Investigation on microstructure and thermal properties of graphene-nanoplatelet/palmitic acid composites, J. Nanopart. Res., 14 (2012) 952.

[60] J. Wang, H. Xie, Z. Xin, Y. Li, L. Chen, Enhancing thermal conductivity of palmitic acid based phase change materials with carbon nanotubes as fillers, Sol. Energy, 84 (2010) 339-344.

[61] A.P. Wemhoff, A.J. Webb, Investigation of nanoparticle agglomeration on the effective thermal conductivity of a composite material, Int. J. Heat Mass Transfer, 97 (2016) 432-438.

[62] L. Zhang, J. Zhu, W. Zhou, J. Wang, Y. Wang, Thermal and electrical conductivity enhancement of graphite nanoplatelets on form-stable polyethylene glycol/polymethyl methacrylate composite phase change materials, Energy 39 (2012) 294-302.

[63] S. Zhang, J.-Y. Wu, C.-T. Tse, J. Niu, Effective dispersion of multi-wall carbon nano-tubes in hexadecane through physiochemical modification and decrease of supercooling, Sol. Energy Mater.Sol.Cells, 96 (2012) 124–130.

[64] T. Zhang, T. Luo, High-Contrast, Reversible Thermal Conductivity Regulation Utilizing the Phase Transition of Polyethylene Nanofibers, ACS Nano, 7 (2013) 7592–7600.

[65] S. Harish, D. Orejon, Y. Takata, M. Kohno, Thermal conductivity enhancement of lauric acid phase change nanocomposite with graphene nanoplatelets Appl. Therm. Eng., 80 (2015) 205-211.
[66] Y. Yuan, N. Zhang, T. Li, X. Cao, W. Long, Thermal performance enhancement of palmitic-stearic acid by adding graphene nanoplatelets and expanded graphite for thermal energy storage: a comparative study, Energy, 97 (2016) 488-497.
[67] E.C. Bayramoglu, Thermal Properties and Stability of n-Octadecane Based Composites Containing Multiwalled Carbon Nanotubes, Polymer Composites, 32 (2011) 904–909.
[68] Y. Feng, R. Wei, Z. Huang, X. Zhang, G. Wang, Thermal properties of lauric acid filled in carbon nanotubes as shape-stabilized phase change materials, Phys. Chem. Chem. Phys., 20 (2018) 7772-7780.
[69] P. Ji, H. Sun, Y. Zhong, W. Feng, Improvement of the thermal conductivity of a phase change material by the functionalized carbon nanotubes Chem. Eng. Sci., 81 (2012) 140-145.
[70] J. Wang, H. Xie, Z. Xin, Y. Li, Increasing the thermal conductivity of palmitic acid by the addition of carbon nanotubes, Carbon, 48 (2010) 3979-3986.
[71] B. Xu, Z. Li, Paraffin/diatomite/multi-wall carbon nanotubes composite phase change material tailor-made for thermal energy storage cement-based composites, Energy, 72 (2014) 371-380.
[72] P.A. Owusu, S. Asumadu-Sarkodie, A review of renewable energy sources, sustainability issues and climate change mitigation, Cogent Eng., 3 (2016) 1167990.
[73] S. Islam, I. Dincer, Development, analysis and performance assessmenet of a combined solar and geo-thermal energy-based integrated system for multi-generation, Sol. Energy, 147 (2017) 328-343.
[74] J.S. Wagner, S.R. Edward, Economic implications of thermal energy storage for concentrated solar thermal power, Renew. Energy, 61 (2014) 81-95.
[75] S. Bruckner, S. Liu, L. Miro, M. Radspieler, L.F. cabeza, E. Lavemann, Industrial waste heat recovery technologies: an economic analysis of heat transformation technologies, Appl. Energy, 151 (2015) 157-167.
[76] T. Schmidt, D. Mangold, H.M. Steinhagen, Central solar heating plants with seasonal storage in Germany, Sol. Energy, 76 (2004) 165-174.
[77] B. Rezaie, B.V. Reddy, M.A. Rosen, Assessment of the thermal energy storage in Friedrichshafen district energy systems, Energy Procedia, 116 (2017) 91-105.
[78] A. Sharma, V.V. Tyagi, C.R. Chen, D. Buddhi, Review on thermal energy storage with phase change materials and applications, Renew. Sustain. Energy Rev., 13 (2009) 318-345.
[79] H. Akeiber, P. Nejat, M.Z.A. Majid, M.A. Wahid, F. Jomehzadeh, I.Z. Famileh, J.K. Calautit, B.R. Hughes, S.A. Zaki, A review on phase change material (PCM) for sustainable passive cooling in building envelopes, Renew. Sustain. Energy Rev., 60 (2016) 1470-1497.
[80] F. Agyenim, N. Hewitt, P. Eames, M. Smyth, A review of materials, heat transfer and phase change problem formulation for latent heat thermal energy storage systems (LHTESS), Renew. Sustain. Energy Rev., 14 (2010) 615-628.
[81] F. Kuznik, D. David, K. Johannes, J.J. Roux, A review on phase change materials integrated in building walls, Renew. Sust. Energy Rev., 15 (2011) 379-391.
[82] A.S. Fleischer, Thermal energy storage using phase change materials: fundamentals and applications, 1st ed., Springer, Heidelberg, Germany, 2015.
[83] S.D. Sharma, K. Sagara, Latent heat storage materials and systems: a review, Int. J. Green Energy, 2 (2005) 1-56.
[84] S.D. Sharma, H. Kitano, K. Sagara, Phase Change Materials for Low Temperature Solar Thermal Applications Res. Rep. Fac. Eng. , 29 (2004) 31-64.
[85] D. Chandra, R. Chellappa, W.-M. Chien, Thermodynamic assessment of binary solid-state thermal storage materials, J. Phys. Chem. Solids, 66 (2005) 235-240.
[86] Y. Quanying, L. Chen, The thermal storage performance of monobasic, binary and triatomic polyalcohols systems, Sol. Energy, 82 (2008) 656-662.

[87] X. Wang, E. Lu, W. Lin, C. Wang, Micromechanism of heat storage in a binary system of two kinds of polyalcohols as a solid–solid phase change material, Energy Convers. Manag., 41 (2000) 135-144.

[88] H. Feng, X. Liu, S. He, K. Wu, J. Zhang, Studies on solid-solid phase transitions of polyols by infrared spectroscopy, Thermochim. Acta, 348 (2000) 175-179.

[89] B. Zalba, J.M. Marin, L.F. Cabeza, H. Mehling, Review on thermal energy storage with phase change: materials, heat transfer analysis and applications, Appl. Therm. Eng., 23 (2003) 251–283.

[90] L.F. Cabeza, A. Castell, C. Barrenec, A.d. Gracia, A.I. Fernande, Materials used as PCM in thermal energy storage in buildings: a review, Renew. Sustain. Energy Rev., 15 (2011) 1675–1695.

[91] V.V. Tyagi, D. Buddhi, PCM thermal storage in buildings: a state of art, Renew. Sustain. Energy Rev., 11 (2007) 1146-1166.

[92] M. Kenisarin, K. Mahkamov, Solar energy storage using phase change materials, Renew. Sustain. Energy Rev., 11 (2007) 1913-1965.

[93] Y. Zhang, G. Zhou, K. Lin, Q. Zhang, H. Di, Application of latent heat thermal energy storage in buildings: state-of-the-art and outlook, Build. Environ., 42 (2007) 2197–2209.

[94] A. Pasupathya, R. velraja, R.V. Seeniraj, Phase chnage materials-based building architecture for thermal management in residential and commercial establishments, Renew. Sustain. Energy Rev., 12 (2008) 39-64.

[95] H. Ge, H. Li, S. Mei, J. Liu, Low melting point liquid metal as a new class of phase change material: An emerging frontier in energy area, Renew. Sustain. Energy Rev., 21 (2013) 331–346.

[96] S. Khare, M.D. Amico, C. Knight, S. McGarry, Selection of materials for high temperature latent heat energy storage, Sol. Energy Mater. Sol. Cells, 107 (2012) 20–27.

[97] C.E. Birchenall, A.F. Riechman, Heat storage in eutectic alloys, Metall. Trans. A., 11 (1980) 1415–1420.

[98] S.L. Chen, Y. Zuo, H. Liang, A.Y. Chang, A thermodynamic description for the ternary Al-Mg-Cu system, Metall. Mater. Trans. A, 28 (1997) 435-446.

[99] S.M. Hasnain, Review on sustainable thermal energy storage technologies, Part I: heat storage materials and techniques, Energy convers. manag., 39 (1998) 1127-1138.

[100] K.B. len, F. Takgil, K. Kaygusuz, Thermal energy storage behavior of $CaCl_2$. $6H_2O$ during melting and solidification, Energy Sources Part A, 30 (2008) 775-787.

[101] V.V. Tyagi, D. Buddhi, Thermal cycle testing of calcium chloride hexahydrate as a possible PCM for latent heat storage, Sol. Energy Mater. Sol. Cells, 92 (2008) 891-899.

[102] K. Nagano, T. Mochida, S. Takeda, R. Domanski, M. Rebow, Thermal characteristics of manganese (II) nitrate hexahydrate as a phase change material for cooling systems, Appl. Therm. Eng., 23 (2003) 229-241.

[103] R. Naumann, H.H. Emons, Results of thermal analysis for investigation of salt hydrates as latent heat-storage materials, J. Therm. Anal. Calorim., 35 (1989) 1009-1031.

[104] J. Paris, M. Falardeau, C. Villeneuve, Thermal storage by latent heat: a viable option for energy conservation in buildings, Energy Sources, 15 (1993) 85-93.

[105] J. Heckenkamp, H. Baumann, Latentwarmespeicher (in German), Sonderdruck aus Nachrichten, 11 (1997) 1075-1081.

[106] A. Abhat, Low temperature latent heat thermal energy storage: heat storage materials, Sol. Energy, 10 (1983) 313-332.

[107] A. Sari, A. Bicer, A. Karaipekli, Synthesis, characterization, thermal properties of a series of stearic acid esters as novel solid–liquid phase change materials, Mater. Lett., 63 (2009) 1213–1216.

[108] E. Oro, A.d. Gracia, A. Castell, M.M. Farid, L.F. Cabeza, Review on phase change materails (PCMs) for cold thermal energy storage applications, Appl. Energy, 99 (2012) 513-533.

[109] M. Akgun, O. Aydin, K. Kaygusuz, Experimental study on melting/solidification characteristics of a paraffin as PCM, Energy Convers. Manag., 48 (2007) 669-678.

[110] H. Bo, E.M. Gustafsson, F. Setterwall, Tetradecane and hexadecane binary mixtures as phase change materials (PCMs) for cool storage in district cooling systems, Energy, 24 (1999) 1015-1028.

[111] M.W. Babich, S.W. Hwang, R.D. Mounts, The search for novel energy storage materials using differential scanning calorimetry, Thermochim. acta, 210 (1992) 83-88.

[112] M.W. Babich, R. Benrashid, R.D. Mounts, DSC studies of new energy storage materials. Part 3. Thermal and flammability studies, Thermochim. Acta, 243 (1994) 193-200.

[113] M.F. Demirbas, Thermal energy storage and phase change materials: an overview, Energy Sources Part B, 1 (2006) 85-95.

[114] D. Buddhi, S.D. Sharma, Measurements of transmittance of solar radiation through stearic acid: a latent heat storage material, Energy Convers. Manag., 40 (1999) 1979-1984.

[115] A.E. Bailey, Melting and solidification of fats, Wiley Interscience, New York, USA, 1950.

[116] D. Feldman, M.M. Shapiro, D. Banu, C.J. Fuks, Fatty acids and their mixtures as phase-change materials for thermal energy storage, Sol. energy mater., 18 (1989) 201-216.

[117] A. Sari, K. Kaygusuz, Thermal and heat transfer characteristics in a latent heat storage system using lauric acid, Energy Convers. Manag., 43 (2002) 2493-2507.

[118] S. Keles, K. Kaygusuz, A. Sari, Lauric and myristic acids eutectic mixture as phase change material for low-temperature heating applications, Int. J. Energy Res., 29 (2005) 857-870.

[119] A. Sari, K. Kaygusuz, Thermal performance of myristic acid as a phase change material for energy storage application, Renew. Energy, 24 (2001) 303–317.

[120] A. Sari, Thermal characteristics of a eutectic mixture of myristic and palmitic acids as phase change material for heating applications, Appl. Therm. Eng., 23 (2003) 1005-1017.

[121] K. Kaygusuz, A. Sari, Thermal energy storage performance of fatty acids as a phase change material, Energy Sources Part A, 28 (2006) 105-116.

[122] D. Feldman, M.M. Shapiro, D. Banu, Organic phase change materials for thermal energy storage, Sol. Energy Mater., 13 (1986) 1-10.

[123] A. Hasan, A.A. Sayigh, Some fatty acids as phase-change thermal energy storage materials, Renew. Energy, 4 (1994) 69-76.

[124] A. Sari, K. Kaygusuz, Thermal performance of palmitic acid as a phase change energy storage material, Energy Convers. Manag., 43 (2002) 863-876.

[125] M.W. Babich, S.W. Hwang, R.D. Mounts, The thermal analysis of energy storage materials by differential scanning calorimetry, Thermochim. acta, 210 (1992) 77-82.

[126] C. Alkan, K. Kaya, A. Sari, Preparation and thermal properties of ethylene glycole distearate as a novel phase change material for energy storage, Mater. Lett., 62 (2008) 1122-1125.

[127] A. Kaizawa, N. Maruoka, A. Kawai, H. Kamano, T. Jozuka, T. Senda, T. Akiyama, Thermophysical and heat transfer properties of phase change material candidate for waste heat transportation system, Heat Mass Transfer, 44 (2008) 763-769.

[128] J.A. Kenar, Latent heat characteristics of biobased oleochemical carbonates as potential phase change materials, Sol. Energy Mater. Sol. Cells, 94 (2010) 1697-1703.

[129] J.L. Zeng, J. Zhang, Y.Y. Liu, Z.X. Cao, Z.H. Zhang, F. Xu, L.X. Sun, Polyaniline/1-tetradecanol composites: Form-stable PCMS and electrical conductive materials, J. Therm. Anal. Cal., 91 (2008) 455-461.

[130] A. Sari, Eutectic mixtures of some fatty acids for low temperature solar heating applications: thermal properties and thermal reliability, Appl. Therm. Eng., 25 (2005) 2100-2107.

[131] A. Sari, K. Kaygusuz, Thermal energy storage characteristics of myristic and stearic acids eutectic mixture for low temperature heating applications, Chinese J. Chem. Eng., 14 (2006) 270-275.

[132] G. Baran, A. Sari, Phase change and heat transfer characteristics of a eutectic mixture of palmitic and stearic acids as PCM in a latent heat storage system, Energy Convers. Manag., 44 (2003) 3227–3246.

[133] A. Sari, K. Kaygusuz, Thermal performance of a eutectic mixture of lauric and stearic acids as PCM encapsulated in the annulus of two concentric pipes, Sol. Energy, 72 (2002) 493-504.

[134] A. Sari, A. Karaipekli, Preparation and thermal properties of capric acid/palmitic acid eutectic mixture as a phase change energy storage material, Mater. Lett., 62 (2008) 903-906.

[135] G.A. Lane, Low temperature heat storage with phase change materials, Int. J. Ambient Energy, 1 (1980) 155-168.

[136] R. Baetens, B.P. Jellea, A. Gustavsend, Phase change materials for building applications: a state-of-the-art review, Energ. Buildings, 42 (2010) 1361-1368.

[137] E. Osterman, V.V. Tyagi, V. Butala, N.A. Rahim, U. Stritih, Review of PCM based cooling technologies for buildings, Energ. Buildings, 49 (2012) 37-49.

[138] P. Feng, Y. Liu, I. Ayub, Z. Wu, F. Yang, Z. Zhang, Techno-economic analysis of screening metal hydride pairs for a 910 MWh_{th} thermal energy storage system, Appl. Energy, 242 (2019) 148-156.

[139] E.A. Pina, M.A. Lozano, L.M. Serra, Thermoeconomic cost allocation in simple trigeneration systems including thermal energy storage, Energy, 153 (2018) 170-184.

[140] J.E. Rea, C.J. Oshman, M.L. Olsen, C.L. Hardin, G.C. Glatzmaier, N.P. Siegel, P.A. Parilla, D.S. Ginley, E.S. Toberer, Performance modeling and techno-economic analysis of a modular concentrated solar power tower with latent heat storage, Appl. Energy, 217 (2018) 143-152.

[141] I. Edmonds, Low cost realisation of a high temperature solar cooker, Renew. Energ., 121 (2018) 94-101.

[142] H. Yang, Y. Wang, Q. Yu, G. Cao, X. Sun, R. Yang, Q. Zhang, F. Liu, X. Di, J. Li, C. Wang, G. Li, Low-cost, three-dimension, high thermal conductivity, carbonized wood-based composite phase change materials for thermal energy storage, Energy, 159 (2018) 929-936.

[143] A.M. Lopez-Sabiron, A. Aranda-Uson, M.D. Mainar-Toledo, V.J. Ferreira, G. Ferreira, Environmental profile of latent energy storage materials applied to industrial systems, Sci. Total Environ., 473-474 (2014) 565-575.

[144] A.M. Lopez-Sabiron, P. Royo, V.J. Ferreira, A. Aranda-Uson, G. Ferreira, Carbon footprint of a thermal energy storage system using phase change materials for industrial energy recovery to reduce the fossil fuel consumption, Appl. Energy, 135 (2014) 616-624.

[145] R. Battisti, A. Corrado, Environmental assessment of solar thermal collectors with integrated water storage, J. Clean. Prod., 13 (2005) 1295-1300.

[146] P. Viebahn, Y. Lechon, F. Trieb, The potential role of concentrated solar power (CSP) in Africa and Europe—A dynamic assessment of technology development, cost development and life cycle inventories until 2050, Energy Policy, 39 (2011) 4420-4430.

[147] E. Oro, A. Gil, A.d. Gracia, D. Boer, L.F. Cabeza, Comparative life cycle assessment of thermal energy storage systems for solar power plants, Renew. Energy, 44 (2012) 166-173.

[148] P. Denholm, G.L. Kulcinski, Life cycle energy requirements and greenhouse gas emissions from large scale energy storage systems, Energy Convers. Manag., 45 (2004) 2153-2172.

[149] L. Scapino, H.A. Zondag, J. Diriken, C.C.M. Rindt, J.V. Bael, A. Sciacovelli, Modeling the performance of a sorption thermal energy storage reactor using artificial neural networks, Appl. Energy, 253 (2019) 113525.

[150] J. Vasquez, A. Reyes, A. Mahn, F. Cubillos, Experimental evaluation of fuzzy control solar drying with thermal energy storage system, Drying Technol., 34 (2016) 1558-1566.

[151] L. Braganca, S.R. Ermolli, H. Koukkari, Phase change materials in buildings, Int J. Sustain. Build. Technol. Urban Development, 2 (2011) 43-51.

[152] S. Mahmoud, A. Tang, C. Toh, R. Al-Dadah, S.L. Soo, Experimental investigation of inserts configurations and PCM type on the thermal performance of PCM based heat sinks, Appl. Energy, 112 (2013) 1349-1356.

[153] M. Ahmed, O. Meade, M.A. Medina, Reducing heat transfer across the insulated walls of refrigerated truck trailers by the application of phase change materials, Energy Convers. Manag., 51 (2010) 383-392.

[154] A. Shukla, D. Buddhi, R.L. Sawhney, Solar water heaters with phase change material thermal energy storage medium: a review, Renew Sustain Energy Rev., 13 (2009) 2119-2125.

[155] A.E. Khadraoui, S. Bouadila, S. Kooli, A. Guizani, A. Farhat, Solar air heater with phase change material: an energy analysis and a comparative study, Applied Therm. Eng., 107 (2016) 1057-1064.

[156] S. Subramanian, V. Pandiyarajan, R. Velraj, Experimental analysis of a PCM based IC engine exhaust waste heat recovery system, Int. Energy J., 5 (2004) 81-92.

[157] H.M. Hoang, D. Leducq, R. Perez-Masia, J.M. Lagaron, E. Gogou, P. Taoukis, G. Alvarez, Heat transfer study of submicro-encapsulated PCM plate for food packaging application, Int. J. Refrig., 52 (2015) 151-160.

[158] D. Leducq, F.T. NDoye, G. Alvarez, Phase change material for the thermal protection of ice cream during storage and transportation, Int. J. Refrig., 52 (2015) 133-139.

[159] S. Braxmeier, M. Hellmann, A. Beck, A. Umboock, G. Pluschke, T. Junghanss, H. Weinlaeder, Phase change material for thermotherapy of Buruli ulcer, J. Med. Eng. Technol., 33 (2009) 559-566.

[160] A. Shukla, A. Sharma, M. Shukla, C.R. Chen, Development of thermal energy storage materials for bio-medical applications, J. Med. Eng. Technol., 39 (2015) 363-368.

[161] Y. Cui, J. Xie, J. Liu, J. Wang, S. Chen, A review on phase change material application in building, Adv. Mech. Eng., 9 (2017) 1-15.

[162] A. Oliver, Thermal characterization of gypsum boards with PCM included: Thermal energy storage in buildings through latent heat, Energ. Buildings, 48 (2012) 1-7.

[163] A.K. Athienitis, c. LIu, D. Hawes, D. Banu, D. Feldman, Investigation of the thermal performance of a passive solar test-room with wall latent heat storage, Build. Environ. , 32 (1997) 405-410.

[164] N.K. Bansal, D. Buddhi, An analytical study of a latent heat storage system in a cylinder, Energy Convers. Manag., 33 (1992) 235-242.

[165] M. Smyth, P. Quinlan, J.D. Mondol, A. Zacharopoulos, D. McLarnon, A. Pugsley, The experimental evaluation and improvements of a novel thermal diode pre-heat solar water heater under simulated solar conditions, Renew. Energ., 121 (2018) 116-122.

[166] K. Kaygusuz, Experimental and theoretical investigation of a solar heating system with heat pump, Renew. Energy, 21 (2000) 79-102.

[167] I. Al-Hinti, A. Al-Ghandoor, A. Maaly, I.A. Naqeera, Z. Al-Khateeb, O. Al-Sheikh, Experimental investigation on the use of water-phase change material storage in conventional solar water heating systems, Energy Convers. Manag., 81 (2010) 1735-1740.

[168] M.A. Fazilati, A.A. Alemrajabi, Phase change material for enhancing solar water heater, an experimental approach, Energy Convers. Manag., 71 (2013) 138-145.

[169] M.H. Mahfuz, M.R. Anisur, M.A. Kibria, R. Saidur, I.H.S.C. Metselaar, Performance investigation of thermal energy storage system with Phase Change Material (PCM) for solar water heating application, Int. Commun. Heat Mass, 57 (2014) 132-139.

[170] D.J. Morrison, S.I. Abdel-Khalik, Effects of phase-change energy storage on the performance of air-based and liquid-based solar heating systems, Sol. Energy, 20 (1978) 57-67.

[171] K.Peippo, P.Kauranen, P.D.Lund, A multicomponent PCM wall optimized for passive solar heating, Energ. Buildings, 17 (1991) 259-270.

[172] S.O. Enibe, Performance of a natural circulation solar air heating system with phase change material energy storage, Renew. Energy, 27 (2002) 69-86.

[173] S.O. Enibe, Thermal analysis of a natural circulation solar air heater with phase change material energy storage, Renew. Energy, 28 (2003) 2269-2299.

[174] M.M. Alkilani, K. Sopian, M.A. Alghoul, M. Sohif, M.H. Ruslan, Review of solar air collectors with thermal storage units, Renew. Sustain. Energy Rev., 15 (2011) 1476-1490.

[175] S. VijayaVenkataRaman, S. Iniyan, R. Goic, A review of solar drying technologies, Renew. Sustain. Energy Rev., 16 (2012) 2652-2670.

[176] S.M. Shalaby, M.A. Bek, A.A. El-Sebaii, Solar dryers with PCM as energy storage medium: a review, Renew. Sustain. Energy Rev., 33 (2014) 110-116.

[177] L.M. Bal, S. Satya, S.N. Naik, Solar dryer with thermal energy storage systems for drying agricultural food products: a review, Renew Sustain Energy Rev., 14 (2010) 2298-2314.

[178] A. Reyes, A. Mahn, F. Vasquez, Mushrooms dehydration in a hybrid-solar dryer, using a phase change material, Energy Convers. Manag., 83 (2014) 241-248.

[179] S.M. Shalaby, M.A. Bek, Experimental investigation of a novel indirect solar dryer implementing PCM as energy storage medium, Energy Convers. Manag., 83 (2014) 1-8.

[180] D. Buddhi, L.K. Sahoo, Solar cooker with latent heat storage : design and experimental testing, Energy Convers. Manag., 38 (1997) 493-498.

[181] S.D. Sharma, D. Buddhi, R.L. Sawhney, A. Sharma, Design, development and performance evaluation of a latent heat storage unit for evening cooking in a solar cooker, Energy Convers. Manag., 41 (2000) 1497-1508.

[182] B. Xu, P. Li, C. Chan, Application of phase change materials for thermal energy storage in concentrated solar thermal power plants: a review to recent developments, Appl. Energy, 160 (2015) 286-307.

[183] N. Sarier, E. Onder, Organic phase change materials and their textile applications: an overview, Thermochim. Acta, 540 (2012) 7-40.

[184] F. Salaun, E. Devaux, S. Bourbigot, P. Rumeau, Thermoregulating response of cotton fabric containing microencapsulated phase change materials, Thermochim. Acta, 506 (2010) 82-93.

[185] E. Jahns, J. Burger, A step forward in personal comfort: PCM nonwovens, Nonwovens World, 14 (2005) 51-54.

[186] H. Shim, E.A. McCullough, B.W. Jones, Using phase change materials in clothing Text. Res. J., 71 (2011) 495-502.

[187] F.R. He, Study on manufacturing technology of phase change materials and smart thermo-regulated textiles, Adv. Mater. Res., 821-822 (2013) 130-138.

[188] N. Sarier, E. Onder, The manufacture of microencapsulated phase change materials suitable for the design of thermally enhanced fabrics, Thermochim. Acta, 452 (2007) 149-160.

[189] X.X. Zhang, X.C. Wang, X.M. Tao, K.L. Yick, Energy storage polymer/MicroPCMs blended chips and thermo-regulated fibers, J. Mater. Sci., 40 (2005) 3729-3734.

[190] Y. Shin, D.I. Yoo, K. Son, Development of thermoregulating textile materials with microencapsulated phase change materials (PCM). II. Preparation and application of PCM microcapsules, J. Appl. Polymer Sci., 96 (2005) 2005-2010.

[191] T.L. Vigo, C.M. Frost, Temperature adaptable hollow fibers containing polyethylene glycols J. Ind. Text., 12 (1983) 243-254.

[192] A. Kuru, S.A. Aksoy, Cellulose–PEG grafts from cotton waste in thermo-regulating textiles, Text. Res. J., 84 (2014) 337-346.

[193] L.T. Yeh, Review of heat transfer technologies in electronic equipment, J. Electron. Packag., 117 (1995) 333-339.

[194] F.L. Tan, C.P. Tso, Cooling of mobile electronic devices using phase change materials, Appl. Therm. Eng. , 24 (2004) 159-169.

[195] S.C. Fok, W. Shen, F.L. Tan, Cooling of portable hand-held electronic devices using phase change materials in finned heat sinks, Int. J. Therm. Sci., 49 (2010) 109-117.

[196] R. Baby, C. Balaji, Experimental investigations on phase change material based finned heat sinks for electronic equipment cooling, Int. J. Heat Mass Transfer., 55 (2012) 1642-1649.

[197] R. Baby, C. Balaji, Thermal optimization of PCM based pin fin heat sinks: an experimental study, Appl. Therm. Eng., 54 (2013) 65-77.

[198] Y.-H. Wang, Y.-T. Yang, Three-dimensional transient cooling simulations of a portable electronic device using PCM (phase change materials) in multi-fin heat sink, Energy, 36 (2011) 5214-5224.

[199] S. Shaikh, K. Lafdi, C/C composite, carbon nanotube and paraffin wax hybrid systems for the thermal control of pulsed power in electronics, Carbon, 48 (48) 813-824.

[200] A. Gil, E. Oro, L. Miro, G. Peiro, A. Ruiz, J.M. Salmeron, L. F.Cabeza, Experimental analysis of hydroquinone used as phase change material (PCM) to be applied in solar cooling refrigeration, Int. J. Refrig., 39 (2014) 95-103.

[201] Y.L. Lu, W.H. Zhang, P. Yuan, M.D. Xue, Z.G. Qu, W.Q. Tao, Experimental study of heat transfer intensification by using a novel combined shelf in food refrigerated display cabinets (Experimental study of a novel cabinets), Appl. Therm. Eng., 30 (2010) 85-91.

[202] B. Gin, M.M. Farid, The use of PCM panels to improve storage condition of frozen food, J. Food Eng., 100 (2010) 372-376.

[203] P.J. Martinez, J.M. Pinazo, A. Velazquez, Passive thermal energy storage in refrigerated trailers, ASHRAE Trans., 109 (2003) 324-328.

[204] I. Arvanitoyannis, E. Psomiadou, C.G. Biliaderis, H. Ogawa, N. Kawasaki, A. Nakayama, Biodegradable films made from low density polyethylene (LDPE), ethylene acrylic acid (EAA), polycaprolactone (PCL) and wheat starch for food packaging applications: part 3, Starch, 49 (1997) 306-322.

[205] D. Mondieig, F. Rajabalee, A. Laprie, H.A.J. Oonk, T. Calvet, M.A. Cuevas-Diarte, Protection of temperature sensitive biomedical products using molecular alloys as phase chnage material, Transfus. Apher. Sci., 28 (2003) 143-148.

[206] C. Wang, M. Hossain, L. Ma, Z. Ma, J.J. Hickman, M. Su, Highly sensitive thermal detection of thrombin using aptamer-functionalized phase change nanoparticles, Biosens. Bioelectron., 26 (2010) 437-443.

[207] K.B. Kim, K.W. Choi, Y.J. Kim, K.H. Lee, K.S. Lee, Feasibility study on a novel cooling technique using a phase change material in an automotive engine, Energy, 35 (2010) 478-484.

[208] J. Shon, H. Kim, K. Lee, Improved heat storage rate for an automobile coolant waste heat recovery system using phase-change material in a fin–tube heat exchanger, Appl. Energy, 113 (2014) 680-689.

[209] D. Zhao, G. Tan, Experimental evaluation of a prototype thermoelectric system integrated with PCM (phase change material) for space cooling, Energy, 68 (2014) 658-666.

[210] Z.H. Rao, S.F. Wang, Y.L. Zhang, Thermal management with phase change material for a power battery under cold temperatures, Energy Sources Part A, 36 (2014) 2287-2295.

[211] V.Pandiyarajan, M.C. Pandian, E.Malan, R.Velraj, R.V.Seeniraj, Experimental investigation on heat recovery from diesel engine exhaust using finned shell and tube heat exchanger and thermal storage system, Appl. Energy, 88 (2011) 77-87.

[212] Y. Chen, W. Luo, J. Wang, J. Huang, Enhanced thermal conductivity and durability of a paraffin wax nanocomposite based on carbon-coated aluminum nanoparticles, J. Phys. Chem. C, 121 (2017) 12603-12609.

[213] S.A. Khateeb, M.M. Farid, J.R. Selman, S. Al-Hallaj, Design and simulation of a lithium-ion battery with a phase change material thermal management system for an electric scooter, J. Power Sources, 128 (2004) 292-307.

[214] S.Y. Wu, X. Tong, C.D. Nie, D.Q. Peng, S.G. Gong, Z.Q. Wang, The effects of various carbon nanofillers on the thermal properties of paraffin for energy storage applications, J. Therm. Anal. Calorim., 124 (2016) 181-188.

[215] A.K. Mishra, B.B. Lahiri, J. Philip, Thermal conductivity enhancement in organic phase change material (phenol-water system) upon addition of Al_2O_3, SiO_2 and TiO_2 nano-inclusions, J. Mol. Liq., 269 (2018) 47-63.

[216] A.K. Mishra, B.B. Lahiri, J. Philip, Effect of surface functionalization and physical properties of nanoinclusions on thermal conductivity enhancement in an organic phase change material, ACS Omega, 3 (2018) 9487-9504.

[217] A.K. Mishra, B.B. Lahiri, J. Philip, Superior thermal conductivity and photo-thermal conversion efficiency of carbon black loaded organic phase change material, J. Mol. Liq., 285 (2019) 640-657.

[218] A.K. Mishra, B.B. Lahiri, V. Solomon, J. Philip, Nano-inclusion aided thermal conductivity enhancement in palmitic acid/di-methyl formamide phase change material for latent heat thermal energy storage, Thermochim. Acta, 678 (2019) 178309.

[219] M. Mehrali, S.T. Latibari, M. Mehrali, T.M.I. Mahlia, H.S.C. Metselaar, Preparation and properties of highly conductive palmitic acid/graphene oxide composites as thermal energy storage materials, Energy, 58 (2013) 628-634.

[220] C. Wang, K. Chen, J. Huang, Z. Cai, Z. Hu, T. Wang, Thermal behavior of polyethylene glycol based phase change materials for thermal energy storage with multiwall carbon nanotubes additives, Energy, 180 (2019) 873-880.

[221] X.L. Qiu, L.X. Lu, Z.X. Zhang, G.Y. Tang, G.L. Song, Preparation, thermal property, and thermal stability of microencapsulated noctadecane with poly (stearyl methacrylate) as shell, J. Therm. Anal. Calorim., 118 (2014) 1441-1449.

[222] T. Kousksou, A. Arid, A. Jamil, Y. Zeraouli, Thermal behavior of building material containing microencapsulated PCM, Thermochim. Acta, 550 (2012) 42-47.

[223] A. Karaipekli, A. Seri, Capric–myristic acid/vermiculite composite as form-stable phase change material for thermal energy storage, Sol. Energy, 83 (2009) 323-332.

[224] M.M. Sedeh, J.M. Khodadadi, Thermal conductivity improvement of phase change materials/graphite foam composites, Carbon, 60 (2013) 117-128.

[225] A. Mills, M. Farid, J.R. Selman, S. Al-Hallaj, Thermal conductivity enhancement of phase change materials using a graphite matrix, Appl. Therm. Eng., 26 (2006) 1652-1661.

[226] X. Py, R. Olives, S. Mauran, Paraffin/porous-graphite-matrix composite as a high and constant power thermal storage material, Int. J. Heat Mass Transfer., 44 (2001) 2727-2737.

[227] V. Shatikian, G. Ziskind, R. Letan, Numerical investigation of a PCM-based heat sink with internal fins: constant heat flux, Int. J. Heat Mass Transfer, 51 (2008) 1488-1493.

[228] L.F. Cabeza, H. Mehling, S. Hiebler, F. Ziegler, Heat transfer enhancement in water when used as PCM in thermal energy storage, Appl. Therm. Eng., 22 (2002) 1141-1151.

[229] J. Fukai, Y. Hamada, Y. Morozumi, O. Miyatake, Effect of carbon-fiber brushes on conductive heat transfer in phase change materials, Int. J. Heat Mass Transfer., 45 (2002) 4781-4792.

[230] J. Fukai, M. Kanou, Y. Kodama, O. Miyatake, Thermal conductivity enhancement of energy storage media using carbon fibers, Energy Convers. Manag., 41 (2000) 1543-1556.

[231] S.A. Angayarkanni, J. Philip, Thermal conductivity measurements in phase change materials under freezing in presence of nanoinclusions, J. Appl. Phys., 118 (2015) 094306.

[232] S.A. Angayarkanni, J. Philip, Tunable thermal transport in phase change materials using inverse micellar templating and nanofillers, J. Phys. Chem. C, 118 (2014) 13972-13980.

[233] A. Karaipekli, A. Sari, Capric-myristic acid/expanded perlite composite as form-stable phase change material for latent heat thermal energy storage, Renew. Energy, 33 (2008) 2599-2605.

[234] S. Harish, K. Ishikawa, S. Chiashi, J. Shiomi, S. Maruyama, Anomalous thermal conduction characteristics of phase change composites with single-walled carbon nanotube inclusions, J. Phys. Chem. C, 117 (2013) 15409-15413.

[235] D. Su, Y. Jia, G. Alva, F. Tang, G. Fang, Preparation and thermal properties of n–octadecane/stearic acid eutectic mixtures with hexagonal boron nitride as phase change materials for thermal energy storage, Energ. Buildings, 131 (2016) 35–41.

[236] Y. Wu, X. Yan, P. Meng, P. Sun, G. Cheng, R. Zheng, Carbon black/octadecane composites for room temperature electrical and thermal regulation, Carbon, 94 (2015) 417–423.

[237] P.C. Sun, Y.L. Wu, J.W. Gao, G.A. Cheng, G. Chen, R.T. Zheng, Room temperature electrical and thermal switching CNT/ hexadecane composites, Adv. Mater. , 25 (2013) 4938–4943.

[238] R. Zheng, J. Gao, J. Wang, S.-P. Feng, H. Ohtani, J. Wang, G. Chen, Thermal percolation in stable graphite suspensions, Nano Lett., 12 (2012) 188−192.

[239] S.C. Lin, H.H. Al-Kayiem, Evaluation of copper nanoparticles-paraffin wax compositions for solar thermal energy storage, Sol. Energy, 132 (2016) 267-278.

[240] S. Jesumathy, M. Udayakumar, S. Suresh, Experimental study of enhanced heat transfer by addition of CuO nanoparticle, Heat Mass Trans., 48 (2012) 965-978.

[241] X. Gao, T. Zhao, G. Luo, B. Zheng, H. Huang, X. Han, R. Ma, Y. Chai, Thermal property enhancement of paraffin-wax-based hydroxyl-terminated polybutadiene binder with a novel

nanoSiO_2-expanded graphite-PW ternary form-stable phase change material, Energy Fuels, 32 (2018) 4016-4024.

[242] Y. Zhong, S. Li, X. Wei, Z. Liu, Q. Guo, J. Shi, L. Liu, Heat transfer enhancement of paraffin wax using compressed expanded natural graphite for thermal energy storage, Carbon, 48 (2010) 300-304.

[243] A. Elgafy, K. Lafdi, Effect of carbon nanofiber additives on thermal behavior of phase change materials, Carbon, 43 (2005) 3067-3074.

[244] X. Fang, L.-W. Fan, Q. Ding, X. Wang, X.-L. Yao, J.-F. Hou, Z.-T. Yu, G.-H. Chen, Y.-C. Hu, K.-F. Cen, Increased thermal conductivity of eicosane-based composite phase change materials in the presence of graphene nanoplatelets, Energy Fuels, 27 (2013) 4041–4047.

[245] J. Wang, H. Xie, Z. Xin, Thermal properties of paraffin based composites containing multi-walled carbon nanotubes, Thermochim. Acta, 488 (2009) 39-42.

[246] Q. Tang, J. Sun, S. Yu, G. Wang, Improving thermal conductivity and decreasing supercooling of paraffin phase change materials by n-octadecylamine-functionalized multi-walled carbon nanotubes, RSC Adv., 4 (2014) 36584-36590.

[247] D.S. Ezhumalai, G. Sriharan, S. Harikrishnan, Improved thermal energy storage behavior of CuO/palmitic acid composite as phase change material, Mater. Today Proc., 5 (2018) 14618-14627.

[248] Z. Chen, F. Shan, L. Cao, G. Fang, Synthesis and thermal properties of shape-stabilized lauric acid/ activated carbon composites as phase change materials for thermal energy storage Sol. Energy Mater. Sol. Cells, 102 (2012) 131-136.

[249] G. Fang, H. Li, X. Liu, Preparation and properties of lauric acid/ silicon dioxide composites as form-stable phase change materials for thermal energy storage, Mater. Chem. Phys., 122 (2010) 533-536.

[250] S. Harish, D. Orejon, Y. Takata, M. Kohno, Thermal conductivity enhancement of lauric acid phase change nanocomposite in solid and liquid state with single-walled carbon nanohorn inclusions, Thermochim. Acta, 600 (2015) 1-6.

[251] F. Tang, L. Cao, G. Fang, Preparation and thermal properties of stearic acid/titanium dioxide composites as shape-stabilized phase change materials for building thermal energy storage, Energ. Buildings, 80 (2014) 352–357.

[252] B. Li, T. Liu, L. Hu, Y. Wang, S. Nie, Facile preparation and adjustable thermal property of stearic acid–graphene oxide composite as shape-stabilized phase change material, Chem. Eng. J., 215-216 (2013) 819–826.

[253] A. Karaipekli, A. Sarı, K. Kaygusuz, Thermal conductivity improvement of stearic acid using expanded graphite and carbon fiber for energy storage applications, Renew. Energy, 32 (2007) 2201–2210.

[254] M.N.A. Hawlader, M.S. Uddin, H.J. Zhu, Encapsulated phase change materials for thermal energy storage: Experiments and simulation, Int. J. Energy Res., 26 (2002) 159-171.

[255] M.N.A. Hawlader, M.S. Uddin, M.M. Khin, Microencapsulated PCM thermal-energy storage system, Appl. Energy, 74 (2003) 195-202.

[256] Y. Ozonur, M. Mazman, H.O. Paksoy, H. Evliya, Microencapsulation of coco fatty acid mixture for thermal energy storage with phase change material, Int. J. Energy Res., 30 (2006) 741-749.

[257] L. Sanchez, P. Sanchez, A.d. Lucas, M. Carmona, J.F. Rodriguez, Microencapsulation of PCMs with a polystyrene shell, Coll. Polymer Sci., 285 (2007) 1377-1385.

[258] A. Sari, C. Alkan, A. Karaipekli, O. Uzun, Microencapsulated n-octacosane as phase change material for thermal energy storage, Sol. Energy, 83 (2009) 1757-1763.

[259] C. Alkan, A. Sari, A. Karaipekli, O. Uzun, Preparation, characterization, and thermal properties of microencapsulated phase change material for thermal energy storage, Sol. Energy Mater. Sol. Cells, 93 (2009) 143-147.

[260] S.H. Lee, S.J. Yoon, Y.G. Kim, Y.C. Choi, J.H. Kim, J.G. Lee, Development of building materials by using micro-encapsulated phase change material, Kor. J. Chem. Eng., 24 (2007) 332-335.

[261] G. Fang, H. Li, F. Yang, X. Liu, S. Wu, Preparation and characterization of nano-encapsulated n-tetradecane as phase change material for thermal energy storage, Chem. Eng. J, 153 (2009) 217-221.

[262] H. Zhang, X. Wang, Synthesis and properties of microencapsulated n-octadecane with polyurea shells containing different soft segments for heat energy storage and thermal regulation, Sol. Energy Mater. Sol. Cells, 93 (2009) 1366-1376.

[263] S. Peng, A. Fuchs, R.A. Wirtz, Polymeric phase change composites for thermal energy storage, J. Appl. Polymer Sci., 93 (2004) 1240-1251.

[264] Y. Hong, G. Xin-shi, Preparation of polyethylene/paraffin compound as a form-stable solid-liquid phase change material, Sol. Energy Mater. Sol. Cells, 64 (2000) 37-44.

[265] A. Sari, Form-stable paraffin/high density polyethylene composites as solid–liquid phase change material for thermal energy storage: preparation and thermal properties, Energy Convers. Manag., 45 (2004) 2033-2042.

[266] I. Krupa, G. Mikova, A.S. Luyt, Phase change materials based on low-density polyethylene/paraffin wax blends, Eu. Polymer J., 43 (2007) 4695-4705.

[267] C. Alkan, A. Sari, O. Uzun, Poly(ethylene glycol)/acrylic polymer blends for latent heat thermal energy storage, AIChe J., 52 (2006) 3310-3314.

[268] C. Alkan, A. Sari, Fatty acid/poly(methyl methacrylate) (PMMA) blends as form-stable phase change materials for latent heat thermal energy storage, Sol. Energy, 82 (2008) 118–124.

[269] A. Sari, A. Karaipekli, M. Akcay, A. Onal, F. Kavak, Polymer/palmitic acid blends as shape-stabilized phase change material for latent heat thermal energy storage, Asian J. Chem., 18 (2005) 439-446.

[270] A. Sari, K. Kaygusuz, Studies on poly(vinyl chloride)/fatty acid blends as shape-stabilized phase change material for latent heat thermal energy storage, Indian J. Eng. Mater. Sci., 13 (2006) 253-258.

[271] N. Sarier, E. Onder, Thermal characteristics of polyurethane foams incorporated with phase change materials, Thermochim. Acta, 454 (2007) 90-98.

[272] N. Sarier, E. Onder, Thermal insulation capability of PEG-containing polyurethane foams, Thermochim. Acta, 475 (2008) 15-21.

[273] A. Sari, K. Kaygusuz, Poly(vinyl alcohol)/fatty acid blends for thermal energy storage, Energy Sources Part A, 29 (2007) 873-883.

[274] A. Sari, A. Karaipekli, Thermal conductivity and latent heat thermal energy storage characteristics of paraffin/expanded graphite composite as phase change material, Appl. Therm. Eng., 27 (2007) 1271-1277.

[275] A. Sari, A. Karaipekli, K. Kaygusuz, Fatty acid/expanded graphite composites as phase change material for latent heat thermal energy storage, Energy Sources Part A, 30 (2008) 464-474.

[276] A. Sari, A. Karaipekli, Preparation, thermal properties and thermal reliability of palmitic acid/expanded graphite composite as form-stable PCM for thermal energy storage, Sol. Energy Mater. Sol. Cells, 93 (2009) 571-576.

[277] W.-m. Guan, J.-h. Li, T.-t. Qian, X. Wang, Y. Deng, Preparation of paraffin/expanded vermiculite with enhanced thermal conductivity by implanting network carbon in vermiculite layers, Chem. Eng. J., 277 (2015) 56-63.

[278] Z. Zhang, X. Fang, Study on paraffin/expanded graphite composite phase change thermal energy storage material, Energy Convers. Manag., 47 (2006) 303-310.

[279] L. Xing, L. Hongyan, W. Shujun, Z. Lu, C. Hua, Preparation and thermal properties of form stable paraffin phase change material encapsulation, Energy Convers. Manag., 47 (2006) 2515-2522.

[280] R.-A. Mitran, D. Berger, C. Matei, Improving thermal properties of shape-stabilized phase change materials containing lauric acid and mesocellular foam silica by assessing thermodynamic properties of the non-melting layer, Thermochim. Acta, 660 (2018) 70-76.

[281] X. Fu, Z. Liu, Y. Xiao, J. Wang, J. Lei, Preparation and properties of lauric acid/diatomite composites as novel form-stable phase change materials for thermal energy storage, Energ. Buildings, 104 (2015) 244-249.

[282] A. Sari, A. Karaipekli, C. Alkan, Preparation, characterization and thermal properties of lauric acid/expanded perlite as novel form-stable composite phase change material, Chem. Eng. J, 155 (2009) 899-904.

[283] Q. Shen, J. Ouyang, Y. Zhang, H. Yang, Lauric acid/modified sepiolite composite as a form-stable phase change material for thermal energy storage, Appl. Clay Sci., 146 (2017) 14-22.

[284] R. Wen, Z. Huang, Y. Huang, X. Zhang, X. Min, M. Fang, Y.g. Liu, X. Wu, Synthesis and characterization of lauric acid/expanded vermiculite as form-stabilized thermal energy storage materials, Energ. Buildings, 116 (2016) 677-683.

[285] X. Zhang, Z. Yin, D. Meng, Z. Huang, R. Wen, Y. Huang, X. Min, Y. Liu, M. Fang, X. Wu, Shape-stabilized composite phase change materials with high thermal conductivity based on stearic acid and modified expanded vermiculite, Renew. Energy, 112 (2017) 113-123.

[286] A. Karaipekli, A. Bicer, A. Sari, V.V. Tyagi, Thermal characteristics of expanded perlite/paraffin composite phase change material with enhanced thermal conductivity using carbon nanotubes, Energy Convers. Manag., 134 (2017) 373-381.

[287] Z. Zhang, G. Shi, S. Wang, X. Fang, X. Liu, Thermal energy storage cement mortar containing n-octadecane/expanded graphite composite phase change material, Renew. Energy, 50 (2013) 670-675.

[288] J. Philip, P.D. Shima, B. Raj, Nanofluid with tunable thermal properties, Appl. Phys. Lett., 92 (2008) 043108-043103.

[289] S.A. Angayarkanni, A.K. Mishra, J. Philip, Effect of polymeric-additives on thermal and electrical conductivity of nanofluids, J. Nanofluids, 5 (2016) 661-668.

[290] S.A. Angayarkanni, J. Philip, Effect of Nanoparticles Aggregation on Thermal and Electrical Conductivities of Nanofluids, J. Nanofluids, 3 (2014) 17–25.

[291] H. Akoh, Y. Tsukasaki, S. Yatsuya, AkiraTasaki, Magnetic properties of ferromagnetic ultrafine particles prepared by vacuum evaporation on running oil substrate, J. Cryst. Growth, 45 (1978) 495-500.

[292] V. Sridhara, L.N. Satapathy, Al_2O_3-based nanofluids: a review, Nanoscale Res. Lett., 6 (2011) 456.

[293] A.G. Kanaras, F.S. Kamounah, K. Schaumburg, C.J. Kiely, M. Brust, Thioalkylated tetraethylene glycol: A new ligand for water soluble monolayer protected gold clusters, Chem. Comm., 20 (2002) 2294-2295.

[294] S.U. Sandhya, S.A. Nityananda, A facile one step solution route to synthesize cuprous oxide nanofluid, Nanomater. Nanotechnol., 3 (2013) 1-7.

[295] H.J. Kim, I.C. Bang, J. Onoe, Characteristic stability of bare Au-water nanofluids fabricated by pulsed laser ablation in liquids, Opt. Laser Eng., 47 (2009) 532-538.

[296] S.W. Lee, S.D. Park, I.C. Bang, Critical heat flux for CuO nanofluid fabricated by pulsed laser ablation differentiating deposition characteristics, Int. J. Heat Mass Transfer., 55 (2012) 6908-6915.

[297] Y. Sun, B. Mayers, T. Herricks, Y. Xia, Polyol synthesis of uniform silver nanowires: A plausible growth mechanism and the supporting evidence, Nano Lett., 3 (2003) 955-960.

[298] F. Bonet, K. Tekaia-Elhsissen, K. Vijaya Sarathy, Study of interaction of ethylene glycol/PVP phase on noble metal powders prepared by polyol process, Bull. Mater. Sci., 23 (2000) 165-168.

[299] C. Wang, J. Yang, Y. Ding, Phase transfer based synthesis and thermophysical properties of Au/Therminol VP-1 nanofluids, Prog. Nat. Sci., 23 (2013) 338-342.

[300] J. Yang, E. Sargent, S. Kelley, J.Y. Ying, A general phase-transfer protocol formetal ions and its application in nanocrystal synthesis, Nat. Mater., 8 (2010) 683-689.

[301] H.-t. Zhu, Y.-s. Lin, Y.-s. Yin, A novel one-step chemical method for preparation of copper nanofluids, J. Coll. Interface Sci., 277 (2004) 100-103.

[302] H. Wang, J.-Z. Xu, J.-J. Zhu, H.-Y. Chen, Preparation of CuO nanoparticles by microwave irradiation, J. Cryst. Growth, 244 (2002) 88-94.

[303] I. Popa, G. Gillies, G. Papastavrou, M. Borkovec, Attractive and repulsive electrostatic forces between positively charged latex particles in the presence of anionic linear polyelectrolytes, J. Phys. Chem. B, 114 (2010) 3170-3177.

[304] B.W. Ninham, On progress in forces since the DLVO theory, Adv. Colloids Interface Sci., 83 (1999) 1-17.

[305] T. Missana, A. Adell, On the applicability of DLVO theory to the prediction of clay colloids stability, J. Coll. Interface Sci., 230 (2000) 150-156.

[306] C. Anushree, J. Philip, Assessment of long term stability of aqueous nanofluids using different experimental techniques, J. Mol. Liq., 222 (2016) 350-358.

[307] P.D. Shima, J. Philip, B. Raj, Influence of aggregation on thermal conductivity in stable and unstable nanofluids, Appl. Phys. Lett., 97 (2010) 153113.

[308] X. Li, D. Zhu, X. Wang, Evaluation on dispersion behavior of the aqueous copper nano-suspensions, J. Coll. Interface Sci., 310 (2007) 456-463.

[309] X. Wei, L. Wang, Synthesis and thermal conductivity of microfluidic copper nanofluids, Particuology, 8 (2010) 262-271.

[310] M. Farahmandjou, S.A. Sebt, S.S. Parhizgar, P. Aberomand, M. Akhavan, Stability investigation of colloidal FePt nanoparticle systems by spectrophotometer analysis, Chin. Phys. Lett., 26 (2009) 027501.

[311] O. Mahian, A. Kianifar, S.A. Kalogirou, I. Pop, S. Wongwises, A review of the applications of nanofluids in solar energy, Int. J. Heat Mass Transfer., 57 (2013) 582-594.

[312] B. Dudda, D. Shin, Effect of nanoparticle dispersion on specific heat capacity of a binary nitrate salt eutectic for concentrated solar power applications, Int. J. Therm. Sci., 69 (2013) 37-42.

[313] W. Yu, H. Xie, A review on nanofluids: preparation, stability mechanisms, and applications, J. Nanomater., 2012 (2012) 435873.

[314] W.N. Mutuku, Ethylene glycol (EG)-based nanofluids as a coolant for automotive radiator, Asia pacific J. Comput. Eng., 3 (2016) 1.

[315] D.G. Subhedar, B.M. Ramani, A. Gupta, Experimental investigation of heat transfer potential of Al2O3/Water-Mono Ethylene Glycol nanofluids as a car radiator coolant, Case Studies Therm. Eng., 11 (2018) 26-34.

[316] G. Saxena, P. Soni, Nano coolants for automotive applications: a Review, Nano Trends, 20 (2018) 9-22.

[317] H. Liu, M. Bai, J. Lv, P. Wang, Y. Wang, C. Hu, Heat transfer analysis of piston cooling using nanofluids in the gallery, Micro Nano Lett. , 10 (2015) 28-33.

[318] B.H. Chun, H.U. Kang, S.H. Kim, Effect of alumina nanoparticles in the fluid on the heat transfer in double-pipe heat exchanger system, Korean J. Chem. Eng., 25 (2008) 966-971.

[319] A.A.A. Arani, O.A. Akbari, M.R. Safaei, A. Marzban, A.A.A.A. Alrashed, G.R. Afmadi, T.K. Nguyen, Heat transfer improvement of water/single-wall carbon nanotubes (SWCNT) nanofluid in a novel design of a truncated double-layered microchannel heat sink, Int. J. Heat Mass Transfer., 113 (2017) 780-795.

[320] M. Nazari, M. Karami, M. Ashouri, Comparing the thermal performance of water, ethylene glycol, alumina and CNT nanofluids in CPU cooling: experimental study, Expt. Therm. Fluid Sci., 57 (2014) 371-377.

[321] M.J. Kao, C.H. Lo, T.T. Tsung, Y.Y. Wu, C.S. Jwo, H.M. Lin, Copper-oxide brake nanofluid manufactured using arc-submerged nanoparticle synthesis system, J. Alloys Comp., 434-435 (2007) 672-674.

[322] T.L. Bergman, Effect of reduced specific heats of nanofluids on single phase, laminar internal forced convection, Int. J. Heat Mass Transfer., 52 (2009) 1240-1244.

[323] A. Chiney, V. Ganvir, B. Rai, Pradip, Stable nanofluids for convective heat transfer applications, J. Heat Trans., 136 (2014) 021704.

[324] J. Buongiorno, L.-W. Hu, S.J. Kim, R. Hannink, B. Truong, E. Forrest, Nanofluids for enhanced economics and safety of nuclear reactors: an evaluation of the potential features, issues, and research gaps, Nuclear Technol., 162 (2008) 80-91.

[325] S.M. Mousavizadeh, G.R. Ansarifar, M. Talebi, Assessment of the TiO2/water nanofluid effects on heat transfer characteristics in VVER-1000 nuclear reactor using CFD modeling, Nuclear Eng. Technol., 47 (2015) 814-826.

[326] H. Kim, Enhancement of critical heat flux in nucleate boiling of nanofluids: a state-of-art review, Nanoscale Res. Lett., 6 (2011) 415.

[327] J. Philip, P.D. Shima, Thermal properties of nanofluids, Adv. Colloid Interface Sci., 183-184 (2012) 30-45.

[328] C.H. Chon, K.D. Kihm, S.P. Lee, S.U.S. Choi, Empirical correlation finding the role of temperature and particle size for nanofluid (Al2O3) thermal conductivity enhancement, Appl. Phys. Lett., 87 (2005) 153107.

[329] S.H. Kim, S.R. Choi, D. Kim, Thermal conductivity of metal-oxide nanofluids: particle size dependence and effect of laser irradiation, ASME J. Heat Transfer, 129 (2007) 298-307.

[330] R.S. Vajjha, D.K. Das, Experimental determination of thermal conductivity of three nanofluids and development of new correlations, Int. J. Heat Mass Transfer., 52 (2009) 4675-4682.

[331] H.A. Mintsa, G. Roy, C.T. Nguyen, D. Doucet, New temperature dependent thermal conductivity data for water-based nanofluids, Int. J. Therm. Sci., 48 (2009) 363-371.

[332] M.P. Beck, Y. Yuan, P. Warrier, A.S. Teja, The thermal conductivity of aqueous nanofluids containing ceria nanoparticles, J. Appl. Phys., 107 (2010) 066101.

[333] M.P. Beck, Y. Yuan, P. Warrier, A.S. Teja, The thermal conductivity of alumina nanofluids in water, ethylene glycol, and ethylene glycol + water mixtures, J. Nanoparticle Res., 12 (2010) 1469-1477.

[334] E.V. Timofeeva, J.L. Routbort, D. Singh, Particle shape effects on thermophysical properties of alumina nanofluids, J. Appl. Phys., 106 (2009) 014304.

[335] K.J. Lee, S.H. Yoon, J. Jang, Carbon nanofibers: a novel nanofiller for nanofluid applications, Small, 3 (2007) 1209-1213.

[336] Y. Yang, E.A. Grulke, Z.G. Zhang, G. Wu, Thermal and rheological properties of carbon nanotube-in-oil dispersions, J. Appl. Phys., 99 (2006) 114307.

[337] P.D. Shima, J. Philip, Tuning of Thermal Conductivity and Rheology of Nanofluids Using an External Stimulus, J. Phys. Chem. C, 115 (2011) 20097–20104.

[338] E.V. Timofeeva, A.N. Gavrilov, J.M. McCloskey, Y.V. Tolmachev, S. Sprunt, L.M. Lopatina, J.V. Selinger, Thermal conductivity and particle agglomeration in alumina nanofluids: Experiment and theory, Phys. Rev. E, 76 (2007) 061203.

[339] S.M.S. Murshed, K.C. Leong, C. Yang, Investigations of thermal conductivity and viscosity of nanofluids, Int. J. Therm. Sci., 47 (2008) 560-568.

[340] W. Yu, H. Xie, X. Wang, X. Wang, Significant thermal conductivity enhancement for nanofluids containing graphene nanosheets, Phys. Lett. A, 375 (2011) 1323-1328.

[341] W. Evans, R. Prasher, J. Fish, P. Meakin, P. Phelan, P. Keblinski, Effect of aggregation and interfacial thermal resistance on thermal conductivity of nanocomposites and colloidal nanofluids, Int. J. Heat Mass Transf., 51 (2008) 1431–1438.

[342] R. Prasher, P.E. Phelan, P. Bhattacharya, Effect of aggregation kinetics on the thermal conductivity of nanoscale colloidal solutions (nanofluid), Nano Lett., 6 (2006) 1529-1534.

[343] J. Wensel, B. Wright, D. Thomas, W. Douglas, B. Mannhalter, W. Cross, H. Hong, J. Kellar, Enhanced thermal conductivity by aggregation in heat transfer nanofluids containing metal oxide nanoparticles and carbon nanotubes, Appl. Phys. Lett. , 92 (2008) 023110.

[344] S. Jana, A. Salehi-Khojin, W.-H. Zhong, Enhancement of fluid thermal conductivity by the addition of single and hybrid nano-additives, Thermochim. Acta, 462 (2007) 45-55.

[345] Y.J. Kim, H. Ma, Q. Yu, Plasma nanocoated carbon nanotubes for heat transfer nanofluids, Nanotechnology, 21 (2010) 295703.

[346] N.R. Karthikeyan, J. Philip, B. Raj, Effect of clustering on the thermal conductivity of nanofluids, Mater. Chem. Phys., 109 (2008) 50-55.
[347] Dae-HwangYoo, K.S. Hong, H.-S. Yang, Study of thermal conductivity of nanofluids for the application of heat transfer fluids, Thermochim. Acta, 455 (2007) 66-69.
[348] Y.J. Hwang, Y.C. Ahn, H.S. Shin, C.G. Lee, G.T. Kim, H.S. Park, J.K. Lee, Investigation on characteristics of thermal conductivity enhancement of nanofluids, Current Appl. Phys., 6 (2006) 1068-1071.
[349] H.E. Patel, T. Sundararajan, S.K. Das, An experimental investigation into the thermal conductivity enhancement in oxide and metallic nanofluids, J. Nanoparticle Res., 12 (2010) 1015-1031.
[350] Q. Yu, Y.J. Kim, H. Ma, Nanofluids with plasma treated diamond nanoparticles, Appl. Phys. Lett., 92 (2008) 103111.
[351] C.H. Li, G. P.Paterson, Experimental investigation of temperature and volume fraction variations on the effective thermal conductivity of nanoparticle suspensions (nanofluids), J. Appl. Phys., 99 (2006) 084314.
[352] H. Zhu, C. Zhang, ffects of nanoparticle clustering and alignment on thermal conductivities of Fe_3O_4 aqueous nanofluids, Appl. Phys. Lett., 89 (2006) 023123.
[353] D. Zhu, X. Li, N. Wang, X. Wang, J. Gao, H. Li, Dispersion behavior and thermal conductivity characteristics of Al2O3–H2O nanofluids, Current Appl. Phys., 9 (2009) 131-139.
[354] X.-j. Wang, D.-s. Zhu, S. Yang, Investigation of pH and SDBS on enhancement of thermal conductivity in nanofluids, Chem. Phys. Lett., 470 (2009) 107-111.
[355] M.J. Assael, N. Metaxa, J. Arvanitidis, D. Christofilos, C. Lioutas, Thermal conductivity enhancement in aqueous suspensions of carbon multi-walled and double-walled nanotubes in the presence of two different dispersants, Int. J. Thermophys., 26 (2005) 647-664.
[356] S.K. Das, N. Putra, W. Roetzel, Pool boiling characteristics of nano-fluids, Int. J. Heat Mass Transfer., 46 (2003) 851-862.
[357] W. Duangthongsuk, S. Wongwises, Measurement of temperature-dependent thermal conductivity and viscosity of TiO_2-water nanofluids, Expt. Therm. Fluid Sci., 33 (2009) 706-714.
[358] B. Yang, Z.H. Han, Temperature-dependent thermal conductivity of nanorod-based nanofluids, Appl. Phys. Lett., 89 (2006) 083111.
[359] L. Chen, H. Xie, Y. Li, W. Yu, Nanofluids containing carbon nanotubes treated by mechanochemical reaction, Thermochim. Acta, 477 (2008) 21-24.
[360] J. Glory, M. Bonetti, M. Helezen, M. Mayne-L'Hermite, C. Reynaud, Thermal and electrical conductivities of water-based nanofluids prepared with long multiwalled carbon nanotubes, J. Appl. Phys., 103 (2008) 094309.
[361] D. Singh, E. Timofeeva, W. Yu, J. Routbort, D. France, D. Smith, J.M. Lopez-Cepero, An investigation of silicon carbide-water nanofluid for heat transfer applications, J. Appl. Phys., 105 (2009) 064306.
[362] J.W. Gao, R.T. Zheng, H. Ohtani, D.S. Zhu, G. Chen, Experimental Investigation of Heat Conduction Mechanisms in Nanofluids. Clue on Clustering, Nano Lett., 9 (2009) 4128-4132.
[363] R.V. Pinto, F.A.S. Fiorelli, Review of the mechanisms responsible for heat transfer enhancement using nanofluids, Appl. Therm. Eng., 108 (2016) 720-739.
[364] J.C. Maxwell, A treatise on electricity and magnetism, 2nd ed., Clarendon Press, London, 1881.
[365] D.A.G. Bruggeman, Berechnung verschiedener physikalischer Konstanten von heterogenen Substanzen. I. Dielektrizitätskonstanten und Leitfähigkeiten der Mischkörper aus isotropen Substanzen (in German), Ann. Phys., 416 (1935) 636-664.
[366] R.L. Hamilton, O.K. Crosser, Thermal conductivity of heterogeneous two-component systems, Ind. Eng. Chem. Fundam., 1 (1962) 187-191.
[367] Z. Hashin, S. Shtrikman, A variational approach to the theory of the effective magnetic permeability of multiphase materials J. Appl. Phys., 33 (1962) 3125.

[368] W. Yu, S.U.S. Choi, The role of interfacial layers in the enhanced thermal conductivity of nanofluids: a renovated Hamilton-Crosser model, J. Nanoparticle Res., 6 (2004) 355-361.

[369] J. Avsec, M. Oblak, The calculation of thermal conductivity, viscosity and thermodynamic properties for nanofluids on the basis of statistical nanomechanics, Int. J. Heat Mass Transfer., 50 (2007) 4331-4341.

[370] Y. Xuan, Q. Li, Investigation on convective heat transfer and flow features of nanofluids, J. Heat Trans., 125 (2003) 151-155.

[371] B.C. Pak, Y.I. Cho, Hydrodynamic and heat transfer study of dispersed fluids with submicron metallic oxide particles, Expt. Heat Transf., 11 (1998) 151-170.

[372] D.H. Kumar, H.E. Patel, V.R.R. Kumar, T. Sundararajan, T. Pradeep, S.K. Das, Model for heat conduction in nanofluids, Phys. Rev. Lett., 93 (2004) 144301.

[373] R. Prasher, P. Bhattacharya, P.E. Phelan, Thermal conductivity of nanoscale colloidal solutions (nanofluids), Phys. Rev. Lett., 94 (2005) 025901.

[374] K.C. Leong, C. Yang, S.M.S. Murshed, A model for the thermal conductivity of nanofluids – the effect of interfacial layer, J. Nanoparticle Res., 8 (2006) 245-254.

[375] E. Yamada, T. Ota, Effective thermal conductivity of dispersed materials, Heat Mass Transfer, 13 (1980) 27-37.

[376] S. K.Gupte, S.G. Advani, P. Huq, Role of micro-convection due to non-affine motion of particles in a mono-disperse suspension, Int. J. Heat Mass Transfer., 38 (1995) 2945-2958.

[377] D.P.H. Hasselman, L.F. Johnson, Effective thermal conductivity of composites with interfacial thermal barrier resistance, J. Compos. Mater., 21 (1987) 508-515.

[378] H. Xie, M. Fujii, X. Zhang, Effect of interfacial nanolayer on the effective thermal conductivity of nanoparticle-fluid mixture, Int. J. Heat Mass Transfer, 48 (2005) 2926–2932.

[379] S.P. Jang, S.U.S. Choi, Role of Brownian motion in the enhanced thermal conductivity of nanofluids, Appl. Phys. Lett., 84 (2004) 4316-4318.

[380] B.-X. Wang, L.-P. Zhou, X.-F. Peng, A fractal model for predicting the effective thermal conductivity of liquid with suspension of nanoparticles, Int. J. Heat Mass Transfer., 46 (2003) 2665-2672.

[381] M. Corcione, Empirical correlating equations for predicting the effective thermal conductivity and dynamic viscosity of nanofluids, Energy Convers. Manag., 52 (2011) 789-793.

[382] K.D. Kihm, C.H. Chon, J.S. Lee, S.U.S. Choi, A new heat propagation velocity prevails over Brownian particle velocities in determining the thermal conductivities of nanofluids, Nanoscale Res. Lett., 6 (2011) 361.

[383] L. Braginsky, V. Shklover, Thermal conductivity of low-particle-concentration suspensions: correlation function approach, Phys. Rev. B, 78 (2008) 224205.

[384] C.J. Ho, L.C. Wei, Z.W. Li, An experimental investigation of forced convective cooling performance of a microchannel heat sink with Al_2O_3/water nanofluid, Appl. Therm. Eng., 30 (2010) 96-103.

[385] H. Tahmooressi, S. Daviran, A. Kasaeian, A. Rashidi, Percolating micro-structures as a key-role of heat conduction mechanism in nanofluids, Appl. Therm. Eng., 114 (2017) 346-359.

[386] R. Prasher, W. Evans, P. Meakin, J. Fish, P. Phelan, P. Keblinski, Effect of aggregation on thermal conduction in colloidal nanofluids, Appl. Phys. Lett., 89 (2006) 143119-143113.

[387] R. Zheng, J. Gao, J. Wang, G. Chen, Reversible temperature regulation of electrical and thermal conductivity using liquid–solid phase transitions, Nat. Commun., 2 (2011) 289.

[388] W.M. Merrill, R.E. Diaz, M.M. Lore, M.C. Squires, N.G. Alexopoulos, Effective medium theories for artificial materials composed of multiple sizes of spherical inclusions in a host continuum, IEEE Trans. Antennas. Propag., 47 (1999) 142-148.

[389] G.L. Pollack, Kapitza Resistance, Rev. Mod. Phys., 41 (1969) 48-81.

[390] Y. Agari, T. Uno, Estimation of thermal conductivities of filled polymers, J. Appl. Polymer Sci., 32 (1986) 5705-5712.

[391] J. Eapen, W.C. Williams, J. Buongiorno, L.-w. Hu, S. Yip, Mean-field versus microconvection effects in nanofluid thermal conduction, Phys. Rev. Lett., 99 (2007) 095901.

[392] Z. Ling, J. Chen, T. Xu, X. Fang, X. Gao, Z. Zhang, Thermal conductivity of an organic phase change material/expanded graphite composite across the phase change range and a novel thermal conductivity model, Energy Convers. Manag., 102 (2015) 202-208.

[393] C.R. Abujas, A. Jove, C. Prieto, M. Gallas, L.F. Cabeza, Performance comparison of a group of thermal conductivity enhancement methodology in phase change material for thermal storage application, Renew. Energy, 97 (2016) 434-443.

[394] X. Li, S. Wu, Y. Wang, L. Xie, Experimental investigation and thermodynamic modeling of an innovative molten salt for thermal energy storage (TES), Appl. Energy, 212 (2018) 516-526.

[395] S.N. Schiffres, S. Harish, S. Maruyama, J. Shiomi, J. A.Malen, Tunable electrical and thermal transport in ice-templated multilayer graphene nanocomposites through freezing rate control, ACS Nano, 7 (2013) 11183-11189.

[396] W. Wanga, X. Yang, Y. Fang, J. Ding, J. Yan, Enhanced thermal conductivity and thermal performance of form-stable composite phase change materials by using b-Aluminum nitride, Appl. Energ. , 86 (2009) 1196–1200.

[397] M. Klauck, A. Grenner, K. Taubert, A. Martin, R. Meinhardt, J. Schmelzer, Vapor-liquid equilibria in binary systems of phenol or cresols + water,+ toluene, and + octane and liquid-liquid equilibria in binary systems of cresols + water, Ind. Eng. Chem. Res., 47 (2008) 5119-5126.

[398] W.L. Bragg, The diffraction of short electromagnetic waves by a crystal, Proc. Camb. Philos. Soc., 17 (1913) 43-57.

[399] U. Holzwarth, N. Gibson, The Scherrer equation versus the 'Debye-Scherrer equation', Nature Nanotech., 6 (2011) 534.

[400] J. Gangwar, B.K. Gupta, S.K. Tripathi, A.K. Srivastava, Phase dependent thermal and spectroscopic responses of different morphogenesis of Al_2O_3 nanostructures, Nanoscale, 7 (2015) 13313-13344.

[401] K. Thamaphat, P. Limsuwan, B. Ngotawornchai, Phase Characterization of TiO_2 Powder by XRD and TEM, Kasetsart J. Nat. Sci., 42 (2008) 357-361.

[402] D.-H. Chen, C.-H. Hsieh, Synthesis of nickel nanoparticles in aqueous cationic surfactant solutions, J. Mater. Chem., 12 (2002) 2412-2415.

[403] K. Cheirmadurai, S. Biswas, R. Murali, P. Thanikaivelan, Green synthesis of copper nanoparticles and conducting nanobiocomposites using plant and animal sources, RSC Adv., 4 (2014) 19507-19511.

[404] T. Rieker, A. Hanprasopwattana, A. Datye, P. Hubbard, Particle size distribution inferred from small-angle X-ray scattering and transmission electron microscopy, Langmuir, 15 (1999) 638-641.

[405] O. Glatter, O. Kratky, Small angle X-ray scattering, Academic press, London, 1982.

[406] T. Morita, Y. Hatakeyama, K. Nishikawa, E. Tanaka, R. Shingai, H. Murai, H. Nakano, K. Hino, Multiple small-angle X-ray scattering analyses of the structure of gold nanorods with unique end caps, Chem. Phys., 364 (2009) 14-18.

[407] C.M. Long, M.A. Nascarella, P.A. Valberg, Carbon black vs. black carbon and other airborne materials containing elemental carbon: physical and chemical distinctions, Environ. Pollut., 181 (2013) 271-286.

[408] G. Binning, C.F. Quate, C. Gerber, Atomic force microscopy, Phys. Rev. Lett., 56 (1986) 930.

[409] B.C. Smith, Fundamentals of Fourier transform infrared spectroscopy, CRC Press, Florida, U.S.A, 2011.

[410] A. Lazaro, C. Penalosa, A. Sole, G. Diarce, T. Haussmann, M. Fois, B. Zalba, S. Gshwander, L.F. Cabeza, Intercomparative tests on phase change materials characterization with differential scanning calorimeter, Appl. Energy, 109 (2013) 415-420.

[411] M. Mehrali, S.T. Latibari, M. Mehrali, H.S. Cornelis Metselaar, M. Silakhori, Shape-stabilized phase change materials with high thermal conductivity based on paraffin/graphene oxide composite, Energy Convers. Manag., 67 (2013) 275-282.

[412] R.M. Saeed, J.P. Schlegel, C. Castano, R. Sawafta, Uncertainty of thermal characterization of phase change material by differential scanning calorimetry analysis, Int. J. Eng. Res. Technol., 5 (2016) 405-412.

[413] S. Bagavathiappan, B.B. Lahiri, T. Jayakumar, J. Philip, Infrared thermography for condition monitoring- a review, Infrared Phys. Technol., 60 (2013) 35-55.

[414] B.B. Lahiri, S. Bagavathiappan, T. Jayakumar, J. Philip, Medical applications of infrared thermography: a review, Infrared Phys. Technol., 55 (2012) 221-235.

[415] B.B. Lahiri, S. Bagavathiappan, R. Shunmugasundaram, J. Philip, T. Jayakumar, Measurement of annular air-gap using active infrared thermography, Infrared Phys. Technol., 61 (2013) 192-199.

[416] B.B. Lahiri, S. Bagavathiappan, C. Soumya, T. Jayakumar, J. Philip, Infrared thermography based studies on mobile phone induced heating, Infrared Phys. Technol., 71 (2015) 242-251.

[417] G. Xia, H. Jiang, R. Liu, Y. Zhai, Effects of surfactant on the stability and thermal conductivity of Al_2O_3/de-ionized water nanofluids, Int. J. Therm. Sci., 84 (2014) 118-124.

[418] C. Hermida-Merino, M. Perez-Rodríguez, A.B. Pereiro, M.M. Pineiro, M.J. Pastoriza-Gallego, Tailoring nanofluid thermophysical profile through graphene nanoplatelets surface functionalization, ACS Omega, 3 (2018) 744-752.

[419] G. Domingues, S. Volz, K. Joulain, J.J. Greffet, Heat transfer between two nanoparticles through near field interaction, Phys. Rev. Lett., 94 (2005) 85901.

[420] J. Eapen, J. Li, S. Yip, Beyond the Maxwell limit: thermal conduction in nanofluids with percolating fluid structures, Phys. Rev. E, 76 (2007) 062501.

[421] C.W. Nan, R. Birringer, D.R. Clarke, H. Gleiter, Effective thermal conductivity of particulate composites with interfacial thermal resistance, J. Appl. Phys., 81 (1997) 6692-6699.

[422] V. Tropsa, A. Ivankovic, J.G. Williams, Predicting residual stresses due to solidification in cast plastic plates, Plast. Rubber Compos., 26 (2000) 468-474.

[423] A. Guinier, G. Fournet, Small-angle scattering of X-rays, 1st ed., John Wiley & Sons, USA, 1955.

[424] I. Mutlay, L.B. Tudoran, Percolation behavior of electrically conductive graphene nanoplatelets/polymer nanocomposites: theory and experiment, Fuller. Nanotub. Car. N., 22 (2014) 413-433.

[425] G. Gnanaprakash, J. Philip, T. Jayakumar, B. Raj, Effect of digestion time and alkali addition rate on physical properties of magnetic nanoparticles, J. Phys. Chem. B, 111 (2007) 7978-7986.

[426] G.-J. Lee, C.K. Kim, M.K. Lee, C.K. Rhee, Facile synthesis of surface oxide free copper nanoparticles by in-situ coating with oleic acid, Powder Technol., 261 (2014) 143-146.

[427] M. Makowska, C. Kajdas, M. Gradkowski, Mechanism of boundary film formation from n-hexadecane, Lubr. Sci., 16 (2004) 101-110.

[428] C. Velez, M. Khayet, J.M. Ortiz de Zarate, Temperature-dependent thermal properties of solid/liquid phase change even-numbered n-alkanes:n-Hexadecane,n-octadecane and n-eicosane, Appl. Energy, 143 (2015) 383–394.

[429] H. Babaei, P. Keblinski, J.M. Khodadadi, Thermal conductivity enhancement of paraffins by increasing the alignment of molecules through adding CNT/graphene, Int. J. Heat Mass Transfer, 58 (2013) 209-216.

[430] J.-S. Yang, C.-L. Yang, M.-S. Wang, B.-D. Chen, X.-G. Ma, Crystallization of alkane melts induced by carbon nanotubes and graphene nanosheets: a molecular dynamics simulation study, Phys. Chem. Chem. Phys., 13 (2011) 15476-15482.

[431] F. El-Tantawy, K. Kamada, H. Ohnabe, In situ network structure, electrical and thermal properties of conductive epoxy resin–carbon black composites for electrical heater applications, Mater. Lett. , 56 (2002) 112–126.

[432] A. Yu, P. Ramesh, X. Sun, E. Bekyarova, M.E. Itkis, R.C. Haddon, Enhanced thermal conductivity in a hybrid graphite nanoplatelet-carbon nanotube filler for epoxy composites, Adv. Mater., 20 (2008) 4740-4744.

[433] R. Prasher, Thermal conductance of single-walled carbon nanotube embedded in an elastic half-space, Appl. Phys. Lett., 90 (2007) 143110.

[434] M. Xing, J. Yu, R. Wang, Experimental study on the thermal conductivity enhancement of water based nanofluids using different types of carbon nanotubes, Int. J. Heat Mass Transfer, 88 (2015) 609-616.
[435] P. Warrier, A. Teja, Effect of particle size on the thermal conductivity of nanofluids containing metallic nanoparticles, Nanoscale Res. Lett., 6 (2011) 247.
[436] G. Chen, Thermal conductivity and ballistic-phonon transport in the cross-plane direction of superlattices, Phys. Rev. B 57 (1998) 14958-14973.
[437] C. Vales-Pinzon, R.A. Medina-Esquivel, J. Ordonez-Miranda, J.J. Alvarado-Gil, Thermal transfer in mixtures of ethylene glicol with carbon coated iron nanoparticles under the influence of a uniform magnetic field, J. Alloys Compd., 643 (2015) S71-S74.
[438] X. Li, Y. Chen, S. Mo, L. Jia, X. Shao, Effect of surface modification on the stability and thermal conductivity of water-based SiO_2-coated graphene nanofluid, Thermochim. Acta, 595 (2014) 6-10.
[439] R. Lenin, P.A. Joy, Role of primary and secondary surfactant layers on the thermal conductivity of lauric acid coated magnetite nanofluids, J. Phys. Chem. C, 120 (2016) 11640–11651.
[440] K. Chu, C.-c. Jia, W.-s. Li, Effective thermal conductivity of graphene-based composites, Appl. Phys. Lett., 101 (2012) 121916.
[441] R.P. Singh, S.C. Kaushik, D. Rakshit, Melting phenomenon in a finned thermal storage system with graphene nano-plates for medium temperature applications, Energy Convers. Manag., 163 (2018) 86-99.
[442] D. Singh, J.Y. Murthy, T.S. Fisher, Effect of phonon dispersion on thermal conduction across Si/Ge interface, J. Heat Transfer, 133 (2011) 122401.
[443] P. Reddy, K. Castelino, A. Majumdar, Diffuse mismatch model of thermal boundary conductance using exact phonon dispersion, Appl. Phys. Lett., 87 (2005) 211908.
[444] B.B. Lahiri, S. Ranoo, A.W. Zaibudeen, J. Philip, Magnetic hyperthermia in magnetic nanoemulsions: Effects of polydispersity, particle concentration and medium viscosity, J. Magn. Magn. Mater., 441 (2017) 310-327.
[445] Y.-X. Zeng, X.-W. Zhong, Z.-Q. Liu, S. Chen, N. Li, Preparation and enhancement of thermal conductivity of heat transfer oil-based MoS_2 nanofluids, J. Nanomater., 2013 (2013) 270490.
[446] L. Yang, X. Chen, M. Xu, K. Du, Roles of surfactants and particle shape in the enhanced thermal conductivity of TiO_2 nanofluids, AIP Adv., 6 (2016) 095104.
[447] J.B. Ferguson, The system water-phenol, J. Phys. Chem., 31 (1927) 757-763.
[448] O.R. Howell, A study of the system water-phenol. part I. Densities, Proc. Royal Soc. Lond. Series A, 137 (1932) 418-433.
[449] H. Guo, N. Zhao, Interfacial layer simulation and effect on Cu-Ar nanofluids thermal conductivity using molecular dynamics method, J. Mol. Liq., 259 (2018) 40-47.
[450] P. Atkins, J.d. Paula, Physical Chemistry, 9th ed., Oxford university press, UK, 2010.
[451] T. Ebata, A. Fujii, N. Mikami, Vibrational spectroscopy of small-sized hydrogen-bonded clusters and their ions, Int. Rev. Phys. Chem., 17 (1998) 331-361.
[452] R. Parthasarathi, V. Subramanian, N. Sathyamurthy, Hydrogen bonding in phenol, water, and phenol-water clusters, J. Phys. Chem. A, 109 (2005) 843-850.
[453] G.M. Lampman, D.L. Pavia, G.S. Kriz, J.R. Vyvyan, Spectroscopy, 4th ed., Cengage Learning, USA, 2010.
[454] R.A. Friedel, Infrared spectra of phenols, J. Am. Chem. Soc., 73 (1951) 2881-2884.
[455] S.T. Latibari, M. Mehrali, M. Mehrali, T.M.I. Mahila, H.S.C. Metselaar, Synthesis, characterization and thermal properties of nanoencapsulated phase change materials via sol-gel method, Energy, 61 (2013) 664-672.
[456] N.L. Cheng, Solvents Handbook, 3rd ed., Chemistry Industry Press, Beijing, 2002.
[457] S.-H. You, I.-Y. Jeong, I.-C. Hwang, S.-J. Park, The solid–liquid equilibrium, excess molar volume and refractive deviation properties of binary systems containing dimethyl carbonate, anisole and phenol, Fluid Phase Equilib., 383 (2014) 21-26.

[458] E.R.H. Jones, Some observations on the system phenol + water, J. Phys. Chem., 31 (1927) 1316-1321.

[459] G. Abbate, U. Bernini, E. Ragozzino, F. Somma, The temperature dependence of the refractive index of water, J. Phys. D: Appl. Phys., 11 (1978) 1167-1172.

[460] J.F. Eykman, Recherches refractometriques, Rec. Trav. Chim., 14 (1895) 185-202.

[461] S.S. Kurtz, S. Amon, A. Sankin, Effect of temperature on density and refractive index, Ind. Eng. Chem., 42 (1950) 174-176.

[462] H.A. Frediani, Refractive index measurements at and above the melting point of solids, Ind. Eng. Chem., 14 (1942) 439-441.

[463] X. Ge, X. Wang, Estimation of freezing point depression, boiling point elevation and vapourization enthalpies of electrolyte solutions, Ind. Eng. Chem. Res., 48 (2009) 2229-2235.

[464] L. Pauling, General Chemistry, 3rd ed., W. H. Freeman and Company, San Francisco, 1970.

[465] S. Park, Y. Lee, Y.S. Kim, H.M. Lee, J.H. Kim, I.W. Cheong, W.G. Koh, Magnetic nanoparticle-embedded PCM nanocapsules based on paraffin core and polyurea shell, Colloid Surface A, 450 (2014) 46-51.

[466] J.E.S. Venart, R.C. Prasad, Thermal conductivity of phenol (C_6H_5OH), J. Chem. Eng. Data 25 (1980) 198-199.

[467] R. Sutherland, R. Davis, W. Seyer, Heat transfer effects-molecular orientation of octadecane, Ind. Eng. Chem., 51 (1959) 585-588.

[468] R.W. Powell, A.R. Challoner, W.F. Seyer, Correspondence. Measurement of thermal conductivity of n-octadecane, Ind. Eng. Chem., 53 (1961) 581-582.

[469] M. Nourania, N. Hamdami, J. Keramat, A. Moheb, M. Shahedi, Thermal behavior of paraffin-nano-Al_2O_3 stabilized by sodium stearoyl lactylate as a stable phase change material with high thermal conductivity, Renew. Energy, 88 (2016) 474-482.

[470] S. Deville, E. Siaz, R.K. Nalla, A.P. Tomsia, Freezing as a path to build complex composites, Science, 311 (2006) 515-518.

[471] K.M. Golden, S.F. Ackley, V.I. Lytle, The percolation phase transition in sea ice, Science, 282 (1998) 2238-2241.

[472] J.L. Barrat, F. Chiaruttini, Kapitza resistance at the liquid—solid interface, Mol. Phys., 101 (2003) 1605-1610.

[473] M. Vladkov, J.L. Barrat, Modeling transient absorption and thermal conductivity in a simple nanofluid, Nano Lett., 6 (2006) 1224-1228.

[474] N. Shenogina, R. Godawat, P. Keblinski, S. Garde, How wetting and adhesion afect thermal conductance of a range of hydrophobic to hydrophilic aqueous interfaces, Phys. Rev. Lett., 102 (2009) 156101.

[475] Z. Ge, D.G. Cahill, P.V. Braun, Thermal conductance of hydrophilic and hydrophobic Interfaces, Phys. Rev. lett., 96 (2006) 186101.

[476] Z. Wang, J.E. Alaniz, W. Jang, J.E. Garay, C. Dames, Thermal conductivity of nanocrystalline silicon: importance of grain size and frequency-dependent mean free paths, Nano Lett., 11 (2011) 2206-2213.

[477] C.-K. Leong, D.D.L. Chung, Carbon black dispersions as thermal pastes that surpass solder in providing high thermal contact conductance, Carbon, 41 (2003) 2459–2469.

[478] A. Sari, K. Kaygusuz, Some fatty acids used for latent heat storage: thermal stability and corrosion of metals with respect to thermal cycling, Renew. Energy, 28 (2003) 939-948.

[479] J. Wang, H. Xie, Z. Xin, Thermal properties of heat storage composites containing multiwalled carbon nanotubes, J. Appl. Phys., 104 (2008) 113537.

[480] M. Mehrali, S.T. Latibari, M. Mehrali, T.M.I. Mahlia, E. Sadeghinezhad, H.S.C. Metselaar, Preparation of nitrogen-doped graphene/palmitic acid shape stabilized composite phase change material with remarkable thermal properties for thermal energy storage, Appl. Energy, 135 (2014) 339-349.

[481] T. Lee, Y.H. Chiu, Y. Lee, H.L. Lee, Thermal properties and structural characterizations of new types of phase change material: anhydrous and hydrated palmitic acid/camphene solid dispersions, Thermochim. Acta, 575 (2014) 81-89.

[482] M.J. Frisch, G.W. Trucks, H.B. Schlegel, G.E. Scuseria, M.A. Robb, J.R. Cheeseman, G. Scalmani, V. Barone, G.A. Petersson, H. Nakatsuji, X. Li, M. Caricato, A. Marenich, J. Bloino, B.G. Janesko, R. Gomperts, B. Mennucci, H.P. Hratchian, J.V. Ortiz, A.F. Izmaylov, J.L. Sonnenberg, D. Williams-Young, F. Ding, F. Lipparini, F. Egidi, J. Goings, B. Peng, A. Petrone, T. Henderson, D. Ranasinghe, V.G. Zakrzewski, J. Gao, N. Rega, G. Zheng, W. Liang, M. Hada, M. Ehara, K. Toyota, R. Fukuda, J. Hasegawa, M. Ishida, T. Nakajima, Y. Honda, O. Kitao, H. Nakai, T. Vreven, K. Throssell, J.A. Montgomery Jr., J.E. Peralta, F. Ogliaro, M. Bearpark, J.J. Heyd, E. Brothers, K.N. Kudin, V.N. Staroverov, T. Keith, R. Kobayashi, J. Normand, K. Raghavachari, A. Rendell, J.C. Burant, S.S. Iyengar, J. Tomasi, M. Cossi, J.M. Millam, M. Klene, C. Adamo, R. Cammi, J.W. Ochterski, R.L. Martin, K. Morokuma, O. Farkas, J.B. Foresman, D.J. Fox, R.B. Gaussian 09, Gaussian Inc. Wallingford CT, (2009).

[483] A.D. Becke, Density-functional exchange-energy approximation with correct asymptotic behavior, Phys. Rev. A, 38 (1988) 3098-3100.

[484] C. Lee, W. Yang, R.G. Parr, Development of the Colle-Salvetti correlation-energy formula into a functional of the electron density, Phys. Rev. B, 37 (1988) 785-789.

[485] R.V. Solomon, S.A. Vedha, P. Venuvanalingam, A new turn in codon–anticodon selection through halogen bonds, Phys. Chem. Chem. Phys., 16 (2014) 7430-7440.

[486] N.J.M. Amezaga, S.C. Pamies, N.M. Peruchena, G.L. Sosa, Halogen bonding: a study based on the electronic charge density, J. Phys. Chem. A, 114 (2010) 552-562.

[487] G. Fang, H. Li, L. Cao, F. Shan, Preparation and thermal properties of form-stable palmitic acid/active aluminum oxide composites as phase change materials for latent heat storage, Mater. Chem. Phys., 137 (2012) 558-564.

[488] Y. Zhang, B. Yang, K. Li, D. Hou, C. Zhao, J. Wang, Electrospun porous poly(tetrafluoroethylene-co-hexafluoropropylene-co-vinylidenefluoride) membranes for membrane distillation, RSC Adv., 7 (2017) 56183-56193.

[489] S. Kahwaji, M.A. White, Prediction of the properties of eutectic fatty acid phase change materials, Thermochim. Acta, 660 (2018) 94-100.

[490] H. Fauzi, H.S.C. Metselaar, T.M.I. Mahlia, M. Silakhori, H. Nur, Phase change material: Optimizing the thermal properties and thermal conductivity of myristic acid/palmitic acid eutectic mixture with acid-based surfactants, Appl. Therm. Eng., 60 (2013) 261-265.

[491] J.L. Zeng, Z. Cao, D.W. Yang, F. Xu, L.X. Sun, X.F. Zhang, L. Zhang, Effects of MWCNTs on phase change enthalpy and thermal conductivity of a solid- liquid organic PCM, J. Therm. Anal. Calorim., 95 (2009) 507–512.

[492] J. Sohns, B. Seifert, E. Hahne, The effect of impurities on the melting temperature and the heat of fusion of latent heat storgae materials, Int. J. Thermphys., 2 (1981) 71-87.

[493] H. Babaei, P. Keblinski, J.M. Khodadadi, Thermal conductivity enhancement of paraffins by increasing the alignment of molecules through adding CNT/grapheneq, Int. J. Heat Mass Transfer, 58 (2013) 209–216.

[494] X. Liu, Z. Rao, Experimental study on the thermal performance of graphene and exfoliated graphite sheet for thermal energy storage phase change material, Thermochim. Acta, 647 (2017) 15-21.

[495] M. Bhattacharya, Polymer nanocomposites—a comparison between carbon nanotubes, graphene, and clay as nanofillers, Materials, 9 (2016) 262.

[496] J.L. Zeng, S.H. Zheng, S.B. Yu, F.R. Zhu, J. Gan, L. Zhu, Z.L. Xiao, X.Y. Zhu, Z. Zhu, L.X. Sun, Z. Cao, Preparation and thermal properties of palmitic acid/polyaniline/exfoliated graphite nanoplatelets form-stable phase change materials, Appl. Energy, 115 (2014) 603-609.

[497] P. Bose, V.A. Amirtham, A review on thermal conductivity enhancement of paraffin wax as latent heat energy storage material, Renew. Sustain. Energy Rev., 65 (2016) 81–100.

[498] P.K. Das, A review based on the effect and mechanism of thermal conductivity of normal nanofluids and hybrid nanofluids, J. Mol. Liq., 240 (2017) 420-446.
[499] S. Shenogin, A. Bodapati, L. Xue, R. Ozisik, P. Keblinski, Effect of chemical functionalization on thermal thermal transport of carbon nanotube composites, Appl. Phys. Lett., 85 (2004) 2229-2231.
[500] Y. Li, X. Zhang, J.M. Munyalo, Z. Tian, J. Ji, Preparation and thermophysical properties of low temperature composite phase change material octanoic-lauric acid/expanded graphite, J. Mol. Liq., 277 (2019) 577-583.
[501] Z. Meng, D. Han, D. Wu, H. Zhu, Q. Li, Thermal Conductivities, Rheological Behaviors and Photo-thermal Properties of Ethylene Glycol-based Nanofluids Containing Carbon Black Nanoparticles, Procedia Eng., 36 (2012) 521 – 527.
[502] A.M. Abyzov, S.V. Kidalov, F.M. Shakhov, Thermal conductivity of the diamond-paraffin wax composite, Phys. Solid State, 53 (2011) 48-52.
[503] S. Pavithra, S. Manikandan, M.K. Saranprabhu, B. Sivapalan, K.S. Rajan, Ultrasonication assisted co-dispersion of nanostructured magnesium-lined paraffin wax and magnesium oxide in a heat transfer fluid for energy related applications, J. Mol. Liq., 271 (2018) 828-837.
[504] S. Ye, Q. Zhang, D. Hu, J. Feng, Core-shell-like structured graphene aerogel encapsulating paraffin: shape-stable phase change material for thermal energy storage, J. Mater. Chem. A, 3 (2015) 4018-4025.
[505] J. Xiang, L.T. Drzal, Investigation of exfoliated graphite nanoplatelets (xGNP) in improving thermal conductivity of paraffin wax-based phase change material, Solar Energy Mater. Sol. Cells, 95 (2011) 1811-1818.
[506] E. Onder, N. Sarier, Thermal regulation finishes for textiles, in: R. Paul (Ed.) Functional finishes for textiles, Woodhead Publishing, Cambridge, UK, 2014, pp. 17-98.
[507] G.B. Tiwari, O.S. Tyagi, S.P. Srivastava, D.C. Pandey, S.K. Goyal, V.B. Kapoor, Phase transition studies in petroleum waxes through FT-IR spectroscopy and calorimetry, Indian J. Chem. Technol., 4 (1997) 29-33.
[508] Z.-T. Yu, X. Fang, L.-W. Fan, X. Wang, Y.-Q. Xiao, Y. Zeng, X. Xu, Y.-C. Hu, K.-F. Cen, Increased thermal conductivity of liquid paraffin-based suspensions in the presence of carbon nano-additives of various sizes and shapes, Carbon, 53 (2013) 277-285.
[509] N. Ukrainczyk, S. Kurajica, J. Sipusic, Thermophysical comparison of five commercial paraffin waxes as latent heat storage materials, Chem. Biochem. Eng. Q., 24 (2010) 129-137.
[510] Z.H. Rao, G.Q. Zhang, Thermal properties of paraffin wax-based composites containing graphite, Energ. Source Part A, 33 (2011) 587-593.
[511] X.-Q. Wang, A.S. Mujumdar, A review on nanofluids - part I: theoretical and numerical investigations Braz. J. Chem. Eng., 25 (2008) 613-630.
[512] P.Keblinski, S.R. Phillpot, S.U.S. Choi, J.A. Eastman, Mechanisms of heat flow in suspensions of nano-sized particles (nanofluids), Int. J. Heat Mass Transfer, 45 (2002) 855-863.
[513] H. He, R. Fu, Y. Han, Y. Shen, X. Song, Thermal conductivity of ceramic particle filled polymer composites and theoretical predictions, J. Mater. Sci., 42 (2007) 6749-6754.
[514] P.E. Khizhnyak, A.V. Chechetkin, A.P. Glybin, Thermal conductivity of carbon black, J. Eng. Phys., 37 (1979) 1073-1075.
[515] R. Azizian, E. Doroodchi, B. Moghtaderi, Influence of Controlled Aggregation on Thermal Conductivity of Nanofluids, J. Heat Transfer, 138 (2016) 021301.
[516] A. Zeiny, H. Jin, L. Bai, G. Lin, D. Wen, A comparative study of direct absorption nanofluids for solar thermal applications, Sol. Energy, 161 (2018) 74-82.
[517] G. Ni, N. Miljkovic, H. Ghasemi, X. Huang, S.V. Boriskina, C.-T. Lin, J. Wang, Y. Xu, M.M. Rahman, T. Zhang, G. Chen, Volumetric solar heating of nano fluids for direct vapor generation, Nano Energ., 17 (2015) 290-301.
[518] R.A. Taylor, P.E. Phelan, T.P. Otanicar, R. Adrian, R. Prasher, Nanofluid optical property characterization: towards efficient direct absorption solar collectors, Nanoscale Res. Lett., 6 (2011) 225.

[519] C.F. Bohren, D.R. Huffman, Absorption and scattering of light by small particles, Wiley, New York, USA, 1998.
[520] D. Tzarouchis, A. Sihvola, Light scattering by a dielectric sphere: perspectives on the Mie resonances, Appl. Sci., 8 (2018) 184.
[521] J.E. McDonald, Visibility reduction due to jet-exhaust carbon particles, J. Appl. Meteor., 1 (1962) 391-398.
[522] K. Tuncbilek, A. Sari, S. Tarhan, G. Ergunes, K. Kaygusuz, Lauric and palmitic acids eutectic mixture as latent heat storage material for low temperature heating applications, Energy, 30 (2005) 677-692.
[523] Z. Yang, Y. Deng, J. Li, Preparation of porous carbonized woods impregnated with lauric acid as shape-stable composite phase change materials, Appl. Therm. Eng., 150 (2019) 967-976.
[524] L. Han, G. Ma, S. Xie, J. Sun, Y. Jia, Y. Jing, Thermal properties and stabilities of the eutectic mixture: 1,6-hexanediol/ lauric acid as a phase change material for thermal energy storage, Appl. Therm. Eng., 116 (2017) 153-159.
[525] J. Zuo, W. Li, L. Weng, Thermal properties of lauric acid/1-tetradecanol binary system for energy storage, Appl. Therm. Eng., 31 (2011) 1352-1355.
[526] A. Dorinson, M.R. McCorkle, A.W. Ralston, Refractive indices and densities of normal saturated fatty acids in the liquid state, J. Am. Chem. Soc., 64 (1942) 2739-2741.
[527] B. Zalba, J. M-Marın, L.F. Cabeza, H. Mehling, Review on thermal energy storage with phase change: materials, heat transfer analysis and applications, Appl. Therm. Eng., 23 (2003) 251-283.
[528] J.U. Maheswari, C. Krishnan, S. Kalyanaraman, P. Selvarajan, Growth and characterization of an organic nonlinear optical material-lauric acid crystal, Mater. Res. Express, 3 (2016) 105101.
[529] Z. Zhang, G. Alva, M. Gu, G. Fang, Experimental investigation on neoctadecane/polystyrene/expandedgraphite composites as formestable thermal energy storage materials, Energy, 157 (2018) 625-632.
[530] Q. Zhang, K. Cui, J. Feng, J. Fan, L. Li, L. Wu, Q. Huang, Investigation on the recovery performance of olefin block copolymer/hexadecane form stable phase change materials with shape memory properties, Sol. Energ. Mat. Sol. Cells, 132 (2015) 632–639.
[531] D. Rozanna, A. Salmiah, T.G. Chuah, R. Medyan, S.Y.T. Choong, M. Saari, A Study on Thermal characteristics of phase change material (PCM) in gypsum board for building application, J. Oil Palm Res., 17 (2005) 41-46.
[532] Z. Xiangfa, X. Hanning, F. Jian, Z. Changrui, J. Yonggang, Preparation and thermal properties of paraffin/porous silica ceramic composite, Compos. Sci. Technol., 69 (2009) 1246-1249.
[533] B. Wu, Y. Zhao, Q. Liu, C. Zhou, X. Zhang, J. Lei, Form-stable phase change materials based on castor oil and palmitic acid for renewable thermal energy storage, J. Therm. Anal. Cal., 137 (2019) 1225-1232.
[534] S. Yu, X. Wang, D. Wu, Microencapsulation of n-octadecane phase change material with calcium carbonate shell for enhancement of thermal conductivity and serving durability: synthesis, microstructure, and performance evaluation, Appl. Energy, 114 (2014) 632-643.
[535] Y. Jiang, D. Wang, T. Zhao, Preparation, characterization, and prominent thermal stability of phase-change microcapsules with phenolic resin shell and n-hexadecane core, J. Appl. Polym. Sci., 104 (2007) 2799-2806.